7th International Conference on

Numerical and Symbolic Computation

Developments and Applications

PROCEEDINGS

April, 10 - 11

ISEL – Instituto Superior de Engenharia de Lisboa

Lisboa, Portugal

SYMCOMP 2025 – 7th International Conference on Numerical and Symbolic Computation: Developments and Applications

Proceedings in digital support (ISBN: 978-989-99410-8-3)

Edited by APMTAC – Associação Portuguesa de Mecânica Teórica, Aplicada e Computacional

Editors: Maria Amélia Loja (IDMEC – IST; ISEL-CIMOSM), Joaquim Infante Barbosa (IDMEC - IST; ISEL-CIMOSM), André Carvalho (IDMEC – IST; ISEL-CIMOSM), Inês Jerónimo Barbosa (IDMEC – IST; ISEL-CIMOSM), Ana Martins (ISEL-CIMOSM; ISEL-CIMA, DM) e José Alberto Rodrigues (ISEL-CIMOSM; ISEL-CIMA, DM)

April 2025

1 – Introduction

The Organizing Committee of SYMCOMP 2025 – 7th International Conference on Numerical and Symbolic Computation: Developments and Applications warmly welcomes all participants and acknowledges the invaluable contributions of the authors, which are essential to the success of this event.

About SYMCOMP 2025

This Seventh International Conference on Numerical and Symbolic Computation is promoted by APMTAC (Associação Portuguesa de Mecânica Teórica, Aplicada e Computacional) and organized under the framework of IDMEC (Instituto de Engenharia Mecânica, IST, Universidade de Lisboa).

As an ECCOMAS Thematic Conference, SYMCOMP 2025 aims to bring together academic and scientific communities engaged in Numerical and Symbolic Computation across diverse fields, fostering collaboration and knowledge exchange.

Main Goals of SYMCOMP 2025

- To establish the state of the art and highlight innovative applications of Numerical and Symbolic Computation in various disciplines, including Engineering, Physics, Mathematics, Economics, Management, Architecture, and more.
- To promote the exchange of ideas and the dissemination of research within the broad scope of Numerical and Symbolic Computation.
- To encourage the participation of young researchers in scientific conferences.
- To facilitate networking among APMTAC members (Portuguese Society for Theoretical, Applied, and Computational Mechanics) and other scientific organizations dedicated to computation, while also fostering new memberships.

A Call for Engagement

We invite all participants to maintain a proactive and collaborative spirit, engaging in discussions, exchanging ideas, exploring research topics, and seeking future partnerships to advance the field.

Acknowledgments

The Organizing Committee of SYMCOMP 2025 extends its deepest gratitude to all colleagues involved in the Scientific Committee, Advisory Committee and Secretariat for their dedication and cooperation. We hope everyone has enjoyed contributing to this project, which we are confident will continue to thrive in the future. Our thanks to you all.

Amélia Loja (IDMEC – IST; ISEL-CIMOSM), Joaquim Barbosa (IDMEC - IST; ISEL-CIMOSM), André Carvalho (IDMEC – IST; ISEL-CIMOSM), Inês Barbosa (IDMEC – IST; ISEL-CIMOSM), Ana Martins (ISEL-CIMOSM; ISEL-CIMA, DM) and José Alberto Rodrigues (ISEL-CIMOSM; ISEL-CIMA, DM)

2 – CONFERENCE BOARD

Chairperson

Maria Amélia Ramos Loja (CIMOSM - ISEL; IDMEC – IST)

Instituto Superior de Engenharia de Lisboa

Rua Conselheiro Emídio Navarro, 1, 1959-007 Lisboa

Email : amelia.loja@isel.pt, ; amelialoja@tecnico.ulisboa.pt

Advisory Committee

- Carlos Mota Soares (IDMEC - IST)
- António Ferreira (FEUP-UP; INEGI - LAETA)

Organizing Committee

- Amélia Loja (IDMEC – IST ; CIMOSM - ISEL)
- Joaquim Infante Barbosa (IDMEC – IST ; CIMOSM - ISEL)
- Inês Barbosa (IDMEC – IST ; CIMOSM - ISEL)
- André Carvalho (IDMEC – IST ; CIMOSM - ISEL)
- Ana Martins (CIMOSM - ISEL, ISEL-CIMA, DM)
- Ana Neves (FEUP – UP)
- José Alberto Rodrigues (CIMOSM - ISEL, ISEL-CIMA, DM)

SCIENTIFIC COMMITTEE

SPONSORS

ECCOMAS – European Community on Computational Methods in Applied Sciences

APMTAC – Associação Portuguesa de Mecânica Teórica, Aplicada e Computacional, (Portuguese Society for Theoretical, Applied and Computational Mechanics), ECCOMAS Member Association;

IDMEC – IST , LAETA – Instituto de Engenharia Mecânica, Laboratório Associado de Energia, Transportes e Aeroespacial (Mechanical Engineering Institute/Associated Laboratory for Energy, Transports and Aeronautics);

ISEL - IPL— Lisbon School of Engineering, Polytechnic University of Lisbon

CIMOSM—Research Centre on Modelling and Optimization of Multifunctional Systems, ISEL - IPL

WOLFRAM RESEARCH

ORGANIZING INSTITUTION:

IDMEC/LAETA – Instituto de Engenharia Mecânica/Laboratório Associado de Energia, Transportes e Aeroespacial (Mechanical Engineering Institute/Associated Laboratory for Energy, Transports and Aeronautics).

GENERAL INFORMATION

SECRETARIAT

Maria José Branquinho

IDMEC - IST – Instituto de Engenharia Mecânica

CPM - Centro de Projecto Mecânico

Av. Rovisco Pais, 1, 1049 - 001 Lisboa

Email: mariabranquinho@tecnico.ulisboa.pt Tel: (+351) 218417351

Registration on SYMCOMP2025

Until Monday, 31/03/2025

PLACE OF THE EVENT

ISEL – Instituto Superior de Engenharia de Lisboa, Edifício C, Auditório Eng. Ferreira Cardoso, Rua Conselheiro Emídio Navarro, 1, 1959-007 Lisboa.

https://maps.app.goo.gl/oYoAQysPfY9JcZAT9

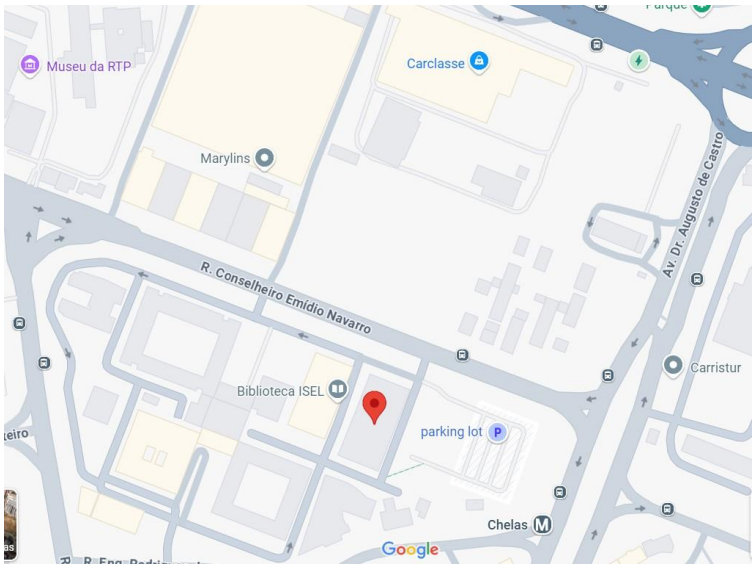

Coffee break

Coffee break will take place at the Conference hall and is open to all the participants. We ask you please to use always your identification.

Lunches

The lunch will take place at restaurant located at ISEL – Instituto Superior de Engenharia de Lisboa, Edifício A . Rua Conselheiro Emídio Navarro, 1, 1959-007 Lisboa

https://maps.app.goo.gl/FfTKJpDfhBZ2kpmF8

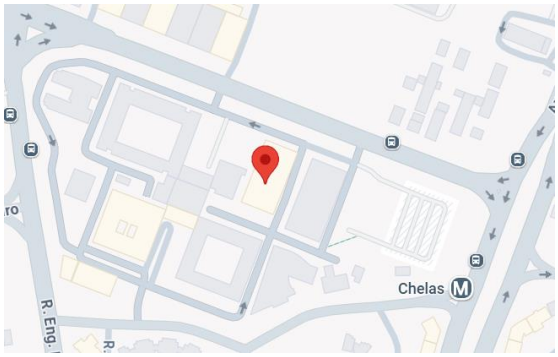

Conference dinner

The Conference dinner will take place at the restaurant of Jupiter Lisboa Hotel, Avenida da República, 46, 1050-195 Lisboa, Thursday, 20:00h.

Link: https://maps.app.goo.gl/ArkJ8tVgqB9E4aUp9

Wolfram/Alpha Pro Awards will be delivered during the dinner.

Participants should arrive there by their own.

Further details will be provided during the conference.

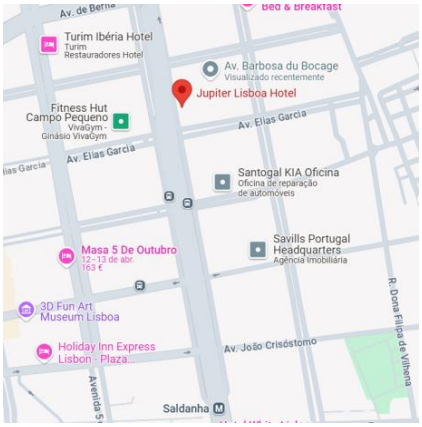

Oral – In-person presentation
Online – Online live

THURSDAY, APRIL, 10

ISEL – Lisbon School of Engineering -Building C

OPENING CEREMONY: 08:15 – 08:25 – (*Room A)*

SP 01 **Oral**	**PLENARY SESSION I (*Room A*) – CHAIR: *Prof. Amélia Loja*** **Joining by Forming of Busbars for Electric Distribution Systems** ***Professor Paulo Martins, Instituto Superior Técnico, Universidade de Lisboa***	**08:30 - 09:15**

ID **A06** **IL01** **Online**	**INVITED LECTURE I (*Room A*) – CHAIR: *Prof. Ana Neves*** **Higher Order Equivalent Layer-wise Theory for Multifield Analysis of Curved Laminated Structures** ***Prof. F. Tornabene, Dr. M. Viscoti and Prof. R. Dimitri*** ***University of Salento, Lecce, Italy***	**09.20 - 09.50**

SESSION I (*Room A*): Computation Techniques in Fluid Flows and Control **CHAIR: *Prof. Aleksandr Cherniaev and Prof. Christina Katsamaki***		**09:50 – 10:50**
ID	**COMMUNICATION TITLE**	**AUTHORS**
A01 **Oral**	**Implementation of an SPH Solver for Quasi-Incompressible Fluids in JULIA**	**Aleksandr Cherniaev**
A53 **Online**	**Optimizing Hypersonic Intakes Through 1D-Based Design Exploration and Multi-Objective Surrogate Modeling**	**Ibrahim Gül, Bayram Celik**
A60 **Oral**	**Some Computational Tools for Solving a Selection of Problems in Control Theory**	**Christina Katsamaki, Alexander Demin, Fabrice Rouillier**

THURSDAY, APRIL, 10

ISEL – Lisbon School of Engineering -Building C

SESSION II (*Room B*): Algebras Structures and Graphic Topology CHAIR: *Prof. Ana Martins*		09:50–10:50
ID	**COMMUNICATION TITLE**	**AUTHORS**
A22 Online	Study of Combinatorial Structures Associated with TORTKARA Algebras	Jesús Baena
A32 Online	Some Results on Graphic Topology Defined on Tournaments	Inés Mora-Caro, Desamparados Fernández-Ternero
A08 Online	Computational Treatment of the Hierarchy of General and Evolution Algebras	Adolfo Vázquez Ruiz, Rafael Vázquez Ruiz, Juan Núñez Valdés

COFFEE BREAK (10:50 – 11:10)

SESSION III (*Room A*): Computational Mechanics I CHAIR: *Prof. Miguel Neves and Prof. André Carvalho*		11:10 – 12:30
ID	**COMMUNICATION TITLE**	**AUTHORS**
A13 Oral	Moment Integration Scheme for Higher-Order Virtual Elements In Inelastic Problems	Yongbin Choi, Tobias Bode, Philipp Junker
A14 Oral	Automating the Derivation of Equations for 1D Mass-Spring-Damper Models in Matlab	Miguel Neves
A51 Oral	Damping from Thermoelasticity in Structures Under Torsional Loading	André Carvalho
A67 Oral	A Spring-cable Multibody Model for Energy Absorbing Structures in Railway Vehicle Crashworthiness	João Milho, David Bronze

LUNCH (12.30-14.00)

THURSDAY, APRIL, 10

ISEL – Lisbon School of Engineering -Building C

ID	INVITED LECTURE II (*Room A*) *CHAIR – Prof. Amélia Loja* .	14.00 - 14.30
IL02 Online	Agentic AI in Healthcare: a New Era Has Arrived Dr. Eva Sousa, University of Hull, Hull, United Kingdom	

SESSION IV (*Room A*): Efficient Numerical Schemes for Singular Problems CHAIR: *Prof. Luísa Morgado and Prof. Luís Ferrás*		14:35 – 15:35
ID	**COMMUNICATION TITLE**	**AUTHORS**
A36 Oral	Numerical Simulation of Current Flows in Disordered Materials	Lara Carvalho, G. Carvalho, Luís Ferrás, Magda Rebelo, Luís Morgado, Maria Morgado
A55 Oral	Time-fractional Advection-diffusion Model for Transient Currents in Disordered Materials	Luís Morgado, Luísa Morgado, Luís Ferrás, Anselmo Falorca
A31 Oral	An IMEX Method for Nonlinear Time-fractional Diffusion Equations	Magda Rebelo, Luís Ferrás, Luísa Morgado, Luís Morgado

SESSION V (*Room B*): Orthogonal Polynomials, Special Functions and Applications CHAIR: *Prof. Zélia Rocha and Prof. Teresa Mesquita*		14:30–15:30
ID	**COMMUNICATION TITLE**	**AUTHORS**
A09 Oral	On Connection Coefficients of D-Orthogonal Polynomials in Terms of Orthogonal Polynomials	Teresa Mesquita, Zélia da Rocha
A10 Online	On Generating Functions of Some Perturbations of a Second-Order Self-Associated Orthogonal Sequence: An Approach Based on Symbolic Computations	Zélia da Rocha
A38 Online	Symbolic Computation Applied in the Context of Quantum Calculus	Ângela Macedo

COFFEE BREAK (15:30 – 15:50)

THURSDAY, APRIL, 10

ISEL – Lisbon School of Engineering -Building C

SESSION VI (*Room A*): Efficient Numerical Schemes for Singular Problems **CHAIR: *Prof. Magda Rebelo and Prof.Luís Ferrás***		**15:50 – 17:10**
ID	**COMMUNICATION TITLE**	**AUTHORS**
A33 **Oral**	**Finite Difference Schemes for Couette flows with Generalised Integral Viscoelastic Models**	**Elias Silva, Magda Rebelo, Luís Ferrás, Luís Morgado, Maria Morgado**
A35 **Oral**	**Finite Difference Methods for Fractional K-BKZ Models**	**Gonçalo Carvalho, L. Carvalho, Luís Ferrás, Magda Rebelo, Luís Morgado, Luísa Morgado**
A39 **Oral**	**Adaptive Mesh Algorithms for Distributed-Order Differential Equations**	**Maria Morgado, Luís Morgado, Luís Ferrás, Magda Rebelo**
A42 **Oral**	**Influence of Relaxation Functions on Viscoelastic Data Fitting: A Parameter Analysis**	**Luís Ferrás, Maria Morgado, Magda Rebelo, Luís Morgado**

SESSION VII (*Room B*): Applications in Health Sciences and Technologies: Numerical Computation Developments **CHAIR: *Prof. Lina Vieira and Prof. Margarida Ribeiro***		**15:50 – 17:10**
ID	**COMMUNICATION TITLE**	**AUTHORS**
A19 **Oral**	**Measuring Thoracic Muscle by Chest CT to Foresee Sarcopenia in Post-Covid 19 Patients**	**Maria Margarida Ribeiro**
A20 **Oral**	**Amputations in Diabetics: Statistical Modeling and Trends in Portugal (2000–2023)**	**Elisabete Carolino**
A30 **Oral**	**Advanced Imaging of Parkinson's: Evaluating the Striatum and Substantia Nigra with Datscan Spect and T2W MRI**	**Luís Mesquita, Margarida Ribeiro, Lina Vieira**
A54 **Oral**	**Mathematical Modeling of Metabolic Reprogramming and Therapeutic Strategies in Non-Small Cell Lung Cancer: A Flux Balance and Variability Analysis Approach**	**José Rodrigues, Jacinta Serpa, João Lopes, Cindy Mendes, Luís Gonçalves**

CONFERENCE DINNER – 20.00H

FRIDAY, APRIL, 11

ISEL – Lisbon School of Engineering -Building C

SP 02 Oral	**PLENARY SESSION II (*Room A*) – CHAIR: *Prof. Amélia Loja*** **Developments in multimodal large language models** ***Professor Arlindo Oliveira, Instituto Superior Técnico, Universidade de Lisboa***	**08:30 - 09:15**

ID **A04** **IL03**	**INVITED LECTURE III (*Room A*) – CHAIR: *Prof. Amélia Loja*** **Incidence of Reputational Periodicity** ***Prof. Peter Mitic (University College London)***	**09.20 - 09.50**

ID **IL04**	**INVITED LECTURE IV (*Room A* – CHAIR: *Prof. Cláudia Casaca*** **Porous Burners: a Review of Modeling Approaches and Applications in the Energy Transition** ***Prof. Isabel Malico (University of Évora)***	**09.55 - 10.25**

COFFEE BREAK (10:30 – 10:50)

SESSION VIII (*Room A*): Simulation and Optimization of Fluid Flow, Heat and Mass Transfer **CHAIR: *Prof. Isabel Malico and Prof. Cláudia Casaca***		**10:50 – 11:50**
ID	**COMMUNICATION TITLE**	**AUTHORS**
A11 Oral	**CFD Analysis of Jet Deflection in Thermal Recuperative Incinerators**	**Francisco Zdanowski, Isabel Malico**
A23 Oral	**Preliminary Simulation Results of a Molten Salt Thermal Storage Tank for Concentrated Solar Power**	**Júnior Mané, Isabel Malico, N. Domingues, P. Horta, Radia El Cadi.**
A40 Oral	**A Machine-Learning–based Framework for Efficient Turn-down Ratio Determination in Porous Burners**	**Sérgio Costa, Isabel Malico, Fernando Janeiro**

FRIDAY, APRIL, 11

ISEL – Lisbon School of Engineering -Building C

SESSION IX (*Room B*): Fractional Differential Equations **CHAIR: *Prof. José Alberto Rodrigues***		**10:50 – 11:50**
ID	**COMMUNICATION TITLE**	**AUTHORS**
A15 **Online**	**Operator Techniques for The Solution of Caputo Fractional Differential Equations**	**Inga Telksniene**
A25 **Online**	**The Operational Spectral Tau Method to Approximate Solution of Functional Differential Equations**	**José Matos, Paulo Vasconcelos, José Matos**
A26 **Online**	**Doing Fractional Calculus in the Tau Toolbox**	**José Matos, Paulo Vasconcelos, José Matos**
A37 **Online**	**Grüss Type Inequalities Within the General Quantum Calculus**	**José Luis Cardoso**

SESSION X (*Room A*): Sustainability and Digital Twins **CHAIR: *Prof. Rui Ruben and Prof. João Milho***		**11:50–12:30**
ID	**COMMUNICATION TITLE**	**AUTHORS**
A52 **Oral**	**How Teaching Methods Can Influence the Carbon Footprint**	**Rui Ruben, Luís Coelho, Judite Vieira, Marcelo Gaspar, Paulo Carvalho, Hachimi Abba, Jorma Sateri, Christian Gotz**
A59 **Oral**	**A Finite Element Model to Study Posterior Malleolus Surgery Approach**	**Guilherme Lopes, Rui Ruben, Inês Barbosa, Joana Contente, Sofia Dantas**

SESSION XI (*Room B*): Computational in Operator Theory and Optimization **CHAIR: *Prof. Ana Martins***		**11:50 - 12:20**
ID	**COMMUNICATION TITLE**	**AUTHORS**
A61 **Online**	**Symbolic Computation Applied to Function Factorization Concept: The Rational Scalar Case**	**Ana Conceição, Jéssica Pires, Celestino Coelho**
A62 **Online**	**Computational Analysis of Levenberg-Marquardt Method in Nonlinear Least Squares Problems**	**Ana Conceição, Vasco Ricardo, Celestino Coelho**

LUNCH (12.30-14.00)

FRIDAY, APRIL, 11

ISEL – Lisbon School of Engineering -Building C

ID	INVITED LECTURE V (*Room A*) – CHAIR: *Prof. João Milho*	14.00 - 14.30
IL05 Oral	Meshless Methods in Mechanics and Biomechanics: Current and Trend Applications Prof. Jorge Belinha, INEGI, ISEP – School of Engineering, Polytechnic of Porto	

SESSION XII (*Room A*): Machine and Deep Learning Techniques Applied to Computational Mechanics CHAIR: *Prof. Jorge Belinha and Prof. Inês Barbosa*		14:30 – 15:30
ID	**COMMUNICATION TITLE**	**AUTHORS**
A16 Oral	Neural Networks to Surrogate Bone Remodelling Analysis in the Calcaneus	Jorge Belinha, Ana Pais, Fernando Alves
A17 Online	A Convolutional Neural Network to Generate Unit Cell Geometries with Target Elastic Properties	Ana Pais, Jorge Lino Alves, Jorge Belinha
A18 Oral	Structural Topology Optimization of the Wheel's Spokes of NASA's Perseverance Rover Using an Advanced Discretization Technique	Daniel Rodrigues, Jorge Belinha, Jure Trdin

SESSION XIII (*Room B*): Artificial Intelligence Applications to Healthcare Datasets CHAIR: *Prof. Inês Barbosa and Prof. Eva Sousa*		14:30–15:30
ID	**COMMUNICATION TITLE**	**AUTHORS**
A02 Online	Synthetic Microscopic Platelets Images Generation Using Wgan-gp	Itunuoluwa Abidoye, Frances Ikeji, Charlie A.Coupland, Simon D. Calaminus, Eva Sousa
A12 Online	A Pilot Study on Fine-Tuning Named Entity Recognition for Clinical Tag Extraction Using Pretrained Language Models: the Tut-all Experience	Adeyemi Victor Gbadamosi, Alberto Moreno, Martin Deutsch, Nick Sander, Claire Cashmore, Eva Sousa
A56 Online	Improving PD-L1 Expression Prediction in non-Small Cell Lung Cancer Using Radiomic Analysis and Ensemble Machine Learning Models on Whole-Body vs 18F-FDG Lung PET/CT Data	Steven Olawale, Azeem Saleem, Ged Avery, Eva Sousa
A57 Online	Improving PD-L1 Expression Prediction in non-Small Cell Lung Cancer Using Radiomic Analysis and Deep Learning Models on Whole-Body VS Lung 18F-FDG PET/CT Data	Steven Olawale, Azeem Saleem, Ged Avery, Eva Sousa

FRIDAY, APRIL, 11

ISEL – Lisbon School of Engineering -Building C

SESSION XIV (*Room A*): Data Analytics and Forecasting CHAIR: *Prof. Ana Martins and Prof. Alda Carvalho*		15:30 – 16:30
ID	**COMMUNICATION TITLE**	**AUTHORS**
A34 Online	Analysis of Thoracic Aortic Aneurysm CTA Scans Using Spatial Statistics	Katalina Rodríguez, Alda Carvalho, R. Valente, José Xavier, António Tomás
A29 Oral	Statistical Analysis and Quantification of Ascending Thoracic Aortic Aneurysms Dynamics	Rodrigo Valente, André Mourato, Alda Carvalho, Moisés Brito, José Xavier, Stéphane Avril, António Tomás, José Fragata
A48 Oral	Short-Term Electric Grid Load Forecasting	Ana Martins, F. Pereira, F. Reis, Hiren Canacsinh, João Lagarto, M. Cardoso, Maria Amorim
A50 Oral	Reliability Analysis and Failure Forecast of Critical Components Under Warranty	José Sobral, Fyodor Subotin

SESSION XV (*Room B*): Computational Mechanics II CHAIR: *Prof. Ana Neves and Prof. Inês Barbosa*		15:30 – 16:30
ID	**COMMUNICATION TITLE**	**AUTHORS**
A63 Oral	Computational Modelling of Incident Solar Radiation and Application for Thermal Loads Calculation in Buildings	Abel Agostinho, Fernando Carreira, Cláudia Casaca
A64 Oral	Analytical and Numerical Study of Carbon/Epoxy Composite Plates Subjected to Uniaxial and Biaxial Loads	Afonso Leite
A65 Oral	Simulating Stresses and Strains in Solid Mechanics Directly from Images Using Convolutional Neural Networks	José Rodrigues, Beatriz Vieira, Stéphane Bordas, Saurabh Deshpande

COFFEE BREAK (16:30 – 16:50)

16:50 – 17:00 - Information about Submissions to Special Issues

Mathematical and Computational Applications (MCA)
Mathematics in Computer Science (MCS)

17:00 – CLOSURE

Contents

PLENARY SESSIONS

JOINING BY FORMING OF BUSBARS FOR ELECTRIC DISTRIBUTION SYSTEMS

J.P.M. Pragana, R.F.V. Sampaio, I.M.F. Bragança, C.M.A. Silva, **P.A.F. Martins**

Professor Paulo Martins
Instituto Superior Técnico, Universidade de Lisboa
Av. Rovisco Pais, 1, 1049-001 Lisboa

Short Bionote:

Paulo Martins is professor of manufacturing at Instituto Superior Técnico, University of Lisbon, Portugal. He obtained a PhD in mechanical engineering from Instituto Superior Técnico in 1991, the habilitation in mechanical engineering from Instituto Superior Técnico in 1999 and the degree of doctor technices honoris causa from the Technical University of Denmark in 2018.

He is Fellow of the International Academy for Production Engineering (CIRP) and was awarded with the (JSTP) Japan Society for Technology of Plasticity International Prize for R&D in Precision Forging in 2021.

He was president of the scientific board of Instituto Superior Técnico from 2009 to 2012, president of the school council of Instituto Superior Técnico from 2017 to 2020 and has been a member of the general council of the University of Lisbon, since 2022.

His research interests include metal forming, joining by forming and metal additive manufacturing. He is co-author of several books and international patents, as well as more than 500 papers in international journals and conferences.

Further information is available at:

https://fenix.tecnico.ulisboa.pt/homepage/ist12470

DEVELOPMENTS IN MULTIMODAL LARGE LANGUAGE MODELS

Professor Arlindo Oliveira
Instituto Superior Técnico, Universidade de Lisboa
Av. Rovisco Pais, 1, 1049-001 Lisboa

Short Bionote:

Distinguished Professor of Instituto Superior Técnico (IST), with the CSE Dept. President of INESC. Distinguished guest professor at Macau University of Science and Technology. Researcher of INESC-ID. Member of the board of CGD. Member of the Portuguese Academy of Engineering, of the Lisbon Academy of Sciences, and of ACM. Senior member of IEEE and fellow of ELLIS.

Education: PhD in EECS from UC Berkeley and MSc and BSc in EECS from IST. Post-graduation in risk management from INSEAD.

Areas of interest: algorithms, machine learning, artificial intelligence, bioinformatics, and CAD

Further relevant information is available at:

https://web.tecnico.ulisboa.pt/arlindo.oliveira/index.htm

INVITED LECTURES

HIGHER ORDER EQUIVALENT LAYER-WISE THEORY FOR MULTIFIELD ANALYSIS OF CURVED LAMINATED STRUCTURES

F. Tornabene[1]*, M. Viscoti[1] and R. Dimitri[1]
1: Department of Innovation Engineering
University of Salento
73100 Lecce, Italy
e-mail: matteo.viscoti@unisalento.it

Keywords: Multifield analysis, laminated shells, smart Materials, generalized differential quadrature, recovery procedure

Abstract *A novel formulation, based on the unified formulation and equivalent layer-wise approach, is introduced for the multifield analysis of curved laminated structures* [1]. *The governing equations, expressed in principal coordinates, are derived from the Master Balance principle* [2] *and they account for the coupling effects between mechanical elasticity, electricity, magnetism, and hygro-thermal conditions* [3]. *In this context, an effective homogenization approach based on the Mori-Tanaka technique is used to determine the equivalent properties of smart materials. Several numerical examples are presented to highlight the accuracy and the computational efficiency of the model compared to refined three-dimensional finite element simulations. In addition, an extensive parametric investigation points out the influence of multifield coupling and governing parameters* [4]. *The model seems to provide highly accurate numerical predictions with a simple modelling procedure, thus representing a useful tool for exploring new applications in various engineering field. The proposed model, indeed, has the advantage to consider various physical phenomena which are not addressed in widely used finite element commercial softwares.*

REFERENCES

[1] Tornabene, F., Viscoti, M., Dimitri, R. “Equivalent layer-wise theory for the hygro-thermo-magneto-electro-elastic analysis of laminated curved shells”, *Thin-Walled Structures*, Elsevier Vol. 198, p. 111751, 2024.
[2] Tornabene, F., *Hygro-Thermo-Magneto-Electro-Elastic Theory of Anisotropic Doubly-Curved Shells*, Esculapio, Bologna, 2023.
[3] Tornabene, F., Viscoti, M., Dimitri, R. “Hygro-thermo-mechanical equivalent layer-wise theory of laminated shell structures”, *Computer Modeling in Engineering and Science*, Tech Science Press Vol. 142, pp. 1697-1765, 2025.
[4] Tornabene, F., Viscoti, M., Dimitri, R. “Magneto-electro-elastic analysis of doubly-curved shells: higher-order equivalent layer-wise formulation”, *Computer Modeling in Engineering and Science*, Tech Science Press Vol. 142, pp. 1767-1838, 2025.

SYMCOMP 2025
Lisbon, 10-11 April 2025

AGENTIC AI IN HEALTHCARE: A NEW ERA HAS ARRIVED

Eva Sousa[1,2*], Zekun Guo[1]

1: Centre of Excellence for Data Science, Artificial Intelligence and Modelling, University of Hull, Hull, United Kingdom

e-mail: e.sousa@hull.ac.uk
web: https://www.hull.ac.uk/work-with-us/research/institutes/data-science-artificial-intelligence-and-modelling

2: Centre for Biomedicine, Hull York Medical School, University of Hull, Hull, United Kingdom
e-mail: eva.sousa@hyms.ac.uk*web: Centre for Biomedicine | Hull York Medical School

Keywords: AI Agents, Healthcare automation, Clinical decision support, Natural language processing

Abstract *The integration of artificial intelligence (AI) agents in healthcare is transforming clinical practice, offering innovative solutions for diagnosis, treatment, and patient management. The idea of creating an agent which can reason, and acting in an autonomous way seems as revolutionary as futuristic. However, AI multi-agent systems, including chatbots for medical consultations, virtual assistants for clinical interventions, embodied AI for daily care and companionship, and decision-support systems for diagnosis, are already increasingly utilized to enhance efficiency, reduce administrative burdens, and improve patient outcomes. Key advancements from the application of AI agents to healthcare include natural language processing (NLP)-based virtual assistants for patient triage, AI-driven decision support for clinicians, and autonomous systems for continuous patient monitoring, within some of their applications. Agentic AI has already demonstrated potential in improving diagnostic efficiency, optimizing resource allocation, and personalizing treatment plans, and promises to take healthcare research by storm, accelerating it and making it more automated.*

Despite these benefits, challenges such as data privacy, explainability, ethical considerations, and algorithmic biases remain primary barriers to widespread adoption. Ensuring regulatory compliance and fostering trust among healthcare professionals and patients are crucial for the successful integration of AI agents into clinical workflows.

Overall, AI agents are poised to play an increasingly vital role in modern healthcare, driving efficiency and innovation while requiring careful implementation to address ethical and practical concerns.

SYMCOMP 2025
Lisbon, 10-11 April 2025

INCIDENCE OF REPUTATIONAL PERIODICITY

Peter Mitic[1*]

1: Department of Computer Science
University College London
66-72 Gower Street, London WC1E 6EA
e-mail: p.mitic@ucl.ac.uk, web: https://www.ucl.ac.uk/computer-science/

Keywords: Reputation, Sentiment, Bandpass filtration, attenuation, roll-off, frequency response

Abstract. *Reputation time series are analysed for periodic affects which might not be visible using simple smoothing techniques. To find possible frequencies that might indicate periodicity, a bandpass filter with a narrow passband, wide stopbands and steep roll-offs is progressively tracked on a day-by-day basis across reputation time series spanning a two-year period. Dominant frequencies are recorded at each stage. The results indicate that periodic cycles exist in the general range of one to six months. This result is significant for reputation management because it indicates when upturns or downturns in reputation are most likely.*

DOI:10.5281/zenodo.15160265

1 INTRODUCTION

Reputation may be formulated as time series of numeric sentiment values [1], in which total sentiment with respect to a given organisation is harvested and scored numerically on a daily basis using *Natural Language processing* and increasingly, *Large Language Models*. The purpose of this study is to examine the extent of periodic effects within reputation time series. An estimate of the period of an organisation's reputation is of benefit because it may reveal persistent failures in reputational management.
The illustration in Figure 1 shows a typical reputation time series: *Apple Corp.*. It has the characteristic rapid sentiment reversals, with some evidence of periodicity, as judged by inter-peak (or inter-tough) distances.

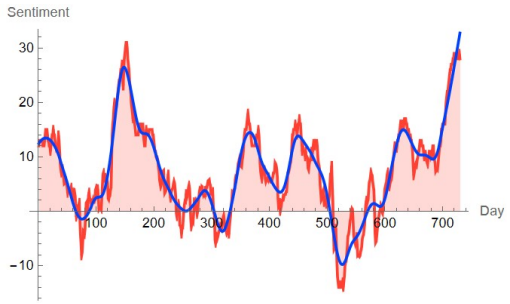

Figure 1: Example of reputation series: Apple Corp., illustrating rapid sentiment reversal and tentative evidence of periodicity. Red trace: empirical data, blue trace: Loess smoothed. Date range 730 days, July 2021-June 2023. Data: *Penta Group*.

1.1 Bandpass Filtration Applied to Reputation

The proposed method for searching for periodic effects in reputation time series is to construct and apply a bandpass filter to the data, as a means to assess the significance of frequency components embedded in the input data. A bandpass filter serves to transmit only frequencies that fall within a certain range (determined by the way in which the filter is structured), whilst minimising frequencies that fall outside that range. The amplitude of the transmitted signal is then a measure of the significance of the transmitted frequency. To apply the method, a bandpass filter is applied at each point defined by the time series. In the context of reputation the points are defined by *days*. The following sequence summarises the principal stages for a single reputation time series.

1. Filter design
2. For each day, t within scope of the data:
   (a) Formulate a bandpass filter based on t

(b) Apply the filter to all days and calculate significance for day t

3. Model the significance profile by a high degree polynomial, P
4. Locate turning points on P
5. Estimate significant frequencies from the highest three peaks

2 TECHNICAL BACKGROUND

2.1 Data and Implementation

Reputation time series from July 2021 to June 2023 for 130 corporate organisations were sourced from *Penta Group* [1]. Each element in the data series for organisation T represents the collective sentiment of all comments expressed for T on a given day. In the *Penta* implementation, daily sentiments are recorded on a scale from -100 (the worst possible) to +100 (the best possible).
The implementation is entirely in *Mathematica* (version 13.3), which allows seamless integration of numeric, symbolic and graphical methods. In particular, the calculus constructs in Section 4 provide the key to period determination.

2.2 Bandpass Filtration

Bandpass filters are used in a variety of applications, such as radios, TVs, and cell phones. They can be used to remove unwanted signals, such as noise, from a signal, or to select a particular range of frequencies for processing. High bandpass filters are used in audio systems to remove low-frequency noise, such as hum. Low bandpass filters are used in telephone systems to remove high-frequency noise, such as hiss.
Frequency filters can, in general, be represented by *frequency response curves* which are plots of standardised frequency (the independent variable) against amplitude (or a simple function thereof, the dependent variable). Figure 2 shows the bandpass profile, the parameters that are needed to characterise it, and derived parameters.
The principal inputs parameters for filter design are listed below. The output for filter design is an amplitude $|H(f)|^2$, dependent on frequency f.

1. f_{pa}: the lower passband frequency; f_{pb}: the upper passband frequency.
2. f_{sa}: the lower stopband frequency; f_{sb}: the upper stopband frequency.
3. f_s: the Nyquist (scaling) frequency
4. A_p: the stopband attenuation; A_s: the passband attenuations.

[1] https://pentagroup.co

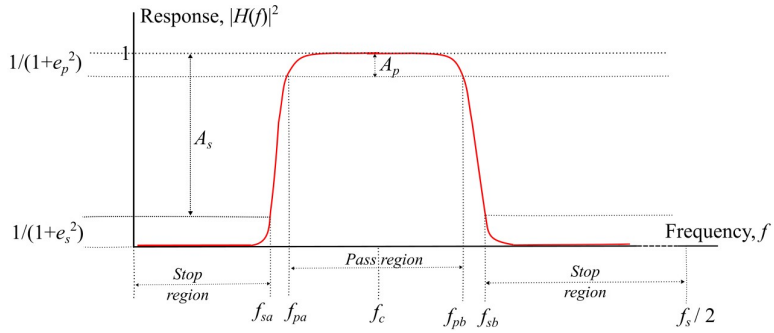

Figure 2: Bandpass filter response characteristics and parameters

The attenuations (i.e. reductions in amplitude) characterise the 'rectangular' nature of the filter profile. The terms e_p and e_s are derived quantities given A_p and A_s, although it more convenient to use them as the primary inputs for the filter design. In Figure 2, f_c is the mean of f_{pa} and f_{pb} if the filter is symmetric (the simplest case). The attenuations in the regions (f_{sa}, f_{sa}) and (f_{pb}, f_{sb}) are known as *roll-offs*.

3 SUPPORTING LITERATURE

This review illustrates instances of filter design and usage for particular purposes. The use of filters in the context of reputation is, aside from this paper, unexplored.

Radio, Radar and Transmission
A general overview of the use of bandpass filters in radio frequency applications may be found in [5]. They include telecoms, in which transmission by fibre networks is important, spectroscopy to block unwanted light scattering, LiDAR, and satellite communications. Recent specific applications include Sekiya et al [6] - the design of an array of single-band bandpass filters for radio astronomy in the UHF band, and Horlbeck et al. [10] - an adjustable bandpass filter for passive radar. Zamuruev et al [11] provide an overview of the main types of radio-frequency filters in radio-frequency systems. Radio-based applications frequently describe physical devices that include bandpass filters. Examples include Wu et al. [7] - for multi-band radio transmission; Xiang et al [8] - for designing a filter that allows a substantial tuning range of operational frequencies, and Durganath and Raja [9] - a delay filter. Further examples are Kiouach et al. [12] and Le et al. [13].

Audio
Ganguly et al. describe a study of speech signal distortion in audio systems, and attempt to filter out as much amplitude and frequency distortion as possible. They demonstrate that phase distortion is normally inaudible to the human ear. Yang et al. [15] designed an adjustable bandpass filter that is connected to a portable audio device such as an

mp3 player. Similarly, Wang et al. [16] describe a physical bandpass filter for 6G mobile communication.

Business and economics
Harvey and Trimbur [4] used bandpass filters to extract business cycles in economic time series. They point out that economic data usually have distinct statistical properties compared to data derived from physical systems (such as in electrical engineering). Typically, the 'sharp-gain' filters used in electronics can cause distortions in economic contexts that make the filter output extremely misleading. They cite the case of 'finding' cycles (which do not really exist) using a 'sharp-gain' filter on white noise, and give stock price changes as an example. However, stock price changes (and reputation) are not white noise. Rather, they are highly auto-correlated. The result from such economic series is a response variability which might not be present in physical systems.

4 IMPLEMENTATION DETAILS

The purpose of the bandpass filtration is to isolate successive narrow frequency bands, and determine which of them are most significant. The principal steps were noted in Section 1.1.

4.1 Filter Design

The designing needs for filtering a narrow bandpass filter 'rectangular-like': high roll-off (i.e. high attenuation), at the expense of signal attenuation within the pass band. This can be a problem in physical systems, but is less so in economic (including reputation) contexts. the passband limits f_{pa} and f_{pa} is best defined by starting with the central frequency f_c and defining the passband semi-width w, so that $f_{pa} = f_c - w$ and $f_{pb} = f_c + w$. Following the method noted by Orfanidis [2] (section 11.6.5 and 11.6.1), the stages in designing a filter with the characteristic profile in Figure 2 are as follows.

Step 1 : Scaling to frequency range $[0, 2\pi]$.

$$\begin{aligned} \omega_{pa} &= \frac{2\pi f_{pa}}{f_s}; \quad \omega_{pb} = \frac{2\pi f_{pb}}{f_s} \\ \omega_{sa} &= \frac{2\pi f_{sa}}{f_s}; \quad \omega_{sb} = \frac{2\pi f_{sb}}{f_s} \end{aligned} \tag{1}$$

Step 2 : Analogue Frequency Mappings (c measures the amplitude ratios in Figure 2) Ω_p and Ω_s are the analogue 'pass' and 'stop' frequencies respectively.

$$\begin{aligned} c = & \quad \frac{\sin(\omega_{pa}+\omega_{pb})}{\sin(\omega_{pa})+\sin(\omega_{pb})} \\ \Omega_p = & \quad \left|\frac{c-\cos(\omega_{pb})}{\sin(\omega_{pb})}\right| \\ \Omega_{sa} = & \quad \frac{c-\cos(\omega_{sa})}{\sin(\omega_{sa})}; \quad \Omega_{sb} = \frac{c-\cos(\omega_{sb})}{\sin(\omega_{sb})} \\ \Omega_s = & \quad \min(|\Omega_{sa}|, |\Omega_{sb}|) \end{aligned} \tag{2}$$

Step 3 : Butterworth Frequency parameters calculation. N_{exact} and its rounded up version N refer to the filter order and Ω_0 is the normalization frequency.

$$N_{exact} = \left|\frac{\log\left(\frac{e_s}{e_p}\right)}{\log\left(\frac{\Omega_s}{\Omega_p}\right)}\right|; \quad N = \lceil N_{exact} \rceil ; \quad \Omega_0 = \frac{\Omega_p}{e_p^{1/N}} \tag{3}$$

Step 4 : Magnitude Response calculation. The output is a single response magnitude, which describes filter profile (as in Figure 2) for a single input frequency f. The other inputs are c (Step 2), N and Ω_0 (Step 3), and the Nyquist (scaling) frequency f_s. The output is the response $|H(f)|^2$ in Figure 2.

$$\omega = \frac{2\pi f}{f_s}; \quad \Omega = \frac{c - \cos[\omega])}{\sin(\omega)}; \quad |H(f)|^2 = \left(1 + (\frac{\Omega}{\Omega_0})^{2N}\right)^{-1} \tag{4}$$

Steps 1-3 can be summarised in a function $\mathcal{B}()$, which is a constructor for a generic Bandpass filter, appropriate for reputational analysis. Equation 5 shows the inputs and outputs.

$$\{\Omega_0, c, N\} = \mathcal{B}(f_{pa}, f_{pb}, f_{sa}, f_{sb}, f_s, e_p, e_s) \tag{5}$$

A second function $\mathcal{H}$ (Equation 6), summarises the magnitude response calculation at a particular frequency f_t (Step 4). Since f_t is identified by a day number, it can take any integer value from 1 to the Nyquist frequency number $\lfloor f_s/2 \rfloor$. The output is a single real number h_t. The output feeds into the next stage in the process, which is to apply the filter to data.

$$h_t = \mathcal{H}(f_t, \Omega_0, c, N, f_s) \tag{6}$$

Some examples of filter construction are shown in Section 5.1.

4.2 The Bandpass Filter applied to data

To apply $\mathcal{H}$ to the entire reputation time series $y_t; (t = 1..f_s)$, a vector of target frequencies $f_1, f_2, ..., f_{\lfloor f_s/2 \rfloor}$ must be defined, and the corresponding values of h_t calculated. The reputation data y_t must be restricted to the corresponding instances of f_t (i.e. up to the

Nyquist frequency). Series f_t and the restricted y_t are then multiplied pairwise, and a root mean square of the products produces a single real-valued positive response R_t at frequency f_t.

$$\begin{aligned} \{h_t\} = &\quad \{\mathcal{H}(f_t, \Omega_0, c, N, f_s)\}; \quad t = 1..\lceil f_s/2 \rceil \\ \{y'_t\} = &\quad \{f_t\ h_t\} \quad t = 1..\lceil f_s/2 \rceil \\ R_t = &\quad \left(\sum_{t=1}^{\lfloor f_s/2 \rfloor} (y'_t)^2 \right)^{1/2} \end{aligned} \tag{7}$$

The sequence in Equations 7 can be summarised in a single function $\mathcal{R}$ (Equation 8). With integer values for the 'target' frequencies f_t, the values of f_t reduce to integers $1..\lfloor f_s/2 \rfloor$. The output R_t is a measure of the significance of the input frequency f_t on the data.

$$R_t = \mathcal{R}(f_t, y_t, \Omega_0, c, N, f_s); \quad t = 1..\lfloor f_s/2 \rfloor \tag{8}$$

To see the effect of all frequencies on the data, function $\mathcal{R}$ has to be applied at frequencies between 1 and the Nyquist number, $\lfloor f_s/2 \rfloor$. The first frequency $f_{t_1} (> 1)$ must be high enough to accommodate the profile of a bandpass filter. Similarly, the last frequency $f_{t_2} (\leq \lfloor f_s/2 \rfloor)$ must be low enough to accommodate the same profile. A value for each R_t in the range $[f_{t_1}..f_{t_2}]$ then needs to be calculated. Algorithm 1 returns a sequence of R_t-values.

Algorithm 1 : Frequency significance calculation.

1. Determine start and end frequencies f_{t_1} and f_{t_2}.
2. For each frequency f_t in $[f_{t_1}..f_{t_2}]$:
   (a) $\{\Omega_0, c, N\} = \mathcal{B}(f_{pa}, f_{pb}, f_{sa}, f_{sb}, f_s, e_p, e_s)$
   (b) $h_t = \mathcal{H}(f_t, \Omega_0, c, N, f_s)$
   (c) $R_t = \mathcal{R}(f_t, y_t, \Omega_0, c, N, f_s)$
3. Return $\{R_t\}$

When Algorithm 1 is embedded in a single procedure $\mathcal{S}$, the necessary inputs are the parameters needed to construct the bandpass filter, the reputation time series, and the start and end frequencies (Equation 9). The output is a list of frequency significance

values $\{R_t\}$ that defines a significance profile for the reputation data y_t. An example plot of $\{R_t\}$ against frequencies f_t is shown in Section 5.2.

$$\{R_t\} = \mathcal{S}(f_{pa}, f_{pb}, f_{sa}, f_{sb}, f_s, e_p, e_s, y_t, f_{t_1}, f_{t_2}) \tag{9}$$

4.3 Period Estimation

The result of applying function $\mathcal{S}$ (Equation 9) is a list of peak frequencies. Typically, for any given organisation, they will not be numerous, and inter-peak distances may vary significantly. Therefore, estimation of a period will be associated with much uncertainty. With those provisos, Algorithm 2 shows the period estimation details. The key part is to express the frequency significance profile $\{R_t\}$ into a continuous form that can be differentiated in order to locate maxima (or minima).

Algorithm 2 : Period Estimation.

1. Fit a high degree polynomial, $P(f)$, to the frequency significance profile $\{R_t\}$
2. Calculate $\frac{dP}{df}$ and $\frac{d^2P}{df^2}$
3. Solve $\frac{dP}{df} = 0$ to give solutions $\{f_1, f_2, ...\}$ subject to $\frac{d^2P}{df^2}\big|_{f_i} < 0$ to detect the maxima
4. Remove negative f_i
5. Extract the maximum 3 f_i, and order by frequency

The result of applying Algorithm 2 is, for each organisation, a triple of the most significant frequencies. Ordering them by frequency is useful for visualisation (Section 5.3. Less reliance should be placed on results that indicate a very high number of days. It would be hard to observe high value periodic effects given the number of days spanned by the data (730) because a consistent pattern cannot be established. Therefore, a nominal upper limit for reportable frequency of a quarter of the number of data data points ($f_s/4$ in Figure 2) is set.

5 RESULTS

5.1 Bandpass filter examples

Figure 3 shows three Bandpass filter examples generated using the sequence in Section 4. They illustrate the idealised profile in Figure 2. Two are centred on the same frequency,

24 (i.e. day 24), with a nominal 3 month span $f_s = 90$. The third is centred at 20. In each case the pass band semi-width is w. The roll-offs are controlled by parameters e_s and e_p: increasing e_s and decreasing e_p produces a steeper roll-off.

- Red: $e_p = 0.5, e_s = 2, f_{pa} = 20; f_{pb} = 28; w = 5$
- Blue: $e_p = 0.3493, e_s = 3, f_{pa} = 23; f_{pb} = 25; w = 1$
- Green: $e_p = 0.05, e_s = 12, f_{pa} = 12; f_{pb} = 28; w = 8$

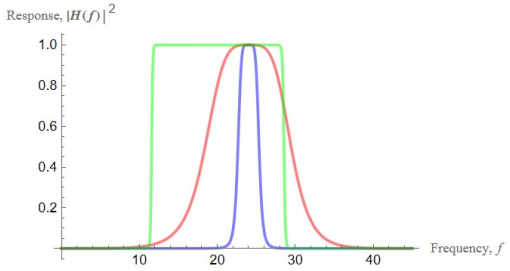

Figure 3: Examples of Bandpass filters. Red: wide pass band, shallow roll-off. Blue: narrow pass band, steep roll-off. Green: very wide pass band, almost vertical roll-off.

5.2 Single Reputation Example

This section shows an example frequency calculation for *Tesco* using Algorithm 2 (Section 4.3). The plot in Figure 4 shows the trace of frequency significance for frequencies between 1 to 270 days. The bandpass region was set at a very small value: 4 days. Parameters e_p and e_s (in Figure 2)were set to 1/3 and 3 respectively to give a very with steep roll-off on either side of the passband region. In this case the three principal frequency peaks are closely packed and are have very similar significance values. Each marks a peak in a region of significance. The fourth highest, 236 days, falls outside the nominal upper limit for reportable frequency number (Section 4.3), so that value would be hard to justify without recourse to more data. The fifth highest peak, at 5 days, is also hard to justify because it falls within the range of 'noise'. The sixth highest peak, 184 days, is on the boundary of the 'justifiable' region. In this case the Loess approximation has smoothed several minor peaks in the range 140-200, so that the 184-day peak can be regarded as an average for that region.

5.3 All Reputation Results

The results of applying Algorithm 2 to the reputation data of all organisations reveals a consistent pattern. There is some periodic effect for each organisation, and it is usually possible to identify three peaks (including the global maximum) in the frequency profile.

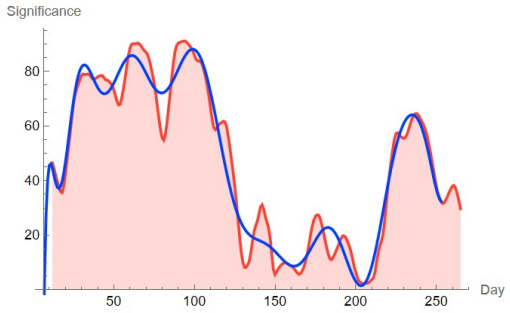

Figure 4: Example of Significant Periods analysis: Tesco, showing the three most significant peaks at 33, 62 and 100 days. Red - Significance profile from $\mathcal{S}()$ (Equation 9). Blue - Loess peaks model (Algorithm 2).

None had fewer than two. For those that had more than three identifiable peaks, peaks 4, 5, ... were insignificant compared to the three principal frequency peaks. Figure 5 shows histograms of the three principal frequencies, all based on a fitting a polynomial of degree 25 to the frequency profiles. Summary statistics corresponding to Figure 5, using a passband width 4, are shown in Table 1 (MAD = *Mean Absolute Deviation*). The figure 25 for degree provided a faithful representation of the frequency profile, whilst removing minor variations. A passband width of 4 is a reasonable wrap around a single target frequency, whilst allowing a small amount of stability from neighbouring frequencies. Both table and histogram indicate frequency peaks in the region of 1-2 months, 3 months and 5-6 months, all with a wide estimation margin.

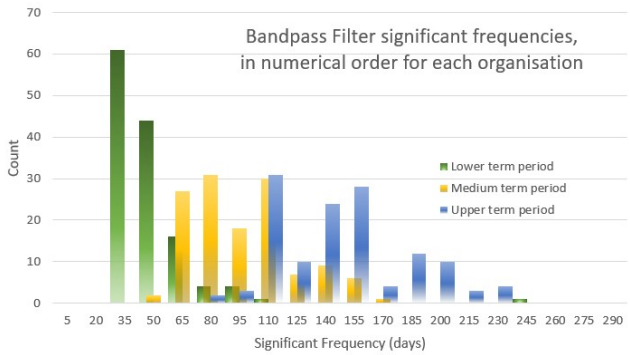

Figure 5: Significant frequencies (in days): all organisations, showing profiles for short, medium and long term periodic effects

5.3.1 Bandpass filter with a shallow roll-off

It is interesting to compare the results of Section 5.3 with corresponding results using an alternative bandpass filter. Noting the advice from Harvey and Trimbur [4] that a

Table 1: Summary statistics of peaks of frequency profiles, all organisations

	Frequency (days)		
Statistic	**Lower**	**Medium**	**Upper**
Mean	41	88	141
SD	22.9	26.3	34.1
Max	231	156	229
Min	21	48	79
Median	37	83	138.5
MAD	21.9	26.8	28.2

Table 2: Summary statistics of peaks of frequency profiles, all organisations, using a 'wide' bandpass filter with a short pass band and shallow roll-offs.

	Frequency (days)		
Statistic	**Lower**	**Medium**	**Upper**
Mean	40	89	141
SD	17.8	28.4	35.8
Max	134	218	258
Min	21	48	79
Median	37	83	138
MAD	22.7	28.0	27.2

bandpass filter with a very sharp roll-off may give misleading results, a bandpass filter with a very shallow roll-off is investigated in this section. Figure 3 shows such a filter (in red), although for consistency with the setup for Section 5.3, the pass band is kept very narrow, at 4 days. Increasing the value of the e_p parameter from 0.3 to 0.5, and decreasing the e_s parameter from 3.0 to 1.0 resulted in roll-offs of approximately 14 days (they were approximately 2 days). With no other changes, Table 2 shows the equivalent statistics for 'wide' filter to those in Table 1. The results for the 'wide' filter are very similar to the results for the original filter.

6 CONCLUSIONS

Using a bandpass filter has revealed 'hidden' periodicity in reputation time series. It should be remembered that the figures given in Section 5.3 (1-6 months) are guidelines, and they should be treated as such. Those involved in risk management should adopt a strategy of continuous monitoring of reputation, and be aware that at approximately 1, 3 and 6 months, there may be an upturn or a downturn in sentiment.

Within an individual calculation, some improvements are possible. The degree of the

polynomial use to model the frequency distribution (Algorithm 2) does not have a theoretical basis. Rather, the only proviso is that the degree should be large enough to model the major features of the frequency profile adequately. Varying the polynomial degree can produce anomalous results, particularly if additional low frequency peaks are detected. This phenomenon does not appear to be due to even or odd numbered degrees. In any single organisation, it is mostly easy to deal with this problem. The list of significant frequencies for each polynomial degree should be scrutinised manually, and outlier degrees should be rejected. An example is for *Astra Zeneca* where the lowest frequencies with pass band width 6 for polynomial degrees 20-30 are $\{29, 27, 28, 29, 35, 34, 66, 65, 34, 35, 35\}$, and two outliers are apparent. Averages can then be calculated for the remainder. Ideally, searching for outliers should be done programmatically, but outlier identification is not always clear in this context. For example, there are cases (such as IBM, British Aerospace or United Healthcare) where the lower significant frequency values fall into two widely-separated clusters, with approximately half in each. For *IBM*, the corresponding lowest frequencies with pass band width 15 are $\{87, 87, 87, 87, 87, 87, 87, 31, 31, 29\}$. In that case, the issue could be resolved by averaging or by a majority decision. The problem is much more acute for wider pass bands.

REFERENCES

[1] Mitic, P. "Reputation, Sentiment, Time Series and Prediction", *Proceedings of the 13th International Conference on Data Science, Technology and Applications (DATA)*, SciTePress, pp. 51-61, 2024, DOI: 10.5220/0012762600003756

[2] "Orfanidis, S.", *Introduction to Signal Processing*, Prentice Hall, 1995

[3] "Huang, W.-H., Hou, T.-B. and Tang,C.-W.", *Design of a bandpass filter with wide passband and wide rejection bandwidth*, Asia Pacific Microwave Conference, Singapore, pp. 905-908, 2009, doi: 10.1109/APMC.2009.5384311

[4] "Harvey, A. C. and Trimbur, T.", *General Model-based Filters for Extracting Cycles and Trends in Economic Time Series*, The Review of Economics and Statistics, **85(2)**, pp. 244-255, 2003, https://www.jstor.org/stable/3211576 and https://doi.org/10.17863/CAM.5200.

[5] "Iridian Technologies", *What are Bandpass Filters Used for?*, 2024, https://www.iridian.ca/learning_center/light-notes/what-are-bandpass-filters-used-for/

[6] "N. Sekiya, K. Sakuma and T. Akahori", *HTS Penta-Band Bandpass Filter for Radio Astronomy Broadband Receiver in the UHF Band*, IEEE Transactions on Applied Superconductivity, **34(3)**, pp. 1-5, 2024, doi:10.1109/TASC.2023.3344420

[7] "Bang Wu, Ke Song, Leiyang Wang and others", *A compact all-frequency absorptive dual-band bandpass filter with T-shaped transmission line absorption branches*, International Journal of Electronics and Communications **177, 155228**, 2024, doi.org/10.1016/j.aeue.2024.155228

[8] "Xiang, Q., Tan, X., Ding, Q., and Zhang, Y.", *A Compact Bandpass Filter with Widely Tunable Frequency and Simple Bias Control*, Electronics, **13(2), 411**, 2024, doi.org/10.3390/electronics13020411

[9] "K. Durganath and M. Raja", *Design of dual band bandpass filter with single notch for global system for mobile communications and comparing group delay with dual ring filter*, AIP Conf. Proc. **2853, 020163**, 2024, doi.org/10.1063/5.0197715

[10] "Horlbeck, Marie, Fiedelak, J., Kurin, T. and others", *Direct Sampling Receiver with an Adjustable Bandpass Filter for Use in Passive Radar with FM Radio*, Proc. 2024 IEEE Radio and Wireless Symposium (RWS) San Antonio TX, IEEE Computer Society, pp. 102-104, 2024, https://cris.fau.de/publications/319726076/

[11] "Sergey Zamuruev, Nikolay Legkiy and others", *Assessment of the Quality of Radio-Frequency Filters Used in the Organization of Communication in Railway Transport in the Production Process*, Transportation Research Procedia **68**, pp. 659-664, 2023, doi.org/10.1016/j.trpro.2023.02.091

[12] Kiouach,F., Aghoutane,B. and El Ghzaoui,M.", *Novel Microstrip Bandpass Filter for 5G mm-Wave wireless communications*, Advances in Electrical Engineering, Electronics and Energy *6, 100357*, 2023, https://doi.org/10.1016/j.prime.2023.100357.

[13] "Yi Le, Hao Liu, Guodong Su, Nan Yang, Pengfei Hu and Jun Liu", *A high-selective multiple-mode bandpass filter design, applicating in both millimeter-wave 5G and WiFi systems*, Microelectronics Journal **149, 106250**, 2024, doi.org/10.1016/j.mejo.2024.106250

[14] "A. Ganguly, A. K. Gupta, S. Uniyal, and others", *Simulation and Integrated Circuit implementation of All pass and Bandpass filter*, International Conference on System, Computation, Automation and Networking (ICSCAN), Pondicherry, India, 2020, pp. 1-5, doi: 10.1109/ICSCAN49426.2020.9262422.

[15] "Yang, H., Chen, M., Zhou, J., Bao, K., Chen, J." *Design of an Active Adjustable Band-Pass Filter*, Multimedia and Signal Processing. CMSP 2012 (eds. Wang, F.L., Lei,J.) *346* Springer, https://doi.org/10.1007/978-3-642-35286-7_76

[16] "Fengjuan Wang, WangLei Ke and Xiangkun Yin", *TSV-Based Hairpin Bandpass Filter for 6G Mobile Communication Applications* IEICE Electronics Express **18(15)** DOI:10.1587/elex.18.20210247

POROUS BURNERS: A REVIEW OF MODELING APPROACHES AND APPLICATIONS IN THE ENERGY TRANSITION

Isabel Malico[1,2]

1: IDMEC, Escola de Ciências e Tecnologia, Universidade de Évora, Évora, Portugal

2: Complex Flow Systems Lab (CFS Lab), Institute of Earth Sciences, Évora, Portugal

e-mail: imbm@uevora.pt

Keywords: Computational Fluid Dynamics, RANS, Flow impingement, recirculation zones, ANSYS FLUENT

Abstract *Porous Burners have emerged as a promising combustion technology for improving energy efficiency, reducing emissions, and enabling fuel flexibility in the context of the global energy transition. Their unique characteristics enhance heat transfer and combustion stabilization making them attractive for various industrial and domestic applications. This review explores the key modelling approaches used to simulate porous burners performance, including numerical and machine learning approaches. Emphasis is placed on how these models contribute to optimizing burner design, predicting combustion behaviour, and integrating alternative fuels such as hydrogen and biofuels. Additionally, the role of porous burners as a means to improve the efficiency and sustainability of heat-intensive processes by reducing emissions and enabling cleaner combustion is explored. By synthesising recent advances, this review provides insights into future research directions and the broader impact of porous burner technology on achieving cleaner and more efficient combustion systems.*

Acknowledgements

Isabel Malico acknowledges *Fundação para a Ciência e a Tecnologia* (FCT) for its financial support via the project LAETA Base Funding (DOI:10.54499/UIDB/50022/2020).

SYMCOMP 2025
Lisbon, 10-11 April 2025

MESHLESS METHODS IN MECHANICS AND BIOMECHANICS: CURRENT AND TREND APPLICATIONS

Jorge Belinha[1]*
1: INEGI – Institute of Science and Innovation in Industrial and Mechanical Engineering
*ISEP – School of Engineering, Polytechnic of Porto
e-mail: job@isep.ipp.pt

Keywords: Computational Mechanics, Computational Biomechanics, meshless methods, radial point interpolation meshless methods, smoothed-particle hydrodynamics, artificial intelligence

Abstract *Computational mechanics emerged with the advent of the first computers and has since undergone significant development. The literature now describes numerous advanced numerical discretization techniques capable of efficiently performing structural analyses. The finite element method (FEM), one of the earliest discrete numerical methods, remains the most popular technique within the computational mechanics research community. FEM is known for its ease of programming, robustness, and ability to provide reasonable approximations. However, despite its efficiency and success, the last decade of the 20th century saw the emergence of new, mature advanced discretization techniques known as meshless methods. Unlike FEM, which discretizes the problem domain using a structured element mesh comprising a grid of nodes and elements, meshless methods discretize the domain with an unstructured nodal distribution. Consequently, meshless methods enable the creation of discrete geometric models directly from medical images or CAD geometries. This meshing advantage is a valuable asset in computational mechanics and biomechanics. This lecture briefly describes the evolution of advanced meshless discretization techniques in these fields, highlighting the most significant ones and their formulations. Furthermore, it presents several challenging numerical applications in computational mechanics and biomechanics developed by the author and his research team. These applications encompass the analysis of transient behavior in bone tissue, the study of elastoplastic behavior in metallic and biological tissues, the structural optimization of mechanical components, the examination of blood fluid flow, the investigation of the structural response of implants and biostructures, and the study of human cells in angiogenesis and their dynamic behavior. Additionally, this lecture addresses the integration of artificial intelligence, demonstrating how meshless artificial neural networks can be used to predict variable fields. The results obtained using meshless methods are compared with FEM solutions to provide insights into their efficiency and accuracy.*

REGULAR COMMUNICATIONS

IMPLEMENTATION OF AN SPH SOLVER FOR QUASI-INCOMPRESSIBLE FLUIDS IN JULIA

Aleksandr Cherniaev[1]*
1: Department of Mechanical, Automotive and Materials Engineering
Faculty of Engineering
University of Windsor
401 Sunset Ave., N9B 3P4, Canada
e-mail: aleksandr.cherniaev@uwindsor.ca,
web: https://www.uwindsor.ca/engineering/mame/cherniaev

Keywords: Julia programming language, smoothed particles hydrodynamics (SPH), solver implementation, incompressible fluids, dam break problem

Abstract *This presentation will discuss the implementation of a smoothed particles hydrodynamics (SPH) solver for quasi-incompressible fluids in the Julia programming language. The following practical aspects will be addressed:*

- *solution of the Navier-Stokes equations for the motion of quasi-incompressible fluids using the SPH method and its algorithmic implementation in Julia;*
- *influence of the choice of a kernel function on the results of numerical simulations;*
- *density summation vs. rate density approach in density calculations;*
- *influence of the neighbor particles search algorithms on the computational cost;*
- *code parallelization;*
- *interaction of the solver with external pre- and post-processing software.*

The dam break problem will be used to validate the solver's predictions against experimental data.

SYMCOMP 2025
Lisbon, 10-11 April 2025

SYNTHETIC MICROSCOPIC PLATELETS IMAGES GENERATION USING WGAN-GP

Itunuoluwa Abidoye[1], Frances Ikeji[1], Charlie A. Coupland[2], Simon D. J. Calaminus[2], Eva Sousa[1,2*]

1: Centre of Excellence for Data Science, Artificial Intelligence and Modelling, University of Hull, Hull, United Kingdom

e-mails: {itunuoluwaabidoye@gmail.com, ikejif@gmail.com, e.sousa@hull.ac.uk*} web: https://www.hull.ac.uk/work-with-us/research/institutes/data-science-artificial-intelligence-and-modelling

2: Centre for Biomedicine, Hull York Medical School, University of Hull, Hull, United Kingdom

e-mail: {hycc29, simon.calaminus, eva.sousa}@hull.ac.uk web: https://www.hyms.ac.uk/research/research-centres-and-groups/centre-for-biomedicine

Keywords: Platelet classification, medical image analysis, Generative Adversarial Networks, WGAN-GP, synthetic data, DenseNet.

Abstract

Introduction: *Data scarcity presents a major challenge in medical imaging. Generative Adversarial Networks (GANs) offer a promising solution by generating synthetic data to augment small datasets.* ***Aim:*** *The primary aim of this study is to evaluate the effectiveness of GAN-based synthetic data generation in enhancing CNN performance for platelet classification.* ***Methods:*** *The initial dataset contained 71 images, categorized into Control, Milrinone, and Zinc-plus-Milrinone classes. Using WGAN-GP, a synthetic dataset of 300 images was generated. These synthetic images were incorporated into the training of CNN models, including DenseNet121 and InceptionV3. Model performance was assessed comparing results from the original and augmented datasets.* ***Results:*** *In the non-augmented dataset, DenseNet121 achieved an accuracy of 81%, with 84% precision, 78% recall, and an F1-score of 81%. For InceptionV3, the non-augmented dataset yielded 82% accuracy, 80% precision, 76% recall, and an F1-score of 78%. However, after incorporating GAN-generated synthetic images, DenseNet121 achieved 97% accuracy, 97% precision, 95% recall, and a 96% F1-score, while InceptionV3 reached 94% accuracy, 93% precision, 90% recall, and 92% F1-score on the GAN-augmented dataset.* ***Discussion/Conclusion:*** *These results highlight the potential of GAN-generated synthetic data to significantly enhance the performance of CNN models in medical image classification, particularly in addressing the limitations of small datasets.*

DOI:10.5281/zenodo.15150483

1. INTRODUCTION

Platelets, are the most important blood cells in haemostasis, being this an important skill on the body well-being maintenance [1,2,3]. Platelets are also known by the name of thrombocytes, have a diameter of 2-4 μm in diameter, and beside small are anucleate. They form aggregates which adhere to damaged vessel surfaces, becoming activated, and transforming into sticky plugs that culminate in thrombus formation which stop the bleeding process [4,5]. Beyond this physical role, platelets are regulated by intricate biochemical pathways, being one of the substances Zinc able to influence this process [5] [6]. Contrarily to red and white blood cells which are more studied not much attention has been placed in precise identification of platelet morphology and function. However, this is vital for diagnosing haematological disorders, as irregularities in shape or behaviour may signal defective function and underlying pathologies [7,8,9,10]. Traditional platelet classification relies on manual microscopic examination, a process prone to interobserver variability and subjectivity, beside very labour intensive [2,11,12]. Automating blood analysis to enhance efficiency and reduce human error is then of extreme importance [13,14], being this true also for platelets. Artificial Intelligence (AI), with the Machine Learning (ML) and Deep Learning (DL), can be revolutionary in this task by enabling rapid, accurate and fully automatic analysis of microscopy images with low error margin [15,16]. DL techniques, such as Convolutional Neural Networks (CNNs), have shown great success in tumour detection, blood cell classification, phenotyping and in other medical imaging tasks, offering high performance solutions for classification, segmentation, and image quality enhancement [17,18,19,20]. Recent studies with CNNs application on classification of aggregates by agonist type and by phenotype morphological changes induced by treatments, demonstrate the potential of DL to automate and refine this field of platelets research [2,5,21]. However, to train the models needed for this research high quality, labelled platelet image datasets become imperative [22]. Datasets augmentation is a regular task of data processing for AI application, where rotations, scaling, and flips of the images are implemented for creating enlarged datasets [23]. Looking into the potentialities of AI for this research field its is possible to see that beside creating the challenge it can also provide the solution. In recent years, generative Adversarial Networks (GANs) have emerged as a transformative approach by synthesizing realistic images to expand datasets [24]. When applied to train AI models GAN based augmentation has improved classification accuracy in applications like liver lesion detection and chest X-ray analysis, suggesting its potential for platelet studies [25,26]. Recent research has explored custom CNN architectures and transfer learning to segment and classify blood cells, including platelets, with models designed to identify morphological changes induced by treatments such as zinc, milrinone, or their combination [5,21]. To address datasets limitations and advance platelet classification, this study compared a Wasserstein GAN with Gradient Penalty (WGAN-GP) generated dataset against traditionally augmented datasets. The performance of eight pre-trained CNNs (DenseNet121, DenseNet169, DenseNet201, VGG16, VGG19, InceptionV3, Inception-ResNetV2, and AlexNet) and two custom CNNs was evaluated using accuracy, precision, recall, and F1-score across original, augmented, and GAN-based synthetic datasets. The objective was to determine whether GAN augmentation enhances classification accuracy and generalizability beyond traditional methods, while also exploring

AI's broader potential to decode platelet morphology and signalling in health and disease.

2. MATERIALS AND METHODS

2.1. Data description

An initial dataset of 71 platelet images was used, categorized into three classes: Control (47 images), Milrinone (14 images), and Zinc plus Milrinone (10 images), as described by Abidoye et al. [27].

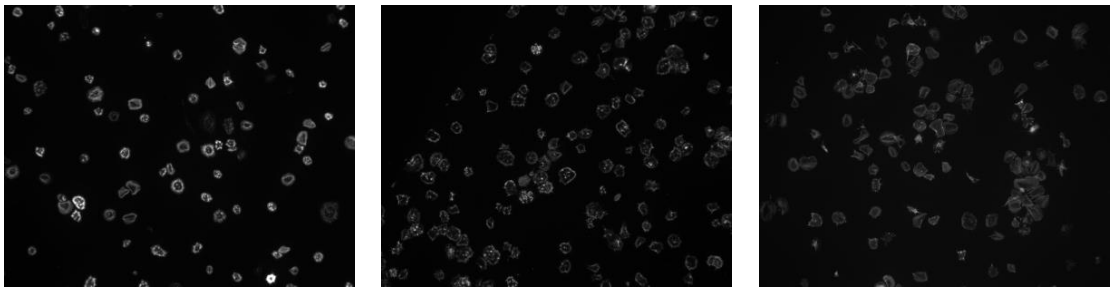

(a) (b) (c)

Figure 1. Sample Images from the Platelet Dataset of each class (a) Control, (b) Milrinone, (c) Zinc plus Milrinone respectively.

This small dataset size presented challenges for training deep neural networks, motivating our augmentation strategies.

2.2. Data preparation and augmentation

The original dataset gave origin to three different ones: two augmented datasets but the traditional techniques and are identified as augmentation Level 1 and Level 2 and one synthetic dataset, created by application of a WGAN-GP. The creation process of these datasets is described with more detail below:

- Level 1 (141 images): Used random oversampling and basic images transformations (flips, rotation, zoom).
- Level 2 (1,463 images): Employed more extensive images transformations (shearing, additional rotation, and zoom ranges) to ensure a much larger dataset.
- Synthetic dataset (300 images): Generated using a WGAN-GP, thereby further expanding the available data for model training and classification.

Each dataset was then divided into training (70%) and validation (30%) sets.

2.3. Transfer learning models

Eight pre-trained CNNs with ImageNet weights were finetuned for this task:

- DenseNet121, DenseNet169, DenseNet201 [28]
- VGG16, VGG19 [29]
- InceptionV3 [30]
- InceptionResNetV2 [30]
- AlexNet [31]

Each model's final layers were adjusted for three classes classification. Additionally, two custom CNNs were designed:

- Custom Model 1: Incorporating Conv2D, BatchNormalization, MaxPooling, Dropout, and two Dense layers.
- Custom Model 2: A simpler architecture with Conv2D and MaxPooling, followed by a single Dense layer.

2.4. GAN data augmentation or GAN data generation

The used WGAN-GP employed to generate synthetic platelet images is illustrated in Figure 2. This method was chosen due to its ability to address stability issues commonly encountered in traditional GAN training by utilizing the Wasserstein distance with a gradient penalty to enforce Lipschitz continuity [32,33].

1. **Generator**: This network transforms a latent noise vector into high-resolution (128×128 or 256×256 pixels) synthetic images using transpose convolutions, batch normalization, and LeakyReLU activations to ensure realistic feature generation.

2. **Critic (Discriminator)**: The discriminator evaluates both real and generated images through convolutional layers, outputting a scalar "realness" score to guide the generator's improvement. To maintain training stability, the critic undergoes multiple updates per generator update before reaching convergence.

GAN training was conducted over 5000 epochs per class (batch size = 128), generating 100 synthetic images per class. These synthetic images were integrated into the dataset and subjected to the same CNN training and evaluation pipeline as the other augmented datasets, enabling direct performance comparisons across augmentation methods.

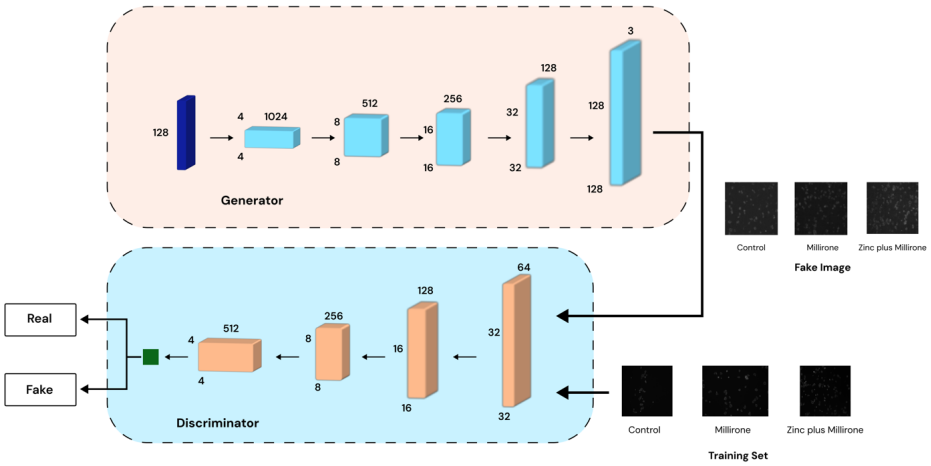

Figure 2. WGAN-GP architecture for synthetic platelet image generation. The generator (top) produces synthetic images, while the discriminator (bottom) evaluates real vs. generated images to refine quality.

2.5. Model training and evaluation

2.5.1. Model training

All CNN models were trained for 100 epochs using:

Optimizer: Adam with a learning rate of 0.001.
Batch Size: 32 (128 tested in some trials).
Loss Function: Categorical cross-entropy for the multi-class classification.

Hyperparameters were tuned for optimal performance. The best-performing checkpoints were saved.

2.5.2. Evaluation metrics

The evaluation metrics used were:

$$Precision = \frac{TP}{TP + FP} \quad (1)$$

$$Recall = \frac{TP}{TP + FN} \quad (2)$$

$$Accuracy = \frac{TP + TN}{TP + TN + FP + FN} \quad (3)$$

$$F1Score = 2 * \frac{(Precision * Recall)}{(Precision + Recall)} \quad (4)$$

Confusion matrices, accuracy and loss plots were generated to visualize classification performance.

3. RESULTS

3.1. Classification results with the original dataset of 71 images

As shown in Table 1, the limited size of the original dataset resulted in moderate model performance. DenseNet121 achieved the highest accuracy at 81%, with a precision of 84%, while other architectures like DenseNet201 and DenseNet169 followed with 76% and 71% accuracy, respectively. However, VGG19 struggled, attaining only 52% accuracy, and the two custom CNN models underperformed significantly, particularly Custom Model 2, which had a precision of only 33%. These results highlight the challenge of training deep learning models with small datasets, reinforcing the need for data augmentation to improve generalizability.

Models (Batch size 32)	Accuracy (%)	F1-Score (%)	Precision (%)	Recall (%)
Custom Model 1	62	56	68	62
Custom Model 2	57	42	33	57
DenseNet121	81	79	84	81
DenseNet169	71	67	77	71
DenseNet201	76	74	83	76
VGG16	57	47	43	57
VGG19	52	45	40	52

VGG19-FF	62	59	63	62
InceptionV3	62	51	46	62
InceptionResNetV2	71	69	76	71
AlexNet	62	56	59	62

Table 1. Classification results with the original dataset of 71 Images for the different classification models with the metrics: accuracy, F1-score, precision and recall.

3.2. Classification results with the augmented dataset level 1 of 141 images

As presented in Table 2, performance improved across most architectures compared to the original dataset. DenseNet201 achieved the highest accuracy at 86%, followed by DenseNet121, DenseNet169, and InceptionV3, which ranged between 79% and 76%. The application of augmentation techniques contributed to enhanced model generalizability. However, Custom Model 2 exhibited significantly lower performance, with an accuracy of only 38% and a precision of 15%, indicating its limited capacity to learn from the expanded dataset.

Models (Batch size 32)	Accuracy (%)	F1-Score (%)	Precision (%)	Recall (%)
Custom Model 1	67	66	69	67
Custom Model 2	38	21	15	38
DenseNet121	79	79	79	79
DenseNet169	79	78	83	79
DenseNet201	86	86	88	86
VGG16	62	62	72	62
VGG19	64	64	68	64
VGG19-FF	76	76	80	76
InceptionV3	76	76	79	76
InceptionResNetV2	71	69	80	71
AlexNet	67	65	66	67

Table 2. Classification results with the traditionally augmented dataset of images, where was performed the Level 1 augmentation (141 images), for the different classification models with the metrics: accuracy, F1-score, precision and recall.

3.3. Classification results with the augmented dataset level 2 of 1,463 images

A substantial jump in performance was observed with the dataset augmented to the level 2 , as shown in Table 3. In these experiments InceptionV3 and InceptionResNetV2 reached 99% accuracy with equally high precision and recall, underscoring the importance of a sufficiently

large, varied dataset. DenseNet201 with a 98% value of accuracy also performed exceptionally.

Models (Batch size 32)	Accuracy (%)	F1-Score (%)	Precision (%)	Recall (%)
Custom Model 1	97	97	97	97
Custom Model 2	88	87	91	88
DenseNet121	97	97	98	97
DenseNet169	97	97	97	97
DenseNet201	98	98	98	98
VGG16	97	97	97	97
VGG19	94	94	94	94
VGG19-FF	95	95	95	95
InceptionV3	99	99	99	99
InceptionResNetV2	99	99	99	99
AlexNet	30	14	9	30

Table 3. Classification results with the traditionally augmented dataset of images, where was performed the Level 2 augmentation (1,463 images), for the different classification models with the metrics: accuracy, F1-score, precision and recall.

3.4. Classification results with the synthetic dataset of 300 Images created by WGAN-GP

GAN-based augmentation, or synthetic data created by the WGAN-GP further enhanced classification outcomes, as shown in Table 4. DenseNet121 and Custom Model 1 both achieved 97% accuracy, while Inception-based models and DenseNet169 also scored above 90%. Although AlexNet improved slightly (74% accuracy), it still lagged behind more modern architectures.

Models (Batch size 32)	Accuracy (%)	F1-Score (%)	Precision (%)	Recall (%)
Custom Model 1	97	94	95	94
Custom Model 2	87	87	87	87
DenseNet121	97	97	97	97
DenseNet169	91	91	93	91
DenseNet201	96	96	96	96
VGG16	83	83	85	83
VGG19	89	89	89	89
VGG19-FF	88	88	89	88
InceptionV3	94	94	95	94
InceptionResNetV2	90	90	90	90
AlexNet	74	75	75	74

Table 4. *Classification results with the synthetic dataset with 300 Images created by the WGAN-GP for the different classification models with the metrics: accuracy, F1-score, precision and recall.*

3.5. Examples of the synthetic images created by WGAN-GP

Figure 3 illustrates the differences between the original dataset and the various augmentation strategies applied to platelet images. The first column has images of the different classes from the the original dataset, followed by images of the traditionally augmented to the Level 1 dataset, where were applied abasic transformations such as flipping and rotation. The third column showcases images from the traditionally augmented Level 2 dataset, incorporating more extensive modifications such as shearing and zooming. Finally, the last column presents images generated using a Wasserstein GAN with Gradient Penalty (WGAN-GP), producing synthetic platelet images that expand the dataset. The progressive transformations highlight the role of each augmentation technique in enhancing dataset diversity and model robustness.

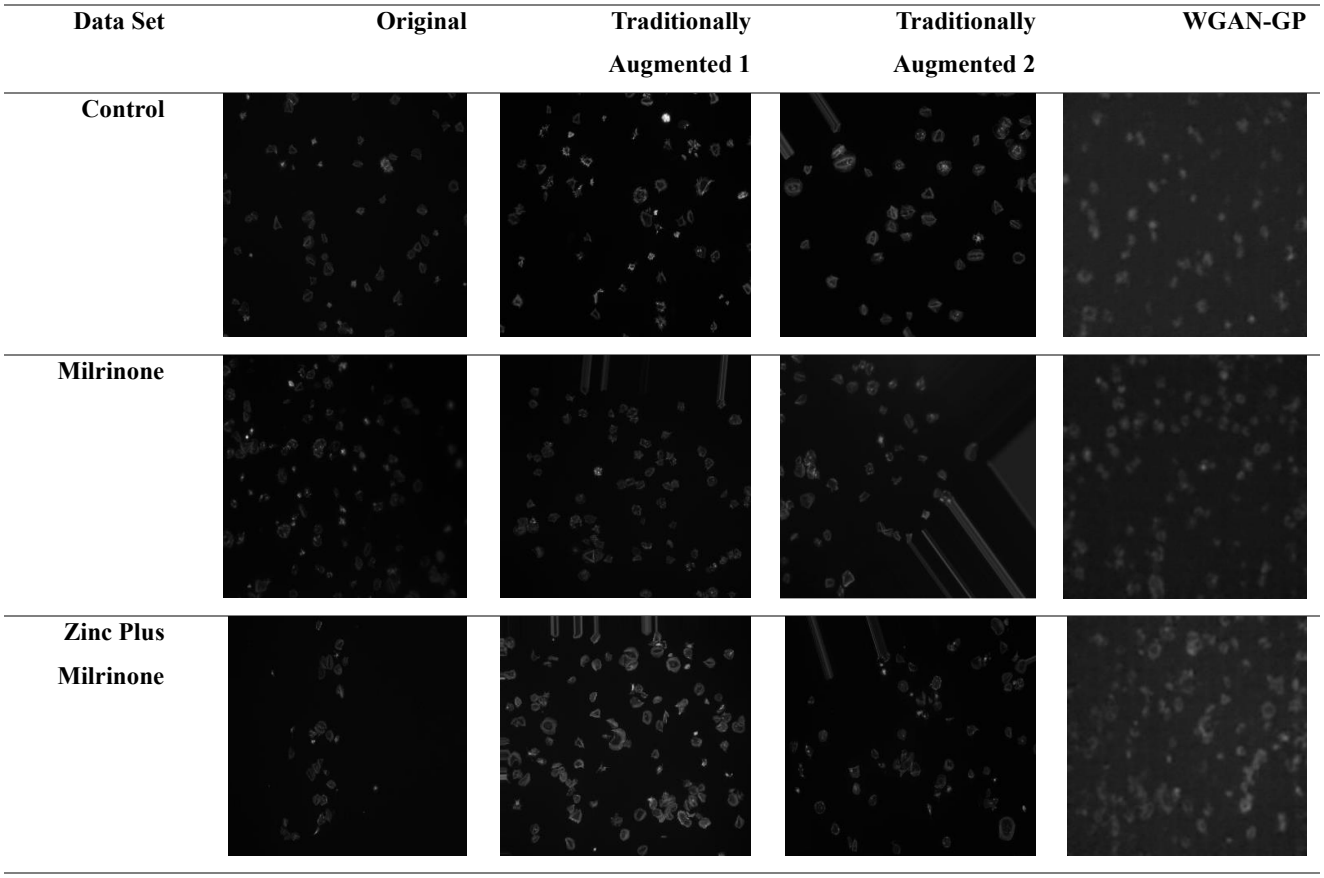

Figure 3. Comparison of original, traditionally augmented, and GAN-generated platelet images. From left to right: Original dataset, Level 1 augmentation, Level 2 augmentation, and WGAN-GP generated images.

4. DISCUSSION

The methodological choices in this study, particularly concerning data augmenta-tion and model selection, significantly influenced the results obtained. The original dataset, consisting of only 71 platelet images, presented a considerable limitation for training deep learning models, leading to suboptimal performance due to overfitting. As observed in previous studies, deep learning models require large and diverse datasets to generalize effectively, and small sample sizes often lead to performance degradation [23,34]. In this study, models trained solely on the original dataset demonstrated moderate performance, with DenseNet121 achieving the highest accuracy at 81%, while simpler architectures such as VGG19 and AlexNet performed significantly worse, with 52% and 62% accuracy, respectively. These findings align with previous work in medical image classification, where small datasets have been shown to negatively impact deep learning models, particularly those with complex architectures [23,34].

To mitigate this issue, two levels of traditional augmentation were applied. The first level (141 images) employed basic transformations such as flipping, rotation, and zooming, whereas the second level (1,463 images) incorporated more extensive modifications, including shearing and additional rotation angles. As reported in Perez et al. [23], data augmentation has been widely acknowledged as a key strategy to mitigate overfitting and improve model robustness in deep learning applications. In line with these findings, the results of this study demonstrated that Level 2 augmentation significantly improved model performance, particularly for deeper architectures. Models such as InceptionV3 and InceptionResNetV2 achieved 99% accuracy, reinforcing existing literature, which suggests that large, diverse datasets enable deep networks to extract more representative features, ultimately leading to superior classification per-formance [32].

Further improvements were observed with GAN-based augmentation, where a WGAN-GP model generated 300 synthetic platelet images after being trained for 5000 epochs per class. As seen in Yi et al. [24] and Frid-Adar et al. [25], GANgenerated data has been shown to effectively enhance deep learning models, particularly in medical imaging applications where data availability is limited. The introduction of synthetic images further improved classification outcomes, with DenseNet121 and Custom Model 1 achieving 97% accuracy, demonstrating the effectiveness of synthetic data generation in complementing real datasets. However, it is important to note that while GANbased augmentation provided substantial improvements, certain challenges remain. Prior studies have reported that GANs can suffer from mode collapse, where the model generates highly similar images, leading to a lack of diversity in the dataset [24]. In this study, the use of WGAN-GP helped mitigate this issue by ensuring more stable training and realistic image generation.

Comparative analysis of augmentation techniques indicates that traditional augmentation provided a strong foundation for improving model generalizability, but further enhanced classification accuracy has been achieved with the GANbased augmentation by introducing synthetic variations.

The expectation was that augmentation would improve model robustness, particularly for deeper architectures, and the results support this hypothesis, but the degree of improvement

varied across models. Some results were somehwat unexpected, as the one of AlexNet's accuracy declining significantly to 30% on Level 2 augmentation, suggesting that its limited capacity for complex feature extraction made it less effective when trained on a highly varied dataset. Contrarily to AlexNet, DenseNet and Inception-ased models exhibited substantial performance gains, this differences align with findings in Sandfort et al. which highlighted that deeper networks require larger and more diverse datasets to optimize feature extraction and classification [22]. These results further support the broader consensus in the literature that data augmentation plays a pivotal role in improving model generalizability, mitigating overfitting, and addressing dataset limitations in deep learning applications. As demonstrated in previous studies, including those on liver lesion classification, chest Xray diagnostics, and histopathology image analysis, augmentation techniques have consistently led to performance improvements across various medical imaging tasks [23,22,25]. Future research should investigate conditional GANs and domain adaptation strategies to enhance data augmentation, improving the diversity and quality of training samples. Additionally, transformerbased architectures should be explored for classification after augmentation, as they have recently shown strong performance in complex image classification tasks. Additionally, expanding the dataset with realworld platelet images and incorporating more sophisticated augmentation strategies, such as adaptive augmentation and metlearning approaches, may further enhance the generalizability and robustness of platelet classification models.

5. CONCLUSIONS

This study investigated platelet image classification using traditional data augmentation (Levels 1 and 2) and a WGAN-GP approach to generate synthetic data. Results showed that extensively augmented datasets (Level 2) and GAN-augmented data both significantly improved classification accuracy for advanced CNN architectures (particularly DenseNet and Inception families). These outcomes underscore the value of combining comprehensive augmentation strategies with GANbased synthetic images, especially in cases where medical image data is limited.

REFERENCES

[1] Vinholt, P. “The Role of Platelets in Bleeding in Patients with Thrombocytopenia and Hematological Disease”, *Clin. Chem. Lab. Med.* Vol. 57, pp.1808–1817, 2012.

[2] Zhou, Y.; Yasumoto, A.; Lei, C.; Huang, C. J.; Kobayashi, H.; Wu, Y.; Yan, S.; Sun, C. W.; Yatomi, Y.; Goda, K.” Intelligent Classification of Platelet Aggregates by Agonist Type”, *eLife* , Vol.. 9, e52938, 2020.

[3] Babker, A. M.; Suliman, R. S.; Elshaikh, R. H.; Boboyorov, S.; Lyashenko, V.” Sequence of Simple Digital Technologies for Detection of Platelets in Medical Images”, *Biomed.* Pharmac. J. Vol. 17, pp. 1–9, 2024.

[4] Hamid, G. A. “Clinical Hematology”, 2013.

[5] Coupland, C. A.; et al. “Platelet Zinc Status Regulates Prostaglandin-Induced Signaling,

Altering Thrombus Formation.", J. *Thromb. Haemost*. Vol. 21 (9), pp. 2545–2558, 2023.
[6] Costa, M. I.; Sarmento-Ribeiro, A. B.; Gonçalves, A. C. "Zinc: From Biological Functions to Therapeutic Potential", *Int. J. Mol. Sci.* Vol 24 (5), pp. 4822, 2023.
[7] Gaydos, L. A.; Freireich, E. J.; Mantel, N." The Quantitative Relation between Platelet Count and Hemorrhage in Patients with Acute Leukemia", *N. Engl. J. Med*. Vol. 266, pp. 905–909, 1962.
[8] Mustafa, M. E.; Mansoor, M. M.; Mohammed, A.; Babker, A. A." Evaluation of Platelets Count and Coagulation Parameters among Patients with Liver Disease", *World J. Pharm. Res*, Vol. 4, pp. 360–368, 2015.
[9] Isbister, J. "Clinical presentations of haematological disease", *Modern Medicine*, Vol.3, pp. 26, 2006.
[10] Goliwas, K. F.; et al. "Methods to Evaluate Cell Growth, Viability, and Response to Treatment in a Tissue Engineered Breast Cancer Model", *Sci. Rep*. Vol. 7 (1), pp. 14326, 2017.
[11] Mohammed, E. A.; Mohamed, M. M.; Far, B. H.; Naugler, C." Peripheral Blood Smear Image Analysis: A Comprehensive Review", *J. Pathol. Inform.* Vol. 5, pp. 9, 2017.
[12] Chen, S.; Zhao, M.; Wu, G.; Yao, C.; Zhang, J. "Recent Advances in Morphological Cell Image Analysis", *Hindawi Limited*, 2012.
[13] Santos-Silva, M. A.; Sousa, N.; Sousa, J. C. "Artificial Intelligence in Routine Blood Tests", *Front. Med. Eng*. Vol. 2, pp. 1369265, 2024.
[14] Farfour, E.; Clichet, V.; Péan de Ponfilly, G.; Carbonnelle, E.; Vasse, M. "Impact of COVID-19 Pandemic on Blood Culture Practices and Bacteremia Epidemiology", *Diagn. Microbiol. Infect. Dis.*, Vol. 107 (1), pp.116002, 2023.
[15] Xu, Y.; et al. "Artificial Intelligence: A Powerful Paradigm for Scientific Research", *Cell Press.* 2021.
[16] Maturana, C. R.; et al. "Advances and Challenges in Automated Malaria Diagnosis Using Digital Microscopy Imaging with Artificial Intelligence Tools: A Review", *Front. Microbiol*. 2022,
[17] Goodfellow, I.; Pouget-Abadie, J.; Mirza, M.; Xu, B.; Warde-Farley, D.; Ozair, S.; Courville, A.; Bengio, Y. "Generative Adversarial Nets", *Advances in Neural Information Processing Systems*; pp 2672–2680, 2014.
[18] Zhang, J.; Xie, Y.; Wu, Q.; Xia, Y. "Medical Image Classification Using Deep Learning", *IEEE Trans. Med. Imaging*, Vol. 37, pp. 1249–1258, 2018.
[19] Li, M.; Jiang, Y.; Zhang, Y.; Zhu, H. "Medical Image Analysis Using Deep Learning Algorithms", *Front. Public Health.* Vol. 11, pp. 1273253, 2023.
[20] Berryman, S.; Matthews, K.; Lee, J. H.; Duffy, S. P.; Ma, H." Image-Based Phenotyping of Disaggregated Cells Using Deep Learning", *Commun. Biol.* Vol. 3 (1), pp. 1399, 2020.
[21] Yao, K.; Rochman, N. D.; Sun, S. X. "Cell Type Classification and Unsupervised Morphological Phenotyping from Low-Resolution Images Using Deep Learning", *Sci. Rep.* Vol. 9 (1), pp.50010, 2019.
[22] Sandfort, V.; Yan, K.; Pickhardt, P. J.; Summers, R. M. "Data Augmentation Using Generative Adversarial Networks (CycleGAN) to Improve Generalizability in CT

Segmentation Tasks", *Sci. Rep*. Vol. 9, pp. 16884, 2019.
[23] Perez, L.; Wang, J. "The Effectiveness of Data Augmentation in Image Classification Using Deep Learning", *arXiv*, 2017.
[24] Yi, X.; Walia, E.; Babyn, P. "Generative Adversarial Network in Medical Imaging: A Review", *Med. Image Anal*. Vol. 58, pp.101552, 2019.
[25] Frid-Adar, M.; Klang, E.; Amitai, M.; Goldberger, J.; Greenspan, H. "Synthetic Data Augmentation Using GAN for Improved Liver Lesion Classification", *IEEE Trans. Med. Imaging*. Vol. 38, pp. 809–818, 2018.
[26] Salehinejad, H.; Colak, E.; Dowdell, T.; Barfett, J.; Georgescu, B. "Synthesizing Chest X-ray Pathology for Training Deep Convolutional Neural Networks". *arXiv.* 2018.
[27] Abidoye, I.; Ikeji, F.; Sousa, E. "Automatic Classification of Platelets Images: Augmented and Non-Augmented Comparison of Pre-trained versus Custom Models" [Poster], *Inspire Leeds 2024, 2*024.
[28] Huang, G.; Liu, Z.; Van Der Maaten, L.; Weinberger, K. Q. "Densely Connected Convolutional Networks", *Proceedings of the IEEE Conference on Computer Vision and Pattern Recognition*, pp 4700–4708, 2017.
[29] Simonyan, K.; Zisserman, A. "Very Deep Convolutional Networks for Large-Scale Image Recognition", *arXiv*, 2015.
[30] Szegedy, C.; Ioffe, S.; Vanhoucke, V.; Alemi, A. Inception-v4," Inception-ResNet and the Impact of Residual Connections on Learning", *Proceedings of the AAAI Conference on Artificial Intelligence*, 2016.
[31] Krizhevsky, A.; Sutskever, I.; Hinton, G. E. "ImageNet Classification with Deep Convolutional Neural Networks", *Advances in Neural Information Processing Systems*, pp 1097–1105, 2012.
[32] Arjovsky, M.; Chintala, S.; Bottou, L. "Wasserstein GAN", *arXiv*, 2017.
[33] Arjovsky, M.; Bottou, L. "Towards Principled Methods for Training Generative Adversarial Networks", *arXiv*, 2017.
[34] Nikhil9ca8. "How Many Images per Class Are Sufficient for Training a CNN". *Available online: https://www.geeksforgeeks.org/how-many-images-per-class-are-sufficient-for-training-a-cnn/* (accessed on 19 September 2024).
[35] Mardani, M.; Gong, E.; Cheng, J. Y.; Vasanawala, S.; Zaharchuk, G.; Alley, M.; Thakur, N.; Han, S.; Dally, W.; Pauly, J. M.; Xing, L. "Deep Generative Adversarial Networks for Compressed Sensing Automates MR"I. *arXiv* 2017.

SYMCOMP 2025
Lisbon, 10-11 April 2025

COMPUTATIONAL TREATMENT OF THE HIERARCHY OF GENERAL AND EVOLUTION ALGEBRAS

Adolfo Vázquez Ruiz[1*], Rafael Vázquez Ruiz[1] and Juan Núñez Valdés[1]

1: Department of Geometry and Topology
Faculty of Mathematics
University of Sevilla
C/ Tarfia s/n, 41012-Seville (Spain)

e-mail: adolfovr3@gmail.com
e-mail = ravaiz401@gmail.com, jnvaldes@us.es

Keywords: algebras, hierarchy, algorithms, complexity, computational time

Abstract. *The concept of the hierarchy of algebras is not too covered in the literature. Indeed, there are very few works on the hierarchy of algebras in general and almost none for any particular type of algebras. In a previous work by one of the authors, the hierarchy of evolution and Lie algebras was studied and that study was used to extend that concept to the hierarchy of associated graphs, although the computational treatment given to that study was not too extensive. This paper delves into this last aspect, theoretically estimating the worst space and time complexity for general algebras and verifying it empirically. Examples near the worst case have been proposed and executed several times per dimension to get a neat scatter-plot. The polynomial fits which optimize their goodness values follow the predicted theoretical laws. Time complexity has been tested for evolution algebras too, yielding no relevant changes w.r.t. the general case. Finally, a deep study on dependences between complexity and the structure of both the input and the output has been carried out. It has been noticed that intricacy of output structure and execution times are highly correlated. Effect of input structure is much weaker.*

DOI:10.5281/zenodo.15160848

Introduction

There are very few references in the literature on the concept of hierarchy of algebras in general, and even less in the case of particular algebras, such as those of Lie, Leibniz, Morgan, Zimbiel and others equally well known, such as evolution algebras, which, unlike all the previous ones, do not have an identity that characterizes them.
About evolution algebras in particular, it was Tian, who introduced them in his doctoral thesis, who first gave the first notions about their hierarchy in his book in 2008 [2], not having later other references in this respect until Cruz, del Valle, Núñez and Pena returned to this question in [1].
In that article, those authors generalized the concept of hierarchy to any algebra and proved that that concept is an invariant under isomorphism of algebras. In fact, they also introduced a new version of the concept of hierarchy for graphs, which, at preset, is still less studied that the one for algebras.
However, in that work the authors do mainly a theoretical study of the question, presenting an algorithm that allowed them obtaining the hierarchy of these algebras, but they only dealt very slightly with the computational aspects of the algorithmic study they carried out, although they did comment that this study remained as an open problem, which they wished to solve in the future.
This paper fills that gap. In it, the authors (one of whom was also the author of that previous article), present a detailed and careful computational study of this issue, addressing computational aspects of the algorithm presented in [1].
The main results of the computational study carried out have been the following. Firstly, it has been proven that the regression for the spatial complexity of the computational treatment of evolution algebras is cubic, as Cruz et al had already conjectured in [1]. To do this, a more powerful computer has been used than the one the authors of that article had used and it has been subjected to random sampling up to dimension 200, in which the measurements are taken separated in time to average the background fluctuations of the base consumption of RAM, ignoring all dispensable programs, all of which produced a definitely very good fit.
Secondly, we have investigated the worst possible case of algebras at a computational level, obtaining several conclusions about the form of these algebras: they must have maximum depth in their hierarchy and produce certain chains in the search set that cause each MPi the corresponding searchi is maximum. In this regard, an attempt has been made to create a random generator of product rules that meet these conditions, in order to provide more examples of unfavorable algebras. For now, an algebra generator with maximum depth in its hierarchy has been obtained, and the density or sparsity of the elements in the product rules can be modulated to show more and less complicated examples.
Also, regarding the presentation, examples have been represented as follows: the product rules are represented in a tensor of voxels (or cubes) and the hierarchies in matrix color maps. This allows for a simple visual check of the hierarchy and structural complexity

of product rules, although there is little intuition that this can be developed to know whether a more complex structure induces more or less connected hierarchies.
The structure of this paper is as follows: Section 1 is mainly devoted to recall some preliminaries concepts and results on the hierarchy of an algebra in general and of an evolution algebra in particular. Based on the algorithm used by Cruz et al. to carry out the computational treatment of the theoretical study that they did in [1] on the hierarchy of algebras, Section 2 shows the most extensive and deep computational treatment that the authors have carried out on this topic, dealing in 5 different subsections with some aspects of the computational treatment of the algorithm, including in them the worst case time complexity (Subsection 2.1), the average runtime growth of a general algebra (Subsection 2.2), the effect of input and output structure on runtimes (Subsection 2.3), the complexity for evolving algebras (Subsection 2.4) and the space complexity (Subsection 2.5). Some examples of algebras and their hierarchies are given in Section 3 and some conclusions in Section 4 followed by the corresponding bibliography used close this contribution.

1 Preliminaries

So that this paper was self-contained, we recall in this section some basic concepts and properties of evolution algebras. For further information, the reader can consult [2, 3], for instance.

1.1 Evolution algebras

Let E be an algebra (not necessarily associative) over a field K, endowed with the multiplication law and let $e_i, i \in \Lambda$ be a basis of E. Then, $e_i \cdot e_j = \sum_{k\in\Lambda} a_{ij}^k\, e_k$, for any $a_{ij}^k \in K$, where only a finite number of *structure constants* a_{ij}^k are not null, for some $i, j \in \Lambda$ fixed. Under these conditions, Tian defined an *evolution algebra* as the one for which exists a basis that verifies $a_{ij}^k = 0$, if $i \neq j$ (that is, $e_i \cdot e_j = 0$, if $i \neq j$). This basis is called *natural*. After renaming the structure constants, one can write $e_i \cdot e_i = \sum_{j=1}^{v} a_{ji}\, e_j$.
Particular cases of evolution algebras are the following.
If the defiining relations are given by $e_i \cdot e_j = 0$, for all i and j, the algebra generated by these generators is said to be a *zero evolution algebra*.
If the defiining relations are $e_i \cdot e_j = 0$, for $i \neq j$ and $e_i^2 = \alpha e_i$, for some $\alpha \in K$, the algebra is said to be a *nonzero trivial evolution algebra*.
If the defining relations are $e_i^2 = \sum_{e_k\in V_i} e_k, \qquad e_i \cdot e_j = 0,\ i \neq j;\ i, j = 1, 2, \ldots, r$, where V_i is a subset of the set V, the evolution algebra is called *graphicable evolution algebra.*.
It is obvious that every graphicable algebra is an evolution algebra, although the converse is not true, in general.

1.2 Hierarchy of an evolution algebra

The main definitions and results shown by Tian in his book [2] about the concept of *hierarchy* of an evolution algebra were the following

Definition 1.1 *An evolution algebra is said to be*

- connected*, if it does not admit a decomposition in direct sum of two proper subalgebras.*
- simple*, if it has no proper evolution ideals.*
- irreducible*, if it has no proper subalgebras.*

Recall that for Tian, a *subalgebra* of an evolution algebra E with natural basis V, is every closed subset on E that is generated by a subset of V.

Theorem 1.2 (Decomposition Theorem) *Let E be a connected evolution algebra. If it is considered as a vector space, then E admits the following decomposition in direct sum of subspaces*

$$E = A_1 \oplus A_2 \oplus \cdots \oplus \dot{+} B, \tag{1}$$

where all the A_i, $i = 1, 2, \cdots, n$, are simple evolution subalgebras, $A_i \cap A_j = \{0\}$, for $i \neq j$ and B is a subspace generated by algebraically transient generators (what Tian denominates a transient space*).*

In that expression, the summation $A_1 \oplus A_2 \oplus \cdots \oplus A_n$ is a direct sum of subalgebras and the symbol $\dot{+}$ denotes a direct sum of subspaces. Tian calls this decomposition a *semidirect-sum decomposition* of an evolution algebra.

Note that, defining an induced multiplication in B_0, denoted by $\overset{1}{\cdot}$, in the following way

$$e_{0,i} \overset{1}{\cdot} e_{0,j} = \rho_{B_0}(e_{0,i} \cdot e_{0,j}), \tag{2}$$

being ρ_{B_0} the projection of E onto B_0, then B_0, equipped with this new product, becomes an evolution algebra and so we can apply the Theorem 1.2 to it, obtaining

$$B_0 = A_{1,1} \oplus A_{1,2} \oplus \cdots \oplus A_{1,n_1} \dot{+} B_1,$$

where all the $A_{1,i}$, $i = 1, \ldots, n_1$ are simple evolution subalgebras of B_0, $A_{1,i} \cap A_{1,j} = \{0\}$, if $i \neq j$, and B_1 is the first transient space spanned by the first algebraically transient generators. This process can be repeated until we reach the i-th level where the transient space becomes trivial (that is, $B_i = \{0\}$).

Definition 1.3 (Hierarchy of an evolution algebra) *The* hierarchy of an evolution algebra *is defined as the decomposition obtained by applying successively the Theorem 1.2 to the algebra E and to the algebras B_i (with the induced product defined above) generated by algebraically transient generators (see Section 1.4).*

1.3 Theoretical aspects of the hierarchy of a generic algebra

This section is a reminder of the theoretical study carried out in citeAbraham to generalize the previous ideas on hierarchy on evolution algebras given by Tian in [2] to the case of any algebra in general.
From here on, $\mathfrak{g}$ will denote a finite n-dimensional algebra defined over a n-dimensional K-vector space V and $\mathfrak{B} = \{e_1, \ldots, e_n\}$ will be a basis of $\mathfrak{g}$.

Definition 1.4 (Persistent set) *Let $S = \{e_i\}_{i\in\Lambda} \subset \mathfrak{B}$ a subset of generators of $\mathfrak{g}$. S is said to be a* persistent *set if for all $i, j \in \Lambda$ there exist $e_{ij_1}, \ldots, e_{ij_p} \in S$, and $a_1, \ldots, a_p \in K$ such that*

$$e_i \cdot e_j = \sum_{k=1}^{p} a_k e_{ij_k} \tag{3}$$

Otherwise, the set S is said to be transient*.*

Tian's characterization of algebraic persistency of the generators of an evolution algebra involved the definition of the *occurrence* of a generator in another one. Tian says that a generator *occurs* in other if the first appears in the expression of the square of the second one as a linear combination of the basis elements. In citeAbraham Tian's *occurrence* concept was generalized through the introduction of a new concept: the *appearance* of a generator in the product of two others. It allows us to characterize the persistency of a set through its relationship with another certain set.

Definition 1.5 (Appearance of a generator in the product of two others) *It is said that the generator $e_k \in \mathfrak{B}$* appears in *$e_i \cdot e_j$, which is denoted by $e_k \dashv e_i \cdot e_j$, if $a_k \neq 0$ in the expression 3.*

The following results, which were proved in citeAbraham, allow to obtain the Decomposition Theorem cited at the end of these paragraphs.

Proposition 1.6 *Let the subset $S = \{e_i\}_{i\in\Lambda} \subset \mathfrak{B}$ formed by generators and consider the set defined by*

$$M = \{e \in \mathfrak{B} \mid \exists\, i, j \in \Lambda,\ \text{with } e \dashv e_i \cdot e_j\} \tag{4}$$

Then, S is persistent if and only if $M \subseteq S$.

Definition 1.7 *A persistent subset of a set of generators of an algebra is said to be* simple *if there is no persistent set strictly contained in it.*

Proposition 1.8 *If $S = \{e_i\}_{i\in\Lambda} \subset \mathfrak{B}$ is a simple persistent set, then $\langle S\rangle$ is a simple subalgebra of $\mathfrak{g}$, where $\langle S\rangle$ denotes the algebra spanned by S.*

Lemma 1.9 *Let $S_1 = \{e_1 \dots e_k\} \subset \mathfrak{B}$ and $S_2 = \{e_{k+1} \dots e_m\}$ $(m \leq n)$ be two persistent sets of the algebra $\mathfrak{g}$, and let $A_1 = \langle S_1 \rangle, A_2 = \langle S_2 \rangle$ be two subalgebras, respectively spanned by S_1 and S_2. Then, it is verified that*

1. *S_i is a system of generators of A_i, $i = 1, 2$.*
2. *$A_1 \oplus A_2 = \langle e_1 \dots e_m \rangle$ (as vector spaces).*

Theorem 1.10 (Decomposition Theorem) *Let $\mathfrak{g}$ be a generic n-dimensional algebra, defined over a K-vector space V of dimension n, and $\mathfrak{B} = \{e_1, \dots, e_n\}$ a basis of $\mathfrak{g}$. Then $\mathfrak{g}$, considered as a vector space, admits a decomposition in a direct sum of subspaces as follows*

$$\mathfrak{g} = A_1 \oplus A_2 \oplus \cdots \oplus A_m \dot{+} B,$$

where A_i, $i = 1, 2 \dots m$ are all simple subalgebras of $\mathfrak{g}$, with $A_i \cap A_j = \{0\}$ for $i \neq j$, B is the vector subspace generated by a transient set of generators, and where $\oplus$ stands for the direct sum of subalgebras and $\dot{+}$ for the direct sum of vector subspaces. This decomposition is named as semidirect sum decomposition of an algebra.

1.4 Construction of the hierarchy of a generic algebra

According to previous study, in citeAbraham is construct the hierarchy of any algebra $\mathfrak{g}$ and it is also shown an algorithmic procedure to obtain it. This algorithmic procedure had the following steps, from which the concept of hierarchy for a generic algebra is introduced.

Step 1: Level 0 of the hierarchy of the algebra.

As proved in the Theorem 1.10, $\mathfrak{g}$ can be decomposed as

$$\mathfrak{g} = A_1 \oplus A_2 \oplus \cdots \oplus A_m \dot{+} B_0,$$

where, according to the proof of the mentioned theorem, B_0 is a vector space generated by a set of transient generators.

The next level is defined as follows

Step 2: Level 1 of the hierarchy of the algebra.

If Λ is the set of indexes of the set of generators $\{e_i\}_{i \in \Lambda} \subset \mathfrak{g}$, we name by $e_{0,k}$ the generators of B_0, with $k \in \Lambda_0 \subset \Lambda$. We define the induced product in B_0, denoted by $\overset{1}{\cdot}$, as follows

$$e_{0,i} \overset{1}{\cdot} e_{0,j} = \rho_{B_0}(e_{0,i} \cdot e_{0,j}),$$

where ρ_{B_0} is the projection of $\mathfrak{g}$ onto B_0. Note that B_0, endowed with that product, inherits the algebra structure from $\mathfrak{g}$. Then, we call B_0 the first algebra induced by $\mathfrak{g}$. Applying the Theorem 1.10 to the algebra $(B_0, \overset{1}{\cdot})$, we obtain that

$$B_0 = A_{1,1} \oplus A_{1,2} \oplus \cdots \oplus A_{1,n_1} \dot{+} B_1,$$

where all $A_{1,i}$, $i = 1, 2 \ldots n_1$ are simple subalgebras of B_0, verifying that $A_{1,i} \cap A_{1,j} = \{0\}$, if $i \neq j$, and B_1 is the vector subspace generated by a set of transient generators in B_0, named as *first transient subspace*. Applying the same idea to B_1, the second level is obtained.

Step 3: Next levels of the hierarchy of the algebra.

After applying the first two steps as many times as necessary, the following decomposition is obtained

$$\begin{gathered}
\mathfrak{g} = A_{0,1} \oplus A_{0,2} \oplus \cdots \oplus A_{0,n_0} \dot{+} B_0 \\
B_0 = A_{1,1} \oplus A_{1,2} \oplus \cdots \oplus A_{1,n_1} \dot{+} B_1 \\
B_1 = A_{2,1} \oplus A_{2,2} \oplus \cdots \oplus A_{2,n_2} \dot{+} B_2 \\
\cdots\cdots\cdots \\
B_{m-1} = A_{m,1} \oplus A_{m,2} \oplus \cdots \oplus A_{m,n_m} \dot{+} B_m \\
B_m = B_{m,1} \oplus B_{m,2} \oplus \cdots \oplus B_{m,h},
\end{gathered}$$

where $A_{k,l}$ is the k-th simple subalgebra of level l, $A_{k,l} \cap A_{k,p} = \{0\}$, if $l \neq p$ and B_k is the k-th transient vector subspace, generated by a set of transient generators in B_{k-1}.

In the last level there is no residual vector space, and that is the reason for the algorithm to end at this precise point (note that this level is reached in any case, as we are working with finite-dimensional vector spaces).

The simple algebras of B_k are called *heads* of the hierarchy, being h the number of heads.

Definition 1.11 (Hierarchy of an algebra) *The term hierarchy of an algebra stands for the decomposition of an algebra in semi-sums of its subalgebras as constructed in the previous algorithmic procedure.*

Note that, according to this Decomposition Theorem 1.10, the hierarchy of an algebra is built over the fundamental concept of simple subalgebra, or equivalently, by linearity, the simple persistent set of generators. This allows us to prove the following two results

Proposition 1.12 *Two isomorphic algebras have the same hierarchy.*

Proposition 1.13 *The hierarchy of any n-dimensional Lie algebra $\mathfrak{g}$, with basis $\{e_1, \ldots, e_n\}$, is*

$$A_{0,i} = \{e_i\}\,,\ 1 \leq i \leq n \tag{5}$$

1.5 The algorithm

In [1], authors observed that computationally, the construction of algorithms that deal with the hierarchy of generic algebras was related with two main concepts that must be kept in mind due to their fundamental character

- The minimal persistent set which contains e_i, denoted by $MP(e_i)$
- The set of generators that must be taken into account to build $MP(e_i)$, denoted by $search(i)$

Both concepts lead to the following algorithm

Input: Product rule of an algebra $\mathfrak{g}$, $e_i \cdot e_j = \sum_{k=1}^{n} \alpha_{ijk} e_k$
Output: Hierarchy of $\mathfrak{g}$
begin
set $m = 0$
set $n = 1$
while $dim(\mathfrak{g}) > 0$ **do**
  set $N := dim(\mathfrak{g})$
  for $i \in \{1, ..., N\}$ **do**
    set $MP(e_i) = \{e_i\}$
    set $search(i) = \emptyset$
    for $j \in (\{1, ..., N\} \setminus \{i\})$ **do**
      if $\alpha_{iij} \neq 0$ **then**
        $e_j \in MP(e_i)$
        $(i, j), (j, i), (j, j) \in search(i)$
      end if
    end for
    for $(\tilde{i}, \tilde{j}) \in search(i)$ **do**
      for $k \in \{1, ..., N\}$ **do**
        if $\alpha_{\tilde{i}\tilde{j}k} \neq 0 \wedge e_k \notin MP(e_i)$ **then**
          $e_k \in MP(e_i)$
          $(l, k) \in search(i)\ \forall l \in MP(e_i), l \neq k$
          $(k, l) \in search(i)\ \forall l \in MP(e_i), l \neq k$
          $(k, k) \in search(i)$
        end if
      end for
    end for
  end for
  for $i \in \{1, ..., N\}$ **do**
    if $e_j \in MP(e_k)\ \forall e_j, e_k \in MP(e_i)$ **then**
      set $A_{m,n} = MP(e_i)$

set $n = n + 1$
set $\mathfrak{g} = \mathfrak{g} \setminus MP(e_i)$
end if
end for
set $m = m + 1$
end while
end

1.6 Preimage Algorithm

By considering the rules attached to the verification procedure to form the subalgebras, we can develop a method that provides random algebras matching a certain hierarchy. We must note the following:

- As a consequence of the $MP(e_i)$ construction proceeding it is clear that $e_j \in MP(e_i) \Rightarrow MP(e_j) \subseteq MP(e_i)$. Then, the $A_{m,n}$ construction criteria requires that, given $\mathcal{B}_{A_{m,n}} = \{e_{m,n_i}\}_{1 \leq i \leq dim(A_{m,n})}$, it is satisfied that $MP(e_{m,n_i}) = MP(e_{m,n_j}) \; \forall \, 1 \leq i, j \leq dim(A_{m,n})$. As a consequence of this, we immediately observe that coupling $\mathcal{B}_{A_{m,n}}$ pairwise can be achieved by reciprocally relating the elements, i.e. by making $e_{m,n_j} \dashv e_{m,n_i} \cdot e_{m,n_i} \; \forall \, 1 \leq i, j \leq dim(A_{m,n}) \shortparallel i \neq j$.

- In order to settle $A_{m,n}$ within the mth $(m > 1)$ depth level, all its generators must satisfy $e_{m-1,o_j} \dashv e_{m,n_i} \cdot e_{m,n_i} \; \forall \, 1 \leq i \leq dim(A_{m,n}); \; 1 \leq j \leq dim(A_{m-1,o}); 1 \leq o \leq N_{m-1}$, i.e. they must be all directly related with all the generators appearing in the previous depth level.

- We can freely relate in a crossed way the generators from one depth level with all the previous depth levels: we either take $e_{m,n_i} \cdot e_{o,p_j}, \; e_{o,p_j} \cdot e_{m,n_i} \neq 0$ or not, where m precedes o. The direct relations from the previous bulletpoint makes that when deleting the previous depth levels from the basis this freedom becomes erradicated, avoiding more coupling than that matching the hierarchy.

- The relations between elements appearing across the same depth level must be considered meticulously in order not to jeopardize the desired structure. For $e_{m,n_i} \in \mathcal{B}_{A_{m,n}}; \; e_{m,o_j} \in \mathcal{B}_{A_{m,o}}$, where $n \neq o$, we may allow in general $e_{m,n_i} \cdot e_{m,o_j} \neq 0$ as these are not tightly coupled. A tighter coupling, meaning $n = o$, forces us to only consider $e_{l,p_k} \dashv e_{m,n_i} \cdot e_{m,n_j}$, where either $l < m$ or $l = m \; \wedge \; p = n$, that is we just allow appearance of elements from either previous depth levels or the same depth and same subalgebra.

It has been tested that quite random and general forms for the input are obtained y employing this algorithm. Hence, authors hypothetize this algorithm nearly characterizes an inverse of the hierarchy function.

E.g., it is easy to check that the examples provided in [1] emerge as a specific case of this method.

The algorithm results in the following:

Input: a hierarchy $\{\{\mathbf{A_{m,n}}\}_{\mathbf{1\leq n\leq N_m}}\}_{\mathbf{0\leq m\leq M}}$ and $\mathcal{P}=\{[0,p(0)]\}\cup\{[\beta_w,p(\beta_w)]\}_w$, where $\beta_w\in\mathbb{K}\setminus\{0\}$ and $p(x)$ are the probabilities of appearance, obviously satisfying $p(0)+\sum_w p(\beta_w)=1$. We will later use $\mathcal{P}\setminus\{[0,p(0)]\}$ and will have to employ renormalized probabilities.
Output: the product rules α_{ijk} of an algebra $\mathfrak{g}$ matching with the previous hierarchy.
begin
set $\alpha_{ijk}=0\ \forall i,j,k$
for $0\leq m\leq M$ **do**
  set $\mathcal{B}_m=\bigsqcup_{n\in N_m}\mathcal{B}_{A_{n,m}}$
  for $e_{m_i}\in\mathcal{B}_m$ **do**
    set $\alpha_{m_im_im_i}=$ *random choice* $\mathcal{P}$
  end for
  for $1\leq n,\hat{n}\leq N_m$ **do**
    for $(e_{mn_i},e_{m\hat{n}_j})\in\mathcal{B}_{A_{m,n}}\times\mathcal{B}_{A_{m,\hat{n}}}\ \shortparallel\ e_{mn_i}\neq e_{m\hat{n}_j}$ **do**
      if $n=\hat{n}$ **then**
        set $\alpha_{(mn_i)(mn_i)(mn_j)}=$ *random choice* $\mathcal{P}\setminus\{[0,p(0)]\}$
        set $\alpha_{(mn_j)(mn_j)(mn_i)}=$ *random choice* $\mathcal{P}\setminus\{[0,p(0)]\}$
        for $e_w\in\left(\bigsqcup_{l<m}\mathcal{B}_l\right)\bigsqcup\mathcal{B}_{A_{m,n}}$ **do**
          set $\alpha_{(mn_i)(mn_j)w}=$ *random choice* $\mathcal{P}$
          set $\alpha_{(mn_j)(mn_i)w}=$ *random choice* $\mathcal{P}$
        end for
      else
        for $e_w\in\mathcal{B}_{\mathfrak{g}}$ **do**
          set $\alpha_{(mn_i)(mn_j)w}=$ *random choice* $\mathcal{P}$
          set $\alpha_{(mn_j)(mn_i)w}=$ *random choice* $\mathcal{P}$
        end for
      end if
    end for
  end for
  if $m\geq 1$ **then**
    for $e_{m_i}\in\mathcal{B}_m$ **do**
      for $e_j\in\bigsqcup_{p<m}\mathcal{B}_p$ **do**
        for $e_k\in\mathcal{B}_{\mathfrak{g}}$ **do**
          set $\alpha_{m_il_jk}=$ *random choice* $\mathcal{P}$
          set $\alpha_{l_jm_ik}=$ *random choice* $\mathcal{P}$
          if $e_j\in\mathcal{B}_{m-1}$ **then**
            set $\alpha_{m_im_ik}=$ *random choice* $\mathcal{P}\setminus\{[0,p(0)]\}$

```
            else
              set α_{m_i m_i k} = random choice P
            end if
          end for
        end for
      end for
    end if
  end for
```

2 The computational study of the hierarchy algorithm

We now procceed to study both the time and space complexity of the latter pseudocode.

The main sources of time complexity come from the outer *while* loop, the construction process of each $MP(e_i)$ and the verification of the conditions over the $MP(e_i)$ to build the $A_{m,n}$.

2.1 Worst Case Time Complexity

In [1] authors focus on the following algebras in order to grasp the time complexity:

$$\begin{cases} e_i \cdot e_i = e_{i+1} & (1 \leq i \leq n-1) \\ e_i \cdot e_{i+1} = e_1 & (1 \leq i \leq n-1) \\ e_i \cdot e_j = 0 & \text{otherwise.} \end{cases} \tag{6}$$

These algebras are defined in such a way that they present a recursive behavior when the Decomposition Theorem 1.10 is applied to them.

These conform a convenient example of computationally demanding algebras as these reach the maximum plausible depth for the hierarchy and they verify that for each iteration *iter* $\exists! j_{0,iter}$ ||

$$\begin{aligned} &MP(e_i)_{iter} = \mathcal{B}_{iter},\ search(i)_{iter} = \mathcal{B}_{iter} \times \mathcal{B}_{iter} \setminus \{(i,i)\}\ \forall i \neq j_{0,iter} \\ &MP(e_{j_{0,iter}}) = \{e_{j_{0,iter}}\},\ search(j_{0,iter}) = \emptyset \end{aligned} \tag{7}$$

where $\mathcal{B}_{iter}$ is the basis after *iter* iterations of the algorithm; i.e. with exception of a single basis element $MP(e_i), search(i)$ reach its maximum possible size. Authors of that article hypothetize these are near to the worst case complexity. We can obtain from the preimage algorithm more demanding cases by taking more dense preimages, though the resulting runtimes do not exceed those of the $\mathfrak{g}_n$ by too much (as they do not present much room for getting more complex).

By rough calculation we can estimate the time complexity of the algorithm. We have to consider both the construction procedure of the $MP(e_i)$, $search(i)$ and the verification

of the necessary condition of the $MP(e_i)$. The latter one, alltogether with the outer *while* loop, takes $\mathcal{O}(n^5)$ to execute. Secondly we have to estimate the time needed to constuct the auxiliary sets. It is complicated to exactly compute the time complexity of this section. Nevertheless, we must bear in mind that for each duple in $search(i)$ we have only one $\hat{k} \in \{1, \ldots, N\}$ leading to $\alpha_{ij\hat{k}} \neq 0$ and therefore enabling further operations. Then, it is easy to check that this part of the process also takes $\mathcal{O}(n^5)$ at most to execute.

The algorithm was transcribed to a local version of Python 3.10 and later executed in a computer with the following components: Intel i7 4770 (3.4 GHz CPU), 16.00 GBs of DDR3 RAM (1600 MHz).

We procceed to measure the runtimes of these precise examples until reaching high dimensions. Several measures for each dimension were performed in order to reduce the error.

A curve fit on the obtained data is done for consecutive polynomial models around the expected order of complexity and write down the order of the polynomial that maximizes the goodness of the fit. In order to avoid overfitting, data was split onto a fitting and a validation set. Both the maximum R^2 and minimum validation $RMSE$ were obtained for a 5th degree regression model (Figure 1). Such result was tested for a range of proportions between the fitting and the validation set, raising the same observations.

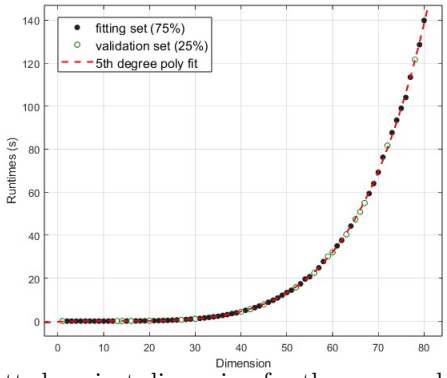

Figure 1: average runtimes plotted against dimension for the proposed $\mathfrak{g}_n$. The curve that best fits the data and minimizes the mean squared errors for the validation data is a 5th degree polynomial.

Implementing a power model also provides a worst case complexity of $\mathcal{O}(n^5)$. This comes as enough evidence to state that, as predicted, the algorithm develops across the dimensions as a quintic function.

2.2 A Hint on the Statistics of Hierarchies: Average Runtime Growth of a General Algebra

Amongst a myriad of algebras we have just analysed a really challenging case in terms of computation. This may not give an idea of the actual efficiency of the algorithm when executed for a random given product rule.

To get the mean time complexity of the algorithm it was tested for 100 random 3-order tensors for each dimension. By analogy with the previous section a curve fit of the averaged runtimes was performed, yielding a time complexity of $\mathcal{O}(n^4)$ (Figure 2). That is, the algorithm is in general more efficient w.r.t. the theoretical prediction obtained via rough calculation. It is due to the fact that for increasing dimension more intricate hierarchies become rare, making that product rules corresponding to the most basic hierarchies spoil the statistics. These hierarchies run a low number of iterations of the outer *while* loop, hence provoking a time complexity of $\mathcal{O}(n^4)$ instead.

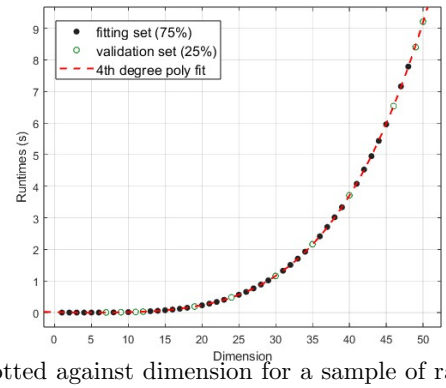

Figure 2: average runtimes plotted against dimension for a sample of random product rules. The curve that best fits the data and minimizes the mean squared errors for the validation set is a 4th degree polynomial.

2.3 Effect of input and output structure on runtimes.

Product rules may vary largely in complexity without even affecting the output hierarchy they induce. Developing intuitive and meaningful metrics on the structure of these 3-order tensors becomes hard. Because of this we will focus on the most obvious source of complexity: the sparsity of the product rules. As a metric of the sparsity of a product rule we can intuitively use:

Definition 2.1 (Sparsity of the Product Rules) *We take the sparsity of the product rules of a general algebra* $\mathfrak{g}$ *as the ratio of the non-zero coefficient of the product rules wrt*

total as

$$\mathcal{S}(\mathfrak{g}) = \frac{card\,(\alpha_{ijk} \neq 0)}{dim(\mathfrak{g})^3} \tag{8}$$

, where α_{ijk} encodes the product rules.

The hierarchy of an algebra is, on the other hand, much simpler and enables us to use more creative ways to characterize the structure of the output. We will mainly use some sort of coupling factor as a metric of the output intricacy. It should become larger for hierarchies featuring larger subalgebras at deeper levels. A first intuitive choice would be to couple each subalgebra with all the basis elements appearing throughout the previous depth levels. Nevertheless, this function is not well behaved, returning extremely high values sometimes. Our second choice would be polynomial instead of recursive. Eventually we used the following metric:

Definition 2.2 (Coupling Factor of a Hierarchy) *As a measure of the complexity of a hierarchy, related with the size of the auxiliary sets of the hierarchy algorithm, we use the sum*

$$\mathcal{CF}\left(\{A_{m,n}\}_{m,n}\right) = \sum_{m,n}(m+1)^2 \cdot dim(A_{m,n})^2 \tag{9}$$

As amongst the vast landscape of product rules those with increasingly more complex hierarchies become more rare as stated in section *2.2*, we will use the preimage algorithm from section *1.6* to get a more varied sample that evaluates the bond between runtimes and the coupling factor.

Random hierarchies were created ranging from 1 to 30 in dimension, sweeping all possible depths and we considered $\mathcal{P} = \{[0, p], [1, 1-p]\}$, where p takes 50 equispaced values from 0 to 1. Its coupling factor was measured. Then the preimage algorithm was executed on them to get random corresponding product rules. Its sparsity was measured. Then the hierarchy computation was performed from these product rules to measure the runtimes.

Firstly, from Figure 3, we infer that the runtimes present a positive significant correlation ($R = 0.92$) with the coupling factor. However, a slight cone shape is obtained, thus indicating underlying heteroscedasticity is going on and thus the coupling factor model employed can be improved.

In Figure 4 it is observed that for low sparsities execution time becomes diminished. However, past from this low sparsity region runtimes do slightly increase as more relations are added. This effect becomes more acute for larger dimensions when compared with smaller ones. It is because a same increase on sparsity leads to a larger addition of bonds in the case of higher dimension. The decrease shown in the curve fit when approaching full sparisty is a mere consequence of overfitting of outliers and must be ignored. It was

not observed when carrying out the same study over specific hierarchies and its preimages.

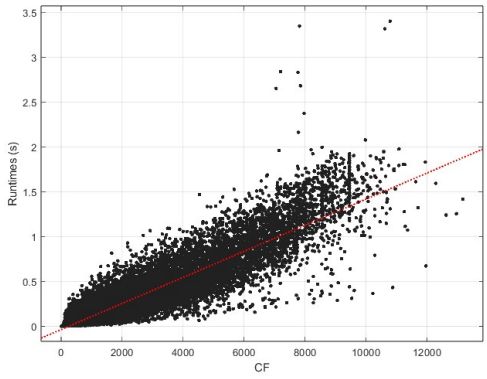

Figure 3: runtimes plotted against the proposed metric for coupling factor. A high correlation between these magnitudes is gotten. Slight heteroscedasticity is observed, indicating the $\mathcal{CF}$ model can be improved.

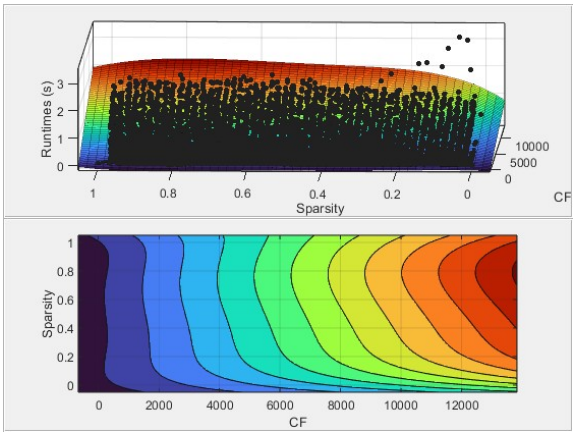

Figure 4: runtimes plotted against $\mathcal{CF}$ and sparsity. A slight increment on runtimes is observed as sparsity gets larger.

From the previous discussions we can derive that sparsity has a slight impact on execution time and it becomes increasingly relevant with dimension. Moreover, the coupling factor explains well the creation of new complex bonds between basis elements and its effect on the runtimes.

2.4 Complexity for Evolution Algebras

In the specific case of evolution algebras we can ensure the existence of a basis for which the product rules become diagonal.

By analogy with the general case, we will derive the time complexity in this case by averaging the runtimes of a large sample of product rules. To generate these product rules we will begin with the root (but random and not unique) case of a diagonal product rule and then we will transform it via applying nonsingular transformations to the basis.

Let $e_i \cdot e_i = \sum_{j=1}^{n} \alpha_{iij} e_j$ be a root case. Let $A = (a_{ij})_{ij}$ be a $n \times n$ regular matrix. Let $\{v_i = Ae_i\}_{i=1}^{n}$ be the new basis. Then, its product rules will be $v_x \cdot v_y = (\sum_{i=1}^{n} a_{ix} ei) \cdot (\sum_{j=1}^{n} a_{jy} ej) = \sum_{i=1}^{n} a_{ix} a_{iy} ei^2 = \sum_{j=1}^{n} \beta_{xyj} e_j$, where $\beta_{xyj} = \sum_{i=1}^{n} a_{ix} \alpha_{iij} a_{iy}$. We look for $\sum_{j=1}^{n} \beta_{xyj} e_j = \sum_{k=1}^{n} \gamma_{xyk} v_k = \sum_{k=1}^{n} \gamma_{xyk} \cdot \sum_{j=1}^{n} a_{jk} e_j = \sum_{j=1}^{n} (\sum_{k=1}^{n} a_{jk} \gamma_{xyk})\, e_j$ and thus $\sum_{k=1}^{n} a_{jk} \gamma_{xyk} = \sum_{k=1}^{n} a_{kx} \alpha_{kkj} a_{ky}$ $\forall j$. Hence,

$$\underline{\gamma}_{xy} = A^{-1} \cdot \alpha^t \cdot \underline{v}_x \odot \underline{v_y} \tag{10}$$

, where $\odot$ denotes the pointwise vector product and $\alpha = (\alpha_{kkj})_{kj}$.

This connects two quite different types of vector products. In addition, it remains coherent with the commutative nature of evolution algebras.

A large sample of random evolution algebras' product rules was built implementing these transformations of root cases. No major differences were measured for the runtimes with respect to the general case. Therefore, restriction to the case of evolution algebras does not simplify the computation process of the hierarchy.

A historical perspective of these algebras can be checked in [5] and more related information can be consulted in other sources ([6] and [7] for instance).

2.5 Space complexity

The space complexity of the algorithm is determined by the input and the two auxiliary sets, $MP\,(e_i)$ and $search\,(i)$. The latter ones mostly contribute to the space complexity within the first iteration of the while loop as these become diminished in length throughout the following iterations. At worst, each $MP\,(e_i)$, $search\,(i)$ will contribute $\mathcal{O}(n)$, $\mathcal{O}(n^2)$ respectively, yielding a total of $\mathcal{O}(n^3)$. This will always lead, considering the $\mathcal{O}(n^3)$ contribution from the input, to a cubic space complexity.

This was first tested in the previously commented computer, whose limited components didn't enable us to reach fairly high dimensions within a reasonable simulation time. Slow growth was observed accross the first 100 dimensions, making it necessary to export the

code to a more capable computer in order to obtain more meaningful data for the curve fit. It was eventually tested in a local version of Python 3.12.7 with a computer consisting of the following components: Intel i7-10700 (2.9-4.8 GHz), 32 GBs of DDR4 RAM (2667 MHz).

Memory usage was pinpointed several times within each dimension until reaching dimension 200, 150 for the average case and the worst one respectively. The several measurements were manually executed so that there was a time gap between each execution, enabling us to minimize fluctuations of the base memory when taking the average of the data. The resulting data was scatter-plotted and tested for consecutive polynomial models of regression both for the worst and random cases (Figure 5). A validation set was also generated taking intermediate as well as further dimensions.

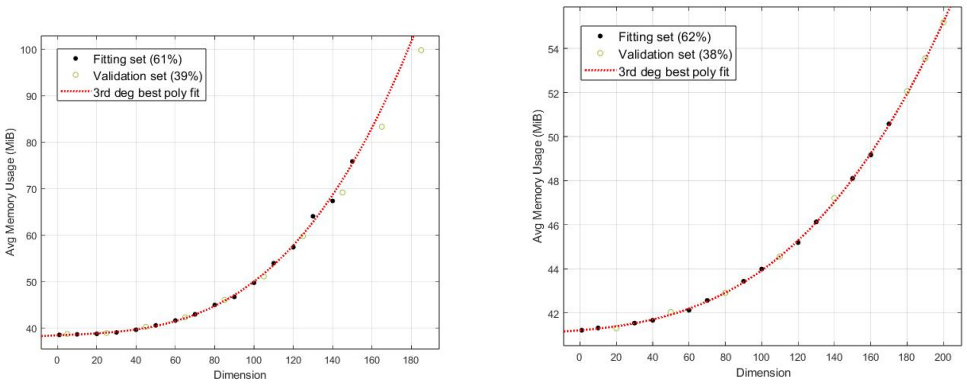

Figure 5: At the left the avg memory usage for the worst cases scatter-plotted against dimension. At the right for random product rules. A 3rd degree polynomial best fits the data.

It was found that a 3rd degree polynomial optimizes the fit and validation goodness for both cases. Moreover, performing a power fit provided confidence intervals exceeding 2 and approaching 3 for the exponents in both situations.

3 Some Examples of Algebras and its Hierarchies

As a convention product rules will be represented by its 3-order tensors using voxels. Depending on sparsity, it will be more convenient to either plot the non-zero entries or the opposite. It will be indicated by the color of the voxels: blue for boolean voxels and red for inverted boolean voxels.

On the other hand, hierarchies will be plotted as matrix colormaps where the rows and

columns represent the depth level and basis element respectively. Within each depth level the same color is assigned to matrix elements conforming a single subalgebra. This provides a faster and more clear understanding of the input and output structure.

The worst case example from [1] can be visualized for 10th dimension as in Figure 6. From the preimage algorithm developed in section *1.6* we can also get the previous hierarchy from a much more dense product rules structure (Figure 6). Both examples present pretty different sparsities (0.018 and 0.955 respectively). Nevertheless, the runtime from the first is slightly lower than the one from the second example (5.76 and 7.63 ms respectively).

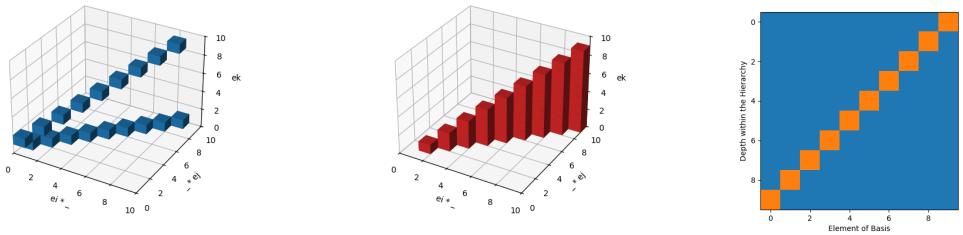

Figure 6: At the left the product rules of the $\mathfrak{g}_{10}$ represented with boolean voxels, where just non-null entries are plotted. At the right its hierarchy, $\bigoplus_{i=10}^{1} \langle e_i \rangle$, as a matrix colormap. Between these two, the product rules of the most dense preimage of the hierarchy $\bigoplus_{i=10}^{1} \langle e_i \rangle$ represented with inverted boolean voxels, i.e. just null entries were plotted.

The next example (Figure 7) can help us gain more intuition about the process described in section *1.6*. Th $\mathcal{CF}$ of this hierarchy is 182, much lower compared to the one for $\mathfrak{g}_{10}$: 385. We therefore obtain lower runtimes: 1.7, 5.5 ms for the least and most dense case respectively. Sparsity variation is narrower this time (0.026 and 0.933), yet runtime difference is much larger. It is due to the fact that the $\mathfrak{g}_n$ presented little room for getting more complex as their auxiliary sets were already the most possibly complex ones. However, in general we have much more margin to fill the auxiliary sets as we increase sparsity.

4 Conclusions and open problems

At present, note that in current mathematics, the computational treatment of any theoretical study carried out on any topic is very important, since it allows, on the one hand, to confirm the results obtained in the theoretical study and, on the other, to open new possibilities of research on questions that may arise regarding that study. Indeed, a computational treatment accompanies practically all the current theoretical studies carried out, therefore it can be considered to be another part of pure mathematics when not long ago this treatment was considered to correspond to applied mathematics.

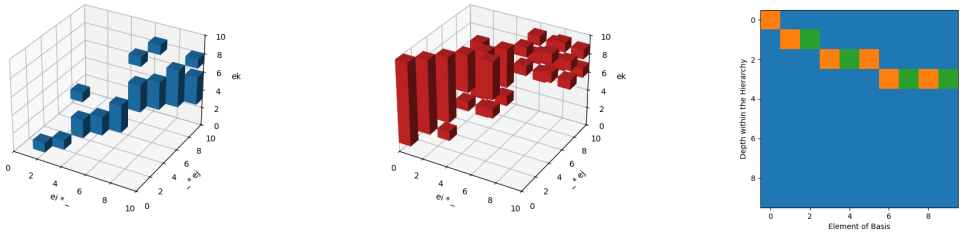

Figure 7: At the right a proposed hierarchy as a matrix colormap. At the left the boolean voxels representing the most sparse product rule matching that hierarchy. Between these two the inverted boolean voxels representing the most dense product rules that provoke that precise hierarchy.

Some years ago, one of the authors of this article, together with other collaborators, carried out research on the concept of hierarchy of algebras in general and evolution algebras in particular (see [1]). This is a concept which until that moment had been little studied, and that still continues to be barely treated by researchers. However, the computational treatment of the study carried out was quite scarce and was limited to revealing some small aspects related to complexity and computational time. In this article the authors address in much more depth and extension the computational treatment carried out by Cruz et al.

The most relevant results obtained by the authors have been the following

- Time complexity is $\mathcal{O}(n^5)$. This confirms the statement made in [1] that the algorithm's complexity is polynomial yet requires many operations in between. Nevertheless, for the range of dimensions treated in this study for the time section (< 80) we have reasonable runtimes, making it feasible to work with the algorithm in this domain.

- Space complexity is $\mathcal{O}(n^3)$. This result is optimistic, as the demand on memory is fixed by the nature of the entry and the first iteration. Therefore, memory overflows can be detected early in the execution of the algorithm and should only occur for dimension intervals much greater than these shown in this work (< 200).

- Intricate hierarchies become more rare as dimension is increased, so evaluating the algorithm over random algebras usually leads to lower execution times, but does typically lead to basic outputs.

- Intricacy of the output is highly correlated with execution time. Complexity of the input has a much more slight effect with the exception of low sparsities, as first additions of non-essential relations become much more relevant. When applied to Evolution Algebras, the algorithm does not present a significantly different demand on the equipment.

And as Open Problems, the authors suggest the following

- Carrying out a computational study on different types of algebras. For example: Lie, Leibniz and Zinbiel algebras. They were not done in this work due to extension requirements.
- Developing more meaningful and better statistically behaved models and metrics both on the input and the output in order to get more neat regression and grasp more information on the relevant dependences in the hierarchy process.
- Studying the possibility of further optimization of the algorithm to reduce complexity and finding out more optimal representations of input data to lower space complexity.
- Finding further generalization of the preimage algorithm from section *1.6* if possible.
- Finding useful application of these procedures to discrete dynamical systems as proposed by Tian.

REFERENCES

[1] Cruz, J.; Del Valle, A.; Núñez, J.; Pena, M. 2021. The concept of hierarchy of algebras and graphs, Journal of Applied Mathematics and Computing 67,233-255.

[2] Tian, J.P., 2008. Evolution Algebras and their Applications. Lecture Notes in Mathematics, Vol 1921. Springer-Verlag, Berlín

[3] Tian, J.P., Vojtechovsky, P., 2006. Mathematical concepts of evolution algebras in non-mendelian genetics, Quasigroups Related Systems 14:1, 111-122.

[4] Núñez, J., Silvero, M., Villar-Liñán, M.T., 2013. Mathematical tools for the future: graph theory and graphicable algebras, Applied Mathematics and Computation 219, 6113-6125.

[5] Ceballos, M., M Falcón, R. , Núñez, J. and F. Tenorio , A. A historical perspective of Tian's evolution algebras, Expositiones Mathematicae 40:3 (September 2022), 819-843.

[6] Boudi N., Cabrera Y., Siles M., 2022. Natural families in evolution algebras, Publications Matemàtiques 66(1), 159-181.

[7] Escobar, J.M., Núñez, J. and Pérez-Fernández, A new one-parameter invariant function for algebras, Mathematics in Computer Science, Math. Comput. Sci. 12 (2018), 143-150.

SYMCOMP 2025
Lisbon, 10-11 April 2025

ON CONNECTION COEFFICIENTS OF d-ORTHOGONAL POLYNOMIALS IN TERMS OF ORTHOGONAL POLYNOMIALS

Teresa A. Mesquita[1*] and Zélia da Rocha [2]

1: Escola Superior de Tecnologia e Gestão, Instituto Politécnico de Viana do Castelo, Rua Escola Industrial e Comercial de Nun' Álvares, 4900-347, Viana do Castelo, Portugal, & Centro de Matemática da Universidade do Porto (CMUP), Rua do Campo Alegre, n. 687, 4169-007 Porto, Portugal
e-mail: teresa.mesquita@fc.up.pt

2: Departamento de Matemática and CMUP
Faculdade de Ciências da Universidade do Porto
Rua do Campo Alegre, n. 687, 4169-007 Porto
e-mail: mrdioh@fc.up.pt

Keywords: d-orthogonal polynomials, d-symmetry, Appell sequences, connection coefficients, symbolic computations.

Abstract. *In this work, we focus on the problem of expressing sequences of d-orthogonal polynomials in terms of sequences of orthogonal polynomials. A general recurrence relation fulfilled by the corresponding connection coefficients is established and symbolically implemented. Results for several particular cases are given, allowing us to study the effect of either the Appell character or the symmetry and d-symmetry of the sequences in those connection coefficients.*

Acknowledgements

The second author was partially supported by CMUP, a member of LASI, which is financed by national funds through FCT - Fundação para a Ciência e a Tecnologia, I.P., under the projects with reference UIDB/00144/2020 and UIDP/00144/2020.

REFERENCES

[1] P. Appell, *Sur une classe de polynômes*, Ann. Sci. Ecole Normale 9 (2) (1880) 119-144.

[2] T. S. Chihara, *An Introduction to Orthogonal Polynomials*, Gordon and Breach, New York, 1978.

[3] K. Douak, *The relation of the d-orthogonal polynomials to the Appell polynomials*, J. Comput. Appl. Math. 70(2) (1996), 279-295.

[4] K. Douak and P. Maroni, *On d-orthogonal Tchebyshev polynomials, I* , Appl. Num. Math., 24 (1997), 23-53.

[5] P. Maroni, *Une théorie algébrique des polynômes orthogonaux. Application aux polynômes orthogonaux semi-classiques*, in : C. Brezinski et al., Eds., Orthogonal Polynomials and their Applications, in: IMACS Ann. Comput. Appl. Math. 9 (Baltzer, Basel, 1991), 95-130.

[6] P. Maroni, *Two-dimensional orthogonal polynomials, their associated sets and co-recursive sets*, Numer. Algorithms 3 (1992), 299-312.

[7] P. Maroni and Z. da Rocha, *Connection coefficients between orthogonal polynomials and the canonical sequence: an approach based on symbolic computation*, Numer Algor 47, (2008), 291–314.

[8] P. Maroni and Z. da Rocha, *Connection coefficients for orthogonal polynomials: symbolic computations, verifications and demonstrations in the Mathematica language*. Numer. Algorithms 63, (2013), 507–520.

[9] Z. da Rocha, *On connection coefficients of some perturbed of arbitrary order of the Chebyshev polynomials of second kind*, Journal of Difference Equations and Applications, 25:1, (2019) , 97-118.

[10] S. Wolfram, *Mathematica*, Virtual Book, www.wolfram.com.

SYMCOMP 2025
Lisbon, 10-11 April 2025

ON GENERATING FUNCTIONS OF SOME PERTURBATIONS OF A SECOND-ORDER SELF-ASSOCIATED ORTHOGONAL SEQUENCE: AN APPROACH BASED ON SYMBOLIC COMPUTATIONS

Zélia da Rocha

Departamento de Matemática
Faculdade de Ciências da Universidade do Porto
Centro de Matemática da Universidade do Porto
Rua do Campo Alegre n. 687, 4169 - 007 Porto, Portugal
e-mail: mrdioh@fc.up.pt, web: http://www.cmup.pt

Keywords: Self-associated sequences, second-degree sequences, semi-classical sequences, perturbed orthogonal polynomials, generating functions, symbolic computations, *Wolfram Mathematica*

Abstract. *Second-order self-associated orthogonal sequences are important cases of second-degree and semi-classical sequences [1, 3]. In this work, we take a fundamental case of those sequences as a starting point and we consider some perturbations of it by modifying its recurrence coefficients by translation and by dilation [2]. In this way, we generate new semi-classical orthogonal sequences. Some of their properties are studied in [7]. Those types of perturbations were also applied to the Chebyshev sequence of the second kind in [4, 5, 6]. In this work, we present a general method to deduce closed formulas for the generating functions of those perturbed sequences for any fixed order of perturbation. We extend a technique employed in [5] that was introduced in [4]. We give results produced by the symbolic implementation of that method in the Mathematica language in both types of perturbations.*

REFERENCES

[1] Maroni, P. Les polynômes orthogonaux auto-associés modulo deux. (French) [Self-associated orthogonal polynomials modulo 2] *Portugal. Math.* Vol. **42(2)** pp. 195–202, 1985.

[2] P. Maroni, Une théorie algébrique des polynômes orthogonaux. Application aux polynômes orthogonaux semi-classiques (in French) [An algebraic theory of orthogonal polynomials. Applications to semi-classical orthogonal polynomials]. In C. Brezin-

ski et al. Eds., Orthogonal Polynomials and their Applications (Erice, 1990), *IMACS Ann. Comput. Appl. Math.* Baltzer, Basel, pp. 95-130, 1991.

[3] Maroni, P.; Tounsi, M. Ihsen, The second-order self-associated orthogonal sequences. *J. Appl. Math.* Vol. **2**, pp. 137-167, 2004.

[4] P. Maroni, M. Mejri, Some perturbed sequences of order one of the Chebyshev polynomials of second kind, *Integral Transforms Spec. Funct.* Vol. **25(1)** pp. 44-60, 2014.

[5] Z. da Rocha, A general method for deriving some semi-classical properties of perturbed second-degree forms: the case of the Chebyshev form of the second kind, *J. Comput. Appl. Math.* Vol. **296** pp. 677-689, 2016.

[6] Z. da Rocha, On the second order differential equation satisfied by perturbed Chebyshev polynomials, *J. Math. Anal.* Vol. **7(1)** pp. 53-69, 2016.

[7] Z. da Rocha, On semi-classical properties of some perturbations of a second-order self-associated orthogonal sequence, in preparation.

Acknowledgements

The author was partially supported by CMUP, a member of LASI, which is financed by national funds through FCT – Fundação para a Ciência e a Tecnologia, I.P., under the projects with reference UIDB/00144/2020 and UIDP/00144/2020.

CFD ANALYSIS OF JET DEFLECTION IN THERMAL RECUPERATIVE INCINERATORS

Francisco Zdanowski[1]*, and Isabel Malico[1,2]

1: IDMEC, Escola de Ciências e Tecnologia, Universidade de Évora, Évora, Portugal

2: Complex Flow Systems Lab (CFS Lab), Institute of Earth Sciences, Évora, Portugal

e-mail: {zdanowski, imbm}@uevora.pt

Keywords: Computational Fluid Dynamics, RANS, Flow impingement, recirculation zones, ANSYS FLUENT

Abstract *Thermal Recuperative Incinerators (TRIs) are widely used in industrial applications for the destruction of volatile organic compounds (VOCs), offering both high combustion efficiency and energy recovery. In these systems, the flow dynamics of fuel and air jets, formed at the burner and air vanes, play a key role in ensuring effective combustion and TRI performance. Accurately predicting the behaviour and interaction of those jets is essential for optimizing combustion efficiency and burner stability. Salvador et al. [1] experimentally observed jet deflection towards one of the lateral walls in a laboratory-scale TRI, caused by the Coandă effect when jets are discharged near walls. However, their combustion simulations did not capture this phenomenon due to the assumption of axisymmetry, a common simplification for seemingly symmetric flows. To analyse in detail the interactions between multiple jets, as well as their interactions with the confining walls in the TRI described by Salvador et al. [1], this study presents 2D computational fluid dynamics (CFD) simulations without the axisymmetry assumption. This allows to capture the jet deflection and its effects. Insights from our previous work [2] provide a foundation for understanding the flow dynamics and heat transfer mechanisms explored in this study. The CFD model is validated against the experimental data from Salvador et al. [1]. The findings provide valuable insights into optimizing TRI design and improving the accuracy of non-axisymmetric flow predictions in TRIs.*

References

[1] S. Salvador, J.-M. Commandré, Y. Kara, “Thermal recuperative incineration of VOCs: CFD modelling and experimental validation”, *Applied Thermal Engineering*, vol. 26, no. 17–18, pp. 2355–2366, doi: 10.1016/j.applthermaleng.2006.02.018.

[2] Zdanowski, F., Malico, I., “CFD analysis of heated twin turbulent plane parallel jets confined by walls: Effects of geometry on flow dynamics and heat transfer”, submitted to *Applied Thermal Engineering*, 2025.

SYMCOMP 2025
Lisbon, 10-11 April 2025

A PILOT STUDY ON FINE-TUNING NAMED ENTITY RECOGNITION FOR CLINICAL TAG EXTRACTION USING PRETRAINED LANGUAGE MODELS: THE TUT-ALL EXPERIENCE

Adeyemi Victor Gbadamosi[1], Alberto Montero[2], Martin Deutsch[2], Nick Sander[2], Claire Cashmore[1], Eva Sousa[1,3*]

1: Centre of Excellence for Data Science, Artificial Intelligence and Modelling, University of Hull, Hull, United Kingdom

e-mail: adeyemi.gbadamosi@yahoo.com, {c.cashmore, e.sousa}@hull.ac.uk
web: https://www.hull.ac.uk/work-with-us/research/institutes/data-science-artificial-intelligence-and-modelling

2: Tut-All Software GmbH, Munich, Germany
e-mail: {alberto.montero, martin.deutsch, nick.sander}@tut-all.com web: http://tut-all.com/mytutall.html

3: Centre for Biomedicine, Hull York Medical School, University of Hull, Hull, United Kingdom
e-mail: eva.sousa@hyms.ac.uk*web: Centre for Biomedicine | Hull York Medical School

Keywords: Named entity extraction, BioElectra, BioLinkBert, PubMedBert, Pretrained language models (PLMs), Tut-All

Abstract *The standard procedure to extract data from medical records is still a laborious process where research analysts examine a wide range of information sources. Hence, there is a strong need to improve automatic data extraction techniques. This study performed fine-tuning of the pretrained language models (PLMs)—BioElectra, PubMedBert, BioLinkBert, and Clinical Longformer—for named entity recognition (NER) in clinical texts. The clinical texts were extracted from records using the Tut-All software and were comprised of abstracts and methods sections. For performance analysis the mean of the F1-score for each named entity tag was used across different hyperparameter optimizations. PubMedBert achieved the best performance results with a mean F1-score of 0.638 and an output range of 0.3. This performance was achieved after training with a learning rate and a weight decay of* 5×10^{-5} *and* 3×10^{-3} *respectively, employing default HuggingFace hyperparameters. Notably, PubMedBert exhibited superior performance on minority entity types, addressing a key challenge in real-world data applications. The optimized model not only expedites information retrieval, but also enhances the overall quality of extracted data, marking a valuable contribution to the data extraction data from medical records.*

DOI:10.5281/zenodo.15160962

1. INTRODUCTION

Over the years, the intersection of healthcare and technology has seen significant breakthroughs, and one of the driving forces behind this change has been the quick development of Natural Language Processing with the use of Pretrained Language Models (PLMs) for Named Entity Recognition (NER) [1].

In the biomedical domain, a fundamental task of Natural Language Processing is the recognition of named entities, such as genes, diseases, species, chemicals, medical codes or drug names [2]. In an era where the volume of medical literature and patient data is growing exponentially the ability of PLMs to extract important entities in an automated way from complex medical texts is essential [3].

The importance of the information in healthcare is in part supported by the growing paradigm of evidence–based medicine, which emerged with the XXI century [4] and is being transformed by the advent of Artificial Intelligence techniques [5]. This new era of evidence–based medicine is not only essential for advancing medical research and exploring the effectiveness of new drugs or side–effects, but mostly to manage the growing amount of data generated [6]. Named Entity Recognition (NER), and PLMs play a crucial role in this process [7].

To create databases used for this supported decision, in clinic or in research, medical researchers synthesize knowledge by combining information from multiple articles information to identify trends, patterns, and inconsistencies [8], [9]. This process is many times done manually but can be greatly streamlined and automatized by applying NER algorithms in the identification and categorization of specific entities within clinical publications [10].

Randomized controlled trials have been for some time the cornerstone of evidence practise medicine, as reliable evidence information for clinical decision [11], [12], [13]. Randomized controlled trials measure the effectiveness of a new intervention or reducing the bias and providing a rigorous tool to examine cause-effect relationships between an intervention and outcomes, due to the randomization of intervention and subjects treated [14]. The possibility to extract and compile the information of multiple registry repositories of randomized controlled trials is hence very attractive as database information used for support to healthcare decisions, development of pharmaceuticals or the creation of policies [15], [16]. By accurately identifying and categorizing key information, NER algorithms can help on revolutionizing clinical trials and ultimately on accelerating health research breakthroughs [17], [18], [19].

This modern era of PLMs began with the introduction of word embedding models, such as Word2Vec [20] and GloVe [21]. These models laid the foundation for algorithms that encode the relationships and contextual meanings of words in a text [20], [21].

Over the years, the field has witnessed significant progress, from the transformer architecture [22] to techniques like Embedding from Language Models (ELMo) [23] and Universal Language Model Fine-Tuning (ULMFiT) [24]. Transformer models have particularly revolutionized natural language processing by demonstrating improved ability to manage dependencies between words in a sentence [25] leading to breakthroughs in NER that align well with Evidence-Based Medicine, with some models already being trained for use in NER of medical entities [25], [26].

Some of these models achieve good results with clinical NER, namely BioElectra [27], PubMedBert [28], [29], [30] , BioLinkBert [31], and Clinical Longformer [32], [33]. These models were then chosen as they demonstrated superior metrics compared to other medically fine-tuned pretrained large language models. All of them have been fine-tuned on medical literature to have adaptations specifically tailored for medical applications [28], [29], [30], [32], [33], [34]. It is important to note that Clinical Longformer has the unique advantage of not being constrained by the 512-token limitation observed in the Bert models, which enhances the model's capacity to capture and interpret extensive medical text, expanding the scope and depth of the possible analysis [33].

The aim of this research was to enhance the accuracy and efficiency of entity extraction, recurring to PLMs in the clinical text databases property of the company Tut-All Software GmbH, located in Karlsruhe, Germany. Tut-All Software GmbH does annotation & data extraction of randomized clinical trials, as well as training of people within this field. By fine-tuning these models on a custom data set using Tut-All databases the research aimed to improve the extraction of predefined medical entities, aiding in the automation of evidence-based medicine. Ultimately, this research aimed to contribute to more efficient data retrieval and better-quality controlled in medical research, helping researchers and practitioners make informed decisions.

2. METHODS

2.1 Data sets

In this study 4 data sets were created and used to train the PLMs in the clinical entities' recognition tasks.

For the creation of the training data sets the randomized clinical trials databases property of Tut-All Software GmbH has been used. This database constitutes 1549 randomized controlled trials manually annotated by research analysts, with the help of a Scientific Workflow Tool (SWT) designed by Tut-All Software GmbH as described in figure 1.

The SWT is a tool where data from randomized controlled trials are selected, assessed and extracted manually and automatically.

These variables are values attributed to the entities, which need to be recognised in each publication. A basic workflow of this process can be also seen in figure 1.

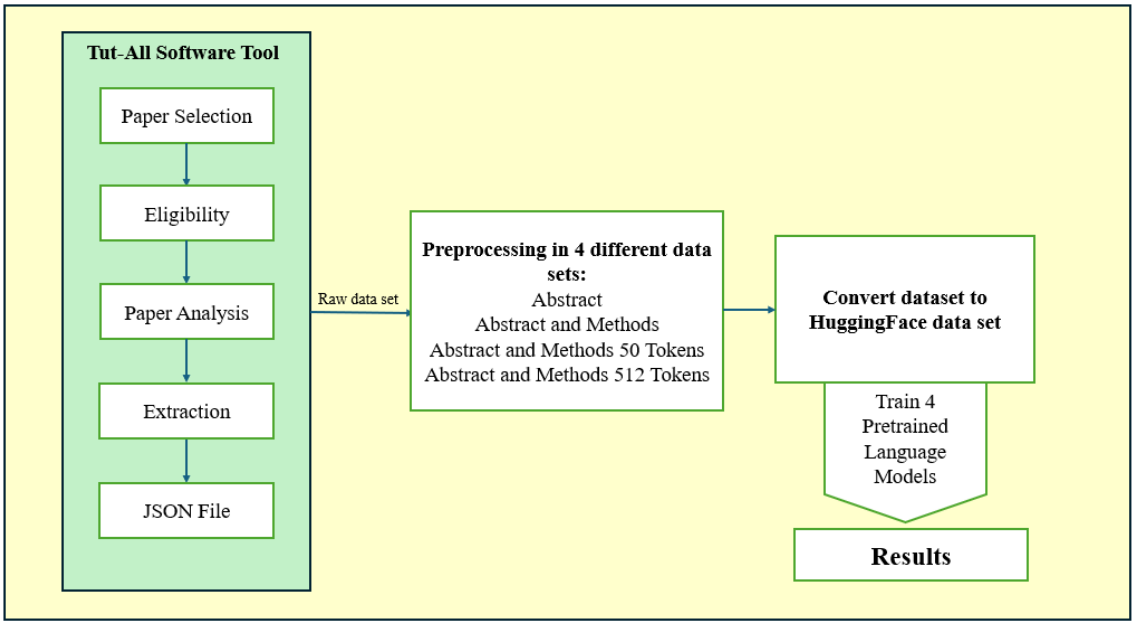

Figure 1. Workflow of the process, from the paper selection and step done with the SWT to the results using the PLMs.

The initial annotation process of the 1549 clinical records originated 2816 tags. These tags represent various entity types within the SWT, such as:

CONDITION: Category of words that describe clinical condition (e.g. COPD, pneumonia, …).
DESIGN: Category of words that describe the design of the study (e.g. Randomized controlled trial double blinded, …).
SUBJECTS: Category of words that describe the subjects of the study (e.g. adults non-smokers, …).
GROUPS: Category of words that describe the samples of randomization (e.g. group A (medication A), group B (medication B), …).

Subsequently, the abstracts and methods of each clinical record were collated with their corresponding tags and organized into a JSON file. Further refining the data set involved identifying and tagging entities within the abstracts and methods based on the context, resulting in the creation of two initial data sets. Recognizing the limitations of BERT-based models, which can only handle 512 tokens, the abstract data set underwent additional segmentation, leading to the generation of two additional data sets with varying total text lengths. The final four data sets created contained:

Abstract only – abstract of the record and the entity in the abstract.
Abstract and methods – abstract from the record merged with the methods increasing the total

length of the text.
Abstract and methods: 50 tokens segments – abstract and method were split into chunks of 50 (words and punctuation) by counting the tokens.
Abstract and methods: 512 tokens segments – abstract and method were split into chunks of 512 tokens (words and punctuation) by counting the tokens.
These summarized characteristics of the resultant data sets used are described in table 1.

	Abstract only	**Abstract with method**	**Abstract and methods (50 tokens)**	**Abstract and methods (512 tokens)**
Total data sets	1549	1549	50046	5563
Training samples	1239	1239	40036	4450
Validation samples	155	155	5005	557
Testing samples	155	155	5005	556

Table *1*. The base description of the data set after processing the raw data from the SWT in preparation for training and fine-tuning. The abstract with methods data has 5 times more texts and 3 times more unique texts in the data.

2.2. Labels

To create the labelled data set for the training raw JSON files have been used, created from the information extracted of randomized controlled trials with the SWT. These raw JSON files contained 1549 dictionaries with 5 identification keys, described below:

PMID: PubMed reference number for records indexed in PubMed
Title: Title of the record
TEXT: Abstract or method depending on what was extracted by the SWT
CONTEXT: Context of the annotated text containing the surrounding words for a biunique mapping
ANNOTATIONS: Entities and their corresponding entity type.

From these identification keys, the context is the reference for the others to be applied after, as it ensured that only the right entity in the text was matched. In figure 2 it is possible to see this process exemplified.

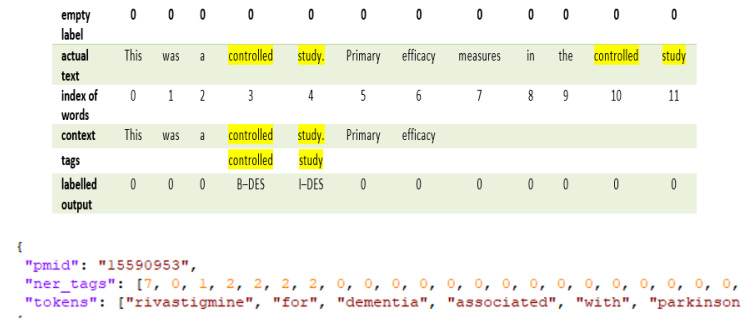

empty label	0	0	0	0	0	0	0	0	0	0	0	0
actual text	This	was	a	controlled	study.	Primary	efficacy	measures	in	the	controlled	study
index of words	0	1	2	3	4	5	6	7	8	9	10	11
context	This	was	a	controlled	study.	Primary	efficacy					
tags				controlled	study							
labelled output	0	0	0	B–DES	I–DES	0	0	0	0	0	0	0


```
{
 "pmid": "15590953",
 "ner_tags": [7, 0, 1, 2, 2, 2, 2, 0, 0, 0, 0, 0, 0, 0, 0, 0, 0, 0, 0, 0, 0, 0,
 "tokens": ["rivastigmine", "for", "dementia", "associated", "with", "parkinson
```


Figure 2. Overview of the labelling methodology, starting from the empty labels to the labelled output with the correct tags and the final tag representations to be used in training.

As can be seen in figure 2, an empty label with equal length to the full–length text was created first. After that, the index of the context in the text was determined by matching the context in the full–length text. This served as the bounding range for the entity type, any other reoccurrence of the entity outside this range was ignored. Wherever no context was found or provided, every occurrence of the entities in the text was matched.
Finally, the entity index was matched in the context with the empty labels. The entity types with very little representations were removed but allowed for some imbalance to mimic real world cases as seen in table 2, by comparing the different numbers of occurrences of each entity. The entity type B–GROUP D, was the one least represented with only 167 entries.
The IOB format was also used, popularized by the CoNLL NER task [35] and initially proposed by Ramshaw & Marcus in 1995 [36]. In this format, "I" designates words inside an entity, "O" denotes non-entity words such as the punctuation, and "B" marks the beginning word of an entity [36]. This classification is used on table 2.

Entities	Abstract only	Abstract and methods	Abstract and methods (50 tokens)	Abstract and methods (512 tokens)
B–SUBJECTS	1853	3661	3661	3661
B–CONDITION	1384	1949	1949	1949
B–DESIGN	826	1393	1393	1393
B–GROUP A	3300	5498	5498	5498
B–GROUP B	2531	4730	4730	4730
B–GROUP C	562	1330	1330	1330
B–GROUP D	167	395	395	395
I–CONDITION	3689	5648	5648	5648
I–DESIGN	3176	5423	5423	5423

I–GROUP A	2098	3030	3030	3030
I–GROUP B	1553	2610	2610	2610
I–GROUP C	548	1303	1303	1303
I–GROUP D	230	348	348	348
I–SUBJECTS	1418	3681	3681	3681
O	538946	2416829	2416829	2416829

Table 2. Distribution of entity types in the 4 data sets.

2.3. Name Entity Recognition Training

For the training and finetuning process with V100 and T4 GPU, Google Colab has been used. The 4 data sets were split into training validation and test on the proportions of 80%, 10%, 10% respectively.
The performance of each model was assessed by comparing the mean F1-score. The ability of the model to learn evenly across all tags was looked at using the F1-score range (the difference between the maximum and minimum F1-score gotten for each tag).
BioElectra model was pretested and was posteriorly trained with the data sets and the learning rate which gave the best convergence F1-score, being these parameters presented in table 3.
Beside BioElectra were applied PubMedBert, BioLinkBert, and Clinical Longformer, which were trained using the best performing hyperparameters, being this information also presented in table 3.
Clinical Longformer is able to accept longer sequences of text, when compared with the other pre trained language models. For this reason, it was trained only with long texts, and hence applied to the data set composed by abstract and methods, as this data set is the only one where individual entry are consistently longer than 512 tokens. It was trained on a max token length of 4096, while the three other models used 512 tokens of maximum length and were applied to the other 3 data sets as well.

2.4. Hyperparameter Tuning

All the hyperparameter combinations used are presented in table 3, for the overall choice of hyperparameters the HuggingFace trainer arguments have been used. The epochs, learning rates and weight decay were varied. To evaluate the model in training and testing the F1-score for each entity type in the model has been computed. The model overall performance is determined by calculating the mean F1-score obtained.
BioElectra and PubMedBert have 108903183 training parameters, while BioLinkBert and Clinical Longformer have 107653647 and 148080399 respectively, these numbers were calculated recurring to the HuggingFace function.
To all training the adamw_torch optimizer has been applied. To preprocess the data sets into tokens the Fast tokenizer was applied. For all the experiments 15 tags have been used in each,

while punctuation marks of the data sets have been included as well.

Model	Applied Learning Rates	Weight Decay	Data set
BioElectra	5×10^{-5}, 1×10^{-5}, 1×10^{-6}, 7.5×10^{-4}, 5×10^{-4}	3×10^{-3}	Abstract
	5×10^{-5}, 1×10^{-5}, 1×10^{-6}, 7.5×10^{-5}, 2.5×10^{-5}	3×10^{-3}	Abstract and methods
	5×10^{-5}, 1×10^{-5}, 1×10^{-6}, 5×10^{-6}, 1×10^{-7}, 1.25×10^{-6}, 7.5×10^{-7}, 2.5×10^{-6}	3×10^{-3}	Abstract and methods: 50 tokens
	5×10^{-5}, 1×10^{-5}, 1×10^{-6}, 1×10^{-4}, 2.5×10^{-5}, 5×10^{-6}, 5×10^{-4}, 3×10^{-5}	3×10^{-3}	Abstract and methods: 512 tokens
	5×10^{-4}	4×10^{-3}	Abstract and methods: 512 tokens
BioLinkBert	7.5×10^{-5}, 5×10^{-4}, 5×10^{-5}	3×10^{-3}	Abstract
	7.5×10^{-5}, 2.5×10^{-5}, 1×10^{-5}, 5×10^{-5}	3×10^{-3}	Abstract and methods
	5×10^{-6}, 1×10^{-6}, 5×10^{-5}	3×10^{-3}	Abstract and methods: 50 tokens
	2.5×10^{-5}, 3×10^{-5}, 5×10^{-5}	3×10^{-3}	Abstract and methods: 512 tokens
PubMedBert	7.5×10^{-5}, 5×10^{-4}, 5×10^{-5}	3×10^{-3}	Abstract
	7.5×10^{-5}, 2.5×10^{-5}, 1×10^{-5}, 5×10^{-5}	3×10^{-3}	Abstract and methods
	5×10^{-6}, 1×10^{-6}, 5×10^{-5}	3×10^{-3}	Abstract and methods: 50 tokens
	2.5×10^{-5}, 3×10^{-5}, 5×10^{-5}	3×10^{-3}	Abstract and methods: 512 tokens
Clinical Longformer	8.5×10^{-5}, 2.5×10^{-5}, 5×10^{-5}, 5×10^{-4}, 1.25×10^{-5}, 1×10^{-5}	3×10^{-3}	Abstract and methods
	5×10^{-5}	1×10^{-3}	Abstract and methods
	5×10^{-5}	5×10^{-3}	Abstract and methods
	5×10^{-5}	5×10^{-4}	Abstract and methods

Table 3. Hyperparameters applied to the training of all 4 PLMs models.

3. RESULTS

The results of the mean F1-scores obtained are presented in table 4. Changing the leaning rates influenced the performance of the PLMs, as different models achieved optimal performance with different learning rates. While BioElectra demonstrated optimal performance with the

learning rate varying between 5×10^{-6} and 1×10^{-4}, for PubMedBert and BioLinkBert, the most effective learning rate was 5×10^{-5}, showcasing their robust performance between the range of 5×10^{-6} to 5×10^{-4}.

Clinical Longformer also exhibited its best performance at a learning rate of 5×10^{-5}; however, its mean F1-score fell below that of PubMedBert, BioLinkBert, and BioElectra.

Among the data sets, the abstract and methods: 50 tokens, consistently produced great results across all models. The removal of punctuation marks from certain data sets did not significantly impact model output, for this reason, all models were evaluated with punctuation included.

PubMedBert achieved better results than the other models, with a mean F1-score of 0.64, closely followed by BioLinkBert at 0.6. Although the differences in results were marginal, the decisive metric was the range, representing the disparity between the maximum and minimum F1-scores for entity types. This range serves as a statistical measure of a model's ability to learn across both majority and minority entity types. PubMedBert achieved a range of 0.3, while BioLinkBert's range was markedly higher at 0.76.

PubMedBert achieved better results when applied to the minority tags, as shown in table 4, where PubMedBert successfully predicted entity type "Group D," while BioLinkBert produced blank predictions for the same category. This underlines PubMedBert's effectiveness in capturing nuances within the data, highlighting its potential for improved performance in handling minority entity types. These values of F1-scores, for the different entities, are in table 4.

	Pretrained Language Models			
Entities	**BioElectra**	**BioLinkBert**	**PubMedBert**	**Clinical Longformer**
B–CONDITION	0.55	0.65	0.59	0.35
I–CONDITION	0.64	0.63	0.59	0.44
B–DESIGN	0.62	0.65	0.63	0.53
I–DESIGN	0.73	0.76	0.74	0.59
B–SUBJECTS	0.59	0.67	0.55	0.33
I–SUBJECTS	0.53	0.60	0.50	0.38
B–GROUP A	0.72	0.69	0.75	0.46
I–GROUP A	0.60	0.55	0.57	0.48
B–GROUP B	0.67	0.56	0.69	0.36
I–GROUP B	0.48	0.53	0.50	0.23
B–GROUP C	0.64	0.61	0.72	0.00
I–GROUP C	0.53	0.36	0.60	0.00
B–GROUP D	0.71	0.00	0.81	0.00
I–GROUP D	0.38	0.00	0.71	0.00
Mean F1-score	0.60	0.60	0.64	0.35

Table 4. Best performing F1-score metrics and mean F1-score for all pretrained language models for each entity.

On figures 3, 4, 5 and 6 it is possible to see the mean F1-score for each PLM on each data set, where it was applied. BioElectra, BioLinkBert and PubMedBert have comparable results. PubMedBert and BioElectra are preferred over BioLinkBert as they learned and gave F1-scores for all entities, while BioLinkBert learned only the majority of entities and failed in the minority entities, which can be seen as an overall worse performance in these figures and is marked as null or lower values on table 4 results.

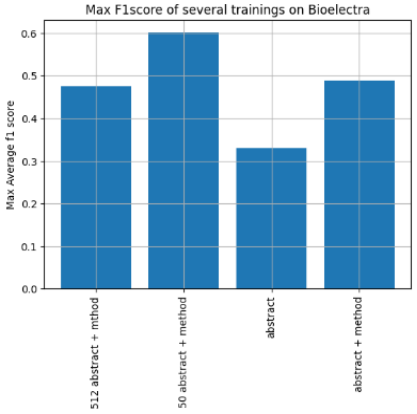

Figure 3. Mean F1-score for BioElectra performance with different data sets.

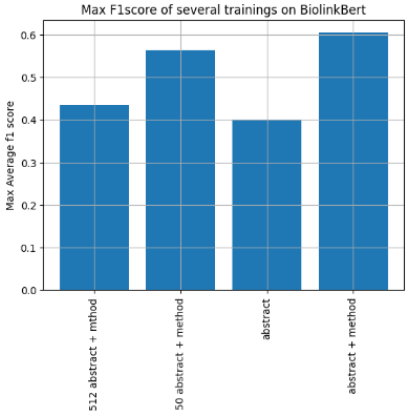

Figure 4. Mean F1-score for BioLinkBert performance with different data sets.

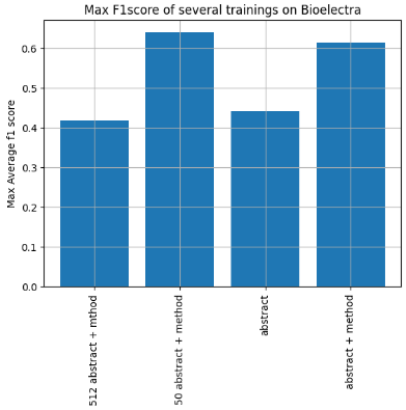

Figure 5. Mean F1-score for PubMedBert performance with different data sets.

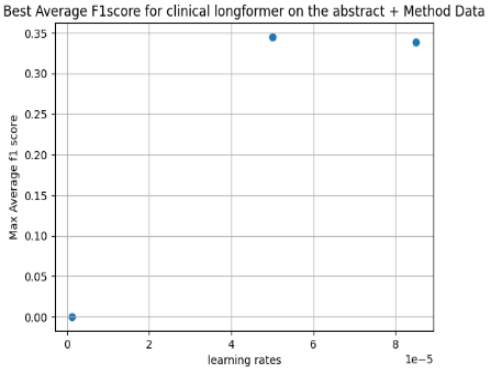

Figure 6. F1-score of the Clinical Longformer, which was trained on the abstract and methods data set.

4. DISCUSSION

This study examined two 4 different Pretrained Language models for clinical entity recognition: pretrained language models (PLMs)—BioElectra, PubMedBert, BioLinkBert, and Clinical Longformer—for named entity recognition (NER) in clinical texts. The clinical tests were extracted in different types of text lengths and clinical entities. From these 4 models tested PubMedBert achieved superior results being able to classify entities in minority data, in which the other models struggled. In real-world scenarios, data imbalances are common, PubMedBert demonstrated its ability to perform well (mean F1-score between 0.60 and 0.81) even when the other models Clinical Longformer and BioLinkBert obtained a F1-score of zero. This disparity is crucial, as it highlights PubMedBert's superior capacity to learn minority tags. The model's performance on skewed data, specifically its ability to produce results for minority tags was demonstrated even without utilizing data balancing techniques.

A surprising outcome was the Clinical Longformer's approximately 50 percent lower mean F1-score compared to other models, despite its capability to process longer text sequences. A different approach was chosen for this model when compared with the other three used models, and this limits the extrapolation of the results. From the literature, it is suggested that the increased length of text would lead to better learning of the models [6], our results contradicted this assumption, and more work needs to be done in uncovering the reasons for these unexpected results. This is not the only surprising result, the data set of abstract and methods with segments of just 50 words, outperformed data sets with longer texts and closely matched the abstract with methods data set, on all models training.

The F1-scores obtained in this work are lower when compared with some other literature studies, but this can be explained by the nature of the data sets as the included data highly influence the results obtained. These results show the importance of the data set format, quality, and labelling processes. Most of the Named Entity Recognition works rely on publicly available data sets that have been refined and labelled to suit the task, resulting in high F1-scores [37], [38]. However, for applications with complex, and interrelated entity types, fitted data sets become necessary. The data set of Tut-All uses intermediary steps of validation, is more segmented than the publicly available, as it has extra preprocessing steps done by internal peer review, refining the data sets publicly available can be more realistic when compared with the public data sets. Hence the results achieved in this research, are most probably more useful for this type of analysis, but also more moderated in results, highlighting the need for further developments to be built upon this work.

Future works can focus on better fine tuning and standardization to achieve better results. The possibility of improving results by segmenting the data set with a focus on using complete sentences for better learning is also considered. To address overfitting and enhance model generalization, increasing the number of data sets is essential.

Finetuning the Clinical Longformer could benefit from warm-up steps [39], potentially improving performance and enabling evaluation of clinical text with extended token lengths. Varying epochs during training helped alleviate overfitting, but this remained a persistent issue.

The adjustment of learning rates and weight decay was crucial for achieving optimal convergence.
Gu et. al has shown that the tagging methodology and dummification could have different results in PubMedBert, future works could explore creating other fitted data sets with other methods [40]. In this research, the data set was chunked by linearly counting a set number of tokens, this can be improved by chunking with full stops or other sentence terminating punctuations. This will ensure the chunks of text from which the models are learning from are complete sentences or phrases. Also, augmentation techniques could be used to improve the data set or more records could be explored using the SWT to increase the data set for future works.
The use of the entities could also be further explored, as the current methods are to label it once, but ignore it in every other occurrence. However, this could potentially confuse the model if they are used in different contexts.
For real clinical application, the trustworthiness of the results is an important factor that could determine if fine-tuned PLMs can be used in the field, without human supervision in the subsequent steps.

5. CONCLUSIONS

Biomedical PLMs can be very useful for automated analysis of clinical entities in scientific texts.
- To fully utilize the biomedical pretrained language models in clinical applications, the performance through refining the data set is necessary.
- Future annotations with more data have the potential to improve the model.

REFERENCES

[1] R. Collobert, J. Weston, J. Com, M. Karlen, K. Kavukcuoglu, and P. Kuksa, “Natural Language Processing (Almost) from Scratch,” 2011.
[2] S. Raza, D. J. Reji, F. Shajan, and S. R. Bashir, “Large-scale application of named entity recognition to biomedicine and epidemiology,” *PLOS Digital Health*, vol. 1, no. 12, Dec. 2022, doi: 10.1371/journal.pdig.0000152.
[3] Y. J. Park, G. J. Yang, C. B. Sohn, and S. J. Park, “GPDminer: a tool for extracting named entities and analyzing relations in biological literature,” *BMC Bioinformatics*, vol. 25, no. 1, Dec. 2024, doi: 10.1186/s12859-024-05710-z.
[4] D. L. Sackett, W. M. C. Rosenberg, J. A. M. Gray, R. B. Haynes, and W. S. Richardson, “Evidence based medicine: what it is and what it isn’t,” *BMJ*, vol. 312, no. 7023, pp. 71–72, Jan. 1996, doi: 10.1136/bmj.312.7023.71.
[5] X. Liu *et al.*, “Reporting guidelines for clinical trial reports for interventions involving artificial intelligence: the CONSORT-AI extension,” *Nat Med*, vol. 26, no. 9, pp. 1364–1374, Sep. 2020, doi: 10.1038/s41591-020-1034-x.

[6] L. Ismail, H. Materwala, A. P. Karduck, and A. Adem, "Requirements of Health Data Management Systems for Biomedical Care and Research: Scoping Review," *J Med Internet Res*, vol. 22, no. 7, p. e17508, Jul. 2020, doi: 10.2196/17508.

[7] S. Liu, A. Wang, X. Xiu, M. Zhong, and S. Wu, "Evaluating Medical Entity Recognition in Health Care: Entity Model Quantitative Study," *JMIR Med Inform*, vol. 12, p. e59782, Oct. 2024, doi: 10.2196/59782.

[8] C. Chakraborty, M. Bhattacharya, S. Pal, and S. S. Lee, "From machine learning to deep learning: Advances of the recent data-driven paradigm shift in medicine and healthcare," Jan. 01, 2024, *Elsevier B.V.* doi: 10.1016/j.crbiot.2023.100164.

[9] L. Hong, M. Luo, R. Wang, P. Lu, W. Lu, and L. Lu, "Big Data in Health Care: Applications and Challenges," *Data Inf Manag*, vol. 2, no. 3, pp. 175–197, Dec. 2018, doi: 10.2478/dim-2018-0014.

[10] J. B. D. . Joshi, *Proceedings, 2016 IEEE International Conference on Big Data : Dec 05-Dec 08, 2015, Washington D.C., USA*. IEEE, 2016.

[11] P. Fernainy, A. A. Cohen, E. Murray, E. Losina, F. Lamontagne, and N. Sourial, "Rethinking the pros and cons of randomized controlled trials and observational studies in the era of big data and advanced methods: a panel discussion," *BMC Proc*, vol. 18, Jan. 2024, doi: 10.1186/s12919-023-00285-8.

[12] M. G. Titler, "Section II: Evidence-Based Practice Chapter 7. The Evidence for Evidence-Based Practice Implementation."

[13] P. B. Burns, R. J. Rohrich, and K. C. Chung, "The levels of evidence and their role in evidence-based medicine," *Plast Reconstr Surg*, vol. 128, no. 1, pp. 305–310, Jul. 2011, doi: 10.1097/PRS.0b013e318219c171.

[14] E. Hariton and J. J. Locascio, "Randomised controlled trials – the gold standard for effectiveness research: Study design: randomised controlled trials," Dec. 01, 2018, *Blackwell Publishing Ltd*. doi: 10.1111/1471-0528.15199.

[15] F. Liu and P. Demosthenes, "Real-world data: a brief review of the methods, applications, challenges and opportunities," Dec. 01, 2022, *BioMed Central Ltd*. doi: 10.1186/s12874-022-01768-6.

[16] K. Yoshida *et al.*, "Use of Data from Multiple Registries in Studying Biologic Discontinuation: Challenges and Opportunities HHS Public Access," 2013.

[17] J. Li *et al.*, "A comparative study of pre-trained language models for named entity recognition in clinical trial eligibility criteria from multiple corpora," *BMC Med Inform Decis Mak*, vol. 22, Sep. 2022, doi: 10.1186/s12911-022-01967-7.

[18] H. Chopra *et al.*, "Revolutionizing clinical trials: the role of AI in accelerating medical breakthroughs," *Int J Surg*, vol. 109, no. 12, pp. 4211–4220, Dec. 2023, doi: 10.1097/JS9.0000000000000705.

[19] H. Chopra *et al.*, "Revolutionizing clinical trials: the role of AI in accelerating medical breakthroughs," *Int J Surg*, vol. 109, no. 12, pp. 4211–4220, Dec. 2023, doi: 10.1097/JS9.0000000000000705.

[20] D. S. Asudani, N. K. Nagwani, and P. Singh, "Impact of word embedding models on text analytics in deep learning environment: a review," *Artif Intell Rev*, vol. 56, no. 9, pp. 10345–10425, Sep. 2023, doi: 10.1007/s10462-023-10419-1.

[21] J. Pennington, R. Socher, and C. Manning, “Glove: Global Vectors for Word Representation,” in *Proceedings of the 2014 Conference on Empirical Methods in Natural Language Processing (EMNLP)*, Stroudsburg, PA, USA: Association for Computational Linguistics, 2014, pp. 1532–1543. doi: 10.3115/v1/D14-1162.
[22] A. Vaswani *et al.*, “Attention Is All You Need.”
[23] M. E. Peters *et al.*, “Deep contextualized word representations,” Feb. 2018, [Online]. Available: http://arxiv.org/abs/1802.05365
[24] J. Howard and S. Ruder, “Universal Language Model Fine-tuning for Text Classification,” Jan. 2018, [Online]. Available: http://arxiv.org/abs/1801.06146
[25] Supriyono, A. P. Wibawa, Suyono, and F. Kurniawan, “Advancements in natural language processing: Implications, challenges, and future directions,” *Telematics and Informatics Reports*, vol. 16, Dec. 2024, doi: 10.1016/j.teler.2024.100173.
[26] M. Košprdić, N. Prodanović, A. Ljajić, B. Bašaragin, and N. Milošević, “From Zero to Hero: Harnessing Transformers for Biomedical Named Entity Recognition in Zero- and Few-shot Contexts,” May 2023, doi: 10.1016/j.artmed.2024.102970.
[27] K. R. Kanakarajan, B. Kundumani, and M. Sankarasubbu, “BioELECTRA:Pretrained Biomedical text Encoder using Discriminators,” 2021. [Online]. Available: https://www.ncbi.nlm.nih.gov/pmc/
[28] R. Tinn *et al.*, “Fine-tuning large neural language models for biomedical natural language processing,” *Patterns*, vol. 4, no. 4, Apr. 2023, doi: 10.1016/j.patter.2023.100729.
[29] Y. Gu *et al.*, “Domain-Specific Language Model Pretraining for Biomedical Natural Language Processing,” *ACM Trans Comput Healthc*, vol. 3, no. 1, Jan. 2022, doi: 10.1145/3458754.
[30] L. Fang, Q. Chen, C.-H. Wei, Z. Lu, and K. Wang, “Bioformer: an efficient transformer language model for biomedical text mining.” [Online]. Available: https://huggingface.co/emilyalsentzer/Bio_ClinicalBERT
[31] M. Yasunaga, J. Leskovec, and P. Liang, “LinkBERT: Pretraining Language Models with Document Links,” Mar. 2022, [Online]. Available: http://arxiv.org/abs/2203.15827
[32] Y. Li, R. M. Wehbe, F. S. Ahmad, H. Wang, and Y. Luo, “A comparative study of pretrained language models for long clinical text,” *J Am Med Inform Assoc*, vol. 30, no. 2, pp. 340–347, Jan. 2023, doi: 10.1093/jamia/ocac225.
[33] Y. Li, R. M. Wehbe, F. S. Ahmad, H. Wang, and Y. Luo, “Clinical-Longformer and Clinical-BigBird: Transformers for long clinical sequences,” Jan. 2022, [Online]. Available: http://arxiv.org/abs/2201.11838
[34] K. R. Kanakarajan, B. Kundumani, and M. Sankarasubbu, “BioELECTRA:Pretrained Biomedical text Encoder using Discriminators,” 2021. [Online]. Available: https://www.ncbi.nlm.nih.gov/pmc/
[35] E. F. Tjong, K. Sang, and F. De Meulder, “Introduction to the CoNLL-2003 Shared Task: Language-Independent Named Entity Recognition.” [Online]. Available: http://lcg-www.uia.ac.be/conll2003/ner/
[36] L. A. Ramshaw and M. P. Marcus, “Text Chunking using Transformation-Based Learning.”
[37] K. Xue, Y. Zhou, Z. Ma, T. Ruan, H. Zhang, and P. He, “Fine-tuning BERT for Joint Entity and Relation Extraction in Chinese Medical Text,” Aug. 2019, [Online]. Available:

http://arxiv.org/abs/1908.07721
[38] A. Jolly, V. Pandey, I. Singh, and N. Sharma, "Exploring Biomedical Named Entity Recognition via SciSpaCy and BioBERT Models," *Open Biomed Eng J*, vol. 18, no. 1, Jun. 2024, doi: 10.2174/0118741207289680240510045617.
[39] I. Beltagy, M. E. Peters, and A. Cohan, "Longformer: The Long-Document Transformer," Apr. 2020, [Online]. Available: http://arxiv.org/abs/2004.05150
[40] Y. Gu *et al.*, "Domain-Specific Language Model Pretraining for Biomedical Natural Language Processing," *ACM Trans Comput Healthc*, vol. 3, no. 1, Jan. 2022, doi: 10.1145/3458754.

SYMCOMP 2025
Lisbon, 10-11 April 2025

MOMENT INTEGRATION SCHEME FOR HIGHER-ORDER VIRTUAL ELEMENTS IN INELASTIC PROBLEMS

Yongbin Choi[1*], Tobias Bode[1], Philipp Junker[1]
1: Leibniz Universität Hannover
Institut für Kontinuumsmechanik
An der Universität 1, Gebäude 8142
30823 Garbsen
e-mail: {choi,bode,junker }@university.ikm.uni-hannover.de

Abstract *In this work, we propose an efficient one-point quadrature scheme for higher-order virtual elements in inelastic problems. By solving the evolution equation at a single integration point per element, our approach significantly reduces computational cost. The method leverages a Taylor series expansion of the pseudo-energy, which naturally decomposes into spatial derivatives and geometric terms based on the initial element coordinates. These derivatives are efficiently computed using automatic differentiation in AceGen, ensuring both accuracy and efficiency. This framework enables robust and computationally efficient simulations of inelastic materials within the VEM approach.*

SYMCOMP 2025
Lisbon, 10-11 April 2025

AUTOMATING THE DERIVATION OF EQUATIONS FOR 1D MASS-SPRING-DAMPER MODELS IN MATLAB

Miguel Matos Neves[1]*, Hugo Policarpo[1,2]
1: IDMEC, Instituto Superior Técnico, Universidade de Lisboa, Lisboa, Portugal
e-mail: miguel.matos.neves@tecnico.ulisboa.pt, web: https://tecnico.ulisboa.pt/pt/

2: CINAV, Escola Naval, Instituto Universitário Militar, Base Naval de Lisboa, Almada, Portugal
e-mail: hugo.policarpo@tecnico.ulisboa.pt, web: https://tecnico.ulisboa.pt/pt/

Keywords: Dynamics, Equations derivation, mass-spring-dashpot, symbolic computation.

Abstract *It is common to spend considerable time writing and implementing equations for 1D mass-spring-damper dynamics models when teaching the simulation of system dynamics using MATLAB ode solvers. These models typically involve masses, springs, and dashpots. In this paper, the authors present a systematic symbolic calculus approach to automate the process of deriving the necessary equations from the model and first principles. This approach utilizes a table, similar to the connectivity table used in finite element analysis. In this paper, the process is limited to 1D cases but can be used for complex systems by extending the symbolic definitions and equations accordingly. These equations are central to the time integration function, such as the ode45 function in MATLAB. This method streamlines the process of quickly writing and testing different models, reducing frustration caused by minor typographical errors that often arise. First, a basic 1D dynamics model is defined using a simple example. Next, a straightforward MATLAB symbolic code that automatically generates the equations for the subroutine called by the Ordinary Differential Equations (ODE) solver is introduced. Finally, the system's response over time is obtained, including the positions and velocities of the system for the given initial conditions.*

DOI:10.5281/zenodo.15161092

1. INTRODUCTION

There are several reasons why one should care about mass-spring systems. In fact, a wide range of engineering problems can be modelled using simple mass-spring systems. The mass-spring-damper model, which consists of discrete masses connected by springs and dampers, is particularly effective for simulating various phenomena. Not only mechanical, it also has an electrical-mechanical analogy, which makes it valuable for solving several other types of problems.

By applying Newton's second law to the forces and dynamic equilibria of the point masses—including the forces exerted by the springs and any external forces—one can derive a second-order differential equations system (as outlined in [1]). These equations can generally be solved using symbolic calculus for simple cases or with ODE solvers for more complex systems. Even though in this paper, only simple systems were considered to obtain the motion equation recurring to Newton's second law, for systems that are more complicated one may use the Lagrange-Hamilton principle.

Creating and implementing equations of motion for 1D mass-spring-damper models is a common exercise in simulating basic system dynamics, particularly in educational contexts. However, this process can be time-consuming and susceptible to minor errors. While there are studies [2,3] that explore the derivation of dynamic models, such as in the robotics industry and car suspension systems, the authors did not find any literature directly addressing the here proposed automatic derivation method. Nonetheless, one assumes that similar efforts may have likely been undertaken.

In this paper, the authors propose a systematic approach to automate the derivation of the necessary equations from the model and first principles. This method utilizes a simple table, similar to the connectivity table used in finite element analysis [4] and the MATLAB programming capacities. While in this paper, this symbolic method is limited to 1D translational cases, it can be extended to more complex systems by adapting the symbolic definitions and equations.

This approach streamlines the process of writing and testing different models, reducing the frustration associated with typo errors that appear when equations are manually coded. The derived equations are compatible with the MATLAB symbolic toolbox, enabling efficient symbolic computations. Additionally, the same equations are compatible with MATLAB’s ODE solvers, such as the ode45 function, allowing for numerical approximations of the system's behaviour.

The structure of the paper is as follows: After this introductory section, the fundamental concepts are presented in section 2. Next, in section 3, a basic 1D dynamics model is defined using an example for which the equations are derived manually and using MATLAB symbolic code that automatically generates the equations. Then it is shown in section 4, for an example of a simplified ¼ car suspension (i.e., only one wheel) how to obtain the system's response over time, including position and velocity for a set of given initial conditions. The paper demonstrates how to use the derived equations for: i) symbolic computation to obtain an analytical solution; and ii) for numerical approximation using the ODE solver. In section 5, it is presented another example, with more masses and connections, to illustrate the potential

of the proposed method. Finally, in section 6, the main conclusions are presented.

2. FUNDAMENTALS

Mass-spring-damper models, as previously mentioned, consist of discrete masses connected by springs and dampers, also discretized for two-point connections. These systems are typically discrete, meaning that the masses are concentrated at specific points, with springs and dashpots (dampers) connecting them.

The forces applied to springs follow Hooke's Law, which states that the force exerted by a spring is proportional to the displacement from its equilibrium length:

$$F_{spring} = -k \cdot (L - L0) \tag{1}$$

Here, k is the spring constant, L is the current length of the spring, and $L0$ is the natural (unstretched) length or rest length of the spring. The force is directed opposite to the displacement, indicating that the spring attempts to restore the system to its equilibrium position.

Dashpots are components that introduce a viscoelastic damping behaviour between the masses. The force exerted by a dashpot is proportional to the rate of change of displacement (velocity), and it opposes the motion:

$$F_{dashpot} = -c \cdot \frac{dL}{dt} \tag{2}$$

where c is the dashpot constant, and dL/dt represents the velocity of the length variation. Dashpots model friction or energy dissipation, such as the action of a car shock absorber or muscle tissue.

To derive the equations of motion for these systems, one first separates the system in several free-body diagrams (one for each mass) and sum the forces acting on each mass, including any external forces $F_{external}$. Using Newton's second law of motion, one obtains the differential equations that govern the motion of the masses in the system.

$$\sum F = m \cdot a \qquad = m \cdot \frac{d^2 y}{dt^2} \tag{3}$$

where the sum of forces F is the net force, m is the mass, and a is the acceleration of the respective mass. The acceleration is the second derivative of displacement with respect to time, and this will lead to a second-order differential equation with the dependent variable y (displacement) and the independent variable t (time).

The system's parameters include the masses m_i, spring constants k_j, and dashpot constants c_j. To fully define the system response, two initial conditions are required for each mass: its initial displacement from a reference point and its initial velocity.

The system may be either unforced, where motion is driven solely by the initial conditions, or it may be forced, with an external excitation $f(t)$. In the unforced case, any motion arises purely from the initial conditions, which may involve the springs being stretched or compressed at $t=0$.

In the next section is illustrated, with one example, how the equation of motion is obtained for the system. It typically results in a linear constant-coefficient second-order ODE.

3. OBTAINING THE SYSTEM OF EQUATIONS

The following mass-spring-dashpot system represents a simplified model of the suspension system of one quarter of an automobile. The mass 1 is the corresponding part from the wheel and suspension and mass 2 is the corresponding part of the vehicle. The input to the system is the time-varying displacement $y_0(t)$ that represents the road position along the time. It is assumed permanent contact of tire with the road. The shock absorber is composed by its massless spring *k2* and massless dashpot *c2*. The vehicle tire is represented by the spring k1 with negligible damping. This example was adopted from [5].

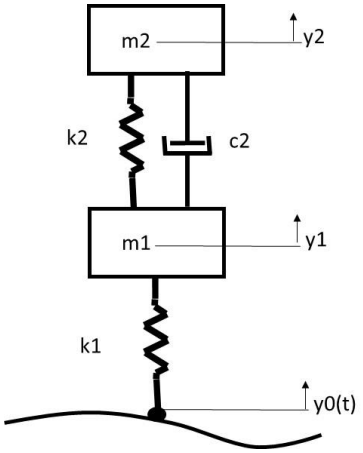

Figure 1. Mass-spring-dashpot system representation of a simplified model of the suspension system of one quarter of an automobile.

3.1. Analytical procedure done manually

Applying Newton's law of motion to the two masses, according to their free-body diagram (see Fig. 2), yields the following system of equations.

$$\begin{cases} m_1 \dfrac{d^2 y_1}{dt^2} = -k_1 * (y_1 - y_0 - L_{01}) + k_2 * (y_2 - y_1 - L_{02}) + c_2 * \left(\dfrac{dy_2}{dt} - \dfrac{dy_1}{dt}\right) \\ m_2 \dfrac{d^2 y_2}{dt^2} = -k_2 * (y_2 - y_1 - L_{02}) - c_2 * \left(\dfrac{dy_2}{dt} - \dfrac{dy_1}{dt}\right) \end{cases} \quad (4)$$

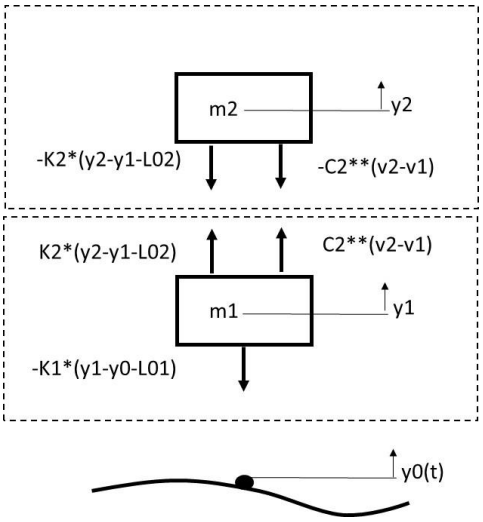

Figure 2. Free-body diagrams for each mass and its external forces

The symbolic procedure allows to input the equations as second ODE.

3.2. Automatizing the obtaining of motion equations procedure with MATLAB

The procedure described in section 3.1 to obtain the equations from the Newton's law of motion to the two masses, according to their free-body diagram, may be implemented computationally to automatically produce the respective equations.

For it, the following code was implemented.

It start by imputing the Number of Connections of each mass M(i), in this case are 2 for mass 1 and 1 for mass 2.

Next, one defines the connectivity table in the following format by line Table(i,:)=[*iM,jM,iK,iC*]; which corresponds to conectivities of mass 'i' with other masses 'j', and corresponding index of de spring and of the dashpot, if present. The following code is the result of this implementation.

```
clear all; close all; clc
%=========================================================================
Orientation='V'  %use H=horizontal Ox or V=Vertical Oy
%=========================================================================
NumberConnectionsM(1)=2; %% 1 springs and (1spring+1dashpots) NumberOfLinesInTable
NumberConnectionsM(2)=1; %% 1 (1spring+ 1dashpots)
%
n1=NumberConnectionsM(1);    %  2
n2=n1+NumberConnectionsM(2); %  3
pointer=[n1,n2]
%
```

```
Table=[1,0,1,0;...  %  conectivities i j knumber cnumber
       1,2,2,2;...  %% 4 means k4 assembled (pretension may be included)
       2,1,2,2];... %% repetition of 2,3,0,2;
```

These are all the inputs needed to obtain the equations of the system. It also considers the two orientation possibilities of the system, all in Ox direction ('H') or all in Oy direction ('V').

```
%=========================================================================

if Orientation=='H'
    strvar='x'
elseif Orientation=='V'
    strvar='y'
else
    display('Orientation used is not implemented')
end
```

The numerical procedure requires that all the equations be of first order differential type, so one need to reduce them to a system of first order equations. Here, one decided to have first all the velocities and after, all the accelerations terms. Based on (4), the following system of first order ODE are obtained.

$$\begin{cases} \dfrac{dy_1}{dt} = y_3 \\ \dfrac{dy_2}{dt} = y_4 \\ \dfrac{dy_3}{dt} = \dfrac{\left[-k_1*(y_1 - y_0 - L_{01}) + k_2*(y_2 - y_1 - L_{02}) + c_2*\left(\dfrac{dy_2}{dt} - \dfrac{dy_1}{dt}\right)\right]}{m_1} \\ \dfrac{dy_4}{dt} = \dfrac{\left[-k_2*(y_2 - y_1 - L_{02}) - c_2*\left(\dfrac{dy_2}{dt} - \dfrac{dy_1}{dt}\right)\right]}{m_2} \end{cases} \tag{5}$$

For it, the following code is implemented.

```
%=====================================================================
nmasses=size(pointer,2)      % number of mass (bodies)
%=====================================================================
for mm=1:nmasses
str= horzcat('d',strvar,'(', num2str(mm), ',1)=',strvar,'(', num2str(mm+nmasses),
');')
eq(mm,1)={str};
end%
```

For each mass, the code goes through the Table lines and the corresponding force terms are added to a string (in the code is the variable str) using MATLAB commands *horzcats*. First, it uses information of column 3 of the Table, i.e. for the springs.

```
for mm=1:nmasses
%=====================================================================
% define lines of table for this mass == from iline to kline
  if mm~=1
  iline=pointer(mm-1)+1;   % next line is pointer(mm-1)+1
  else                     % where pointer=[n1,n2,n3];
  iline=1;                  % avoid index zero inside pointer(mm-1)
  end                      %
  kline=pointer(mm);
  %=====================================================================
  %str='('; % needed
  str= horzcat('d',strvar,'(', num2str(nmasses+mm), ',1)=(')
  %=====================================================================
for ii=iline:kline
  if (Table(ii,3)~=0)
  %====================== SPRINGS ============================
  if (Table(ii,1)>Table(ii,2))
      Lsignal='-';
  strX=sprintf(['%s %s%i%s%s%i %s%s'],'Because assumes: ',...
               strvar,Table(ii,1),'>',strvar,Table(ii,2),' => ',Lsignal);
  else
      Lsignal='+';
      strX=sprintf(['%s %s%i%s%s%i %s%s'],'Because assumes:', ...
                    strvar,Table(ii,1),'<',strvar,Table(ii,2),' => ',Lsignal);
  end
  display(strX);
  aux=horzcat('-k(',num2str(Table(ii,3)),')*(',strvar,'(',num2str(Table(ii,1)),')-
',...

strvar,'(',num2str(Table(ii,2)),')',...

Lsignal,'L0(',num2str(Table(ii,3)),'))');
  str=horzcat(str,aux);
  end %if(Table(ii,3)~=0)
  %=====================================================================
```

After, it uses information of column 4 of the Table, i.e. for the dashpots.

```
  %=========================DASHPOTs==========================
  if (Table(ii,4)~=0)
  aux=horzcat('-
c(',num2str(Table(ii,4)),')*(d',strvar,'(',num2str(Table(ii,1)),')-
d',strvar,'(',num2str(Table(ii,2)),'))');
  str=horzcat(str,aux);
  end
```

```
  %================================================================
end %ii
str=horzcat(str,')/m(',num2str(mm),');');
eq(nmasses+mm,1)={str};
end% mm%=============================================================================
```

Finally, it write the equations to the display and to a txt file.

```
%eq
g0=[eq(1:nmasses)]
gy=[eq(nmasses+1:2*nmasses)]
display('Remark: It assumes i>j ==> xi>xj and signals of forces are according to
it')
display('Remark: Remove any x(0) replace by x0 value or expression and dx(0) as 0
or expression')
writecell([g0; gy],'C_tab.txt','Delimiter','tab')
```

Running this code with the input data, one gets the required equations in the display as well as in the file C_tab.txt.

```
dy(1,1)= y(3);
dy(2,1)= y(4);
dy(3,1)= (-k(1)*(y(1)-y(0)-L0(1))-k(2)*(y(1)-y(2)+L0(2))-c(2)*(dy(1)-dy(2))))/m(1);
dy(4,1)= (-k(2)*(y(2)-y(1)-L0(2))-c(2)*(dy(2)-dy(1))))/m(2);
```

(4)

These equations are correct, see equations (3).

4. SOLVING THE SYSTEM OF DIFFERENTIAL EQUATIONS

4.1. Using symbolic computation toolbox of the MATLAB

For simple systems, it may be solved using MATLAB's the symbolic computation toolbox, as exemplified by the following code.

```
clear all; clc

syms u1(t) u2(t) u3(t) u4(t) t

m = [110; 1900];
k = [136; 16];
c = [0; 176];
%==================== Put Eqs here ======================================
ode1 = diff(u1) == u3;
ode2 = diff(u2) == u4;
ode3 = diff(u3) ==  (k(1)*.05*sin(3*pi*t)-c(2)*(u3-u4)-k(2)*(u1-u2)-k(1)*u1)/m(1);
ode4 = diff(u4) ==  (c(2)*(u3-u4)+k(2)*(u1-u2))/m(2);
odes = [ode1; ode2; ode3; ode4]
```

```
cond1 = u1(0) == 0;
cond2 = u2(0) == 0;
cond3 = u3(0) == 0;
cond4 = u4(0) == 0;
conds = [cond1; cond2; cond3; cond4];
[u1Sol(t),u2Sol(t),u3Sol(t),u4Sol(t)] = dsolve(odes,conds)


VpaU1=vpa(u1Sol); tt=0:0.01:5; YY=matlabFunction(VpaU1); yy=real(YY(tt));
plot(tt,yy); hold on
VpaU2=vpa(u2Sol); tt=0:0.01:5; YY2=matlabFunction(VpaU2); yy2=real(YY2(tt));
plot(tt,yy2)
grid on
legend('u1Sol','u2Sol','Location','best')
title('Analytical Solution')
```

The code generates the following plot (Fig. 3) for the position of the masses. It presents the idea and coding, but it is only a first quick prototype. This helps teachers, but to learn one recommends that students practice for several examples. Animations were considered out of scope of this manuscript but are also important for the analysis.

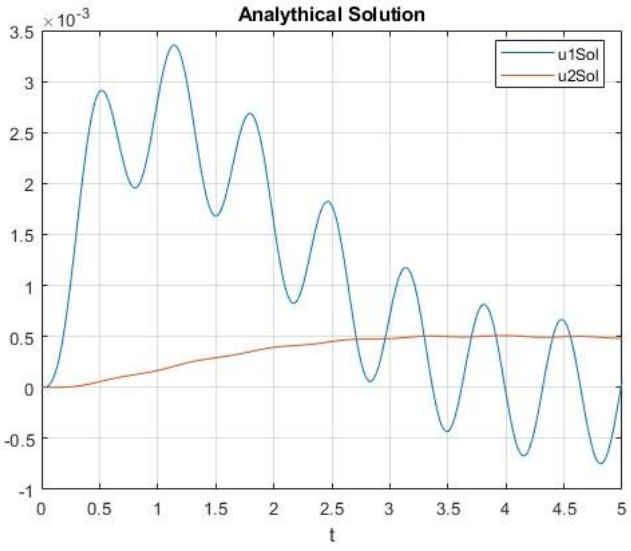

Figure 3. Plot of positions in time obtained with the Symbolic Toolbox

This is the expected plot, where the wheel (u1) oscillates more, dissipating energy, while the chassis (u2) oscillates less.

4.2. Using numerical computation with ODEs of the MATLAB

In general, it may be solved using numerical MATLAB's integration of ODEs . The following code exemplifies it.

```
clear all; clc
m = [110; 1900];
k = [136; 16];
c = [0; 176];
opts = odeset(RelTol=1e-8,AbsTol=1e-8);
[t, y] = ode45 (@spring, [0 5], [0,0,0,0],opts, m, k, c);
plot (t, y(:, 1), t, y(:, 2));
```

```
function yp = spring (t, y, m, k, c)
yp = zeros(4,1);
yp(1) = y(3);
yp(2) = y(4);
yp(3) = (k(1)*.05*sin(3*pi*t)-c(2)*(y(3)-y(4))-k(2)*(y(1)-y(2))-k(1)*y(1))/m(1);
yp(4) = (c(2)*(y(3)-y(4))+k(2)*(y(1)-y(2)))/m(2);
```

The above script runs ode45 with the function ***spring*** and produces the following result (Fig. 4), which is practically equal to the one obtained with the Symbolic Toolbox.

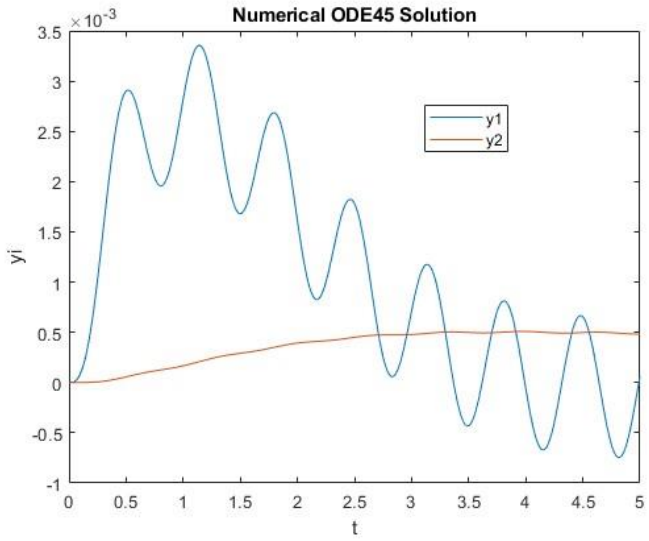

Figure 4. Plot of positions in time obtained with ode45 with function *spring*.

5. EXAMPLE WITH MORE CONNECTIONS

To illustrate the potential of the method to generate the motion equations, let us consider another example. In principle, one can have as many finite masses and connections as necessary.

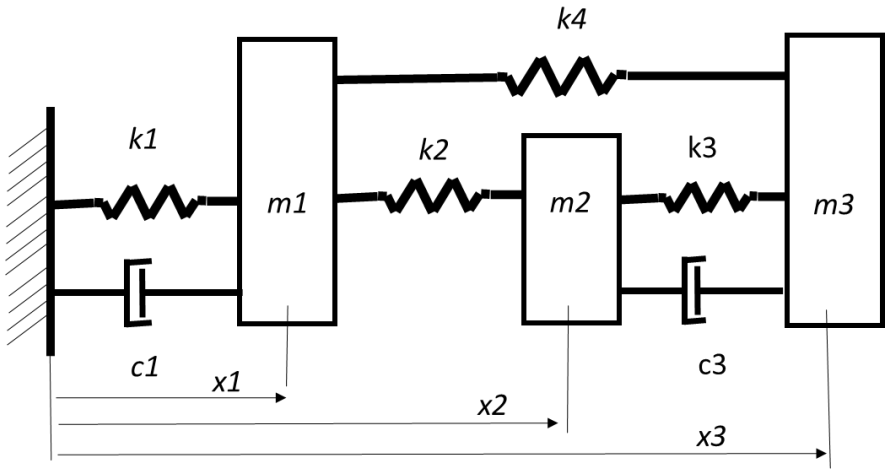

Figure 5. A three masses system

To obtain the equations of motion for the system of the Fig.5, one needs to give the orientation (in this case is horizontal) and the connectivity table. The mass 1 has three connections, because the spring 1 and dashpot 1 count as one. The masses 2 and 3 have two connections each.

```
clear all; close all; clc
%=========================================================================
Orientation='H'  %use H=horizontal Ox or V=Vertical Oy
NumberConnectionsM1=3; %% 2 springs and (1spring+ 1dashpots) NumberOfLinesInTable
NumberConnectionsM2=2; %% 1 springs and (1spring+ 1dashpots)
NumberConnectionsM3=2; %% 1 springs and (1spring+ 1dashpots)
n1=NumberConnectionsM1;    %  4
n2=n1+NumberConnectionsM2; %  7
n3=n2+NumberConnectionsM3; % 10
pointer=[n1,n2,n3]
Table=[1,0,1,1;...  % conectivities i j knumber cnumber
       1,3,4,0;...  %% 4 means k4 assembled (pretension may be included)
       1,2,2,0;...  % conectivities i j knumber cnumber
       2,1,2,0;...  %repetition of 1,2,2,0
       2,3,3,3;...  % conectivities i j knumber
       3,1,4,0;...  %% repetition 4 means k4 assembled
       3,2,3,3];    %repetition of 2,3,3,0;   %3,2,0,3
```

These are all the necessary inputs to obtain the equations for the system. It also

considers the orientation of the system, in this case are all in Ox direction ('H').

Running the code described in the section 3.2 with the orientation information and the Table given, it produces the motion equations of the system, in the display as well as in the file C_tab.txt. The equations obtained in this case are:

```
dx(1,1)=x(4);
dx(2,1)=x(5);
dx(3,1)=x(6);
dx(4,1)=(-k(1)*(x(1)-x(0)-L0(1))-c(1)*(dx(1)-dx(0))-k(4)*(x(1)-x(3)+L0(4))-k(2)*(x(1)-
x(2)+L0(2)))/m(1);
dx(5,1)=(-k(2)*(x(2)-x(1)-L0(2))-k(3)*(x(2)-x(3)+L0(3))-c(3)*(dx(2)-dx(3)))/m(2);
dx(6,1)=(-k(4)*(x(3)-x(1)-L0(4))-k(3)*(x(3)-x(2)-L0(3))-c(3)*(dx(3)-dx(2)))/m(3);
```

(5)

Like in section 4.2, these equations can now be solved using MATLAB's numerical integration of ODEs. The following code exemplifies it.

```
function [] =  MyTest()
%=====================================================
m=[15; 25;5]; X0=[1.; 1.5;1.6]; V0=[0.; 0.;0.];
k=[23; 25;16;30]; L0=[1; 0.5;0.1;0.5]; c=[30; 2; 2; 5];
t0=0; tf=20;
%=====================================================
[t, y] = ode45 (@ode_Ndof, [t0 tf], [X0',V0'],[], m, k, c, L0);
figure(1)
plot (t, y(:, 1), t, y(:, 2),t, y(:, 3));
legend('position1','position2','position3')
figure(2)
plot (t, y(:, 4), t, y(:, 5),t, y(:, 6));
legend('veloc1','veloc2','veloc3')
%=====================================================
function dx = ode_Ndof(t,x, m, k, c,L0)
%
 x0=0; dx0=0; %fixed on the left
 dx(1,1)=x(4);
 dx(2,1)=x(5);
 dx(3,1)=x(6);
 dx(4,1)=(-k(1)*(x(1)-x0-L0(1))-c(1)*(dx(1)-dx0)-k(4)*(x(1)-x(3)+L0(4))-
k(2)*(x(1)-x(2)+L0(2)))/m(1);
 dx(5,1)= (-k(2)*(x(2)-x(1)-L0(2))-k(3)*(x(2)-x(3)+L0(3))-c(3)*(dx(2)-
dx(3)))/m(2);
 dx(6,1)= (-k(4)*(x(3)-x(1)-L0(4))-k(3)*(x(3)-x(2)-L0(3))-c(3)*(dx(3)-
dx(2)))/m(3);
end
end
```

The above function runs ode45 with the function ***spring*** and produces the following result (Fig. 6).

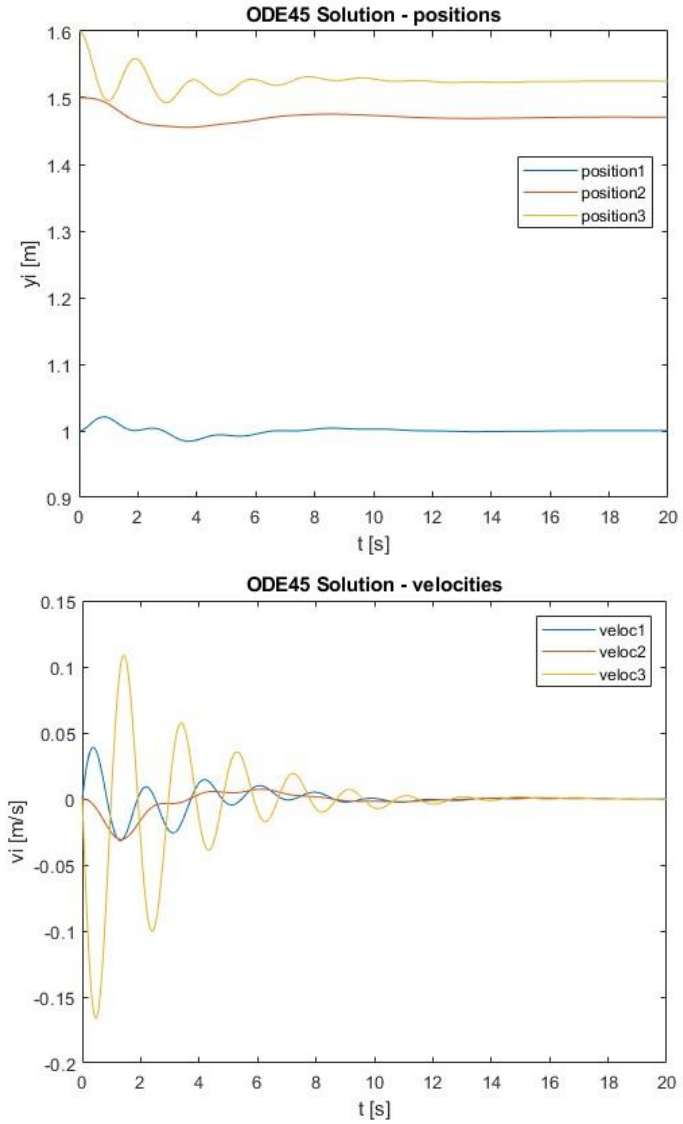

Figure 6. Plot of positions in time obtained with ode45 with function *MyTest*.

Note that the system has in its initial position the spring 4 in traction, while the others are in their rest length position. When the system is released from its initial position, it undergoes into free vibration and is damped by the two dashpots up to the final equilibrium position. Therefore, body 3 starts by moving back, which is the expected behaviour. The example illustrates how the automatic derivation of motion equations can be applied to help with these analyses.

6. CONCLUSIONS

In this paper is presented a tool that automatically derives the equations of motion for mass-spring-damper systems based on Newton's Second Law. The method requires only a connectivity table detailing the connections between masses, springs, and dampers. Initially, the approach is limited to one-dimensional translational motion with external forces or unconstrained motion.

This paper introduces the concept and provides a basic prototype of the code, though it is still in its early stages. For instance, the connectivity table can be enhanced to eliminate redundant connections when multiple masses are involved, reducing any repetitive input. With further refinement, the tool has the potential to automatically generate all the necessary code for system analysis, including reading input data for springs, dampers, masses, and initial conditions from an external file.

This method aims to assist educators in teaching complex systems involving multiple masses, springs, and dampers. However, it is recommended that students first practice deriving the equations of motion manually to deepen their understanding. While animations would be valuable for visualizing these systems, they were beyond the scope of this work.

To solve the equations of motion, one initially used MATLAB's symbolic tools, followed by the ode45 Runge-Kutta numerical integration method to compute the system's response. A comparison of the results confirmed the accuracy of the approach.

In conclusion, while obtaining analytical solutions is important, engineers are typically more interested in the qualitative characteristics of the solutions, such as resonance and beats. This method provides a quick way to assess these important system behaviours.

ACKNOWLEDGEMENTS

The authors acknowledge Fundação para a Ciência e a Tecnologia (FCT) for its financial support via the project LAETA Base Funding (DOI: 10.54499/UIDB/50022/2020).

REFERENCES

[1] Nuno MM Maia, F Marulo, C. Zang, J. Cooper, T. Silva, Dario Di Maio, Alex Carrella, *Structural dynamics in engineering design*, John Wiley & Sons (2024).

[2] Park, Y., *An Automatic Program of Generation of Equation of Motion and Dynamic Analysis for Multi-body Mechanical System using GNU Octave*, J. Appl. Comput. Mech., 7(3) (2021) 1687-1697 DOI: 10.22055/JACM.2020.33826.2293

[3] Park, Y., *Development of an Educational Code of Deriving Equations of Motion and Analyzing Dynamic Characteristics of Multibody Closed Chain Systems using GNU Octave for a Beginner*, J. Appl. Comput. Mech., 8(1) (2022) 232-244, DOI: 10.22055/JACM.2021.38021.3132

[4] Reddy, J.N., *Mechanics of Laminated Composite Plates. Theory and Analysis*, CRC Press, New York, 1997

[5] *"A Spring/Damper Suspension ODE Problem"* (From Recktenwald Problem 26, pp732-3). https://www.cs.utexas.edu/~cline/CS323E/Springs.pdf

SYMCOMP 2025
Lisbon, 10-11 April 2025

OPERATOR TECHNIQUES FOR THE SOLUTION OF CAPUTO FRACTIONAL DIFFERENTIAL EQUATIONS

Inga Telksnienė[1*], Zenonas Navickas[2], Raimondas Čiegis[1] and Minvydas Ragulskis[2]

1: Mathematical Modelling Department
Faculty of Fundamental Sciences
Vilnius Gediminas Technical University
Sauletekio 11, LT-10223 Vilnius, Lithuania
e-mail: {inga.telksniene, raimondas.ciegis}@vilniustech.lt

2: Department of Mathematical Modelling
Faculty of Mathematics and Natural Sciences
Kaunas University of Technology
Studentu 50, LT-51368 Kaunas, Lithuania
e-mail: {zenonas.navickas, minvydas.ragulskis}@ktu.lt

Keywords: Fractional differential equation, operator calculus, fractional power series expansion

Abstract. *An operator-based technique for the construction of solutions to Caputo fractional differential equations (FDEs) is presented. The proposed methodology is based on the concept of fractional order power series, with the solutions to the considered FDE initially expressed as a series expansion with fractional exponents. The FDE is then transformed into an equivalent ordinary differential equation (ODE) of a special form obtained via a nonlinear independent variable transformation. This reduction allows the use of classical techniques developed for ODEs, and once the ODE is solved, the solution is mapped back to obtain the solution to the original FDE. This approach enables the application of established semi-analytical and numerical techniques for ODEs to effectively solve Caputo FDEs.*

SYMCOMP 2025
Lisbon, 10-11 April 2025

NEURAL NETWORKS TO SURROGATE BONE REMODELLING ANALYSIS IN THE CALCANEUS

Ana Pais[1*], Jorge L. Alves[1] and Jorge Belinha[1,2]

1: Institute of Science and Innovation in Mechanical and Industrial Engineering
Campus da FEUP, R. Dr. Roberto Frias 400, 4200-465 Porto
e-mail: {anapais,falves}@fe.up.pt

2: Department of Mechanical Engineering
School of Engineering
Polytechnic of Porto
R. Dr. António Bernardino de Almeida 431, 4249-015 Porto
e-mail: job@isep.ipp.pt

Keywords: calcaneus, bone remodeling, multi-layer perceptrons, finite element method

Abstract.
Conventional numerical approaches, such as the finite element method (FEM) can effectively model complex processes like bone remodeling. However, they often require considerable computational resources. Recent advances in machine learning and deep learning have shown significant promise in computational mechanics, offering comparable predictive accuracy with greatly reduced runtime [1]. A neural network framework—based on surrogate models constructed with Multi-Layer Perceptrons (MLPs) is proposed to predict bone remodeling outcomes in the calcaneus, both in intact form and with fractures. A comprehensive dataset was assembled to train and validate the MLP models under two conditions: (1) an intact calcaneus and (2) a fractured calcaneus with a surgical screw. The MLP predicting density for the intact bone outperformed the fracture model, largely due to the greater variability in the latter's dataset. When the fracture did not significantly alter the trabecular structure, the predictive accuracy improved. Finally, evaluating the structural responses showed that the trabecular arrangement inferred by the neural network tends to be stiffer than the FEM-based distribution. This increased stiffness is attributed to the smoother density fields predicted by the MLP models.

REFERENCES

[1] A. Pais, J. L. Alves, and J. Belinha, "Predicting trabecular arrangement in the proximal femur: An artificial neural network approach for varied geometries and load cases," *Journal of Biomechanics*, vol. 161, no. November, p. 111860, 2023,

SYMCOMP 2025
Lisbon, 10-11 April 2025

A CONVOLUTIONAL NEURAL NETWORK TO GENERATE UNIT CELL GEOMETRIES WITH TARGET ELASTIC PROPERTIES

Ana Pais[1*], Jorge L. Alves[1] and Jorge Belinha[1,2]

1: Institute of Science and Innovation in Mechanical and Industrial Engineering
Campus da FEUP, R. Dr. Roberto Frias 400, 4200-465 Porto
e-mail: {anapais,falves}@fe.up.pt

2: Department of Mechanical Engineering
School of Engineering
Polytechnic of Porto
R. Dr. António Bernardino de Almeida 431, 4249-015 Porto
e-mail: job@isep.ipp.pt

Keywords: convolutional neural networks, reverse homogenization, unit cell design

Abstract. *Complex non-linear mapping between the input and output data is one of the advantages of neural networks. The aim of this work is to train a neural network to generate unit cell geometries for a given constitutive elastic matrix.*
The generator, based on convolutional neural networks (CNN) is based on the concept of the Generative aversarial network (GAN) where the generator takes a random noise vector $\mathbf{z}$ *and generates an image* $\mathbf{G}(\mathbf{z})$*. While in GANs the discriminator is trained to distinguish between real and generated images, in this work, the properties of the generated image are instead evaluated during training and compared to the input (target) properties. A dataset consisting on a collection of various geometries and their respective elastic properties was created. All of these geometries underwent homogenization using periodic boundary conditions. To lessen their impact on the homogenized constitutive matrix, the lattice was modeled as a biphasic material, with the solid phase having the material's properties and the remaining area of the representative volume element (RVE) being treated as the void phase a very low Young's modulus. A uniform mesh of square 2D elements was used, enabling the imposition of periodic boundary conditions.*
The trained generator CNN results show that the network is able to generate unit cell geometries with the desired elastic properties.

SYMCOMP 2025
Lisbon, 10-11 April 2025

STRUCTURAL TOPOLOGY OPTIMIZATION OF THE WHEEL'S SPOKES OF NASA'S PERSEVERANCE ROVER USING AN ADVANCED DISCRETIZATION TECHNIQUE

Jure Trdin[1], Jorge Belinha[1,2] and Daniel Rodrigues[1,2,3]

1: Department of Mechanical Engineering
School of Engineering
Polytechnic of Porto
Rua Dr. António Bernardino de Almeida, n.431, 4200-072 Porto
e-mail: job@isep.ipp.pt

2: Institute of Science and Innovation in Mechanical and Industrial Engineering
Campus da FEUP, Rua Dr. Roberto Frias 400, 4200-465 Porto, Portugal
email: drodrigues@inegi.up.pt

3: Department of Mechanical Engineering
University of Aveiro
Campo Universitário De Santiago 3810-193 Aveiro, Portugal

Keywords: NNRPIM; meshless methods; structural topology optimization; space vehicles

Abstract *In the space industry, the continuous effort to reduce the weight of structural components is of utmost importance due to the high cost of launching mass into space. Structural analyses and optimizations with numerical methods are crucial in achieving this goal by minimizing material usage while ensuring structural integrity and more optimal performance. The objective of the present work is to implement and demonstrate the accuracy and effectiveness of meshless methods in numerical studies compared to the Finite Element Method (FEM), focusing on designing cost-effective and lightweight components. Additionally, a topology optimization study is performed on the spoke of NASA's Rover Perseverance wheel, resulting in a more optimized structure with significantly reduced mass and lower mechanical stresses. By utilizing structural optimization, this work not only highlights the diverse applications and benefits of integrating structural optimization in the product design phase but also contributes to the ongoing efforts in the space industry to reduce material mass and enhance performance, addressing the challenges associated with launching mass into space while ensuring adequate structural resistance. Furthermore, this work also contributes to developing meshless methods in structural optimization, showcasing its effectiveness and potential in designing cost-effective and lightweight components.*

MS6 - MEASURING THORACIC MUSCLE BY CHEST CT TO FORESEE SARCOPENIA IN POST-COVID 19 PATIENTS

Maria M. C.P. Ribeiro[1,2,3] *, Marta S.C. Sarmento[4]
1: Department of Diagnostic Sciences, Therapeutic and Public Health
Lisbon School of Health Technology
Av. D. João II, Lote 4.69.01
1990-096 Lisboa

2: Chemical Engineering Department
ISEL –Superior Institute of Engineering of Lisbon
Rua Conselheiro Emídio Navarro, 1
1959-007 Lisboa

3: H&TRC - Health and Technology Research Centre https://htrcenter.wordpress.com/

e-mail: margarida.ribeiro@estesl.ipl.pt, web: http://www.estesl.ipl.pt; https://www.isel.pt/

4: Cleerly Inc.
Campo Grande, 28, 3º D 1700-093 Lisboa; e-mail: marta.sarmento@cleerlyhealth.com, web: https://cleerlyhealth.com/

Keywords: Chest CT; Skeletal Muscle Index; Sarcopenia; Cross Sectional Area; Muscle mass.

Sarcopenia is characterized by progressive and generalized loss of strength and muscle mass, and may be a manifestation of post-COVID-19 syndrome.
The diagnosis of sarcopenia can be obtained on Computed Tomography (CT) images using Cross Sectional Area (CSA) measurement.
Quantify total CSA (CSAt), pectoral muscle (CSAp) and Skeletal Muscle Index (SMI) to predict the development of sarcopenia in post-Covid-19 patients.

In 48 chest CT scans of post-Covid-19 adult patients, a slice at T4 level, was selected, at the level of descending and ascending aorta, as anatomic references. The CSAt of the pectoralis major muscle and total CSA of the pectoral, intercostal, paraspinal, dentate, latissimus dorsi and subscapularis muscles were calculated using ImageJ® software. The Skeletal Muscle Index (SMI) value was also calculated. A scale of 16 pixels/cm was determined and the background of the images was eliminated. Pixels were converted into a grey scale, then using the threshold technique (59 and 168), into binary images. A GE system with 64 rows, were used.

DOI:10.5281/zenodo.15161113

The average total muscle area was (136.2 cm^2) and the pectoral muscle area was (34.9 cm^2). The maximum calculated value of the total SMI was 74.12 cm^2/m^2 and 26.16 cm^2/m^2 for the pectoral muscle. The correlation between BMI and the variables CSAt and SMIt did not show statistically significant results (R^2=0.036 and R^2=0.049): P>0.05

No values were found for comparison of patients with sarcopenia in populations with similar characteristics.

BMI isn't a good predictor of CSAt and SMIt values, however it was concluded that a decrease in SMIt leads to a decrease in Bone Mass Index (BMI) in post-Covid-19 patients, which may represent an indicator of the development of sarcopenia. Women were more likely to develop sarcopenia.

1. INTRODUCTION

Post-COVID-19 syndrome is defined as the signs and symptoms that develop during or after infection with SARS-CoV-2 and persist for 12 weeks or longer [1, 2]. Sarcopenia is also a syndrome characterized by progressive and generalized loss of muscle mass and strength [3].

Several studies of chest computed tomography (CT) scans show that muscle weakness is one of the symptoms after COVID-19, suggesting that sarcopenia may be a late manifestation of this infection [1, 4- 6].

Sarcopenia can be diagnosed using CT scans by measuring the Cross-Sectional Area (CSA) and calculating the Skeletal Muscle Index (SMI). CSA is usually measured at the L3/L4 level; however, previous studies to determine skeletal muscle mass have shown a correlation between CSA values calculated at the L3 level and the T4 level.

As patients with post-COVID-19 syndrome already have a chest CT scan, CSA can be measured without exposing patients to further radiation by performing an additional abdominal CT scan [3, 4, 7-11].

Currently, increased attention has been paid to sarcopenia in patients with COVID-19 due to its potential effects. However, the associations between sarcopenia and COVID-19 outcomes have not been fully clarified [12].

1.1. OBJECTIVES

This study aims to quantify the total CSA (CSA_t), the pectoral muscle CSA (CSA_p), and the SMI in order to foresee the development of sarcopenia in patients after COVID-19.

2. METHODOLOGY

2.1 Sample

The sample consisted of 48 chest Computed Tomography (CT) scans. For this study 27 male and 21 female exams, in post-COVID-19 follow-up, were selected. The individuals were aged over 18 and underwent chest CT in clinical practice, in an expiratory protocol, for follow-up of SARS-CoV-2.

Patients who did not undergo this protocol and who did not have information on weight and height for subsequent calculation of Body Mass Index (BMI), were excluded.

2.2. Procedure description

The selected scans for this study were carried out on the same equipment model 16-slice CT scanner (GE BrightSpeed; GE Healthcare, Milwaukee, WI, USA).

The chest CT scans were used and visualized using the RadiAnt® software (DICOM PACS medical image viewer [13]) in order to select the correct sections included in the study, as well as consulting the technical parameters used to obtain the images and their scale.

The patients were positioned in the supine position, head first, with their upper limbs positioned above the head, out from the thoracic area. Images were acquired with the following parameters: 512x512 matrix; slice thickness 1.25 mm; slice interval of 1.25 mm; tube potential of 120 kV and the current of 120 mAs. The images were processed using the smooth body filter.

According to previous studies, the T4 vertebra was selected as the reference point for muscle quantification, therefore, the axial slice referring to the emergence of the descending and ascending aorta artery was selected in each exam (Figure 1).

The level was then confirmed through the vertebra count procedure. The images of the selected slices were recorded in JPEG format, and processed using the ImageJ® software.

In this software, the first step was to set the scale of the images with the "straight line" tool (16 pixels equivalent to 1 cm, previously calculated in RadiAnt® [13]).

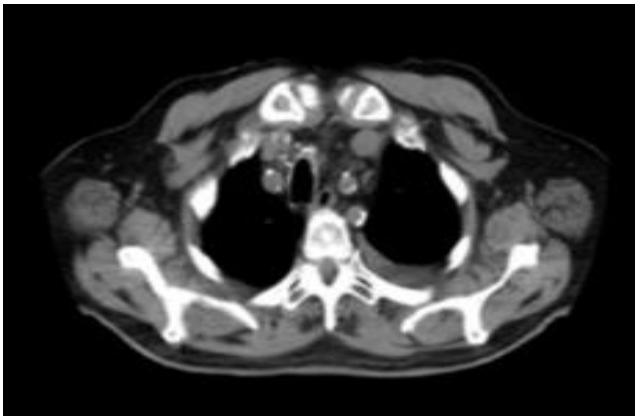

Figure 1: Original CT image, at T4 level, selected at RadiAnt®.

The obtained values were entered in the "analyze→set scale" menu. Then, a Region of Interest (ROI) was drawn around the CT images using the "oval selections" tool, to erase the image background ("edit→clear outside") (Figure 2B).

For muscle quantification on ImageJ®, it is necessary to convert the images into binary images, thus the threshold technique was applied [14]. The thresholding technique identifies regions with pixels of similar intensity, turning grey-scale images into binary images. In each image, the pixels' conversion was done creating grayscale images using the "type→8-bit" tool in the "image" menu.

Then, the images were converted to binary with the "threshold→set" tool, located at the "image→adjust" menu. According to previous studies and the quality of the provided images, the threshold range was defined between 59 and 168 [14].

After applying the threshold, the black pixels of the binary images identify soft tissues, and the white pixels indicate the remaining tissues, specifically bone, fat, and air [5-7] (Figure 2C).

Since the spinal cord and heart are also represented by black pixels, ROIs were delineated around them and filled in using the 'fill' tool in the 'edit' menu, so that the pixels inside them became white, preventing them from being quantified as muscle (Figure 2D).

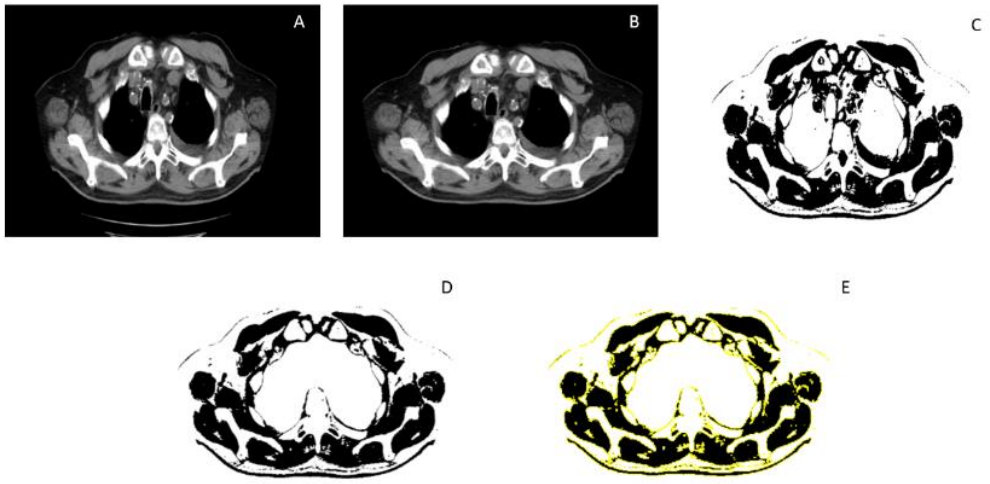

Figure 2 - Total thoracic muscle processing and quantification in ImageJ software.
A) Original axial image. B) Image after background removal. C) Binary image after applying the threshold. D) Binary image after removal of the spinal cord and heart. E) Selection of all pixels corresponding to muscle tissue (black).

Lastly, in the "analyze→set measurements" menu the "area" variable was selected. To quantify CSA_t, the pectoral, intercostal, paraspinal, dentate, latissimus dorsi, and subscapularis muscles were considered (Figure 3). All the black pixel representing these muscles were selected by the "create selection" tool (Figure 2E). CSAt value was given by the "measure" tool. (Figure 3)

To quantify CSAp, only the pectoral muscles were outlined using the ‘freehand selection’ tool and their background was erased in the ‘edit→clear outside’ menu (Figure 4).

Figure 3: Image representing the muscles for total CSA quantification, at T4 level, after processing at ImageJ®.

Figure 4: Image representing the pectoral muscle for pectoral CSA quantification, at T4 level, after processing at ImageJ®.

After performing this procedure in the 48 CT images, BMI (Body Mass Index) (BMI = Weight/Height2, kg/m2), SMIt (SMIt = CSAt/Height2, cm2/m2), and SMIp (SMIp = CSAp/Height2, cm2/m2) were calculated for each patient [15-16].

3. RESULTS

Patient data and results are exhibited in Table 1.

Table 1: Patient characteristics variables and results table showing mean values, standard deviation (SD), and minimum and maximum values per variable. Caption: Body Mass Index (BMI), Total Cross-Sectional Area (CSA_t), Pectoral Cross-Sectional Area (CSA_p), Total Skeletal Muscle Index (SMI_t), Pectoral Skeletal Muscle Index (SMI_p).

Patients			
Average, SD and limits	48 (all patients)	27 (male patients)	21 (female patients)
Age	62,5 ± 12,1 (31-84)	68 ± 11,1 (43-84)	56 ± 9,7 (31-69)
Height	1,66 m ± 0,09 (1,44-1,85)	1,71 m ± 0,06 (1,58-1,85)	1,60 m ± 0,08 (1,44-1,75)
Weight	80 kg ± 13,8 (52-113)	80 kg ± 11,4 (52-98)	80 kg ± 16,7 (58,80-113)
BMI	29,1 kg/m^2 ± 5,1 (17,58-43,06)	27,2 kg/m^2 ± 3,5 (17,58-33,25)	31,5 kg/m^2 ± 5,9 (21,87-43,06)
CSA_t	136,2 cm^2 ± 26,4 (97,13-216,26)	144 cm^2 ± 26,5 (104,48-216,26)	126 cm^2 ± 23 (97,13-171,26)
CSA_p	34,9 cm^2 ± 10 (22,64-77,38)	37,7 cm^2 ± 11,3 (25,37-77,38)	31,2 cm^2 ± 6,8 (22,64-47,32)
SMI_t	49,6 cm^2/m^2 ± 9,6 (32,53-74,12)	49,4 cm^2/m^2 ± 9 (35,36-73,10)	49,8 cm^2/m^2 ± 10,5 (32,53-74,12)
SMI_p	12,7 cm^2/m^2 ± 3,5 (8,52-73,10)	12,9 cm^2/m^2 ± 3,8 (35,36-73,10)	12,3 cm^2/m^2 ± 3 (8,52-20,48)

The mean BMI value of all patients was 29,1 kg/m^2.

CSA_t and CSA_p mean values were, 136.2 cm^2 and 34.9 cm^2, respectively.

SMI_t values varied between 32.53 and 74.12 cm^2/m^2 and SMI_p between 8.52 and 73,10 cm^2/m^2.

The corresponding mean values were 49,6 cm^2/m^2 and 12.7 cm^2/m^2. The correlation between BMI and the variables CSA_t and SMI_t did not show statistically significant results (R^2=0.0036 and R^2=0.049): P>0.05, as shown in Figures 5 and 6.

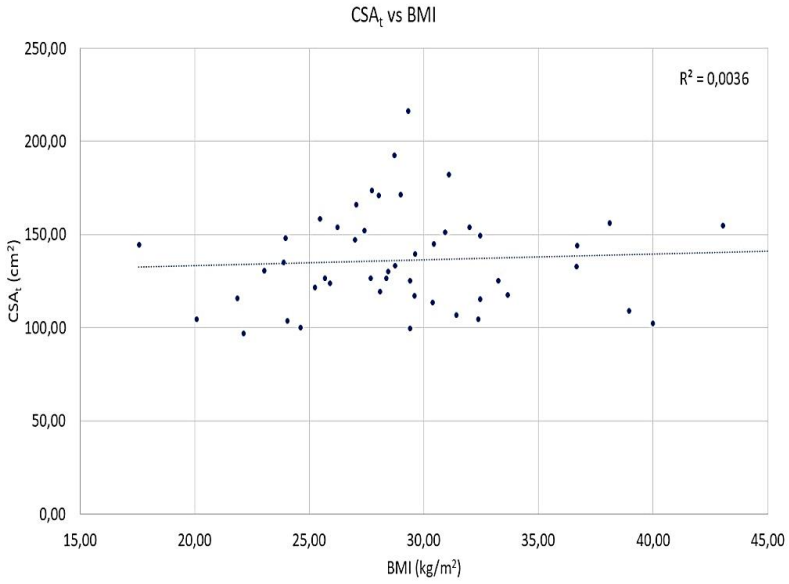

Figure 5: Graph showing correlation between CSA_t and BMI. Caption: Body Mass Index (BMI), Total Cross-Sectional Area (CSA_t).

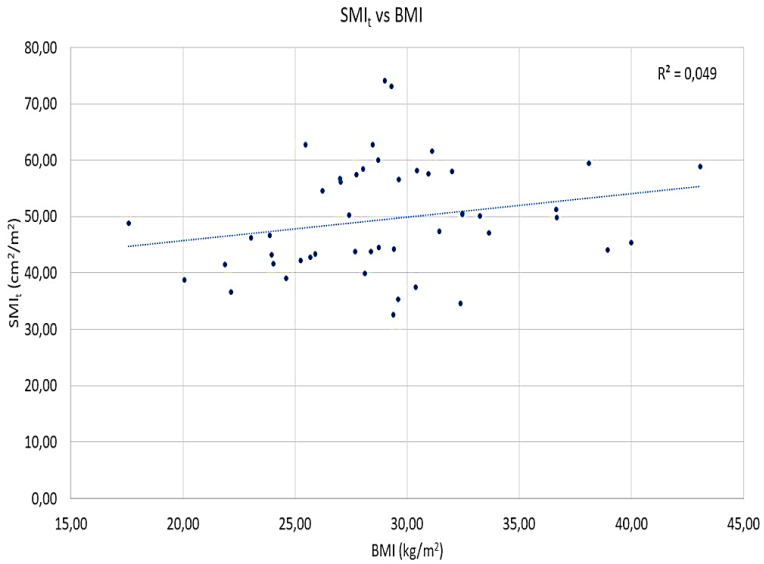

Figure 6: Graph showing correlation between SMI_t and BMI. Caption: Body Mass Index (BMI), Total Skeletal Muscle Index (SMI_t).

4. CONCLUSION

According to the obtained results, we can conclude that BMI is not a good indicator of CSA_t and SMI_t, however, the correlation between BMI and SMI_t shows that a decrease in the values of BMI leads to a decrease in SMI_t values BMI in post-Covid-19 patients, which may represent an indicator of the development of sarcopenia.

CSA_t value discrepancies between male and female patients predict women are more likely to develop sarcopenia. Similar results were obtained in another study, where it was concluded that female patients have a higher tendency to develop this syndrome. The same study was carried out on an Asian population, so we cannot use its values as reference values due to the phenotypic differences [16-17].

Although it was proven that the use of T4 is a valid method to measure skeletal muscle mass [4, 8, 11], there are insufficient reference values. Consequently, a comparison between CSA measurements performed at the T4 level, between general population and patients in post-COVID-19 follow-up and sarcopenia cannot be performed.

Sarcopenia should be routinely screened in clinical practice using available methods; therefore, the prevention and treatment of sarcopenia may prevent the worsening of COVID-19.
The limitations of this study also include a small cohort of patients and no interobserver variability assessed.

STATEMENTS

Nothing to declare

REFERENCES

[1] W. L. C. do Nascimento, D. M. Moura, K. De Oliveira Almeida, M. Gomes-Neto, S. F. de Oliveira Jezler, and I. G. N. Alves, “Lung and physical function in post COVID-19 and clinical and functional associations: a cross-sectional study in Brazil,” Rev Assoc Med Bras, vol. 69, no. 4, 2023, doi: 10.1590/1806-9282.20221436.

[2] B. Long et al., “Clinical update on COVID-19 for the emergency and critical care clinician: Medical management,” Jun. 01, 2022, W.B. Saunders. doi: 10.1016/j.ajem.2022.03.036.

[3] D. Vogele et al., “Sarcopenia - Definition, Radiological Diagnosis, Clinical Significance,” Jun. 08, 2022, Georg Thieme Verlag. doi: 10.1055/a-1990-0201.

[4] Z. N. Tekin, B. D. Karatekin, M. B. Dogan, Z. Bilgi, and B. Dogruoz Karatekin, “Pectoralis muscle area measured at T4 level is closely associated with adverse COVID-19 outcomes in hospitalized patients,” 2022. [Online]. Available:

https://www.researchgate.net/publication/363032232
[5] A. Surov et al., "Prognostic Role of the Pectoralis Musculature in Patients with COVID-19. A Multicenter Study," Acad Radiol, vol. 30, no. 1, pp. 77–82, Jan. 2023, doi: 10.1016/j.acra.2022.05.003.
[6] K. Piotrowicz, J. GÄ…sowski, J. P. Michel, and N. Veronese, "Post-COVID-19 acute sarcopenia: physiopathology and management," Oct. 01, 2021, Springer Science and Business Media Deutschland GmbH. doi: 10.1007/s40520-021-01942-8.
[7] Y. Ishida et al., "Formula for the cross-sectional area of the muscles of the third lumbar vertebra level from the twelfth thoracic vertebra level slice on computed tomography," Geriatrics (Switzerland), vol. 5, no. 3, Sep. 2020, doi: 10.3390/GERIATRICS5030047.
[8] R. Sumbal, A. Sumbal, and M. M. Ali Baig, "Which vertebral level should be used to calculate sarcopenia in covid 19 patients? A systematic review and meta-analysis," Clin Nutr ESPEN, vol. 56, pp. 1–8, Aug. 2023, doi: 10.1016/j.clnesp.2023.04.022.
[9] G. Schinas et al., "Radiologic Features of T10 Paravertebral Muscle Sarcopenia: Prognostic Factors in COVID 19," J Clin Med Res, vol. 15, no. 7, pp. 368–376, 2023, doi: 10.14740/jocmr4963.
[10] J. W. Kim et al., "Prognostic Implication of Baseline Sarcopenia for Length of Hospital Stay and Survival in Patients with Coronavirus Disease 2019," Journals of Gerontology - Series A Biological Sciences and Medical Sciences, vol. 76, no. 8, pp. E110–E116, Aug. 2021, doi: 10.1093/gerona/glab085.
[11] H. C. van Heusden et al., "Feasibility of assessment of skeletal muscle mass on a single cross-sectional image at the level of the fourth thoracic vertebra," Eur J Radiol, vol. 142, Sep. 2021, doi: 10.1016/j.ejrad.2021.109879.
[12] Wang, Yuhan et al. "Sarcopenia and COVID-19 Outcomes." Clinical interventions in aging vol. 18 359-373. 9 Mar. 2023, doi:10.2147/CIA.S398386
[13] Medixant, "RadiAnt DICOM Viewer."
[14] L. Reinking, "ImageJ Basics," Jun. 2007. [Online]. Available: http://rsb.info.nih.gov/ij/
[15] K. Engelke, O. Museyko, L. Wang, and J. D. Laredo, "Quantitative analysis of skeletal muscle by computed tomography imaging—State of the art," Oct. 01, 2018, Elsevier (Singapore) Pte Ltd. doi: 10.1016/j.jot.2018.10.004.
[16] E. Y. Kim, K. H. Jun, S. Y. Kim, and H. M. Chin, "Body mass index and skeletal muscle index are useful prognostic factors for overall survival after gastrectomy for gastric cancer: Retrospective cohort study," Medicine (United States), vol. 99, no. 47, p. E23363, Nov. 2020, doi: 10.1097/MD.0000000000023363.
[17] S. W. Moon et al., "Reference values of skeletal muscle area for diagnosis of sarcopenia using chest computed tomography in Asian general population," J Cachexia Sarcopenia Muscle, vol. 13, no. 2, pp. 955–965, Apr. 2022, doi: 10.1002/jcsm.12946. Multicenter Study," Acad Radiol, vol. 30, no. 1, pp. 77–82, Jan. 2023, doi: 10.1016/j.acra.2022.05.003.

AMPUTATIONS IN DIABETICS: STATISTICAL MODELING AND TRENDS IN PORTUGAL (2000–2023)

E. Carolino[1,2] *, J. P. Matos [2], D. Ricardo[2] and M. Rosário Ramos[4;5]
1: H&TRC, Health & Technology Research Center, ESTeSL- Escola Superior de Tecnologia da Saúde, Instituto Politécnico de Lisboa, Portugal, e-mail: etcarolino@estesl.ipl.pt
2: ISAMB, Instituto de Saúde Ambiental, Faculdade de Medicina da Universidade de Lisboa, Portugal
3: ESTeSL, Escola Superior de Tecnologia da Saúde, Instituto Politécnico de Lisboa, Portugal, e-mail: fulgenciomatos@estesl.ipl.pt and diogo.ricardo@estesl.ipl.pt
4: Universidade Aberta, and CEG (Centro de Estudos Globais), Portugal, e-mail: MariaR.Ramos@uab.pt
5: CEAUL, Faculdade de Ciências, Universidade de Lisboa, Portugal

Keywords: Amputation, Diabetes, Poisson Regression, Negative Binomial Regression, Projections

Abstract *Amputation, whether surgical or traumatic, entails the loss of a body segment due to irreparable injury caused by trauma, vascular conditions, or other pathologies. Among individuals with diabetes, amputation remains one of the most feared and recognized outcomes. However, early diagnosis and timely intervention could prevent approximately 50% of diabetes-related amputations and ulcerations. This retrospective observational cross-sectional study draws on data from the Hospital Morbidity Database (BDGDH), provided by the Central Administration of the Health System (ACSS) under the Ministry of Health. This study focuses on amputations in diabetic patients in Portugal, particularly from 2000 to 2023. It aims to update statistical results and projections using current data to inform health planning and optimize resource allocation. The research uses data from the Hospital Morbidity Database, analysing factors such as year, age group, gender, and diagnosis codes. Poisson regression and Negative Binomial models were applied to estimate annual amputation rates and forecast future trends. The findings will help compare national trends with international standards, guiding public health policies and supporting prevention and early diagnosis programs to reduce the socio-economic impact of amputations.*

Acknowledgment: This work is partially financed by national funds through FCTFundaçãao para a Ciência e a Tecnologia FCT/MCTES under the projects:UIDP/05608/2020. DOI 10.54499/UIDP/05608/2020 (https://doi.org/10.54499/UIDP/05608/2020), UIDB/05608/2020. DOI 10.54499/UIDB/05608/2020 (https://doi.org/10.54499/UIDB/05608/2020) – Elisabete Carolino and UIDB/00006/2020. DOI: 10.54499/UIDB/00006/2020 (https://doi.org/10.54499/UIDB/00006/2020) – Rosário Ramos.

SYMCOMP 2025
Lisbon, 10-11 April 2025

STUDY OF COMBINATORIAL STRUCTURES ASSOCIATED WITH TORTKARA ALGEBRAS

J. Baena[1*], M. Ceballos[2] and D. Fernández[1]

1: Dpto. Geometría y Topología.
Facultad de Matemáticas
Universidad de Sevilla
c/ Tarfia s/n, 41012, Seville (Spain)
e-mail: jebago1997@gmail.com, desamfer@us.es

2: Dpto. de Ingeniería
Escuela de Ingeniería
Universidad Loyola Andalucía
Av. de las Universidades, s/n, 41704 Dos Hermanas, Sevilla (Spain)
e-mail: mceballos@uloyola.es

Keywords: Graph, combinatorial structure, Tortkara algebra, algorithm, complexity

Abstract.
Tortkara algebras are a novel class of non-associative algebras introduced by A. S. Dzhumadil'daev, who showed that every Zinbiel algebra with the commutator as multiplication is a Tortkara algebra. These algebras satisfy an identity that blends symmetry and alternation. Research has since focused on their structural properties, relationships with Zinbiel and other non-associative algebras, and their classification under various conditions. In particular, nilpotent Tortkara algebras of dimension less than or equal to six have been classified both geometrically and algebraically by I. Gorshkova, I. Kaygorodovc, and M. Khrypchenkod. Potential applications include mathematical physics, especially in theories that model complex interactions and symmetries, as well as emerging roles in cryptography and algebraic models for nonlinear dynamical systems.
In this work, we present a method to associate finite-dimensional Tortkara algebras, defined over a fixed basis B, with combinatorial structures in the form of directed graphs, where full triangles may appear. We investigate the properties of these digraphs for algebras of dimensions 2 and 3, providing a detailed analysis of the corresponding Tortkara algebra types in each case. Additionally, we study the combinatorial structures of three vertices associated with these algebras and classify their typology. Finally, we implement algorithmic procedure in order to find out if a given combinatorial structure is associated or not with a Tortkara algebra. Our results offer new insights into the link between non-associative algebras and combinatorial structures opening a new research line in the theory of Tortkara algebras and their applications.

SYMCOMP 2025
Lisbon, 10-11 April 2025

PRELIMINARY SIMULATION RESULTS OF A MOLTEN SALT THERMAL STORAGE TANK FOR CONCENTRATED SOLAR POWER

Júnior Mané[1]*, Isabel Malico[1,2], Nuno Domingues[3,4], Radia Ait El Cadi[5], and Pedro Horta[5]

1: IDMEC, Escola de Ciências e Tecnologia, Universidade de Évora, Portugal
e-mail: d57485@alunos.uevora.pt, web: http://www.idmec.tecnico.ulisboa.pt/

2: Universidade de Évora, Complex Flow Systems Lab, Évora, Portugal
e-mail: imbm@uevora.pt, web: https://www.uevora.pt/

3: Instituto Politécnico de Lisboa, Inst. Sup. de Engenharia de Lisboa, Lisboa, Portugal
e-mail: nuno.domingues@isel.pt, web: https://www.isel.pt/

4: Unit for Innovation and Research in Engineering (UnIRE), Lisboa, Portugal
web: https://sites.google.com/view/unire/

5: Universidade de Évora, Renewable Energies Chair, Nossa Sra. da Tourega, Portugal
e-mail: {radia.aitelcadi, phorta}@uevora.pt, web: https://www.catedraer.uevora.pt/

Keywords: Computational Fluid Dynamics, Thermocline tank, Porous media, Packed-bed

Abstract *Molten salt thermal storage systems play a critical role in concentrated solar power (CSP) plants, ensuring energy storage and dispatchability. Among these, thermocline tanks offer the potential for cost reduction, compared to the standard thermal storage system implemented in CSP plants: a two-tank solution (for hot and cold fluid, individually). This paper presents initial results from a Computational Fluid Dynamics (CFD) simulation of the 2.86 MWh_{th} thermocline-tank installed at the EMSP – Évora Molten Salt Platform. The tank incorporates a filler material to enhance thermal stratification. The CFD model integrates the transport equations for mass, momentum and energy, along with closure models to account for the pressure drop imposed by the presence of the filler material and the heat transfer between the molten salts and the filler material. Validation of the model is conducted using experimental data from the literature. The simulation investigates the thermal performance of the tank during the discharging phase, where the axial temperature at the centerline of the tank was monitored periodically. The results were obtained for a simplified geometry of the tank as more improvements can still be made in future work to ensure the accuracy of the model.*

DOI:10.5281/zenodo.15161128

1. INTRODUCTION

Thermal energy storage systems (TES) are an essential technology to increase the efficiency of the integration of intermittent renewable energies. For optimal operation and improvement of the system efficiency, a study of the storage system is essential. In the study and implementation of a system of this type, it is necessary to consider the conditions of production (variability of the solar radiation between day and night, the climate of the place and the season of the year, among others) and consumption (periods, seasonality and intensity, among others). In solar thermal applications it is very interesting to have a TES mechanism capable of collecting energy at times of high radiation for later use in periods of absence of sun.
In the scope of such studies, computational fluid dynamics (CFD) are helpful and key to pre-prototyping works. This study presents the initial results from a CFD simulation of the 2.86 MWh_{th} NEWSOL dual media thermocline-tank implemented at ESMP – Évora Molten Salt Platform. The work presented intends to be the starting point for a more focused and intricate analysis on the heat and mass transfer phenomena of this category of TES.

2. PROBLEM DESCRIPTION AND MODELLING APPROACH

The 2.86 MWh_{th} NEWSOL thermocline-tank implemented at ESMP – Évora Molten Salt Platform consists of a single cylindrical vertical tank filled with molten-salts, which serve as heat transfer fluid, and slag pebbles that compose the filler material. To facilitate the analysis, the tank simulated in this work is a simplification of the real NEWSOL tank, which is equipped with an inlet and an outlet at the bottom (for cold) and top (for hot) of the lateral wall of the tank. As first analysis and baseline study, in the current model, it is assumed that on a discharging phase, the inlet and outlet are located at the bottom and top of the tank, respectively, occupying all the boundary and creating a plug flow. A simple schematic of the simulated tank as well as the computational domain is shown in Figure 1.

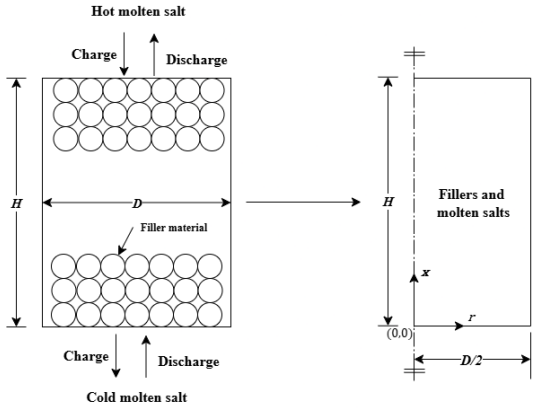

Figure 1. Schematic diagram of the simplified simulated tank and computational domain.

In the following subsections, a transient, two-dimensional, CFD model is presented to account for the flow, heat and mass transfer phenomena within the packed-bed NEWSOL

thermocline tank. The thermal non-equilibrium model is considered to account for the different temperatures of molten salt and solid fillers. The following assumptions are taken to simplify the analysis:

- The fluid flow and heat transfer are symmetrical about the axis. As such, the governing equations for transport within the tank become two-dimensional.
- The flow of molten salt through the packed-bed region is laminar and incompressible.
- The solid fillers behave as a continuous, homogeneous, and isotropic porous medium, and the solid medium is not described as independent particles.

3. GOVERNING EQUATIONS

Transient, two-dimensional governing equations based on the volume-averaging approach [1] are presented to model the heat transfer and fluid flow inside the NEWSOL thermocline tank.

3.1. Continuity equation

$$\frac{\partial(\varepsilon\rho_{\mathrm{l}})}{\partial t} + \nabla \cdot [\rho_{\mathrm{l}}\vec{u}] = 0 \tag{1}$$

where ε is the bed porosity, ρ_{l} is the density of molten salt and $\vec{u}$ is the superficial velocity vector of the fluid where $\vec{u} = \vec{u}_r\vec{e_r} + \vec{u_x}\,\vec{e_x}$.

3.2. Momentum equation

$$\frac{\partial(\rho_{\mathrm{l}}\vec{u})}{\partial(\varepsilon t)} + \frac{\nabla\cdot(\rho_{\mathrm{l}}\,\vec{u}\vec{u})}{\varepsilon^2} = \nabla\cdot(\mu\nabla\vec{u}) - \nabla p + \rho_{\mathrm{l}}\vec{g} - \left(\frac{\mu}{K} + \frac{C_{\mathrm{F}}\rho_{\mathrm{l}}}{\sqrt{K}}|\vec{u}|\right)\vec{u} \tag{2}$$

where μ is the molten salt dynamic viscosity, p is the pressure, $\vec{g}$ is the gravitational force and $\left(\frac{\mu}{K} + \frac{C_{\mathrm{F}}\rho}{\sqrt{K}}|\vec{u}|\right)\vec{u}$ is a packed-bed momentum source term where the first-term is a viscous loss term and the second one an inertial loss term. K is the permeability of the packed-bed and C_{F} the inertial coefficient. Both parameters are calculated through empirical correlations, as follows [2]:

$$K = \frac{d_p^2\varepsilon^3}{150(1-\varepsilon)^2} \tag{3}$$

$$C_F = \frac{1.75}{\sqrt{150\ \varepsilon^3}} \tag{4}$$

where d_{p} is the filler material particle diameter.

3.3. Energy equation for the molten salt

$$\frac{\partial(\varepsilon\rho_{\mathrm{l}}c_{p,\mathrm{l}}T_{\mathrm{l}})}{\partial t} + \nabla\cdot\left(\rho_{\mathrm{l}}c_{p,\mathrm{l}}\,\vec{u}\,T_{\mathrm{l}}\right) = \nabla\cdot\left(k_{\mathrm{l,eff}}\nabla T_{\mathrm{l}}\right) + h_{\mathrm{ls}}\,a_{\mathrm{ls}}\,(T_{\mathrm{l}} - T_{\mathrm{s}}) \tag{5}$$

where $c_{p,\mathrm{l}}$ is the molten salt specific heat, T_l and T_s are the molten salt and solid fillers temperature, respectively, $k_{\mathrm{l,eff}}$ is the fluid effective thermal conductivity, h_{ls} is the interstitial heat transfer coefficient between the fluid and solid fillers and a_{ls} is the interfacial area density, which is calculated as follows, assuming that the filler particles are spherical:

$$a_{\mathrm{ls}} = \frac{6(1-\varepsilon)}{d_\mathrm{p}} \tag{6}$$

3.4. Energy equation for the solid filler

$$\frac{\partial\left((1-\varepsilon)\rho_s c_{p,s} T_\mathrm{s}\right)}{\partial t} = \nabla\cdot\left(k_{\mathrm{s,eff}}\nabla T_\mathrm{l}\right) + h_{\mathrm{ls}}\, a_{\mathrm{ls}}(T_\mathrm{s} - T_\mathrm{l}) \tag{7}$$

where ρ_s is the solid filler density, $c_{p,s}$ is the solid filler specific heat and $k_{\mathrm{s,eff}}$ is the solid filler effective thermal conductivity.

4. EMPIRICAL CORRELATIONS AND HEAT TRANSFER PARAMETERS

4.1. Effective thermal conductivity, k_{eff}

For the effective thermal conductivity of molten salt and solid fillers we considered the application of an equivalent to the parallel model to obtain these parameters. In [3] more can be found regarding this model.

4.2. Interstitial heat transfer coefficient, h_{ls}

The volumetric interstitial heat transfer coefficient is an important parameter to account for in packed bed porous media modelling when a non-equilibrium model approach is being used as it makes the link for the heat transfer between the solid fillers and the heat transfer fluid. This parameter is often obtained by experiments where an empirical correlation is formulated depending on the specific parameters of each simulation (e.g., Reynolds and Prandtl number, porosity of the packed bed, etc.). For the current numerical model, the heat transfer coefficient used is a fixed value of $204.21\ \mathrm{W/(m^2\ K)}$ calculated from Eq. (8) for a reference temperature of 170 ºC, which is the inlet temperature for the discharge cycle and based on the following empirical correlation which is well suited for a wide range of Reynolds numbers and packed bed porosities [4].

$$h_{\mathrm{ls}} = \frac{k_\mathrm{l}\left[2+1.1\, Re_\mathrm{p}^{0.6} Pr^{1/3}\right]}{d_\mathrm{p}^2} \tag{8}$$

where Re_p is the particle filler Reynolds number, and Pr is the Prandtl number.

5. MATERIAL PROPERTIES

The molten salt used in NEWSOL tank is a mixture of 60 wt% $NaNO_3$ and 40 wt% KNO_3 where its thermophysical properties are temperature-dependent and can be found at [5]. As for the solid fillers (slag pebbles), except density, which is constant, the other thermophysical properties used in the model are also temperature dependent and can be found at [6].

6. BOUNDARY CONDITIONS

For each process (charging/discharging) the boundary conditions are given as follows:

6.1. Charging process

Top inlet: $\dot{m}_{\text{in}} = \rho_{\text{l,in}} \cdot A_{\text{in}} \cdot u_{x,\text{in}} = 5.3\ kg/s, u_{r,\text{in}} = 0, \text{and}\ T_{\text{l}} = T_{\text{s}} = T_{\text{in}} = 170℃$ (9)

where $\dot{m}_{\text{in}}$ is the inlet mass flow of molten salt, $\rho_{\text{l,in}}$ is its density calculated at the inlet temperature, T_{in}, A_{in} is the surface area of the inlet, and $u_{x,\text{in}}$ is the inlet velocity, normal to the inlet area.

Bottom outlet: outflow boundary condition where:

$$\partial\vec{u}/\partial x = 0,\ \partial T_{\text{l}}/\partial x = 0,\ \partial T_{\text{s}}/\partial x = 0 \quad (10)$$

Exterior Wall: a constant heat flux, q_{w}, is imposed at the wall considering the conductive heat transfer through the layers that constitute the lateral wall of the tank and the convective heat transfer between the exterior surface of the wall and the exterior environment. The following equation is used to calculate the imposed heat flux:

$$q_{\text{w}} = \frac{T_{\text{avg}} - T_{\infty}}{\frac{1}{\text{h}_{\text{conv}}} + \sum_{i=1}^{n}\left(\ln\left(\frac{R_{\text{l}}+t_1}{R_{\text{l}}}\right) + \ln\left(\frac{R_{\text{l}}+t_1+t_2}{R_{\text{l}}+t_1}\right) + \cdots + \ln\left(\frac{R_{\text{l}}+t_1+\cdots+t_n}{R_{\text{l}}+e_1+\cdots+e_{t-1}}\right)\right)} \quad (11)$$

where T_{avg} is the average fluid temperature between the maximum and minimum temperatures inside the tank, T_{∞} is the ambient air temperature considered to be 25 ℃, n is the number of wall layers (1 is the steel liner, 2 is the thermal concrete, 3 is insulation layer, and 4 the structural concrete layer), R_{l} is the tank inner radius and t_n the thickness of the n^{th} layer. h_{conv} is the heat transfer coefficient taken from an empirical correlation for incompressible flow over a cylinder [7]:

$$Nu = h_{\text{conv}} D/k_{\text{air}} = 0.632\ Re_{\text{D}}^{1/2} Pr^{1/3}, \quad Re_{\text{D}} = \frac{u_{\text{air}} D}{\nu_{\text{air}}} \quad (12)$$

where Nu is the Nusselt number, D is the diameter of the tank, u_{air} is the air velocity, assumed as $5\ \text{ms}^{-1}$, and k_{air} and ν_{air} are, respectively, the thermal conductivity and the kinematic viscosity of air at the ambient temperature. Re_D is the Reynolds number based on the tank diameter and Pr is the Prandtl number.

Symmetry boundary condition: Since, for the purpose of this work, an axisymmetric model was considered, a symmetry boundary condition was assumed in the tank along its axis.

6.2. Discharging process

Bottom inlet: same conditions as in eq. (9)
Top outlet: outflow boundary condition with the same conditions as in eq. (10).
Exterior wall: the same conditions as in eqs. (11) and (12).
Symmetry boundary condition: same conditions as described for the charging process.

7. NUMERICAL METHODS

The governing equations described above are solved using the finite volume method [8] and the CFD commercial software ANSYS Fluent v. 2024 R2 [9]. As already described, these equations are solved considering the volume-averaged equations for a porous medium and the non-thermal equilibrium model to account for the local temperature differences between the molten salt and the solid fillers. Gravity is set on the axial direction. The SIMPLE algorithm is employed for the pressure-velocity coupling [10]. The pressure term is discretized by a second order scheme, and momentum and energy equations are discretized by the second order upwind scheme. A first order implicit method is employed for discretization of the transient term. The under-relaxation factors are set to 0.3, 1, 0.7, and 0.5, for pressure, density, momentum and energy, respectively. The simulations are performed for a time-step of 1 s and a mesh with 4000 elements. The governing equations are solved for each time step until the residuals for continuity and momentum equations reduce to less than 10^{-3}, and 10^{-6} for the energy equation.

8. MODEL VALIDATION

The current model was validated with the experimental results of Pacheco et. al. [11] and the numerical results of Cabello Nuñez et. al. [6].

8.1. Validation with Pacheco et al.'s experimental results

In Pacheco et al.'s experiments, a molten-salt thermocline thermal storage system for parabolic trough plants was analysed and compared with the standard two-tank molten salt system [11]. The tank considered is a 2.3 MWh_{th} thermocline tank with a length of 5.9 m and a diameter of 3 m. Quartzite rocks were used as filler material and molten salt with the same chemical composition and thermophysical properties as mentioned in the material properties subsection were used. Other geometric parameters and properties used for validation with Pacheco et al.'s experiments can be found at [4]. The validation is performed for the axial temperature profiles of the molten salt in the storage tank at each 30 minutes of a discharging cycle. A good agreement between the experimental and numerical results is obtained even though some deviations exist. The average error percentage between the numerical and experimental results for each 30 min profile is approximately $\pm$ 1%, and the standard deviation and RMSE are also of the same order of magnitude, which indicates that the heat and mass transfer inside a packed bed thermocline tank can be well predicted by this current numerical model.

8.2. Validation with Cabello Nuñez et al.'s experimental results

Cabello Nuñez et al. [6] performed a numerical analysis of a hybrid thermal storage system composed of a single medium and a dual medium thermocline tank which used slag pebbles as filler material and molten salt as heat transfer fluid. Both tanks had a 20×20 m^2 design and the simulations used in the validation were conducted for the dual medium tank. Other geometric parameters and properties used in the model for this validation can be found at [6]. During the charging process the temperature at the bottom of the tank was monitored, and when the outlet

temperature at this location increased by 30 ℃ the process was ended and immediately the discharge process started. The same monitoring activity occurred for the discharging phase but at the top of the tank. The validation is performed for the first full cycle of operation where the axial temperature of the molten salt in the storage tank at the end of the charge and discharge process is compared. The simulation is conducted for a time-step of 1s and a mesh of 8000 elements. The validation shows good agreement between the experimental and numerical results even though there are some deviations. The average error between the experimental and numerical results is around 3% for the charge and 1.5% for the discharge.

9. RESULTS AND DISCUSSION OF PRELIMINARY CFD SIMULATION

In the present work, preliminary results for the simplified NEWSOL tank geometry were carried out. A simulation is performed for a discharge cycle where the molten salts enter at the bottom of the tank at 170 ºC and with a mass flow rate of 5.3 kg/s. The full discharge cycle lasted 96 minutes. A uniform temperature distribution through all the tank and equivalent to the maximum temperature in the tank at the end of a charge cycle (490 ºC) was considered as initial condition. Additionally, the fluid was initially at rest. The results obtained can be seen in Figure 2 where the axial temperature of the tank taken at the centerline is presented for each 24 minutes of the simulation. As shown, a transient thermocline evolution inside the tank was observed. In this case, at the end of the discharge cycle, one can highlight that the temperature at the outlet of the tank (approximately 440 ºC) is inferior to the temperature taken at the same location during the whole cycle, which is the maximum temperature at the end of a charge cycle (490 ºC).

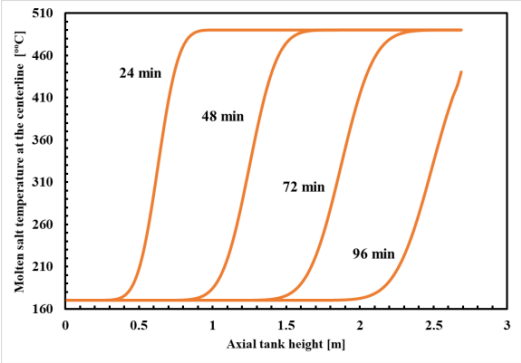

Figure 2. Simplified NEWSOL tank geometry preliminary simulation results.

10. CONCLUSIONS

In this study, a transient, two-dimensional numerical model is presented to perform preliminary CFD simulations of the 2.86 MWh_{th} NEWSOL thermocline-tank installed at the ESMP – Évora Molten Salt Platform. The model was successfully validated with experimental and numerical results from the literature. Then, the model was employed to obtain preliminary simulation results regarding a discharge process of the packed bed NEWSOL thermocline tank. It is found that the simulation presents results according to what is expected where a transient thermocline evolution in the tank is observed, although the available output energy at the end of the

discharge cycle is inferior to what is possible to retrieve through all the cycle. The simulations presented in the work are preliminary. For a start, mesh and time-step independence studies are being carried out to ensure the accuracy of the predictions. Additionally, improvements to the model can still be made. For example, more realistic initial conditions will be considered and the treatment of the heat transfer between the tank walls and the exterior will be improved. Nevertheless, these preliminary results show the potential of the proposed model to simulate the NEWSOL thermocline tank.

11. ACKNOWLEDGEMENTS

The authors acknowledge Fundação para a Ciência e a Tecnologia (FCT) for its financial support via the project LAETA Base Funding (DOI: 10.54499/UIDB/50022/2020) and the PhD grant 2024.01497.BD (Júnior Mané).

REFERENCES

[1] M. Quintard and S. Whitaker, "One- and Two-Equation Models for Transient Diffusion Processes in Two-Phase Systems," in *Advances in Heat Transfer*, vol. 23, Elsevier, 1993, pp. 369–464. doi: 10.1016/S0065-2717(08)70009-1.

[2] Sabri Ergun, "Fluid Flow Through Packed Columns," vol. 48, pp. 89–94, 1952.

[3] A. Nakayama, "Effective thermal conductivity of porous media," in *Advances in Heat Transfer*, vol. 56, Elsevier, 2023, pp. 51–111. doi: 10.1016/bs.aiht.2023.05.006.

[4] C. Xu, Z. Wang, Y. He, X. Li, and F. Bai, "Sensitivity analysis of the numerical study on the thermal performance of a packed-bed molten salt thermocline thermal storage system," *Appl. Energy*, vol. 92, pp. 65–75, Apr. 2012, doi: 10.1016/j.apenergy.2011.11.002.

[5] A. Abdulla and K. S. Reddy, "Effect of operating parameters on thermal performance of molten salt packed-bed thermocline thermal energy storage system for concentrating solar power plants," *Int. J. Therm. Sci.*, vol. 121, pp. 30–44, Nov. 2017, doi: 10.1016/j.ijthermalsci.2017.07.004.

[6] F. Cabello Núñez, J. López Sanz, and F. Zaversky, "Analysis of steel making slag pebbles as filler material for thermocline tanks in a hybrid thermal energy storage system," *Sol. Energy*, vol. 188, pp. 1221–1231, Aug. 2019, doi: 10.1016/j.solener.2019.07.036.

[7] W. A. Khan, J. R. Culham, and M. M. Yovanovich, "Fluid Flow Around and Heat Transfer From an Infinite Circular Cylinder," *J. Heat Transf.*, vol. 127, no. 7, pp. 785–790, Jul. 2005, doi: 10.1115/1.1924629.

[8] S. V. Patankar, *Numerical heat transfer and fluid flow*. in Series in computational methods in mechanics and thermal sciences. Washington, D.C.: Hemisphere, 1980.

[9] ANSYS, "FLUENT software." Accessed: Mar. 25, 2025. [Online]. Available: https://www.ansys.com/products/fluids/ansys-fluent

[10] S. V. Patankar and D. B. Spalding, "A calculation procedure for heat, mass and momentum transfer in three-dimensional parabolic flows," *Int. J. Heat Mass Transf.*, vol. 15, no. 10, pp. 1787–1806, 1972, doi: 10.1016/0017-9310(72)90054-3.

[11] W. J. Kolb, "James E. Pacheco Steven K. Showalter".

SYMCOMP 2025
Lisbon, 10-11 April 2025

THE OPERATIONAL SPECTRAL TAU METHOD TO APPROXIMATE SOLUTION OF FUNCTIONAL DIFFERENTIAL EQUATIONS

J. M. A. Matos[1], P. B. Vasconcelos[2*] and J. A. O. Matos[2]

1: CMUP - Centro Matemática da Universidade Porto
Instituto Superior de Engenharia do Porto
Instituto Politécnico do Porto
e-mail: jma@isep.ipp.pt, web: https://cmup.fc.up.pt/tautoolbox/

2: CMUP - Centro Matemática da Universidade Porto
School of Economics and Management
University of Porto
e-mail: {jamatos,pjv}@fep.up.pt, web: https://cmup.fc.up.pt/tautoolbox/

Keywords: Functional Differential Equations, Tau Toolbox

Abstract. *In this study, we present a step-by-step operational implementation of the Tau method to approximate solutions for functional differential equations. These equations include, but are not limited to, delay differential equations, pantograph delay differential equations, and forward-backward differential equations. The Tau method, a spectral technique, is well-suited for obtaining highly accurate approximate solutions across a wide range of differential problems. One of its key advantages is its versatility in addressing both initial value and boundary value problems, which is crucial for solving the targeted problems. This methodology is added to the* `Tau Toolbox` *a software package specially designed for solving differential equations using the Lanczos' Tau method. By leveraging the* `Tau Toolbox`*, we achieve efficient solutions that not only compare favorably with other methods documented in the literature but also offer an intuitive interface.*

SYMCOMP 2025
Lisbon, 10-11 April 2025

DOING FRACTIONAL CALCULUS IN THE TAU TOOLBOX

J. A. O. Matos[1*], P. B. Vasconcelos[1] and J. M. A. Matos[2]

1: CMUP - Centro Matemática da Universidade Porto
School of Economics and Management
University of Porto
e-mail: {jamatos,pjv}@fep.up.pt, web: https://cmup.fc.up.pt/tautoolbox/

2: CMUP - Centro Matemática da Universidade Porto
Instituto Superior de Engenharia do Porto
Instituto Politécnico do Porto
e-mail: jma@isep.ipp.pt, web: https://cmup.fc.up.pt/tautoolbox/

Keywords: Fractional Calculus, Fractional Differential Equations, Tau Toolbox

Abstract. *Fractional calculus has garnered significant attention for its ability to model complex systems with memory and hereditary properties. However, practical applications remain limited due to the lack of efficient and automated computational tools to perform these computations. This paper presents a numerical approach for fractional calculations, utilizing orthogonal polynomials within the* `Tau Toolbox`*. The* `Tau Toolbox` *is a versatile software package designed for solving integro-differential equations using the Lanczos' Tau method, and it is available for both* `MATLAB/Octave` *and* `Python`*. The library supports a variety of orthogonal polynomial families, including Chebyshev (first to fourth order), Legendre, Gegenbauer, Jacobi, Laguerre, Hermite, and Bessel polynomials, allowing flexibility in solving different classes of integro-differential problems.*
We also explore the spectral Tau method to approximate solutions of fractional differential equations, which are then solved using advanced matrix computations.
We provide a comprehensive analysis of the method's accuracy and efficiency through various test cases, illustrating its performance compared with existing approximation methods.

STATISTICAL ANALYSIS AND QUANTIFICATION OF ASCENDING THORACIC AORTIC ANEURYSMS DYNAMICS

Rodrigo Valente[1]*, André Mourato[1], Alda Carvalho[2,3], Moisés Brito[1], José Xavier[1], Stéphane Avril[4], António Tomás[5], José Fragata[5,6]

1: UNIDEMI, NOVA School of Science and Technology, Lisbon, Portugal
e-mail: {rb.valente, af.mourato}@campus.fct.unl.pt; {moisesbrito, jmc.xavier}@fct.unl.pt
2: DCeT, Universidade Aberta, Lisbon, Portugal
e-mail: alda.carvalho@uab.pt
3: CEMAPRE/ISEG Research, Universidade de Lisboa, Lisbon, Portugal
4: École des Mines de Saint-Étienne, University of Lyon, Inserm, Sainbiose U1059, France
e-mail: avril@emse.fr
5: Department of Cardiothoracic Surgery, Santa Marta Hospital, Lisbon, Portugal
e-mail: {acruztomas, jigfragata}@gmail.com
6: Department of Surgery and Human Morphology, NOVA Medical School, Lisbon, Portugal

Keywords: Principal Component Analysis (PCA), Clustering Analysis, Ascending Thoracic Aortic Aneurysm (ATAA), Wall Motion Quantification

Abstract *Understanding the biomechanical behaviour of Ascending Thoracic Aortic Aneurysms (ATAA) is vital for improving clinical outcomes and predictions. Despite significant advancements in this regard computational models, the role of patient-specific wall and aortic root dynamics remains underexplored. This study employs Principal Component Analysis (PCA) and clustering techniques to quantify and categorise motion patterns in 87 ATAA patients using gated CT angiography. By segmenting and tracking deformation across 21 cardiac phases with automated Python-based tools, we identified motion characteristics. PCA was applied to analyse key parameters associated with deformation and clinical patient characteristics, with subsequent components capturing localized variations and asymmetries. Clustering analysis was then used to categorize patients into distinct motion-based subgroups, revealing biomechanical differences that could influence disease progression and surgical planning. Notably, significant aortic root motion was detected, challenging traditional static boundary conditions in computational fluid dynamics (CFD) and Fluid-Structure Interaction (FSI) models. These findings underscore the necessity of incorporating patient-specific motion data into simulations to enhance risk stratification and optimise treatment strategies. By bridging the gap between computational modelling and clinical application, this research provides a refined methodology for assessing ATAA biomechanics and advancing precision medicine in vascular surgery.*

Acknowledgements *The authors acknowledge the Portuguese Fundação para a Ciência e a Tecnologia (FCT - MCTES) for its financial support via the project AneurysmTool (doi: 10.54499/PTDC/EMD-EMD/1230/2021). A. Mourato and R. Valente are also grateful to FCT for the PhD grants UI/BD/151212/2021 and 2022.12223.BD, respectively.*

SYMCOMP 2025
Lisbon, 10-11 April 2025

ADVANCED IMAGING OF PARKINSON'S: EVALUATING THE STRIATUM AND SUBSTANTIA NIGRA WITH T2W MRI AND DATSCAN SPECT

Luís Mesquita[1], Maria Margarida Ribeiro[1] and Lina Vieira L[1,2,3]

[1] Escola Superior de Tecnologia da Saúde, Instituto Politécnico de Lisboa. Av. D. João II, lote 4.69.01, Parque das Nações, 1990-096 Lisboa, Portugal
[2] CIMOSM, ISEL – Grupo de Investigação em Modelação e Otimização de Sistemas Multifuncionais, Rua Conselheiro Emídio Navarro, 1, 1959-007 Lisboa, Portugal.
[3] H&TRC, Health & Technology Research Center, Escola Superior de Tecnologia da Saúde de Lisboa, Instituto Politécnico de Lisboa, Av. D. João II, lote 4.69.01, Parque das Nações, 1990-096 Lisboa, Portugal

e-mails: {luispmesquita@outlook.com; margarida.ribeiro@estesl.ipl.pt; lina.vieira@estesl.ipl.pt}

Keywords: Parkinson's Disease, T2W MRI, DaTSCAN SPECT, Striatum, Substantia Nigra.

Parkinson's disease (PD) is a progressive neurodegenerative disorder characterized by the degeneration of dopaminergic neurons in the pars compacta of the substantia nigra, whose projections reach the striatum. Single Photon Emission Computed Tomography (SPECT) and Magnetic Resonance Imaging (MRI) are widely used for the evaluation of PD, providing complementary information on molecular and morphological alterations, respectively.
This study aimed to compare segmentation methods applied to DaTSCAN SPECT and T2-weighted MRI (T2W MRI) images in differentiating healthy controls (HC) from PD patients, and to investigate the relationship between striatal dopaminergic loss and structural alterations in the substantia nigra.
A total of 173 volumetric brain images were analyzed, including 91 DaTSCAN SPECT (49 HC and 42 from PD patients) and 82 T2W MRI (40 HC and 42 PD). Data were obtained from the Parkinson's Progression Markers Initiative (PPMI) database (www.ppmi-info.org/data).
DaTSCAN SPECT images were segmented using four methods: Manual, ThreeBox, Threshold, and Atlas. For T2W MRI images, the intensity and volume of the substantia nigra (SN), as well as the integrity and presence of nigrosome-1, were evaluated. The Binding Potential Index (BPI) was calculated for all segmentation methods applied to SPECT images. The correlation between dopaminergic loss in the striatum and SN was determined using Spearman's correlation coefficient.
The ThreeBox method showed the best performance in distinguishing between HC and PD, while the Threshold method had the lowest discrimination power. BPI analysis revealed a progressive and linear trend of dopaminergic loss in the striatum. For T2W MRI segmentations, the separation between HC and PD based on SN intensity and volume was weak. Correlations between SN intensity and volume with BPI were weak and negative, indicating no significant association between these variables.

DOI:10.5281/zenodo.15164512

1. INTRODUCTION

Parkinson's disease (PD) is a progressive neurodegenerative disorder characterized by the selective loss of dopaminergic neurons, primarily located in the pars compacta of the substantia nigra (SNc). This neuronal loss leads to the degeneration of axons projecting from this region to the basal ganglia, particularly the striatum (1,2). This projection is known as the nigrostriatal dopaminergic pathway, and its impairment results in decreased dopaminergic neurotransmission. This pathophysiological alteration underlies the characteristic neurological symptoms, such as resting tremors, muscular rigidity, bradykinesia, and postural instability (1–3).

The early detection and diagnosis of PD are among the greatest challenges faced by the medical and scientific communities. The variability in clinical presentation, the absence of symptoms in preclinical stages, and the rate of disease progression make early diagnosis of PD challenging (4). These challenges are highlighted by the high percentages of dopamine activity reduction or neurodegeneration observed in certain structures when the first diagnostic tests are performed. Generally, before the onset of the first symptoms, there is a presynaptic dopaminergic neuronal loss of 60 to 80%, detected in Single-Photon Emission Computed Tomography (SPECT) scans (5). Furthermore, as the disease progresses, uptake levels may decrease by up to 90% (6,7).

In the 1990s, with the development of radiopharmaceuticals (such as 123I-FP-CIT, or DaTSCAN, and Technetium-99m TRODAT-1) with affinity for the dopamine transporter (DAT), new molecular imaging methods emerged with relevance for PD (8,9). SPECT studies gained great importance, as they allow for the *in vivo* assessment of DAT concentration and can distinguish PD patients from healthy individuals, with sensitivity and specificity above 90% (10).

The images obtained through SPECT are subject to different quantification methodologies, with no widespread consensus in the scientific community on which should be preferred (11,12). On one hand, some studies present manual segmentation methodologies, but these have limitations in reproducibility, time consumption, and intra- and inter-observer variability (13). On the other hand, semi-automatic and automatic methodologies have been developed, with particular emphasis on the ThreeBox and TwoBox methods (14,15), as well as the application of Artificial Intelligence (AI) classifiers (16–18).

Magnetic Resonance Imaging (MRI) is also typically used in PD to assess brain structures and establish a differential diagnosis with other neurodegenerative diseases. This assessment is possible due to the presence of neuromelanin (NM) in various brain regions, particularly in the substantia nigra (SN). NM has paramagnetic properties and easily binds to metals such as iron, which increases tissue transverse relaxation rates. This phenomenon benefits PD studies using MRI, as it results in a hypersignal in the SN region (19–21). Thus, morphological measurements and signal quantification in the SN region via MRI could serve as essential diagnostic biomarkers for detecting neurodegenerative diseases such as PD.

NM is a dark pigment produced in the cytosol of catecholaminergic neurons through the oxidation of excess dopamine into quinones and is stored in NM autophagic lysosomes, where it binds to metals such as copper, zinc, and iron (22). In healthy individuals and at normal concentrations, NM has neuroprotective functions by removing toxic substances from the cytosol and preventing neurotoxicity. However, beyond certain concentrations and due to neurodegeneration, NM is released, carrying metals and organic chemicals that have accumulated over the years. This release into the intracellular space triggers microglial activation, producing pro-inflammatory and reactive molecules that respond to foreign bodies, leading to further neuronal death and NM release. This creates a vicious cycle that disrupts normal neuronal function and contributes to neurodegenerative diseases such as PD (22,23).

Several studies have explored this topic, involving different brain structures, segmentation techniques, and MRI weightings, leading to discrepancies between manual and automatic segmentations (21, 22–28). However, no single MRI weighting has been identified as the best for studying PD, rather, a combination of different weightings can provide complementary information on the structural, functional, and metabolic changes occurring in the brains of patients with this condition. The choice of the most suitable weighting depends on the study's objective, resource availability, and data quality (21).

Both SPECT and MRI are techniques that can assist in PD diagnosis, and to date, few studies have investigated both techniques together (29,30). The combined study of these two techniques is recent and requires further research (21,29).

1.1. OBJECTIVES

This study aimed to compare segmentation methods applied to DaTSCAN SPECT and T2-weighted MRI images in differentiating healthy controls (HC) from PD patients, and to investigate the relationship between striatal dopaminergic loss and structural alterations in the substantia nigra.

2. METHODOLOGY

The images used in this work were obtained from the PPMI database, an international, multicentre, and longitudinal study that gathers data from various clinical centers around the world, including the United States, Europe, Israel, and Australia (31).

This database represents a milestone in the clinical study of Parkinson’s disease progression and aims to enhance the understanding of the disease and drive research toward improving Parkinson’s disease treatment and tailoring it to each patient.

2.1. Sample

The selected sample consists of images from two groups: patients with PD and HC. In SPECT, 49 images of HC and 42 images of patients with PD were selected. In MRI, 40 images of HC and 42 images of patients with PD were chosen, with these being the same patients who have SPECT images. The HC in SPECT and MRI are different, meaning that the 49 HC with SPECT images are different from the 40 HC with MRI images, as it was not possible to find the same HC with both techniques in the database. The HC dataset is characterized by subjects aged 30 or over, without first degree family history of PD. The MRI images are T2w weighted. The software used for this study was 3D Slicer (version 5.2.2).

2.2. DaTSCAN SPECT Segmentation

The DaTSCAN SPECT segmentation was studied by four different segmentation methodologies: Manual Segmentation, ThreeBox, Threshold and Anatomic Atlas.

2.2.1. Manual Segmentation

The manual segmentation aims to replicate the practices performed in a clinical environment. Thus, a fully manual segmentation was carried out, targeting the high-intensity regions in the striatum. A reference region was evaluated by segmenting a ROI in the parieto-occipital parenchyma. In this methodology, only the most intense regions in the striatum were segmented to attempt to exclude Partial Volume Effects (PVEs). The parieto-occipital region naturally presents some variability between segmentations due to being a manual methodology, however, its segmentation was limited to the same brain region and only the two axial slices showing the highest DaTSCAN uptake were segmented (32).

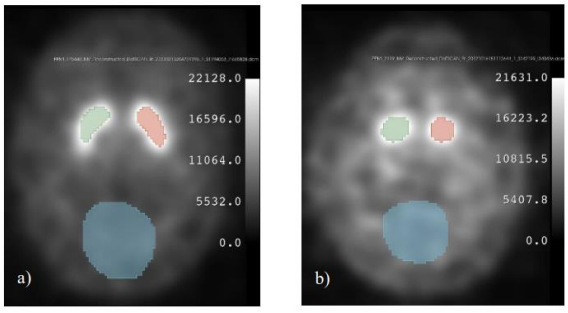

Figure 1 -Manual segmentation on axial slices of a DaTSCAN SPECT image of a HC (a) and a DP patient (b). Left side of striatum (green ROI), right side (blue ROI) and reference region (blue ROI).

2.2.2. ThreeBox

Three fixed ROIs were defined to identify the left and right striatum, as well as the parieto-occipital parenchyma region. Using an image of a HC, ROIs similar to those described in Oliveira et al. (2014) were applied. The reference ROI was modified, extending a few millimeters to extract more background noise information. The striatal ROIs were also slightly adjusted. Their dimensions are 40×60 mm², while the reference ROI measures 82×36 mm². To enable a more precise comparison with the manual methodology, the ThreeBox method segmented only the two slices with the highest DaTSCAN uptake (14).

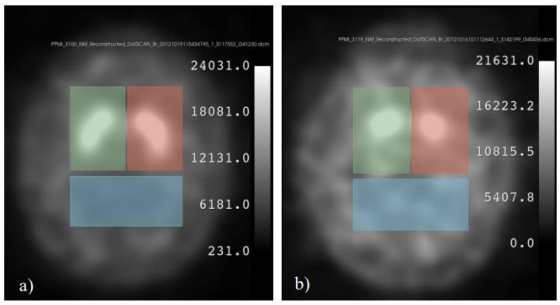

Figure 2 - ThreeBox segmentation on axial slices of a DaTSCAN SPECT image of a HC (a) and a DP patient (b). Left side of striatum (green ROI), right side (blue ROI) and reference region

2.2.3. Threshold

The thresholding methodology defines a value above which pixels with equal or higher intensity are segmented. Since the images are normalized, the threshold value was fixed at 50% of the maximum intensity. A visual analysis confirmed that the 50% threshold correctly segments the striatal regions. The reference region was also segmented using a thresholding approach, but with two values: 10% and 30%, where all pixels within this range were included in the segmentation (14, 15).

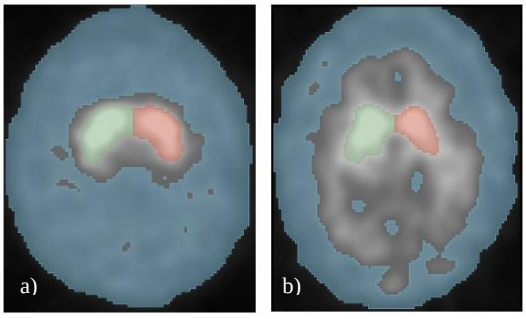

Figure 3 - Threshold segmentation on axial slices of a DaTSCAN SPECT image of a HC (a) and a DP patient (b). Left side of striatum (green ROI), right side (blue ROI) and reference region (blue ROI).

2.2.4. Anatomic Atlas

The final segmentation methodology for SPECT images utilizes an anatomical atlas of the putamen, globus pallidus, and caudate nucleus, based on a template provided by the Montreal Neurological Institute (MNI) ICBM 2009a Nonlinear Symmetric. This atlas offers excellent resolution and detail for T1, T2, proton density, and T2* images (33).

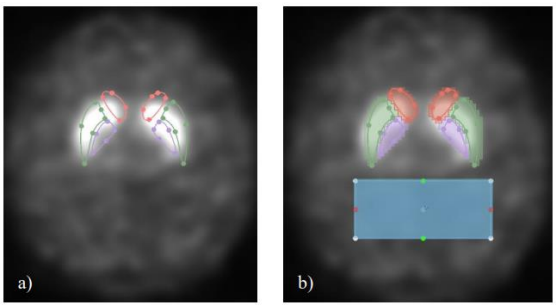

Figure 4 - Anotomic Atlas in a SPECT DaTSCAN image. (a) MNI template and (b) adjustment and extrapolation of MNI template.

In this approach, the T1 atlas was used for ROI placement due to its superior structural definition. However, the ROIs were mapped onto different atlas versions, ensuring precise anatomical correspondence across all imaging weightings. The obtained ROIs were applied to a healthy volunteer, revealing that part of the radiopharmaceutical uptake was excluded in the region between the caudate nucleus, putamen, and globus pallidus, as shown in Figure 4 (a). To address this issue, the originally defined ROIs were extrapolated to fully incorporate the radiopharmaceutical uptake (Figure 4 (b)). The reference region was defined similarly to the ThreeBox methodology. As with that approach, only the two axial slices with the highest radiopharmaceutical uptake were considered.

2.3. MRI T2 Segmentation

The segmentation methodology applied to MRI images was performed through manual segmentation, assessing the SN, nigrosome-1, and the presence of the swallow-tail sign**.** The SN is a structure that cannot be precisely identified in T2-weighted MRI (T2W MRI) images. Its subregions, the SNr (substantia nigra pars reticulata) and SNc, lack sufficient contrast and intensity for confident segmentation. The SNr can be difficult to distinguish from the cerebral peduncle. The SNc appears as a hyperintense region in T2W MRI but, like the SNr, its boundaries are complex to delineate. In this study, the SN region was segmented based on its anatomical location, encompassing both the SNr and SNc. Nigrosome-1 is characterized as a hyperintense region, though its anatomical position may vary. It is typically found in the dorsolateral and caudal region of the SN, which was the targeted area in this study. The swallow-tail sign is intrinsically linked to nigrosome-1. If nigrosome-1 is not visible, the swallow-tail sign cannot be identified.

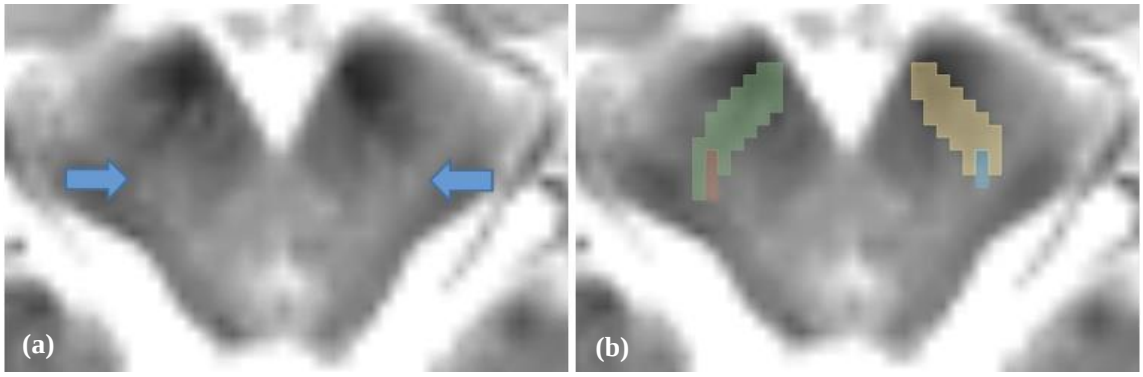

Figure 6 - HC subject where nigrossomes-1 are visible (a) and the segmentation of the SN and nigrossomes-1 (b) on the axial plane of a MRI T2w image.

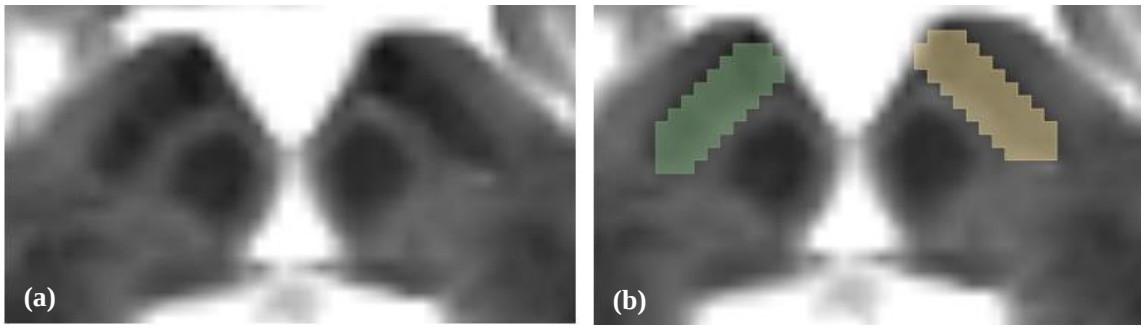

Figure 5 - PD patient without visible nigrossomes-1 (a) and the segmentation of SN (b) on the axial plane of a MRI T2w image.

The segmentation of MRI images involved importing the original images into the 3D Slicer software, normalizing pixel intensity, identifying the axial section of the midbrain with the best structural definition, and finally performing the segmentation. Pixel intensity normalization is a crucial step in medical image processing, as these images are compared with each other, and intensity is a significant variable. To achieve this, the images were normalized between values of 0 and 255, where 0 is the lower limit and 255 is the upper limit, using a 98th percentile upper threshold. This approach provided better contrast between midbrain structures.

In this study, only one axial section of the midbrain was segmented. Precisely identifying the SN is complex, and segmenting a single section helps reduce variability between segmentations. Nigrosome-1 has low contrast, making its volumetric segmentation challenging. The selection of the best axial section for segmentation was based on the following criteria: presence of nigrosome-1 and identification of the section with its largest area. If nigrosome-1 was not visible, the selection focused on identifying the section where the hypointense region characteristic of the SNr and cerebral peduncle was most evident. Identifying the intermediate section of the red nuclei also assisted in segmentation, as its axial plane aligns with the SN.

2.4. Statistical Analysis

The statistical analysis was performed using Microsoft Excel 2016. The characterization of the results involved calculating the following variables:

- The contralateral mean of the Binding Potential Index (BPI) from SPECT images, signal intensity, and SN volume from MRI images for the HC group and patients with PD (including the standard deviation);
- Also, in SPECT, the percentage variation of the variables from the previous point between the HC group and patients with PD, using the following equation:

$$\%\, BPI\ Variation = \frac{\overline{BPI}_{HC} - \overline{BPI}_{PD}}{\overline{BPI}_{HC}} * 100$$

- Calculation of the mean intensity and volume of the striatum and nigrossomes-1, and the presence, unilateral or bilateral, of the swallow-tail.
- Calculation of the Spearman correlation coefficient and the corresponding p-value for the relationship between SN volume and BPI, as well as for the relationship between SN intensity and BPI.

3. RESULTS AND DISCUSSION OF RESULTS

The studied sample comprised HC and PD patients, evaluated through DaTSCAN SPECT and T2W MRI. For the DaTSCAN SPECT analysis, the HC group included 49 subjects with a mean age of 66.9 ± 8.3 years, consisting of 25 males and 24 females. The PD group for DaTSCAN SPECT consisted of 42 subjects, with a mean age of 60.2 ± 8.7 years, comprising 26 males and 16 females. Regarding the T2W MRI analysis, the HC group included 40 subjects with a mean age of 61.7 ± 9.5 years, of which 23 were males and 17 were females. The PD group included 42 subjects, with a mean age of 61.4 ± 8.7 years, comprising 26 males and 16 females.

Table 1 - Characterization of the studied sample.

Group	Exam	Subjects	Mean Age (±σ)	Genre (M/F)
HC	DaTSCAN SPECT	49	66.9 ± 8.3	25/24
	MRI	40	61.7 ± 9.5	23/17
PD	DaTSCAN SPECT	42	60.2 ± 8.7	26/16
	MRI	42	61.4 ± 8.7	26/16

HC-Health Controls; PD- Parkinson's Disease

3.1. DaTSCAN SPECT

Manual Segmentation

The BPI mean achieved using the manual segmentation was 2.768 (± 0.480) for the HC group and 1.727 (± 0.409) for PD patients. The % BPI variation is, there for 37.608%. This shows that this methodology is promising, however, the standard deviation is expressive and could lead to false positives. In other studies (9), it is was achieved 2.24 and 0.90 for BPI measures on HC and DP patients, respectively. Nevertheless, this methodology is intrinsically vulnerable to the observer on the positioning of ROIs and implies variations on BPI measurements.

ThreeBox Segmentation

The BPI mean achieved using the ThreeBox segmentation was 1.028 (± 0.222) for the HC group and 0.509 (± 0.133) for PD patients. Accordingly, the percentage variation in BPI between the groups was 50.49%. These results are consistent with findings from previous studies (14). Moreover, this methodology demonstrated superior performance in distinguishing between HC and PD patients.

Threshold Segmentation

The BPI mean achieved using the Threshold segmentation was 2.561 (± 0.256) for the HC group and 2.129 (± 0.269) for PD patients. The % BPI variation is, there for, 16.868%. This result shows a very close BPI measure. One explanation is due to the fact that threshold values are fixed and pre-defined for every normalized image.

Anatomic Atlas Segmentation

The BPI mean achieved using the Anatomic Atlas segmentation of the putamen was 1.951 (± 0.512) for the HC group and 0.774 (± 0.270) for PD patients. The % BPI variation is 60.331%. For the globus pallidus, the BPI mean calculate was 1.758 (± 0.455) for the HC group and 0.941 (± 0.314) for PD patients. The % BPI variation is, for the globus pallidus, 46.490%. For the caudate nucleus, the BPI mean calculate was 1.591 (± 0.397) for the HC group and 1.020 (± 0.285) for PD patients. The % BPI variation is, for the caudate nucleus, 35.895%. These results shows that the putamen has more evidence of dopaminergic neurodegeneration in the striatum.

Evolution of PD with ThreeBox segmentation

The ThreeBox segmentation achieved the better results in the distinction from HC and DP patients. Therefore, this methodology was used to study the evolution of the disease, being the follow-up visits baseline, 12 months and 24 months.

At the baseline, the BPI mean was 0.509 (± 0.133). At the 12 months assessment it was 0.458

(± 0.124) and 0.420 (± 0.135) at the 24 months mark. The percentage deviation of BPI relative to the baseline is 9.969% for the 12 months mark, and 17.389% for the 24 months mark. These results indicate that PD neurodegeneration is progressive and linear.

3.2. T2W MRI

The T2W MRI segmentations intended to study the intensity and volume of the striatum and nigrossomes-1, and the presence, unilateral or bilateral, of the swallow-tail.

The mean intensity of the striatum was 79.513 (± 12.325) and 72.047 (± 11.891), and the mean volume was 43.000 (± 6.823) and 42.821 (± 8.111) for HC and PD patients, respectively. These results are poor for the discrimination of HC and PD patients. The means are very similar and have an expressive standard deviation.

The unilateral and bilateral presence of nigrosomes-1 was accounted for. In the HC group, there were 8 images with unilateral presence, 32 images with bilateral presence, and 1 image where nigrosomes-1 could not be identified. In the group of patients with PD, 12 images with unilateral presence, 11 images with bilateral presence, and 19 images where no nigrosome-1 could be visualized.

3.3. DaTSCAN SPECT and T2W MRI

The results obtained with the SPECT and T2W MRI images were correlated using Spearman's correlation. The variables used were the mean intensity of the striatum with BPI, and the volume of the striatum with BPI. The calculated results indicate that there is a weak correlation between volume or intensity and BPI. The p-value is greater than 0.05 for all correlations, indicating a non-significant difference.

Table 1 - Spearman's correlation between the volume of the striatum and BPI, and the intensity of the striatum and BPI.

	Volume - BPI		**Intensity - BPI**	
	Left	Right	Left	Right
(coefficient)	-0.084	-0.059	-0.018	-0.134
P (p-value)	>0.05	>0.05	>0.05	>0.05

For this correlation, it was used the BPI calculations for the ThreeBox methodology, given that it presented better discrimination results between HC and PD patients. The segmentation relative to the intensity and volume of SN presented higher oscillation and lower distinction between the two groups, which, in part, explains the weak correlation between T2W MRI and DaTSCAN SPECT.

There weren't found studies in the literature that correlate DaTSCAN SPECT and T2W MRI. However, other more advanced MRI techniques such as NM contrast (30) or T2* (19) are more frequently studied and demonstrate better correlation results between loss of dopaminergic functions in the striatum.

The absence of studies between the two mentioned techniques can be explained by the limitations inherent in evaluating the SN in T2W MRI. The boundaries of the SN in T2W MRI are hardly visible and very complex to identify. As observed through various segmentations, there is no obvious separation between the SN and the cerebral peduncle, and between the SNr and the SNc, which corroborates other articles (34, 35). This limitation is a crucial factor in SN evaluation, as it prevents an accurate segmentation of its region. These limitations result in greater variability of outcomes, which may explain the weak correlation of the indicators, as well as the fluctuation of values in the intensity and volume of the SN, mentioned in the previous subsection.

This study allows to conclude that T2W MRI isn't an ideal tool for evaluating PD. On the other hand, more advanced MRI techniques, including diffusion imaging (36), SWI weighting (37), magnetization transfer contrast (MTC) (35), and MRI with high magnetic fields (38), show potential as quantitative biomarkers for PD.

4. CONCLUSION

The methodologies developed in this study successfully addressed the proposed objectives. The ThreeBox segmentation method proved to be a robust and effective approach for distinguishing between HC and PD patients, demonstrating a high degree of separation in the BPI values. Among the tested methods, it was considered the most appropriate for evaluating DaTSCAN uptake in SPECT images due to its strong discriminative power, reduced intra-variability (owing to the use of fixed ROIs), and its ability to minimize PVEs.

Manual segmentation also produced discriminatory results. However, it's limited by its time-consuming nature. The anatomical atlas-based segmentation confirmed that dopaminergic degeneration in PD is more pronounced in the putamen compared to the caudate nucleus. Despite a higher degree of variability, this method can still contribute to the identification of PD and allows for structure-specific analysis of the basal ganglia.

The threshold-based segmentation, when used in isolation, was not sufficient to differentiate between groups. Nonetheless, it may serve as a preliminary step within more complex segmentation protocols.

The longitudinal analysis using the ThreeBox methodology across baseline, 12-month, and 24-month acquisition periods revealed a progressive and linear decline in striatal dopaminergic activity, reinforcing the potential of this method for monitoring disease progression. Further studies are recommended to explore its application in correlating imaging findings with clinical stages of PD.

The utility of SPECT in assessing dopaminergic function is well established in clinical practice, with a substantial body of literature developed over the past three decades. Although recent advances in MRI have improved its diagnostic potential, in this study, T2W MRI did not prove to be the most suitable technique for evaluating the SN or nigrosome-1 in PD. While minor differences between HC and PD groups were observed, they were minimal.

Finally, the correlation between SN intensity and volume with BPI values was weak, negative, and statistically non-significant, indicating no relevant association. This result may be attributed to the high variability observed in the MRI measurements.

ACKNOWLEDGE

This work is partially financed by national funds through FCT/MCTES national support through the UIDP/05608/2020. DOI 10.54499/UIDP/05608/2020 (https://doi.org/10.54499/UIDP/05608/2020), UIDB/05608/2020. DOI 10.54499/UIDB/05608/2020 (https://doi.org/10.54499/UIDB/05608/2020) and IPL/ IDI&CA2023/I2P2_MPS_ESTeSL.

REFERENCES

[1] Erkkinen MG, Kim M, Geschwind MD. Clinical Neurology and Epidemiology of the Major Neurodegenerative Diseases. Cold Spring Harb Perspect Biol. 2018;

[2] Dickson DW. Neuropathology of Parkinson disease. Park Relat Disord. 2018;46(Suppl 1):S30–3.

[3] Postuma RB, Berg D, Stern M, Poewe W, Olanow CW, Oertel W, et al. MDS clinical diagnostic criteria for Parkinson's disease. Mov Disord. 2015;30(12):1591–601.

[4] Tatsch K, Poepperl G. Nigrostriatal dopamine terminal imaging with dopamine transporter SPECT: An update. J Nucl Med. 2013;54(8):1331–8.

[5] Miller DB, Callaghan JPO. Biomarkers of PD - Present and Future. Metabolism [Internet]. 2014;64(3):S40–6. Available from: http://dx.doi.org/10.1016/j.metabol.2014.10.030

[6] Ming CS, Amaro E, Ferraz HB, Hoexter MQ, Goulart FO, Wagner J, et al. Neuroimaging of the dopamine transporter in Parkinson's disease: First study using [99mTc]-TRODAT-1 and SPECT in Brazil. Arq Neuropsiquiatr. 2006;64(3 A):628–34.

[7] Patel A, Simon S, M Elangoven I, Amalchandran J, S Jain A, S T. Dopamine Transporter maging with Tc-99m TRODAT-1 SPECT in Parkinson's isease and its orrelation with linical isease everity. Asia Ocean J Nucl Med Biol [Internet]. 2019;7(1):22–8. Available from: http://www.ncbi.nlm.nih.gov/pubmed/30705908%0Ahttp://www.pubmedcentral.nih.gov/article render.fcgi?artid=PMC6352051

[8] Costa DC, Verhoeff NPLG, Cullum ID, Ell PJ, Syed GM., Barret J, et al. In vivo characterisation of 3-iodo-6-methoxybenzamide 123I in humans. Eur J Nucl Med. 1990;16:813–6.

[9] Booij J, Hemelaar JTGM, Speelman JD, De Bruin K, Janssen AGM, Van Royen EA. One-day protocol for imaging of the nigrostriatal dopaminergic pathway in Parkinson's disease by [123I]FPCIT SPECT. J Nucl Med. 1999;40(5):753–61.

[10] Brigo F, Matinella A, Erro R, Tinazzi M. [123I]FP-CIT SPECT (DaTSCAN) may be a useful tool to differentiate between Parkinson's disease and vascular or drug-induced parkinsonisms:

A meta-analysis. Eur J Neurol. 2014;21(11):1369-e90.
[11] Vieira L, Costa DC, Almeida P. The influence of number of counts in the myocardium in the determination of reproducible functional parameters in gated-SPECT studies simulated with GATE. Rev Esp Med Nucl Imagen Mol. 2015;36(6):339-440.
[12] Chilra P, Gnesin S, Allenbach G, Monteiro M, Prior JO, Vieira L, Pires Jorge JA. Cardiac PET/CT with Rb-82: optimization of image acquisition and reconstruction parameter**s.**EJNMMI Physics. 2017, 4(1):10
[13] Verhoeff NPLG, Kapucu O, Sokole-Busemann E, Van Royen EA, Janssen AGM. Estimation of dopamine D2 receptor binding potential in the striatum with iodine-123-IBZM SPECT: Technical and interobserver variability. J Nucl Med. 1993;34(12):2076–84.
[14] Oliveira FPM, Borges Faria D, Campos Costa D, Tavares JMRS. A robust computational solution for automated quantification of a specific binding ratio based on [123I]FP-CIT SPECT 59 images. Q J Nucl Med Mol Imaging. 2014;58(1):74–84.
[15] Alexandre-Santos L, Trevisan AC, Pitella FA, Tumas V, Silvah JH, Kato M, et al. Assessment of different regions of interest-based methods for [99mTc]Tc DAT-SPECT quantification using an anthropomorphic striatal phantom. EJNMMI Phys [Internet]. 2022;9(1). Available from: https://doi.org/10.1186/s40658-022-00519-2
[16] Augimeri A, Cherubini A, Cascini GL, Galea D, Caligiuri ME, Barbagallo G, et al. CADA—computer-aided DaTSCAN analysis. EJNMMI Phys [Internet]. 2016;3(1). Available from: http://dx.doi.org/10.1186/s40658-016-0140-9
[17] Natacha V. Avaliação do potencial de técnicas de machine learning no diagnóstico diferencial da doença de Parkinson com base em imagem molecular. Institupo Superior de Engenharia de Lisboa, Escola Superior de Tecnologia da Saúde de Lisboa; 2022.
[18] Gaurav R, Valabrègue R, Yahia-Chérif L, Mangone G, Narayanan S, Arnulf I, et al. NigraNet: An automatic framework to assess nigral neuromelanin content in early Parkinson's disease using convolutional neural network. NeuroImage Clin. 2022;36(October).
[19] Depierreux F, Parmentier E, Mackels L, Baquero K, Degueldre C, Balteau E, et al. Parkinson's disease multimodal imaging: F-DOPA PET, neuromelanin-sensitive and quantitative ironsensitive MRI. npj Park Dis [Internet]. 2021;7(1):1–10. Available from: http://dx.doi.org/10.1038/s41531-021-00199-2
[20] Sasaki M, Shibata E, Tohyama K, Takahashi J, Otsuka K, Tsuchiya K, et al. Neuromelanin magnetic resonance imaging of locus ceruleus and substantia nigra in Parkinson's disease. Neuroreport. 2006;17(11):1215–8.
[21] Martin-Bastida A, Pietracupa S, Piccini P. Neuromelanin in parkinsonian disorders: an update. Int J Neurosci [Internet]. 2017;127(12):1116–23. Available from: http://dx.doi.org/10.1080/00207454.2017.1325883
[22] Zucca FA, Vanna R, Cupaioli FA, Bellei C, De Palma A, Di Silvestre D, et al. Neuromelanin organelles are specialized autolysosomes that accumulate undegraded proteins and lipids in aging human brain and are likely involved in Parkinson's disease. npj Park Dis [Internet]. 2018;4(1). Available from: http://dx.doi.org/10.1038/s41531-018-0050-8
[23] Carballo-Carbajal I, Laguna A, Romero-Giménez J, Cuadros T, Bové J, Martinez-Vicente M, et al. Brain tyrosinase overexpression implicates age-dependent neuromelanin production in Parkinson's disease pathogenesis. Nat Commun [Internet]. 2019;10(1). Available from: http://dx.doi.org/10.1038/s41467-019-08858-y
[24] Blazejewska AI, Schwarz ST, Pitiot A, Stephenson MC, Lowe J, Bajaj N, et al. Visualization of nigrosome 1 and its loss in PD: Pathoanatomical correlation and in vivo 7T MRI. Am Acad 60 Neurol. 2013;81:534–40.
[25] Castellanos G, Fernández-Seara MA, Lorenzo-Betancor O, Ortega-Cubero S, Puigvert M,

Uranga J, et al. Automated Neuromelanin Imaging as a Diagnostic Biomarker for Parkinson's Disease. Mov Disord. 2015;30(7):945–52.
[26] Garg A, Appel-Cresswell S, Popuri K, McKeown MJ, Beg MF. Morphological alterations in the caudate, putamen, pallidum, and thalamus in Parkinson's disease. Front Neurosci. 2015;9(MAR):1–14.
[27] Miller CPK, Muller J, Noecker AM, Matias C, Alizadeh M, McIntyre C, et al. Automatic Segmentation of Parkinson Disease Therapeutic Targets Using Nonlinear Registration and Clinical MR Imaging: Comparison of Methodology, Presence of Disease, and Quality Control. Stereoact Funct Neurosurg. 2023;101(2):146–57.
[28] Egger K, Amtage F, Yang S, Obmann M, Schwarzwald R, Köstering L, et al. T2* Relaxometry in Patients with Parkinson's Disease: Use of an Automated Atlas-based Approach. Clin Neuroradiol. 2016;28(1):63–7.
[29] Kuya K, Ogawa T, Shinohara Y, Ishibashi M, Fujii S, Mukuda N, et al. Evaluation of Parkinson's disease by neuromelanin-sensitive magnetic resonance imaging and 123I-FP-CIT SPECT. Acta radiol. 2018;59(5):593–8.
[30] Isaias IU, Trujillo P, Summers P, Marotta G, Mainardi L, Pezzoli G, et al. Neuromelanin imaging and dopaminergic loss in parkinson's disease. Front Aging Neurosci. 2016;8(AUG):1 12.
[31] PPMI. Parkinson's Progression Markers Initiative | Who We Are. [Internet]. Parkinson's Progression Markers Initiative; 2022. [cited November 2022] Available from: https://www.ppmi- info.org/about-ppmi/who-we-are/.
[32] Moon HS, Barbour D. Washington University Open Scholarship Computational Imaging Methods for Analysis of DaTScan SPECT Images. 2020;
[33] Hida K, Nonokuma M, Kuwabara Y, Tani T, Takano K, Yoshimitsu K. Creation and validation of an I-123 FP-CIT template for statistical image analysis using high-resolution SPECT for parkinsonian patients. Ann Nucl Med. 2016;30(7):477–83.
[34] Oikawa H, Sasaki M, Tamakawa Y, Ehara S, Tohyama K. The substantia nigra in Parkinson disease: Proton density-weighted spin-echo and fast short inversion time inversion-recovery MR findings. Am J Neuroradiol. 2002;23(10):1747–56.
[35] Bolding MS, Reid MA, Avsar KB, Roberts RC, Gamlin PD, Gawne TJ, et al. Magnetic transfer contrast accurately localizes substantia nigra confirmed by histology. Biol Psychiatry. 2013;73(3):289–94.
[36] Saeed U, Compagnone J, Aviv RI, Strafella AP, Black SE, Lang AE, et al. Imaging biomarkers in Parkinson's disease and Parkinsonian syndromes: Current and emerging concepts. Transl Neurodegener. 2017;6(1):1–25.
[37] Schwarz ST, Afzal M, Morgan PS, Bajaj N, Gowland PA, Auer DP. The "swallow tail" appearance of the healthy nigrosome - A new accurate test of Parkinson's disease: A case control and retrospective cross-sectional MRI study at 3T. PLoS One. 2014;9(4).
[38] Cosottini M, Frosini D, Pesaresi I, Donatelli G, Cecchi P, Costagli M, et al. Comparison of 3T and 7T susceptibility-weighted angiography of the substantia nigra in diagnosing Parkinson disease. Am J Neuroradiol. 2015;36(3):461–6.

SYMCOMP 2025
Lisbon, 10-11 April 2025

AN IMEX METHOD FOR NONLINEAR TIME-FRACTIONAL DIFFUSION EQUATIONS

M. Rebelo [1*], L. Ferrás [2], L. F. Morgado [3] and M. L. Morgado[4]

1: Mathematics Department and Center for Mathematics and Applications (NOVA Math), Nova School of Science and Technology – Portugal
e-mail: msjr@fct.unl.pt

2: Faculty of Engineering, University of Porto, Portugal
email: lferras@fe.up.pt

3: Department of Physics, UTAD and Instituto de Telecomunicações -Lisboa , Portugal
email:lmorgado@utad.pt

4: Department of Mathematics, UTAD and Center for Computational and Stochastic Mathematics, Instituto Superior Técnico, Lisbon, Portugal
email: luisam@utad.pt

Keywords: time-fractional diffusion equations, nonlinear diffusion, IMEX scheme

Abstract. *In this talk we focus on the numerical analysis of the time-fractional diffusion problem:*

$$\begin{aligned}
&\frac{\partial^\alpha u}{\partial t^\alpha}(x,t) = \mathcal{L}(u)(x,t) + f(x,t), \quad x \in \Omega,\ t > 0,\\
&u(x,0) = u_0(x), \quad x \in \Omega,\\
&u(x,t) = 0, \quad x \in \partial\Omega,
\end{aligned}$$

where

$$\mathcal{L}(u)(x,t) = \frac{\partial}{\partial x}\left(D(u)\frac{\partial u}{\partial x}(x,t)\right),$$

with $\Omega = (a,b)$, $b > a$, $\alpha \in (0,1)$, and $D : \mathbb{R} \to \mathbb{R}$ is the diffusion coefficient, which depends on u. The fractional derivative is considered in the Caputo sense. We propose a numerical method that approximates the operator $\mathcal{L}(u)(x,t)$ using a second-order finite difference scheme, while the time discretization follows an implicit-explicit (IMEX) approach. We also present numerical experiments and results to illustrate the performance of the method.

Acknowledgments: This work is financially supported by national funds throughthe FCT/MCTES (PIDDAC), under the project 2022.06672.PTDC - iMAD - Improving the Modelling of Anomalous Diffusion and Viscoelasticity: solutions to industrial problems, with DOI 10.54499/2022.06672.PTDC.

SYMCOMP 2025
Lisbon, 10-11 April 2025

SOME RESULTS ON GRAPHIC TOPOLOGY DEFINED ON TOURNAMENTS

D. Fernández-Ternero and I. Mora-Caro*

Dpto. Geometría y Topología.
Facultad de Matemáticas
Universidad de Sevilla
c/ Tarfia s/n, 41012, Seville (Spain)
e-mail: desamfer@us.es, inemorcar1@alum.us.es

Keywords: Tournament, finite space, graphic topology

Abstract. *A large number of researchers have studied the problem of topologization of combinatorial structures, for example in [3] and [4]. Within the framework of topologies defined on locally finite graphs, the graphic topology was developed in [2]and [1].*
In this work, we continue the research about the graphic topology defined on finite indecomposable tournaments (complete digraphs), begun in [1]. We deduce a characterization of indecomposable tournaments with few vertices. We verify that the minimum number of vertices such that there exist non-isomorphic indecomposable tournaments with homeomorphic graphic topologies is six. Finally, we implement algorithmic procedure in order to check if a finite tournament is indecomposable and, if so, obtain the finite space associated with it.

REFERENCES

[1] J. Dammak and R. Salem, Graphic topology on tournaments, *Adv. Pure Appl. Math.* **9**(4): 279-–285, 2018.

[2] S. M. Jafarian Amiri, A. Jafarzadeh and H. Khatibzadehan, Alexandroff topology on graphs, *Bull. Iranian Math. Soc.* **39**(4): 647-–662, 2013.

[3] D. Nogly and M. Schladt, Digital Topology on Graphs, *Comput. Vis. Image Und.*, **63**(2): 394–396, 1996.

[4] H. O. Zomam, Out-graphic topology on directed graphs, *J. Math. Comput. Sci.* **13** Article ID 14, 2023.

SYMCOMP 2025
Lisbon, 10-11 April 2025

FINITE DIFFERENCE SCHEMES FOR COUETTE FLOWS WITH GENERALISED INTEGRAL VISCOELASTIC MODELS

E. Silva[1*], M. Rebelo[2], L. L. Ferrás [3], L. F. Morgado [4] and M. L. Morgado [5]

1: Centro de Matemática e Aplicações, Universidade NOVA de Lisboa, Portugal
e-mail: ebo.silva@campus.fct.unl.pt

2: Department of Mathematics, Faculdade de Ciências e Tecnologia, Centro de Matemática e Aplicações, Universidade NOVA de Lisboa, Portugal
e-mail: msjr@fct.unl.pt

3: Faculty of Engineering, University of Porto, Portugal
e-mail: lferras@fe.up.pt

4: Department of Physics, School of Science and Tecnhology, University of Trás-os-Montes e Alto Douro, Vila Real, Portugal & Instituto de Telecomunicações-Lisboa
e-mail: lmorgado@utad.pt

5: Department of Mathematics, School of Science and Tecnhology, University of Trás-os-Montes e Alto Douro, Quinta de Prados, 5001-801 Vila Real, Portugal & Center for Computational and Stochastic Mathematics, Instituto Superior Técnico, Universidade de Lisboa
e-mail: luisam@utad.pt

Keywords: Finite difference schemes, Mittag-Leffler function, generalised Maxwell model

Abstract. *This work presents a numerical approach for solving the equations governing small deformation transient flows. We consider the generalized Maxwell model, incorporating the Mittag-Leffler function as the relaxation modulus, coupled with the Cauchy momentum equation. Our methodology effectively addresses common numerical issues associated with solving fractional viscoelastic flow equations while preserving the model's ability to fit real data accurately.*

Acknowledgments: This work is financially supported by national funds throughthe FCT/MCTES (PIDDAC), under the project 2022.06672.PTDC - iMAD - Improving the Modelling of Anomalous Diffusion and Viscoelasticity: solutions to industrial problems, with DOI 10.54499/2022.06672.PTDC.

SYMCOMP 2025
Lisbon, 10-11 April 2025

ANALYSIS THORACIC AORTIC ANEURYSM CTA SCANS USING SPATIAL STATISTIC

Katalina, Oviedo Rodríguez[1,2]*, Alda Carvalho[2,3,4], Rodrigo Valente[5], José Xavier[5] and António Tomás[6]

1: Escuela de Matemática, Facultad de Ciencias Exactas y Naturales,
Universidad Nacional, Heredia, Costa Rica,
e-mail: katalina.oviedo.rodriguez@una.ac.cr
2: DCeT, Universidade Aberta, Lisbon, Portugal,
3: CEMAPRE/ISEG Research, Universidade de Lisboa, Lisbon, Portugal,
4: CIMOSM, Instituto Politécnico de Lisboa, Lisbon, Portugal
e-mail: alda.carvalho@uab.pt
5: UNIDEMI, NOVA School of Science and Technology, Lisbon, Portugal
e-mail: rb.valente@campus.fct.unl.pt, jmc.xavier@fct.unl.pt
6: Department of Cardiothoracic Surgery, Santa Marta Hospital, Lisbon, Portugal
e-mail: acruztomas@gmail.com

Keywords: Instructions, international conference, algebraic, symbolic computation

Abstract *This study leverages spatial statistics to analyze the spatial distribution of the aorta, aiming to better understand the biomechanical behavior of Ascending Thoracic Aortic Aneurysms (ATAA) and its impact on clinical outcomes. CTA angiography was performed on 87 ATAA patients. Experimental variograms were computed for various variables, such as maximum diameter, from which key parameters of interest were extracted. These parameters were then analyzed over time to assess temporal patterns. The goal of this analysis was to identify whether similar patterns or behaviors emerge in features from CTA scans of patients with aneurysms of similar sizes, ultimately aiming to statistically validate the quality of the CTA scans.*

DOI:10.5281/zenodo.15167567

1. INTRODUCTION

The Ascending Thoracic Aortic Aneurysm (ATAA) is a degenerative process of the thoracic aorta and a severe vascular disease characterized by the progressive dilation of the thoracic aorta due to the weakening of the aortic wall. The structure and function of the aorta can be affected by factors such as age, genetic, and lifestyle factors [1][2]. Aneurysm is one of the most common diseases associated with the aorta, and its rupture is a major cause of mortality in adults over 65 years old [3].

The aneurysm size is determined based on diameter measurements, which may slightly vary depending on the imaging technology used, such as ultrasound or computed tomography angiography (CTA). According to studies, elective repair is recommended when the maximum diameter (Dmax) exceeds 55 mm or when the lesion grows more than 1 cm per year [4]. However, it has been observed that these parameters are not sufficient, as there are cases of patients with maximum diameters smaller than the indicated threshold who experience aneurysm rupture, as well as cases of patients with larger diameters who do not experience rupture [5][6].

This study presents an exploratory analysis of the characteristics of ATAAs in a sample of patients using spatial statistics. Specifically, the variogram and the parameters sill and range are used to characterize the maximum diameters of the ascending aortas obtained from CTA angiography scans.

2. METHODS

2.1. Data

The dataset used in this study consists of several variables collected from 87 patients. Each patient contains variables that vary in spatial and temporal dimensions. Spatially, the variables are measured in equally distributed rings across the centerline, and temporally, representing different instances of the cardiac cycle measured in 5% increments associated with a time step in the cine CTA. The variable selected for this analysis was the maximum diameter of the ring at the given time point in millimeters. The data allows temporal analysis to observe and measure changes in the recorded parameters. The analysis presented in this work focuses on three patients, as they represent three distinct patient groups discussed in Section 3.2.

2.2 Empirical Variogram and Model Fitting

The variogram is a tool from geostatistics that allows analyzing the spatial relationship present in the data. To define it, it is necessary to define the regionalized variable [7][8]. A regionalized variable is a random variable for each region used. It is denoted by:

$$\{Z(s): s \in D \subset R^n\}.$$

Each $Z(s)$ is a random variable. The variogram γ is defined as:

$$\gamma(h) = \frac{1}{2} E\left[\left(Z(s) - Z(s+h)\right)^2\right]$$

where h is the vector (distance and direction) separating the values of the points. The variogram γ can be estimated by the empirical variogram $\hat{\gamma}$, defined as:

$$\hat{\gamma}(h) = \frac{1}{2|N(h)|} \sum_{(i,j)\in N(h)} \left(Z(i) - Z(j)\right)^2$$

where $N(h) = \{(i,j): \|i-j\| = h\}$, that is, the number of pairs with separation vector h.

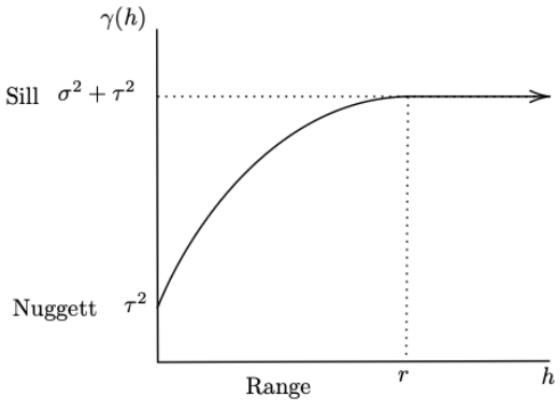

Figure 1: Theorical model of variogram.

The variogram is a tool in geostatistics that captures spatial patterns in data. It stores information about how the properties of data change with distance and direction between sample points. The variogram helps to identify spatial relationships, revealing trends or uniformities in the data. It can be used to classify areas with similar behaviors. This ability to detect spatial patterns makes the variogram useful not only in geostatistics but also in any data analysis where spatial structure is important, helping to better understand and model the phenomena being studied.

Once the empirical variogram has been calculated, model fitting can be performed using well-known parametric models. In this work, the skgstat library in Python will be used, which provides a variety of variogram models [7][9] such as

- *Spherical*: This model describes a gradual increase in variability with distance, until it stabilizes at a maximum range.

- *Exponential*: The exponential model describes variability that increases continuously and more rapidly with distance.
- *Gaussian*: Similar to the exponential model but with a smoother decrease.
- *Matern*: This model is a generalization of the previous ones and includes an additional parameter that controls the smoothness of the function.
- *Stable*: The stable model is used for phenomena that show irregular variability, even at large distances.
- *Cubic*: Variability increases or decreases cubically with distance.

2.2 Data processing

The data processing for this study involved the calculation of experimental variograms for each patient, with measurements taken at multiple time points. In this work, only the maximum diameters were considered, which were used to assess spatial dependencies and quantify variability across different distances. The following steps were carried out to compute the variogram and its parameters:

1. *Data collection*: For each patient, the data was read from their corresponding file. Each dataset contained a series of observations taken over time, which included various spatial measurements of the region of interest. These data points served as the foundation for the subsequent analysis.
2. *Distance setup*: A predefined set of distances, ranging from 0 to 19 units, was selected to characterize the spatial relationship between the measurement points. These distances represent the intervals over which the differences in the data points were calculated and compared.
3. *Variogram calculation*: For each observation, the experimental variogram was computed using the selected distances. The variogram quantifies the spatial correlation between the measurements at different distances by calculating the squared differences between the values and their spatial lag. The variogram also provides insights into the spatial structure and dependencies of the data.
4. *Parameter estimation*: In addition to calculating the experimental variogram, key parameters of the variogram model were estimated. Twenty experimental variograms were calculated (one for each time point: 0%, 5%,10%, etc.) for each patient. Then, the models mentioned in the previous subsection were used to construct 20 theoretical variograms for each patient with each model. The goal was to determine which model best fits the experimental variograms for each patient (Figure 2). To achieve this, the Normalized Root Mean Squared Error (NRMSE) was calculated for each patient and each model. NRMSE is a metric used to assess the accuracy of a model's predictions while accounting for the scale of the data. It is a variation of the Root Mean Squared Error (RMSE) but normalized to make it more interpretable across different datasets [10].

As a result, each patient had 20 NRMSE values per model. These NRMSE values were then averaged to determine which model best fit the data for each patient, and the model with the lowest average was selected as the best fit for that patient. Finally, a database was created, listing each patient along with the best fitting model and the parameters. These parameters include:

- *Nugget*: This parameter represents the small-scale variation or noise in the data, typically reflecting measurement error or fine-scale variability. It corresponds to the value of the variogram at distance zero.
- *Sill*: The sill represents the plateau level of the variogram, indicating the point at which the spatial correlation between measurements becomes negligible, and further increases in distance no longer influence the variance.
- *Range*: The range is the distance at which the variogram reaches the sill, indicating the effective spatial distance over which measurements are correlated.

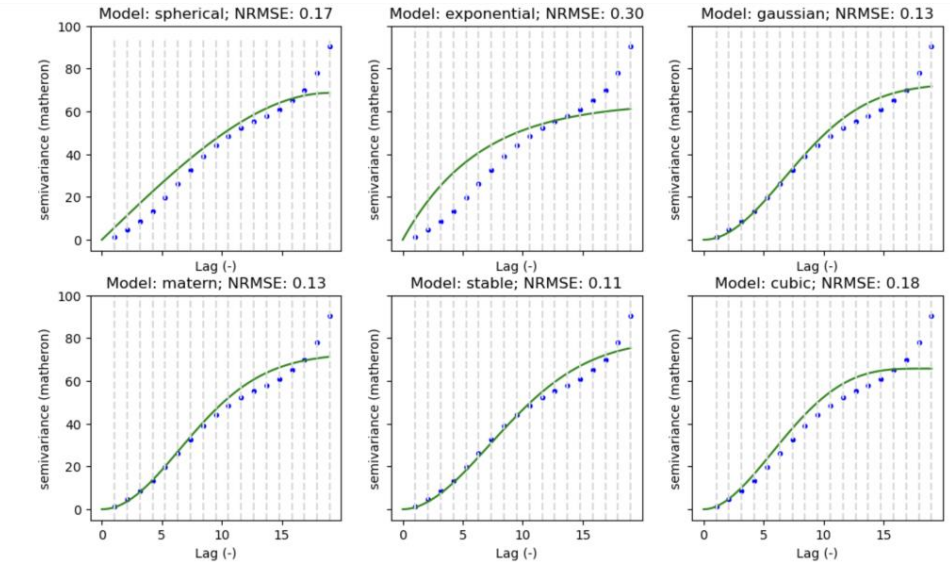

Figure 2: Selection of the model that best fits based on the NRMSE for patient 5 at time 0. For this patient the best model is "stable".

3. RESULTS

3.1. Analysis of the Empirical Variogram

The first observation is that the variogram is a useful tool for identifying patient groups. Initially, a group of patients was identified whose variogram exhibits an increasing trend (Figure 3). This suggests that the aneurysm is located at one of the extremes of the studied area or, less commonly, tends to concentrate towards one of those extremes.

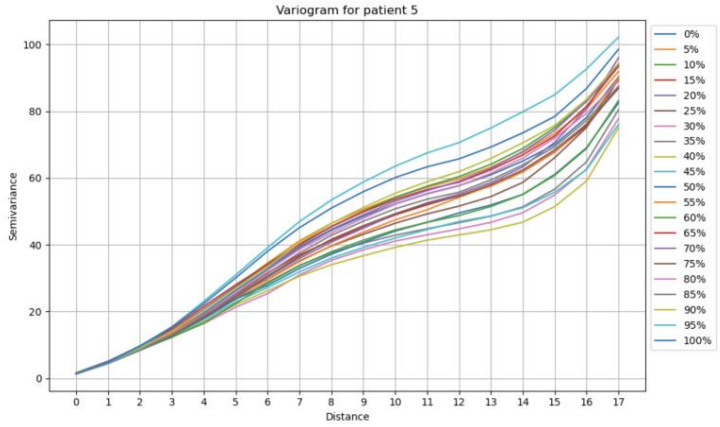

Figure 3: Empirical variograms for patient 5.

On the other hand, the following variogram (Figure 4) shows a curvature at medium distances, which may indicate that the aneurysm is located at the center of the ascending aorta.

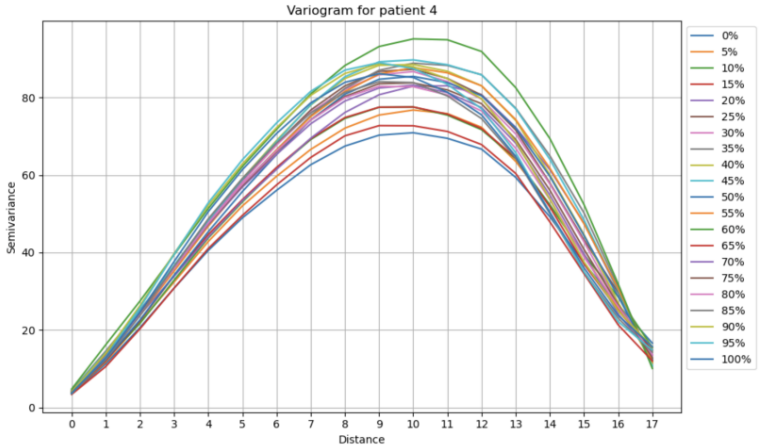

Figure 4: Empirical variograms for patient 4.

This confirms that the variogram preserves the spatial information of the aneurysm in the aorta; however, this is not such a relevant finding since it is easy to observe with tomography and by measuring the maximum diameters.

It can also be observed that there are important threshold values. It could be said that from 0 to 15, the variogram can be considered constant, which would indicate a uniform distribution along the ascending aorta. Values between 15 and 120 could be considered indicative of a more notable or evident aneurysm, depending on the previously discussed groups. Finally, values between 120 and 200 could indicate corrupted data. Regarding the latter, there were instances where some corrupted data were found, which were subsequently corrected.

3.2. Analysis of the variograms parameters

Once the variogram model is set for each patient, a range study is conducted, as it can provide information on elasticity or deformation depending on the distance [9]. This is because the range indicates how much influence one sample has over another (correlated measures) and the sill gives the trend of the variogram for distances quite large. An explanation will be given regarding the interpretation of the range and sill over time.

If the range is low, this suggests that the aorta does not easily propagate its deformation during systole, which may indicate local stiffness. If the range is high, the deformation of the aorta propagates over a greater distance, which may suggest a more elastic aorta, contributing to the propagation of deformation at higher ranges. That is, if one part of the aorta deforms, this deformation influences more distant sections. This is a typical behavior of a structure with low resistance to stress and a high capacity to distribute tensions.

There are cases where both high and low ranges may occur over time. This could indicate a time-dependent elastic response. If the fluctuations follow a pattern, it may be possible to analyze whether the aorta shows signs of fatigue or stress depending on time.

Now, the sill and range of some particular cases of patients will be analyzed. First, we will look at patient 2 who have small aneurysms but large deformations (Figure 5). Then, patient 18, who have large aneurysms (Figure 6). Finally, patient 30 who have small aneurysms with minor deformations (Figure 7).

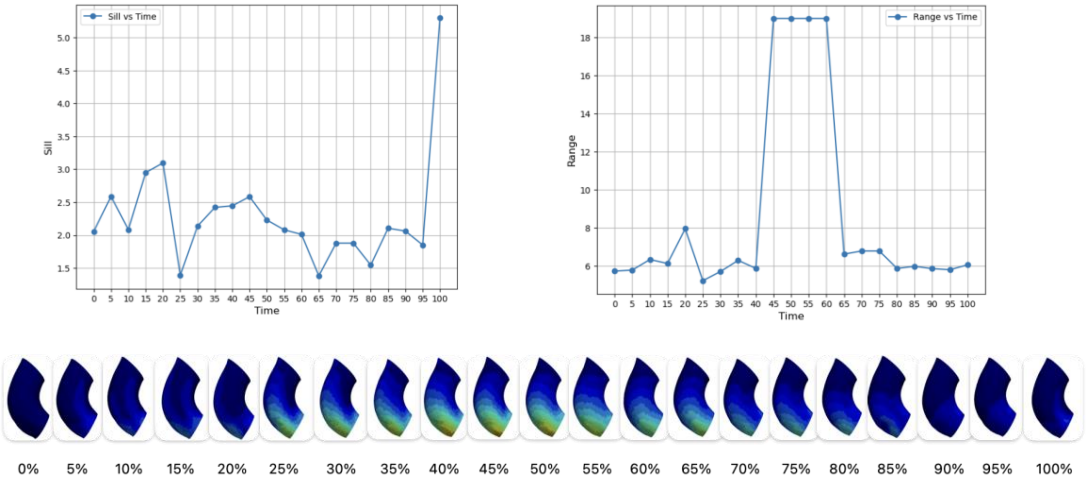

Figure 5. Patient 2: sill and range (top); and aneurysm deformation of the ascending aorta (bottom) throughout the cardiac cycle.

In the case of patient 2, despite having a small aneurysm, there is low variability (see sill, Figure 5) due to the large deformation. Additionally, the variability fluctuates, indicating that the aorta exhibits some complexity in its structure. On the other hand, the range suggests

correlation at short ranges, specifically in the time intervals from 0 to 40 and 65 to 100, indicating greater stiffness in the ascending aorta. There is total correlation in the time interval from 45 to 60, suggesting that blood pressure during the cardiac cycle affects all maximum diameters.

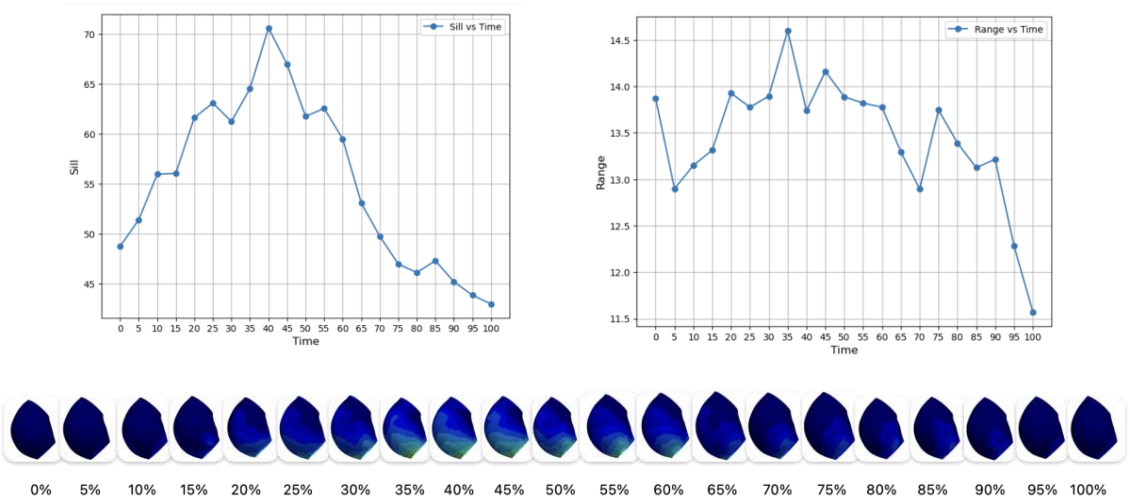

Figure 6. Patient 18: sill and range (top); and aneurysm deformation of the ascending aorta (bottom) throughout the cardiac cycle.

Patient 18 has a large aneurysm and high maximum variability (see sill, Figure 6). Additionally, it has long ranges, indicating that at almost all time intervals, most of the diameters are correlated.

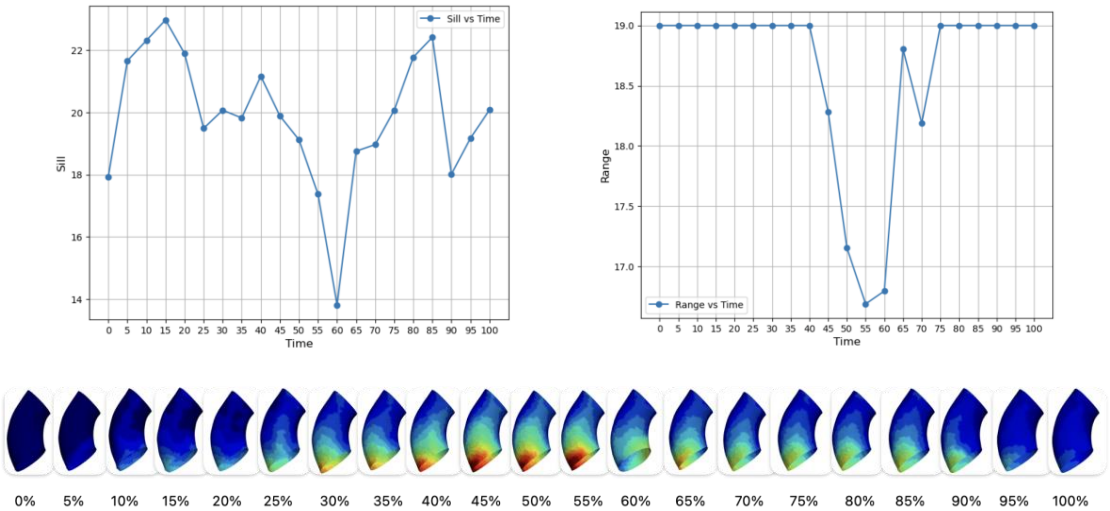

Figure 7. Patient 30: sill and range (top); and aneurysm deformation of the ascending aorta (bottom) throughout the cardiac cycle.

Patient 30 has a small aneurysm with a minor deformation. The maximum variability is not very high, and the ranges are large, indicating that this patient has a more elastic aorta.

CONCLUSION

This study provides an initial approach to analyzing ATAAs using spatial statistics. The findings suggest that spatial statistics can be a valuable tool for identifying patterns in aneurysms, such as their location in the ascending aorta through variograms. However, further exploration is needed to assess the effectiveness of the sill and range parameters in studying elasticity and stiffness.

REFERENCES

[1] Dieter, R.; Dieter, R.; Dieter, R., III. Diseases of the Aorta; Springer: Berlin/Heidelberg, Germany, 2019.2.
[2] Pasta, S.; Rinaudo, A.; Luca, A.; Pilato, M.; Scardulla, C.; Gleason, T.G.; Vorp, D.A. Difference in hemodynamic and wall stress ofascending thoracic aortic aneurysms with bicuspid and tricuspid aortic valve. J. Biomech. 2013, 46, 1729–1738.
[3] Pham, Tuan D., and Jonathan Golledge. "Pattern analysis of imaging markers in abdominal aortic aneurysms." 2013 6th International Conference on Biomedical Engineering and Informatics. IEEE, 2013.
[4] Erbel, R.; Aboyans, V.; Boileau, C.; Bossone, E.; Bartolomeo, R.D.; Eggebrecht, H.; Evangelista, A.; Falk, V.; Frank, H.; Gaemperli,O.; et al. 2014 ESC guidelines on the diagnosis and treatment of aortic diseases. Eur. Heart J. 2014, 35, 2873–2926.
[5] Maiti, S.; Thunes, J.R.; Fortunato, R.N.; Gleason, T.G.; Vorp, D.A. Computational modeling of the strength of the ascendingthoracic aortic media tissue under physiologic biaxial loading conditions. J. Biomech. 2020, 108, 109884.5.
[6] Farzaneh, S.; Trabelsi, O.; Avril, S. Inverse identification of local stiffness across ascending thoracic aortic aneurysms. Biomech.Model. Mechanobiol. 2019, 18, 137–153.
[7] Webster, R., & Oliver, M. Geostatistics for environmental scientists. John Wiley & Sons, 2007.
[8] Carvalho, M.L, & Natário, I. *Análise de Dados Espacias*. Congresso Anual: Sociedade Portuguesa de Estatística, 2008.
[9] 3-Mahdi, E., Abuzaid, A.H., & Atta, A. Empirical variogram for achieving the best valid variogram. Communications for Statistical Applications and Methods 27.5, pp. 547-568. 2020.
[10] Hyndman, Rob J., and Anne B. Koehler. "Another look at measures of forecast accuracy." *International journal of forecasting* 22.4 (2006): 679-688.

SYMCOMP 2025
Lisbon, 10-11 April 2025

FINITE DIFFERENCE METHODS FOR FRACTIONAL K-BKZ MODELS

G. Carvalho[1*], L. Carvalho[2], M. Rebelo[4], L. L. Ferrás [3], L. F. Morgado [2,5] and M. L. Morgado [2,6]

1: Department of Mathematics, School of Science and Tecnhology, University of Trás-os-Montes e Alto Douro, Quinta de Prados, 5001-801 Vila Real, Portugal
e-mail: al78885@alunos.utad.pt

2: Department of Physics, School of Science and Tecnhology, University of Trás-os-Montes e Alto Douro, Vila Real, Portugal
e-mail: al76447@alunos.utad.pt

3: Faculty of Engineering, University of Porto, Portugal
e-mail: lferras@fe.up.pt

4: Department of Mathematics, Faculdade de Ciências e Tecnologia, Centro de Matemática e Aplicações, Universidade NOVA de Lisboa, Portugal
e-mail: msjr@fct.unl.pt

5: Instituto de Telecomunicações-Lisboa
e-mail: lmorgado@utad.pt

6: Center for Computational and Stochastic Mathematics, Instituto Superior Técnico, Universidade de Lisboa
e-mail: luisam@utad.pt

Keywords: Finite differences, frame-invariant model, viscoelastic flows

Abstract. *This work introduces a numerical method for solving fractional viscoelastic fluid flows governed by a constitutive equation that combines the K-BKZ integral model with a fractional memory function (u is the velocity and σ_{xy} the shear stress):*

$$\rho\frac{\partial u(t,y)}{\partial t} = -G\int_0^t (t-s)^{-1-\beta} E_{\alpha-\beta,-\beta}\left(-\frac{G}{V}(t-s)^{\alpha-\beta}\right)\frac{1}{1+0.3\dot{\gamma}_0^2(t-s)^2}\int_s^t \frac{\partial^2 u(z,y)}{\partial y^2}\,dz\,ds,$$

$$\sigma_{xy}(t,y) = -G\int_0^t (t-s)^{-1-\beta} E_{\alpha-\beta,-\beta}\left(-\frac{G}{V}(t-s)^{\alpha-\beta}\right)\frac{1}{1+0.3\dot{\gamma}_0^2(t-s)^2}\int_s^t \frac{\partial u(z,y)}{\partial y}\,dz\,ds.$$

Acknowledgments: This work is financially supported by national funds throughthe FCT/MCTES (PIDDAC), under the project 2022.06672.PTDC - iMAD - Improving the Modelling of Anomalous Diffusion and Viscoelasticity: solutions to industrial problems, with DOI 10.54499/2022.06672.PTDC.

SYMCOMP 2025
Lisbon, 10-11 April 2025

NUMERICAL SIMULATION OF CURRENT FLOWS IN DISORDERED MATERIALS

L. Carvalho[1*], G. Carvalho[2], L. L. Ferrás [3] M. Rebelo[4], L. F. Morgado [1,5] and M. L. Morgado [2,6]

1: Department of Physics, School of Science and Tecnhology, University of Trás-os-Montes e Alto Douro, Vila Real, Portugal
e-mail: al76447@alunos.utad.pt

2: Department of Mathematics, School of Science and Tecnhology, University of Trás-os-Montes e Alto Douro, Quinta de Prados, 5001-801 Vila Real, Portugal
e-mail: al78885@alunos.utad.pt

3: Faculty of Engineering, University of Porto, Portugal
e-mail: lferras@fe.up.pt

4: Department of Mathematics, Faculdade de Ciências e Tecnologia, Centro de Matemática e Aplicações, Universidade NOVA de Lisboa, Portugal
e-mail: msjr@fct.unl.pt

5: Instituto de Telecomunicações-Lisboa
e-mail: lmorgado@utad.pt

6: Center for Computational and Stochastic Mathematics, Instituto Superior Técnico, Universidade de Lisboa
e-mail: luisam@utad.pt

Keywords: Finite differences, electrical current flows, disordered materials, nonlinear diffusion

Abstract. *This paper is concerned with the numerical simulation of the flow of an electrical current through a thin layer of disordered semiconductor materials. This layer is situated between two parallel electrodes, and an external electric field is applied perpendicular to these electrodes, driving the current flow. The drift-diffusion equations, which couple the carrier concentration and electric field, are fundamental to model charge transport in organic semiconductor based devices. Since the concentration-dependent mobility makes the problem more complex to solve, we propose an IMEX numerical scheme.*

Acknowledgments: This work is financially supported by national funds throughthe FCT/MCTES (PIDDAC), under the project 2022.06672.PTDC - iMAD - Improving the Modelling of Anomalous Diffusion and Viscoelasticity: solutions to industrial problems, with DOI 10.54499/2022.06672.PTDC.

SYMCOMP 2025
Lisbon, 10-11 April 2025

GRÜSS TYPE INEQUALITIES WITHIN THE GENERAL QUANTUM CALCULUS

J. L. Cardoso

1: Polo CMAT - UTAD
Math Department, School of Sciences and Technology
University of Trás-os-Montes e Alto Douro
Quinta de Prados, 5000-801 Vila Real, Portugal
e-mail: jluis@utad.pt, web: http://www.cmat.pt

Keywords: Grüss inequalities, Grüss-type inequalities, general quantum operator, β-difference operator, β-derivative, quantum derivative, β-integral

Abstract. *We assume that $I \subseteq \mathbb{R}$ is an interval and $\beta : I \to I$ a strictly increasing and continuous function with a single fixed point $s_0 \in I$, satisfying $(s_0 - t)(\beta(t) - t) \leq 0$ for all $t \in I$, where the equality occurs only when $t = s_0$.*

Hamza et al. introduced the general quantum operator, $D_\beta[f](t) := \dfrac{f\big(\beta(t)\big) - f(t)}{\beta(t) - t}$ when $t \neq s_0$ and $D_\beta[f](s_0) := f'(s_0)$ when $t = s_0$. It generalizes the Jackson q-derivative operator D_q as well as the Hahn (quantum derivative) operator, $D_{q,\omega}$.
We exhibit Grüss type inequalities for the corresponding inverse operator, the β-integral. In addition, by introducing the concept of β-Riemann-Stieltjes integral, we also obtained Grüss type inequalities associated with it.

Acknowledgement The author thanks the support by Portuguese funds, through the Portuguese Foundation for Science and Technology ("FCT-Fundação para a Ciência e a Tecnologia"), through the Projects UIDB/00013/2020 and UIDP/00013/2020.

REFERENCES

[1] A. E. Hamza, A. M. Sarhan, E. M. Shehata and K. A. Aldwoah, "A general quantum difference calculus", *Adv. Difference Equ.*, Vol. **182**, pp. 1-19, 2015

[2] J. L. Cardoso, "Variations around a general quantum operator", *Ramanujan J.*, Vol. **54**, pp. 555-569, 2021

[3] J. L. Cardoso, E. M. Shehata "Hermite-Hadamard inequalities for quantum integrals: A unified approach", *Appl. Math. Comput.*, Vol. **463**, 2024

SYMCOMP 2025
Lisbon, 10-11 April 2025

SYMBOLIC COMPUTATION APPLIED IN THE CONTEXT OF QUANTUM CALCULUS

Ângela Macedo

Departamento de Matemática & CMAT, Polo CMAT-UTAD
Universidade de Trás-os-Montes e Alto Douro, Quinta de Prados, 5000-801 Vila Real, Portugal
e-mail: amacedo@utad.pt, web: http://www.cmat.pt

Keywords: Quantum calculus, Jackson q-derivative, Jackson q-integral, symbolic computation

Abstract. *The well-known q-analogues, $e_q(z)$ and $E_q(z)$, of the classical exponential function are defined through infinite series, whose sums can be expressed in closed form using infinite products. In this work, we aim to leverage symbolic computation to analyze the behavior of these q-exponentials with respect to the parameter q and the variable z*

Acknowledgement The author thanks the support by Portuguese funds through the Portuguese Foundation for Science and Technology ("FCT-Fundação para a Ciência e a Tecnologia"), through the Projects UIDB/00013/2020 and UIDP/00013/2020.

REFERENCES

[1] Gasper G. and Rahman M., *Basic Hypergeometric Series*, Cambridge Univ. Press, Cambridge, UK, 1990.
[2] M.H. Annaby, A.E. Hamza, K.A. Aldwoah, *Hahn Difference Operator and Associated Jackson-Nörlund Integrals*, J. Optim. Theory Appl. 154 (1) (2012), 133–153.
[3] Kac, V.G. and Cheung, P., *Quantum Calculus*, Springer: New York, NY, USA, 2002, Volume 113.

SYMCOMP 2025
Lisbon, 10-11 April 2025

ADAPTIVE MESH ALGORITHMS FOR DISTRIBUTED-ORDER DIFFERENTIAL EQUATIONS

M. L. Morgado[1], L. F. Morgado[2], L. L. Ferrás[3] and M. Rebelo [4]

1: Department of Mathematics, University of Trás-os-Montes e Alto Douro and Center for Computational and Stochastic Mathematics, Instituto Superior Técnico, Universidade de Lisboa, Portugal
e-mail: luisam@utad.pt

2: Department of Physics, University of Trás-os-Montes e Alto Douro and Instituto de Telecomunicações, Lisboa, Portugal
e-mail: lmorgado@utad.pt

3: Faculty of Engineering, University of Porto, Portugal
e-mail: lferras@fe.up.pt

4: Department of Mathematics, Faculdade de Ciências e Tecnologia, Centro de Matemática e Aplicações, Universidade NOVA de Lisboa, Portugal
e-mail: msjr@fct.unl.pt

Keywords: Finite differences, distributed-order derivatives, adaptive mesh algorithms

Abstract. *This work focuses on numerically solving distributed-order fractional differential equations, in which the non-integer order derivatives are given in terms of Caputo definition. Because typical solutions of fractional differential equation exhibit a singularity at the origin, non-uniform meshes are commonly used to overcome the decrease of the convergence order of standard numerical schemes. Here, we review the main contributions in the development of efficient numerical schemes and explore adaptive mesh algorithms for the numerical solution of this kind of equations.*

Acknowledgments: This work is financially supported by national funds throughthe FCT/MCTES (PIDDAC), under the project 2022.06672.PTDC - iMAD - Improving the Modelling of Anomalous Diffusion and Viscoelasticity: solutions to industrial problems, with DOI 10.54499/2022.06672.PTDC.

A MACHINE-LEARNING–BASED FRAMEWORK FOR EFFICIENT TURN-DOWN RATIO DETERMINATION IN POROUS BURNERS

Sérgio Cavaleiro Costa[1]*, Isabel Malico[1,2] and Fernando M. Janeiro[3,4]
1: IDMEC
Escola de Ciências e Tecnologia
Universidade de Évora
R. Romão Ramalho, 59, 7000-671 Évora, Portugal
e-mail: smcac@uevora.pt, web: http://www.idmec.tecnico.ulisboa.pt/

2: Complex Flow Systems Lab (CFS Lab)
Institute of Earth Sciences
Universidade de Évora
R. Romão Ramalho, 59, 7000-671 Évora, Portugal
e-mail: imbm@uevora.pt, web: https://cfslab.wixsite.com/cfslab

3: Department of Mechatronics Engineering
School of Science and Technology
University of Évora
R. Romão Ramalho, 59, 7000-671 Évora, Portugal
web: https://www.uevora.pt/

4: Instituto de Telecomunicações
Instituto Superior Técnico
Av. Rovisco Pais, 1049-001 Lisboa, Portugal
e-mail: fmtj@uevora.pt

Keywords: Porous Media, Burner turndown, Combustion, Stability, Gaussian Process Classifier, CFD

Abstract *Establishing the turn-down ratio, the ratio of maximum and minimum fuel inlet velocity, is a critical step in the design and operation of porous burners. While conventional approaches rely on extensive computational fluid dynamics (CFD) simulations or exhaustive experimental studies over a broad range of operating conditions, these can become prohibitively time-consuming and costly. This work proposes a machine-learning–based methodology, specifically utilizing a Gaussian Process Classifier (GPC), to significantly reduce the effort needed to determine the turn-down ratio of a two-layer porous burner. In the proposed framework, an initial set of CFD simulations is used to train the GPC, which learns a probabilistic classification boundary distinguishing stable from*

unstable combustion regimes in a multidimensional parameter space. Subsequently, an active learning strategy identifies regions of highest classification uncertainty—near the stable–unstable transition. Only these uncertain regions are resampled with additional CFD runs in subsequent iterations. By focusing computational resources on the boundary zone, the method quickly refines the stable-unstable line without expending effort far inside clearly stable or unstable regions. The Gaussian Process Classifier yields a smoothly varying probability field that not only locates the stable combustion limit (where probability of stability is 0.5) but also quantifies confidence in that boundary by mapping probability contours (e.g., 0.4, 0.6). Results show that this adaptive approach can cut the total number of simulations compared to uniform sweeps, while maintaining or improving boundary-resolution fidelity. This technique is broadly applicable to porous burner designs and can be readily extended to other thermal or reactive flow systems.

SYMCOMP 2025
Lisbon, 10-11 April 2025

INFLUENCE OF RELAXATION FUNCTIONS ON VISCOELASTIC DATA FITTING: A PARAMETER ANALYSIS

L. L.Ferrás [1*,2], M. L. Morgado[3], M. Rebelo [4] and L. F. Morgado [5]

1: Faculty of Engineering, University of Porto, Portugal
email: lferras@fe.up.pt

2: Centro de Estudos de Fenómenos de Transporte, University of Porto, Portugal

3: Department of Mathematics, UTAD and Center for Computational and Stochastic Mathematics, Instituto Superior Técnico, Lisbon, Portugal
email: luisam@utad.pt

4: Mathematics Department and Center for Mathematics and Applications (NOVA Math), Nova School of Science and Technology – Portugal
e-mail: msjr@fct.unl.pt

5: Department of Physics, UTAD and Instituto de Telecomunicações -Lisboa , Portugal
email:lmorgado@utad.pt

Keywords: Mittag-Leffler function, exponential function, algebraic functions, fractional calculus, singularities

Abstract. *In this work, we investigate the influence of different relaxation functions on the numerical solution of integral equations commonly used to model viscoelastic materials. We analyse the behaviour of various relaxation functions and conduct a parameter study. The advantages and disadvantages of the proposed relaxation functions are evaluated in terms of their potential to introduce singularities in the integral equations, their ability to fit experimental data, and their physical relevance.*

Acknowledgments: This work is financially supported by national funds throughthe FCT/MCTES (PIDDAC), under the project 2022.06672.PTDC - iMAD - Improving the Modelling of Anomalous Diffusion and Viscoelasticity: solutions to industrial problems, with DOI 10.54499/2022.06672.PTDC.

SYMCOMP 2025
Lisbon, 10-11 April 2025

SHORT-TERM ELECTRIC GRID LOAD FORECASTING

Ana Alexandra Martins[1,2,3]*, Fernando Pereira[1], Francisco Reis[1], Hiren Canacsinh[1], João Lagarto[1,4], Margarida Cardoso[5], Maria José Amorim[1]

1: ISEL - Instituto Superior de Engenharia de Lisboa
Polytecnhic University of Lisbon
Rua Conselheiro Emídio Navarro 1, 1959-007, Lisboa, Portugal
e-mail: ana.martins@isel.pt
fjp@deea.isel.ipl.pt; joao.lagarto@isel.pt; hiren.canacsinh@isel.pt; maria.jose.amorim@isel.pt; francisco.reis@isel.pt

2: Research Centre for Mathematics and Applications (CIMA), Instituto Superior de Engenharia de Lisboa (ISEL/IPL)
Av. Conselheiro Emídio Navarro 1, 1959-007 Lisboa, Portugal

3: Centro de Investigação em Modelação e Otimização de Sistemas Multifuncionais (CIMOSM)
Instituto Superior de Engenharia de Lisboa (ISEL/IPL)
Av. Conselheiro Emídio Navarro 1
1959-007 Lisboa, Portugal

4: INESC-ID
Rua Alves Redol 9, 1000-029, Lisboa, Portugal

5: ISCTE IUL (Instituto Universitário de Lisboa) and Business Research Unit, BRU-IUL
Lisbon, Portugal
margarida.cardoso@iscte-iul.pt

Keywords: Electrical grid, Neuronal Networks, Short-term load forecasting.

Abstract *This paper addresses the problem of short-term load forecasting on an electric power grid. Accurate load prediction plays an important role on multiple aspects of electric grid operation and management, including risk assessment, maintenance and outage planning, coordination between different grid operators, contributing to improve efficiency and resiliency.*

A prediction model based on artificial neural networks are employed to process data from the Portuguese power grid with a 15 minute sampling interval. In addition to the grid load data, additional inputs were added, including weather information and results from

clustering of the time series. The system produces a 24 hour load forecast, for each 15 minute.

Acknowledgements This work was supported by Instituto Politécnico Lisboa (IPL) with reference IPL/IDI&CA2023/ELForcast2_ISEL and Fundação para a Ciência e a Tecnologia, grants UID/MAT/04674/2013, UIDB/00315/2020 (DOI: 10.54499/UIDB/00315/2020) and UIDB/50021/2020 (DOI: 10.54499/UIDB/50021/2020).

SYMCOMP 2025
Lisbon, 10-11 April 2025

RELIABILITY ANALYSIS AND FAILURE FORECAST OF CRITICAL COMPONENTS UNDER WARRANTY

José Sobral[1]* and **Fyodor Subotin**[2]

1: Mechanical Engineering Department
Instituto Superior de Engenharia de Lisboa (ISEL)
Instituto Politécnico de Lisboa (IPL)
Rua Conselheiro Emídio Navarro, 1, 1959-007 Lisboa, Portugal
e-mail: jsobral@dem.isel.pt

Centre for Marine Technology and Ocean Engineering (CENTEC)
Instituto Superior Técnico, Universidade de Lisboa, Lisboa, Portugal

Centro de Investigação em Modelação e Optimização de Sistemas Multifuncionais (CIMOSM)
Instituto Superior de Engenharia de Lisboa (ISEL), Instituto Politécnico de Lisboa (IPL), Lisboa, Portugal

2: Mechanical Engineering Department
Instituto Superior de Engenharia de Lisboa (ISEL)
Instituto Politécnico de Lisboa (IPL)
Rua Conselheiro Emídio Navarro, 1, 1959-007 Lisboa, Portugal
e-mail: A48792@alunos.isel.pt

Keywords: Reliability analysis, warranty, predictive maintenance, analytic hierarchy process

Abstract *Companies need to produce durable, safe, and quality products and adopt the best strategies to deal with the occurrence of failures when needed. This not only reduces the risk of failure but also enhances customer confidence. The present study was developed in the cargo handling and lifting industry in a way to identify critical components installed in assets based on data from failure records, and based on the results achieved, develop a reliability analysis on such critical components, allowing to describe their behavior on operating time. The reliability analysis was developed based on statistical theory, using numerical computation through specialized software. It was possible to describe the reliability, the probability of failure, the failure rate, and other characteristics that allow us to predict these probabilities for a specific operating time. Furthermore, a forecast of warranty returns was prepared through the analysis of sales vs returns, which provided an important tool to predict the failures during the warranty period, and thus plan interventions and the need for spare parts, optimizing the entire management of interventions to be carried out in the future. It is also shown that the use of computational tools in this field enhances faster and more visible results.*

DOI:10.5281/zenodo.15161179

1. INTRODUCTION

The topic of reliability in the cargo handling and lifting industry plays a crucial role in operational efficiency, safety, and customer satisfaction. Failures in load handling and lifting equipment pose a significant challenge. Unscheduled downtimes resulting from these failures compromise operator safety and disrupt operations. Identifying and mitigating these failures early is essential to maintaining productivity and workplace safety.

The costs associated with equipment failures are substantial and multifaceted. They include repair and replacement expenses, production losses, and possible contractual penalties for delivery delays. Additionally, indirect costs, such as loss of customer trust and damage to the company's reputation, must not be overlooked.

Frequent or unexpected failures can lead to a shortage of replacement parts, extending equipment downtime and increasing customer dissatisfaction, which can lead to contract losses, complaints, and reputational damage to the company. Unreliable equipment results in delays and disruptions that directly impact customers. Therefore, efficient spare parts inventory management and accurate maintenance forecasting are essential.

Predicting warranty returns is crucial for risk management and cost control. Analysing historical maintenance data can help to identify patterns and anticipate potential failures. This knowledge allows companies to plan with anticipation, reduce downtime, and minimize costs associated with warranty returns.

Advanced predictive maintenance techniques, the use of real-time monitoring systems, and data analysis are effective strategies to enhance reliability. Additionally, continuous operator training and the implementation of best maintenance practices can significantly contribute to reducing failures and improving equipment performance.

This study addresses issues related to equipment failures, inherent costs, warranty return forecasts, and the implications of a potential shortage of spare parts, ultimately highlighting the strategic importance of reliability for the competitiveness and sustainability of operations.

The main objectives of this study are to identify critical warranty components in a load handling and lifting company and to analyse their reliability, thereby promoting the organization's continuous improvement. This part of the study was achieved by using computational means, enhancing the results in a shorter time, and improving the visualization of distinct features.

The paper is structured into five sections. The first section makes an introduction to the theme, and the second section refers to the selection of critical items on assets, allowing to conduct further deep failure analysis. The third section deals with reliability theory and its importance, the fourth section presents a case study where a specific computational tool was used, and the fifth section discusses the results and presents some conclusions and future work.

2. SELECTION OF CRITICAL ITEMS

The selection of critical items can be performed using several tools and methods. In the present study it was done using the Analytic Hierarchy Process (AHP) methodology. The AHP methodology was developed in the 1970s by Thomas L. Saaty at the Wharton Business School. It can be described as a multicriteria decision-making approach in which several factors are organized into a hierarchical structure [1].

2.1. Description of AHP methodology

According to Saaty [2], AHP is a methodology that uses pairwise comparisons, based on expert opinions, to derive priority scales.
In addition to simplifying the decision-making process by allowing direct comparisons between options, this method provides a greater understanding of the relationships between different alternatives in terms of compatibility [3].
According to Taherdoost [4], AHP is a valuable tool and one of the most comprehensive systems for decision-making in complex situations that require the consideration of multiple criteria, incorporating both quantitative and qualitative factors.
The AHP application process begins when a complex problem is broken down into more manageable parts, helping to structure the issue in a logical and organized manner, facilitating the independent analysis and comparison of each component.
The objective represents the desired outcome or guiding purpose of the decision-making process. The criteria are specific factors that serve as the basis for evaluating and analysing different alternatives. The alternatives refer to the various choices available for assessment about the criteria [5].
Once the logical hierarchy is designed, decision-makers can systematically evaluate the alternatives. This is done through pairwise comparisons for each previously established criterion. During these comparisons, decision-makers can use specific data related to the alternatives or make subjective judgments. This flexibility allows for the incorporation of both objective and subjective information into the decision-making process [6].
According to Saaty [2], Vargas [6], and Wollmann et al. [7], the process consists of five main phases:

1. Problem definition;
2. Structuring the decision hierarchy;
3. Construction of pairwise comparison matrices;
4. Determination of the relative weight of each element in the hierarchical structure;
5. Data consistency verification.

2.2. Use of the Analytic Hierarchy Process

Any situation that requires structuring, measurement, and involving multiple criteria is a good candidate for the use of the Analytic Hierarchy Process. Broad areas where AHP has been successful include: Choice, Prioritization/Evaluation, Resource Allocation, Quality Management, Public Policy, Healthcare, or Strategic Planning. This methodology is valuable in these contexts due to its ability to handle multiple criteria, facilitating strategic and complex decision-making [8].
One of the most comprehensive studies on AHP was conducted by Emrouznejad and Marra [9]. In this study, 8441 articles were analysed from the Web of Science database, covering an extensive period from 1979 to 2017. The study divided the evolution of AHP into three distinct periods. In the first period (1979-1990), the focus was on building the theoretical foundations of AHP; the second period (1991-2001) saw an increase in practical applications in fields such as computer science, mathematics, business, and management; and finally, the third period

(2002-2017) was characterized by the expansion of AHP into areas such as the fuzzy approach. A more recent study performed by Madzík and Falát [10] analysed 34530 documents related to AHP, published between 1980 and 2021, and obtained from the Scopus database. The authors of this study report that the remarkable growth of publications on this method is due to the ease of application, logic, and flexibility of the process. Decision-making is present in virtually all areas of research and has been applied in sectors such as engineering, computer science, business and management, mathematics, and social sciences.

3. RELIABILITY

3.1. Introduction

Reliability is one of the quality characteristics demanded by consumers from product manufacturers or service providers. Unfortunately, when asked about the meaning of reliability, consumers' answers tend to be unclear. Some may mention that the product must always function correctly, without failures, or that it should perform its function adequately when needed. Others, however, may have difficulty explaining the exact meaning of reliability to them [11].

From a technical point of view, reliability is a characteristic of an item, expressed by the probability that the item will perform its function under specific conditions over a determined period. Generally, this probability is denoted as *R(t)*. Qualitatively, reliability can be defined as the ability of the item to remain functional. From a quantitative perspective, reliability specifies the probability that no operational interruptions will occur during a predetermined time interval. This formal definition highlights that reliability does not prevent redundant parts from failing. However, even when failures occur, reliability considers the capacity for repair without operational interruption at the item or system level. The concept of reliability, therefore, applies to both non-repairable and repairable items [12].

Formally, reliability is viewed as both an engineering and probabilistic concept. Both of these perspectives form the fundamental basis for reliability studies. The engineering notion of reliability deals with design and analysis activities that extend the life of an item by controlling its potential failure modes. Examples include designing more robust and durable components, protecting against adverse environmental conditions, minimizing loads and stresses applied to an item during its use, and implementing a preventive maintenance program to reduce the occurrence of failures [13].

In summary, reliability refers to the ability of a product or service to perform its function over time, being a combination of performance characteristics, durability, and maintainability [11]. Reliability is defined by the EN 13306 standard [14] as the "*ability of an item to perform a required function under given conditions, over a given period of time*.

3.2. Statistical distributions

A reliability analysis uses statistical distributions where times to failure are fitted. The most widely used is the Weibull distribution due to its flexibility and adequacy to most of the

studies presented in industrial cases.
Other studies use other statistical distributions as the Normal distribution, the Exponential distribution, or the Lognormal distribution.
Because of the massive use of Weibull distribution and its application in the case study presented in section 4, it will be described in more detail, addressing its fundamental characteristics and distinctive properties.

3.3. Weibull distribution

The Weibull Distribution is a continuous probability distribution named in honour of Waloddi Weibull, who described it in detail in 1951. Since then, the Weibull distribution has become one of the most referenced lifetime distributions in reliability engineering. The Weibull Distribution is capable of accurately describing the failure times observed in various types of components and phenomena [15].
The probability density function for the Weibull Distribution in its triparametric form is given by Equation (1):

$$f(t) = \left(\frac{\beta}{\eta}\right) \cdot \left(\frac{t-\gamma}{\eta}\right)^{\beta-1} \cdot e^{-\left(\frac{t-\gamma}{\eta}\right)^{\beta}} \quad (1)$$

where:

- $f(t) \geq 0, t \geq \gamma, \beta > 0, \eta > 0, -\infty < \gamma < +\infty$
- β is the shape parameter
- η is the scale parameter (or characteristic life)
- γ is the position parameter

The parameter γ is referred to as the threshold, warranty time, or, more commonly, the initial life. From a statistical perspective, it is a location parameter. This means that changing γ while the other parameters remain constant will result in a shift of the density curve along the horizontal axis [16].
The parameter η is referred to as the characteristic life. From a statistical perspective, it is a scale parameter. It indicates the time at which there is a 63.2% probability of failure.
The third parameter, also known as the slope of the Weibull Distribution, is represented by the symbol β. From a statistical perspective, β is a shape parameter. The main characteristics of the shape parameter (β) can be highlighted [17] [18]:

- If β < 1 – The failure rate decreases over time (infant mortality);
- If β = 1 – Indicates random failures, constant and independent of time (Exponential distribution);
- If β > 1 – The failure rate increases over time (wearout);
- If 3 < β < 4 – The failure rate approaches a Normal distribution;
- If β > 3.4 – Indicates severe wear failures.

The main domains where the Weibull distribution has been commonly applied are [17]:

- Warranty analysis
- Maintenance and renewal
- Modeling material strength

- Modeling wear
- Modeling electronic failures
- Modeling corrosion

If the failure can occur at any moment, it is assumed that the location parameter is equal to zero, and the Weibull distribution is represented in its biparametric form, with the probability density function represented by Equation (2):

$$f(t) = \left(\frac{\beta}{\eta}\right) \cdot \left(\frac{t}{\eta}\right)^{\beta-1} \cdot e^{-\left(\frac{t}{\eta}\right)^{\beta}} \quad (2)$$

When the failures are random in time, it means that the shape parameter is equal to one, the Weibull distribution is resumed to its monoparametric form, as Equation (3):

$$f(t) = \left(\frac{1}{\eta}\right) \cdot e^{-\left(\frac{t}{\eta}\right)} \quad (3)$$

The main methods for estimating the parameters of the chosen distribution are the Least Squares Regression (Rank Regression) and the Maximum Likelihood Method (MLE).
Reliability can be determined by Equation (4), hen dealing with the triparametric representation:

$$R(t) = e^{-\left(\frac{t-\gamma}{\eta}\right)^{\beta}} \quad (4)$$

The probability of failure can be easily determined because it is the complementary value of reliability, obtained by Equation (5):

$$F(t) = 1 - R(t) \quad (5)$$

The above theory supports computational applications in the field of reliability analysis, complemented with a more exhaustive theory about failure rate determination, conditional reliability, confidence intervals, and more.

4. CASE STUDY

The present case study deals with the reliability analysis and failure forecast of components installed in equipment in the cargo handling and lifting industry.

4.1. Selection

According to the AHP methodology described in Section 2, the main objective was to identify the critical component that had the most impact on the organization's warranties in recent years. The selected criteria were the number of failures, the average cost per repair, and the average repair time.
This choice of criteria allowed for a comprehensive analysis of the efficiency and effectiveness of the repair operations, considering both the quantitative aspect of the failures and the economic and time factors involved in the repair processes. In Figure 1, the hierarchical structure for this case study can be observed.

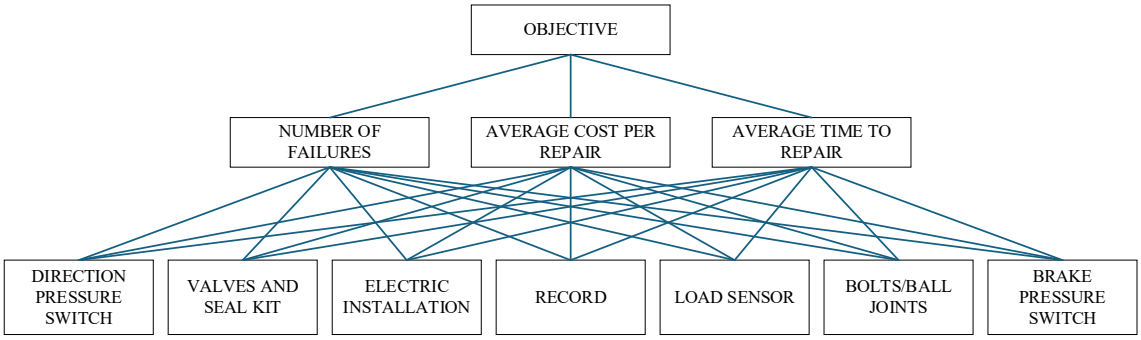

Figure 1. Hierarchical structure.

After the design of the hierarchical structure and the definition of the criteria and alternatives, the next phase involves pairwise comparisons. The comparisons of the criteria were made by company experts, and the comparison between the alternatives was based on the historical record of component failures.

Based on the set of standardized criteria, it becomes possible to derive the relative weights. The weights indicate the relative importance of each criterion concerning the others, achieving in this study the following results:

- Number of Failures = 0.544
- Average Cost per Repair = 0.243
- Average Time to Repair = 0.213

By analyzing the values resulting from the priority vector of the criteria, it is concluded that the Number of Failures is the most significant criterion, representing 54.4%. Next is the Average Time to Repair, which represents 24.3%, and last, the Average Cost per Repair, with 21.3%. These values reflect the relative relevance of each criterion in the decision-making process, highlighting the specific contribution of each in the overall evaluation.

Follows a consistency analysis of the methodology, aiming to assess the coherence and robustness of the comparisons made. This procedure is essential to verify the consistency of the comparisons performed, ensuring the strength and reliability of the results in the context of the analysis. This involves analyzing the collected data to ensure that the comparisons made during the decision-making process align with logical and coherent standards. The evaluation of data consistency was confirmed. In the present context, the matrix is considered consistent, as the Consistency Ratio (*CR*) is less than 0.10. This conclusion indicates that the comparisons made are coherent and exhibit an acceptable level of consistency, strengthening the credibility of the results obtained in the analysis.

Upon completing the consistency analysis phase for the top level of the hierarchy, the same process is now applied to the lower level. In other words, the alternatives are compared against each other, but this time for each of the specific criteria.

Based on historical data, the alternatives considered for this study are: Direction Pressure Switch, Valves and Seal Kit, Electrical Installation, Record, Load Sensor, Bolts/Ball Joints, and Brake Pressure Switch.

After the comparisons of the alternatives for each criterion and confirming the consistency

of such comparisons, the priority vector of each alternative concerning each of the criteria and the weights of the criteria was obtained.
It was then possible to calculate the overall weight of each alternative about the objective. In this sense, and according to the theory of AHP, the weights of the criteria are multiplied by the priority vectors of the alternatives, then the total value is obtained by summing the resulting products. By applying this methodology, the weights of each alternative about the objective were obtained, and they can be observed in Table 1.

Direction Pressure Switch	26.71%	**1º**
Bolts/Ball Joints	17.98%	2º
Vlaves and Seal Kit	17.62%	3º
Electricall Installation	14,90%	4º
Brake Pressure Switch	8.33%	5º
Load Sensor	7.95%	6º
Record	6.51%	7º

Table 1. Global weight for each alternative.

Analysing the results, it can be observed that the Direction Pressure Switch is the most important component, with 26.71%. Then, this was the item selected for a further and more accurate reliability analysis.

4.2. Reliability analysis

To begin the reliability analysis, the failures of the selected component in the last 2 years were analyzed through the ERP (Enterprise Resource Planning) system and by consulting existing work sheets.
With the identification of the failures, the serial numbers of the equipment that had failures related to the direction pressure switch were obtained. In total, 50 failures in 20 different pieces of equipment were analysed in this study.
Some components under the analysis, despite being only 2 years in service, experienced 6 failures.
Table 2 presents the times to failure (in hours) of the selected components.
The present study used a computational tool called Reliability4All. It was specially developed by a team of Reliability Engineers and was provided free of charge for conducting the analyses in this work. On the tool's home page, the Life Data Analysis module was selected.

Equipament	Failure 1	Failure 2	Failure 3	Failure 4	Failure 5	Failure 6
6740	701	1466				
7153	739					
1288	1636	3483	3821	4746		
1330	1156	2479	3357	5671		
6891	1410	2047	2835	3453	4123	4780
1833	1151	2083	3078			
1313	1204	2135	4187	5104	6722	
6767	1351	1820				
6990	2043	2849	3926	4600		
6678	1887	2938	3477			
8067	560					
6985	1582					
9824	4417	6624	7512			
2591	3927	4575				
1106	284	996				
7162	517					
6718	2109					
6886	1987	2591	3466			
3996	638					
9559	669					

Table 2. Time to failure of the component.

In this analysis, exact times to failure were chosen. Suspended times were not initially used. The distribution chosen for this analysis was the triparametric Weibull distribution, as it is, according to the literature, the most suitable for warranty studies.

The MLE (Maximum Likelihood Estimation) method was selected for parameter estimation, as it is considered one of the best methods for estimating parameters for sample sizes above 30 [19].

By calculating the parameters under the stated conditions and assuming a 90% confidence interval, the following values were obtained:

- Shape parameter (β) = 1.23
- Scale parameter (η) = 986.88 hours
- Location parameter (γ) = 277.30 hours

With these values, it is possible to determine the probability of failure or reliability for a given time, as well as the failure rate and other relevant information. Figure 2 illustrates the probability density function for the component under analysis.

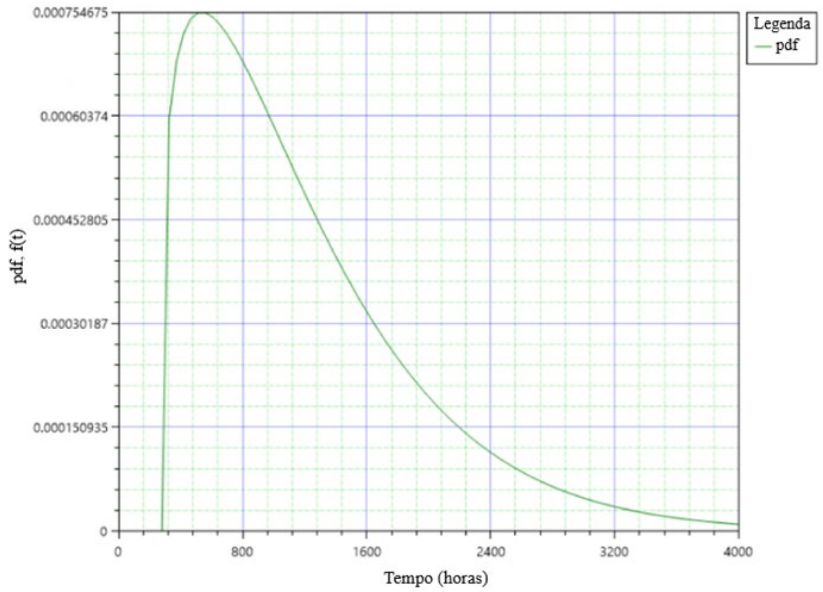

Figure 2. Probability density function.

Figure 3 shows the graphical representation of the evolution of the probability of failure in time.

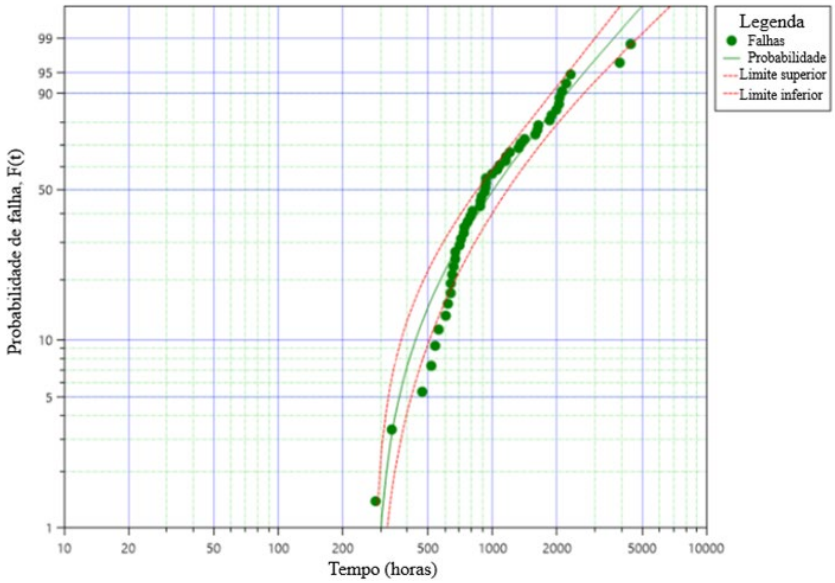

Figure 3. Cumulative probability of failure.

As the shape parameter is higher then 1 it means that the failure rate is increasing in time, as shown in Figure 4.

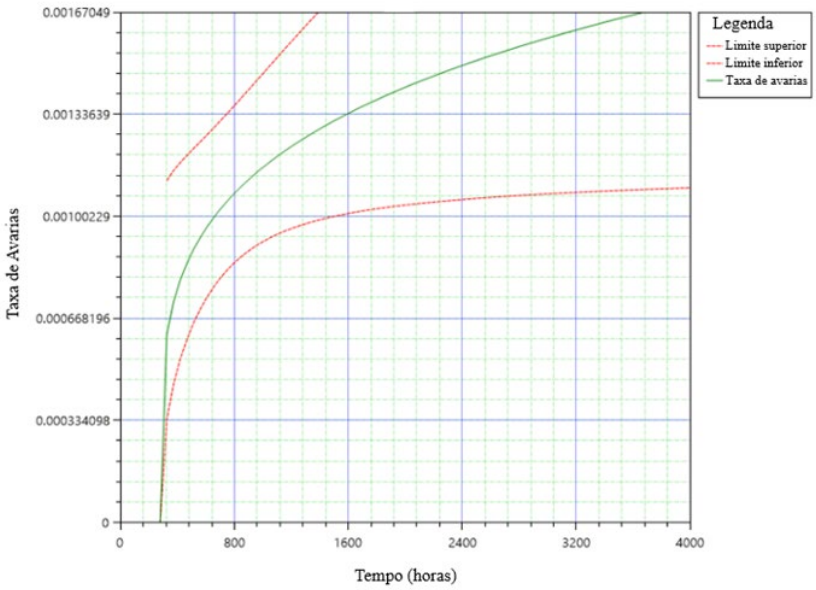

Figure 4. Failure rate.

By using the theory and analytical equations, the reliability, *R(t)*, for the direction pressure switch for any time of operation can be easily determined. For example, for 1000 hours of operation, a reliability of 0.5062 is achieved. This is confirmed by the software tool, as illustrated in Figure 5.

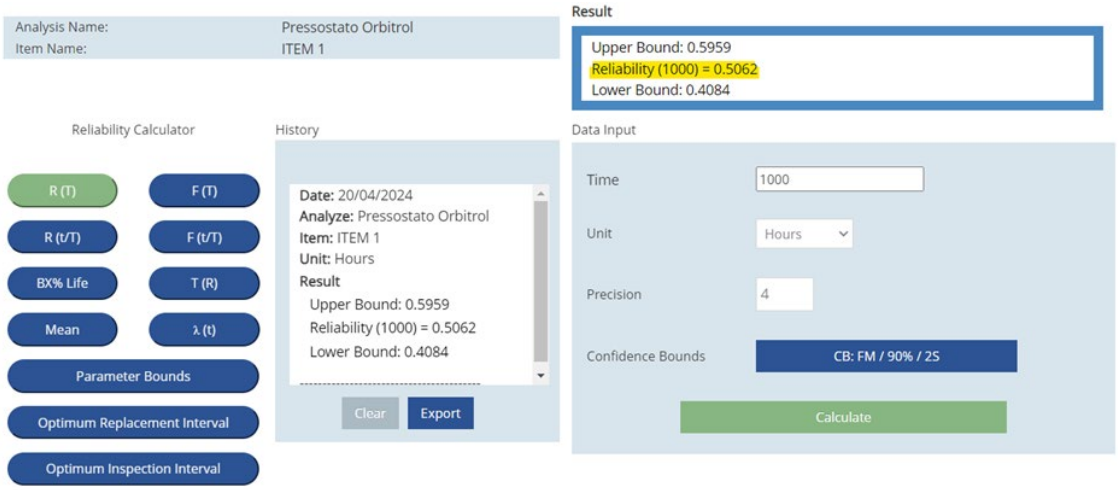

Figure 5. Printscreen of the reliability tool for 1000 hours

In the above figure are also visible the reliability values expected for reliability, considering the confidence interval of 90% (reliability from 0.4084 to 0.5959)
The next step refers to the inclusion of suspended times in the analysis. These times represent the time elapsed from the component's installation until the date of analysis without any recorded failure. In this sense, instead of being considered a failure, it is treated as a suspension. Thus, it was possible to determine the current hours of the equipment since the last recorded failure or since its initial installation.
Accordingly, an analysis of the failure times was performed to obtain the suspended (S) and failure (F) data to be used in this analysis. For the triparametric Weibull Distribution, similar to the previous analysis, the Maximum Likelihood Estimation (MLE) method was used for analysis. By calculating the parameters under the stated conditions, with a 90% confidence interval, 50 failures, and 12 suspensions, the following parameter values were obtained:

- Shape parameter (β) = 1.69
- Scale parameter (η) = 1435.85 hours
- Location parameter (γ) = 9.90 hours

The scale parameter (η), or the characteristic life of the component, in this case, indicates that by 1435.85 hours, approximately 63.2% of the pressure switches will have failed. With the introduction of suspended data, there was a clear improvement in the characteristic life of the component compared to the scale parameter value (986.88 hours) obtained in the first analysis. The position parameter (γ), or the initial life of the pressure switch, changed from 277.30 hours in the previous analysis to 9.90 hours with the inclusion of suspended data, meaning that the component has a possibility of failing almost immediately after being put into operation.
Similarly, it is possible to obtain graphical representation for the probability density function, probability of failure, reliability, and failure rate. Figure 6 shows the value for the reliability at 1000 hours of operation when suspended times are considered.

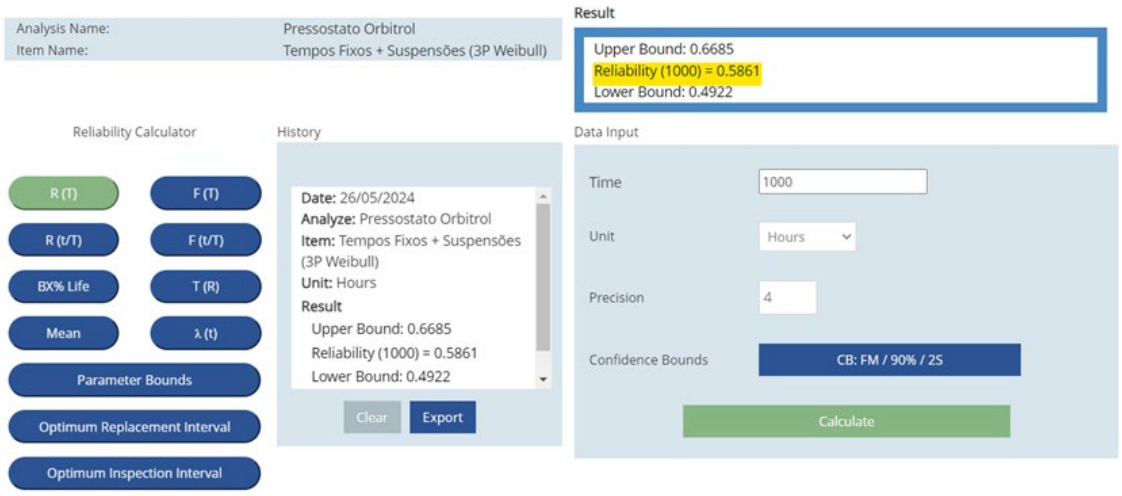

Figure 6. Printscreen of the reliability tool for 1000 hours (with suspensions)

As it can be seen, the result is a little better (0.5861 instead of 0.5062), confirming that the inclusion of suspended data gives a more real and positive results.

4.3. Failure forecast

To begin the failure forecast analysis, the failures of the studied component in the last 2 years were analysed. With the use of the computational tool, it was also possible to forecast returns within the warranty period. For this purpose, the Warranty Analysis - NRI (Non-Repairable Items) software module was selected, as the warranties analysed in this study involve situations where the damaged component is replaced rather than repaired.
The first step was to identify the number of units sold and the returns for each month in 2023. These data were then entered into a Nevada Chart, which can be observed in Table 3.

Period	Sales	Returns											
		feb/23	mar/23	apr/23	may/23	jun/23	jul/23	aug/23	sep/23	oct/23	nov/23	dec/23	jan/24
jan/23	21	3	3	2	1	3	2	1	1	1	1	1	1
feb/23	18		2	2	0	1	1	1	1	1	1	0	0
mar/23	17			6	1	1	2	1	3	1	1	0	1
apr/23	7				0	0	2	0	1	0	1	0	1
may/23	19					1	0	0	1	2	1	0	1
jun/23	8						0	1	0	0	0	0	0
jul/23	16							2	1	1	0	1	2
aug/23	9								2	0	1	0	0
sep/23	5									1	2	0	0
oct/23	7										1	1	1
nov/23	16											4	1
dec/23	11												1
jan/24	14												
feb/24	7												
mar/24	10												

Table 3. Sales and returns of the component under analysis.

With the triparametric Weibull distribution, the following parameters were determined:

- Shape parameter (β) = 0.5102
- Scale parameter (η) = 9.59 months
- Location parameter (γ) = 0.99 months

This means that about 63.2% of the sold items will fail after 9.6 months.
This simulation allows us to obtain the previsional number of returns during the warranty period for the next 4 months (Table 4).

Period	Sales	feb/24	mar/24	apr/24	may/24
jan/23	21	0,05	0,04	0,04	0,04
feb/23	18	0,4	0,36	0,33	0,3
mar/23	17	0	0	0	0
apr/23	7	0,11	0,1	0,09	0,08
may/23	19	0,76	0,67	0,6	0,54
jun/23	8	0,44	0,38	0,34	0,3
jul/23	16	0,61	0,52	0,46	0,41
aug/23	9	0,45	0,37	0,32	0,28
sept/23	5	0,17	0,14	0,11	0,1
oct/23	7	0,39	0,3	0,25	0,21
nov/23	16	1,37	0,94	0,73	0,59
dec/23	11	2,49	0,94	0,64	0,5
jan/24	14	0,42	3,39	1,27	0,87
feb/24	7		0,21	1,69	0,64
mar/24	10			0,3	2,42
	Total	**7,64**	**8,37**	**7,17**	**7,28**

Table 4. Forecast for returns of the component under analysis.

During the study, it was possible to record the number of returns for the months under observation and compare it with the forecast presented in Table 6. By comparing the forecasted numbers with the actual figures, the following variations were observed:

- **February 2024**: The simulation predicted 7.64 warranty returns, while the actual number was 8, resulting in a percentage deviation of 4.48%.
- **March 2024**: The simulation predicted 8.37 warranty returns, while the actual number was 9, with a percentage deviation of 7.02%.
- **April 2024**: The simulation predicted 7.17 warranty returns, while the actual number was 7, resulting in a percentage deviation of -2.49%.
- **May 2024**: The simulation predicted 7.28 warranty returns, while the actual number was 8, with a percentage deviation of 9%.

These results indicate that the simulation forecasts are quite close to the actual values, with minor discrepancies that can be attributed to unidentified equipment or inherent forecasting variabilities. Nonetheless, it is possible to affirm that this warranty forecasting model can continue to be used for a more efficient management of returns during the warranty period.

5. CONCLUSIONS AND FUTURE WORK

This work aimed to conduct a detailed reliability analysis and warranty return forecasting using robust statistical and analytical methods. The AHP methodology was essential for identifying the critical component among all evaluated items, allowing the hierarchical ranking of components based on their importance, ensuring that the study focused on the most relevant parts for the company's specific needs. This approach facilitated prioritization

and provided a solid foundation for the subsequent reliability analysis steps.
The reliability analysis was developed using statistical models to determine the most suitable distribution for the failure data (Weibull distribution). After that, a new analysis was also conducted to include suspended data. With the introduction of suspended data into the Weibull distribution, a significant improvement was observed in the component's characteristic life compared to the value obtained in the first analysis. In summary, incorporating suspended data significantly improves the reliability of the models.
To complete the study, a warranty return forecast was conducted based on monthly sales in 2023 and the subsequent recorded warranty returns. The model's accuracy was validated by comparing forecasted values with actual results, where the maximum percentage deviation was 9%. This result indicates that the developed model is reliable and can be used for future warranty return predictions.
This study demonstrated the effectiveness of combining different analytical and statistical methods for reliability analysis and warranty return forecasting and the advantage of using computational tools in this type of analysis. Furthermore, the practical application of this study's findings can lead to significant improvements in warranty management and the reliability of analysed systems within the company's structure.
For future work, it is recommended to explore the integration of machine learning techniques and big data analytics to enhance prediction accuracy and the effectiveness of reliability analysis.
Additionally, it is suggested that all components exhibiting recurring failures undergo a reliability analysis to determine their useful life expectancy and ensure an adequate stock supply based on the number of existing equipment units. Implementing such measures is essential to ensure operational continuity and optimize resource management. Lastly, by contributing to predictive maintenance, these measures promote a culture of continuous improvement within the organization. In this way, the company increases the reliability and lifespan of its equipment, optimises resources, and enhances customer satisfaction.

REFERENCES

[1] Kostagiolas, P., "Measuring libraries' intellectual capital", *In Managing intellectual capital in libraries* (pp. 87–127). Chandos Publishing. https://doi.org/10.1016/B978-1-84334-678-4.50004-9, 2012

[2] Saaty, T. L., "Decision making with the analytic hierarchy process", *International Journal of Services Sciences*, 1(1), 83–98. https://doi.org/10.1504/IJSSCI.2008.017590, 2008

[3] Lee, M. C., Wang, W., & Wang, H. Y., "A method of performance evaluation by using the analytic network process and balanced score card", *In Proceedings of the 2007 International Conference on Convergence Information Technology (ICCIT 2007)*, (pp. 235–240). IEEE. https://doi.org/10.1109/ICCIT.2007.4420266, 2007

[4] Taherdoost, H., "Decision making using the analytic hierarchy process (AHP): A step by step approach", *International Journal of Economics and Management Systems*, Vol. 2, 2017

[5] Khaira, A., & Dwivedi, R. K., "A state of the art review of the analytic hierarchy process", *Materials Today: Proceedings*, 5(2), 4029–4035. https://doi.org/10.1016/j.matpr.2017.11.663, 2018
[6] Vargas, R. V., "Using the analytic hierarchy process (AHP) to select and prioritize projects in a portfolio", *PMI Global Congress 2010* - North America, 2010
[7] Wollmann, D., Steiner, M. T. A., Vieira, G. E., & Steiner, P. A., "Details of the analytic hierarchy process technique for the evaluation of health insurance companies", *Gestão & Produção*, 21(3), 583–593. http://dx.doi.org/10.1590/S0103-65132013005000070, 2014
[8] Forman, E. H., & Gass, S. I., "The analytic hierarchy process—An exposition", *Operations Research*, 49(4), 469–486. https://doi.org/10.1287/opre.49.4.469.11231, 2001
[9] Emrouznejad, A., & Marra, M., "The state of the art development of AHP (1979–2017): A literature review with a social network analysis", *International Journal of Production Research*, 55(22), 6653–6675. https://doi.org/10.1080/00207543.2017.1334976, 2017
[10] Madzík, P., & Falát, L., "State-of-the-art on analytic hierarchy process in the last 40 years: Literature review based on Latent Dirichlet Allocation topic modelling", *PLoS ONE*, 17(5), e0268777. https://doi.org/10.1371/journal.pone.0268777, 2022
[11] Elsayed, E. A., "*Reliability engineering (3rd ed.)*", Wiley-Blackwell. Rutgers University. ISBN: 978-1-119-66592-2, 2021
[12] Birolini, A., "*Reliability engineering: Theory and practice (5th ed.)*", Springer. https://doi.org/10.1007/978-3-540-49390-7, 2007
[13] Modarres, M., Kaminskiy, M. P., & Krivtsov, V., "*Reliability engineering and risk analysis: A practical guide (3rd ed.)*", CRC Press. https://doi.org/10.1201/9781315382425, 2016
[14] CEN, "*EN 13306 – Maintenance - Maintenance terminology*". Comité Européen de Normalisation. Bruxelles. Belgium, 2017
[15] Lai, C.-D., "*Generalized Weibull distributions (1st ed.)*", Springer. https://doi.org/10.1007/978-3-642-39106-4, 2014
[16] Rinne, H., "*The Weibull distribution: A handbook (1st ed.)*", CRC Press. https://doi.org/10.1201/9781420087444, 2008
[17] O'Connor, A., Modarres, M., & Mosleh, A., "*Probability distributions used in reliability engineering*", Center for Risk and Reliability, University of Maryland. ISBN: 978-0-9966468-1-9, 2016
[18] Galar, D., & Kumar, U., "*Chapter 6 - Prognosis. In eMaintenance - Essential Electronic Tools for Efficiency*", (pp. 311–370). ISBN 978-0-12-811153-6, Academic Press, Elsevier. https://doi.org/10.1016/B978-0-12-811153-6.00006-3, 2017
[19] Ikbal, N. A. M., Halim, S. A., & Ali, N., "Estimating Weibull parameters using maximum likelihood estimation and ordinary least squares: Simulation study and application on meteorological data", *Mathematics and Statistics*, 10(2), 269–292. https://doi.org/10.13189/ms.2022.100201, 2022

SYMCOMP 2025
Lisbon, 10-11 April 2025

DAMPING FROM THERMOELASTICITY IN STRUCTURES UNDER TORSIONAL LOADING

André R. D. Carvalho[1,2*]

1: CIMOSM, ISEL - Instituto Superior de Engenharia de Lisboa,
Instituto Politécnico de Lisboa,
Rua Concelheiro Emídio Navarro 1, 1959-007 Lisboa, Portugal
e-mail: andre.carvalho@isel.pt, web: http://cimosm.isel.pt

2: IDMEC, ISEL - Instituto Superior de Engenharia de Lisboa,
Instituto Politécnico de Lisboa,
Rua Concelheiro Emídio Navarro 1, 1959-007 Lisboa, Portugal

Keywords: Thermoelasticity, Damping, Solid Elements, Harmonic Simulation

Abstract. *The study of damping is a fundamental area in mechanical vibrations. Damping is the cause of the loss of energy in vibrating structures. However, the process in which the energy is dissipated depends on the material properties, structure, and other parameters. One of the base sources of damping in solid materials is the conversion of energy into heat, which can be modeled using the thermoelastic model. This model couples the standard mechanical wave equation with the heat equation and predicts that the dissipated energy is converted into Entropy. While thermoelastic damping is more prominent in smaller structures (e.g., microresonators), it is present in all structures under any deformation that generates a change in volume, albeit at the lower end of the frequency spectrum. The main goal of this paper is to determine the damping profile with the frequency generated by the torsional load in non-circular cross-section structures using a Finite Element Analysis with 3D solid elements. The simulation results show that, while the thermoelastic damping generated by torsion is smaller than the one generated by bending, it cannot be ignored for some noncircular cross-sectioned geometries.*

1 INTRODUCTION

Thermoelastic damping is an intrinsic phenomenon in all structures and is a fundamental source of structural energy dissipation [5, 4]. The thermoelastic model originates from first principles, coupling the elastic wave equation with the heat conduction equation. Although its theoretical foundation was established in the 1950s [1, 3], the complexity of the model required the advent of modern computational methods for in-depth analysis [19, 2, 21, 13, 3, 4].

DOI:10.5281/zenodo.15164446

Damping arises from irreversible entropy generation caused by deformation-induced internal heat fluxes. This energy dissipation mechanism is especially significant in both very small and very large structures operating at low frequencies [4, 11, 9, 8]. At the microscale, temperature effects substantially influence vibration behavior and must be carefully considered [22, 23, 24, 15]. As such, a thorough understanding of thermoelastic damping is essential for designing optimized mechanical systems.
Depending on the application, damping can be either detrimental or beneficial. For instance, in microresonators, excessive damping may degrade performance [22, 23, 20], whereas in microscale damping devices, it plays a crucial functional role [12, 7, 10, 15, 20]. While there are some previous works regarding the effect of torsion in thermoelasticity, most use simplified 1D models or focus only on the thermal side of the problem, [15, 24, 18]. The main goal of this work is to study the behavior of damping generated by the thermoelastic model in geometries under torsional loads. A 3D quadratic solid Finite Element Analysis is used to give more accurate results. Solid elements are computationally more demanding due to the requirement for finer meshes to accurately capture bending and torsional phenomena. However, they offer greater versatility and insight into local phenomena, such as detailed temperature variation across the thickness [4].
This article is structured into four sections: Introduction, Materials and Methods, Results and Discussion, and Conclusions. The Materials and Methods section elaborates on the formulation of the thermoelastic model and the 3D quadratic hexahedral solid elements. The Results and Discussion section covers the mesh generation process, convergence studies, and simulation results. The Conclusions section provides a summary of the study findings.

2 MATERIALS AND METHODS

2.1 The Thermoelastic Model

The thermoelastic model or linear thermoelasticity dynamic model results from the complete coupling of the elastic wave equation with the heat equation and is given by (1):

$$\begin{cases} \rho\ddot{\mathbf{u}} - \mu\nabla^2\mathbf{u} - (\lambda+\mu)\nabla(\nabla\cdot\mathbf{u}) + \gamma\nabla\theta = f \\ \rho C_p\dot{\theta} - k\nabla^2\theta + \gamma T_0(\nabla\cdot\dot{\mathbf{u}}) = q, \end{cases} \tag{1}$$

where $\mathbf{u}$ is the displacement vector ($\mathbf{u} = [u_x, u_y, u_z]^T$), θ is the temperature variation, f is the body load and q is the body heat flux. All function quantities are functions of the Euclidean coordinates and time. The constants in the model are the material properties: density (ρ), Lamé constants (μ and λ), specific heat capacity (C_p), and thermal conductivity (k).
The Lamé constants are given by:

$$\lambda = \frac{\nu E}{(1+\nu)(1-2\nu)}, \tag{2a}$$

$$\mu = \frac{E}{2(1+\nu)}, \tag{2b}$$

where E is the Young modulus and ν is the Poisson coefficient.
Since temperature is critical to the problem, all coefficients must be specified at the same base temperature T_0, the point around which linearization is performed in the thermoelastic model. Finally, the coefficient γ is the coupling term and is given by:

$$\gamma = (3\lambda + 2\mu)\alpha, \tag{3}$$

where α is the linear thermal expansion coefficient since equation (1) is a linearized equation, it is only valid for small deformations and small temperature variations: $\frac{\theta}{T_0} \ll 1$.

2.2 Energy flow and balance in the thermoelastic model

Because it couples two fields in a single system, the thermoelastic model has some particularities regarding energy flow, especially when compared with the standard elastic wave equation. Analyzing the energy flow makes it possible to understand the phenomena behind the damping predicted by this model. A complete representation of the energy flow in the system can be seen in Figure 1.

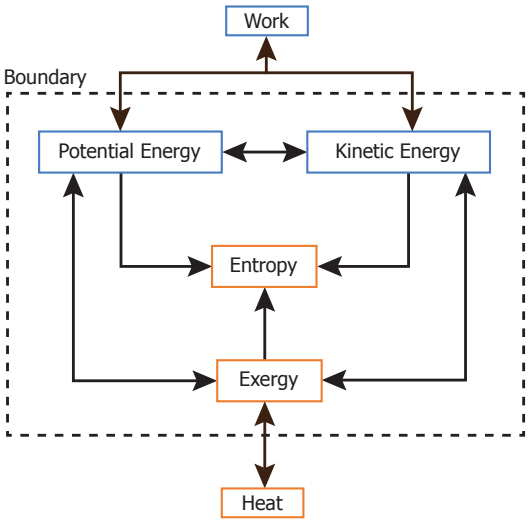

Figure 1: Energy flow in the thermoelastic model. The wave equation originates energies marked in blue, and energies marked in orange are originated by the heat equation, [4].

The only non-conservative energy in the domain is the work lost to irreversible Entropy generation. One of the characteristics of the equation (1) is that the damping term is not explicit, much unlike all other damping models used in mechanical vibrations. Damping

occurs by generating irreversible Entropy due to the existing internal heat fluxes. The irreversible entropy is generated whenever there is a heat flux in the material, and the total energy lost this way is given by the Gouy-Stodola theorem, [19]:

$$W_S = \frac{k}{T_0} \iint_\Omega \nabla\theta \cdot \nabla\theta \, \mathrm{d}V \, \mathrm{d}t, \tag{4}$$

where W_S is the work lost to irreversible entropy.
In light of the First Law of Thermodynamics, the complete energy balance is given by the following equation:

$$\Delta U = \mathcal{V} + \mathcal{T} + \mathcal{B} + W_S = W - Q, \tag{5}$$

where ΔU is the variation of the internal energy, $\mathcal{V}$ is the mechanical potential energy, $\mathcal{T}$ is the kinetic energy and $\mathcal{B}$ is the Exergy of the system. W and Q are the work and heat flows in the system (through the boundaries or in form of volumetric sources).
Since this study is focused on harmonic analysis, all conservative energies in a cycle are zero, and all boundaries will be considered Adiabatic ($Q = 0$), the Equation 5 reduces to:

$$\Delta U_{\text{cycle}} = W_{S_{\text{cycle}}} = W_{\text{cycle}}, \tag{6}$$

From Equation 6, the dissipated energy can be determined either by computing the work done to the system or by determining the energy lost to entropy (Equation 4). However, neither measure is a suitable quantifier for the system damping since it is susceptible to resonance. As such, they are not generic or comparable enough. An alternative is to use the loss angle or an equivalent damping factor.
The loss angle is a quantity widely used in material science to characterize damping in viscoelastic materials and is the phase of a complex Young modulus definition:

$$E^* = E' + E''\mathrm{i} = E(1 + \tan(\phi_E)\mathrm{i}) \tag{7}$$

where E^* is the dynamic modulus, E' is the storage modulus (reduces to the Young Modulus in purely elastic materials), E'' is the loss modulus that quantifies the dissipated elastic energy, and ϕ_E is the loss angle.
The loss angle is related to the hysteretic model and the hysteretic damping coefficient:

$$\phi_E = \arctan \eta \tag{8}$$

where η is the hysteretic damping coefficient.
For the hysteretic model, the damping coefficient can be extracted from Equation 4 using:

$$\eta(\omega) = \frac{W_{S_{\text{cycle}}}}{\pi k \Re(X)^2}, \tag{9}$$

where k is the stiffness of the spring, and X is the complex amplitude of the displacement. The denominator of Equation 9 is the maximum potential energy in a cycle. The equivalent hysteretic damping coefficient is also known in the literature as the quality factor (Q_{TED}^{-1})[1], [25, 14, 17].

2.3 Finite Element model

The thermoelastic model was implemented on an in-house Finite Element Analysis software in 2D quadrilateral and 3D hexahedral solid elements (linear and quadratic), [4]. The software was written in C++ and Intel® Math Kernel Library performs the linear algebra routines.
For this study, a solid standard 27 nodes quadratic hexahedral 3D element was defined according to the Figure 2.

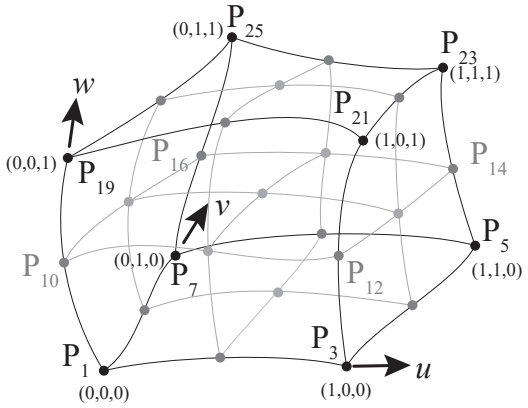

Figure 2: Twenty seven node 3D quadratic solid element.

The full discretized version of Equation 1 is given by Equation 10

$$\boldsymbol{\mathcal{M}} \begin{bmatrix} \ddot{\mathbf{u}}_x \\ \ddot{\mathbf{u}}_y \\ \ddot{\mathbf{u}}_z \\ \ddot{\boldsymbol{\theta}} \end{bmatrix} + \boldsymbol{\mathcal{C}} \begin{bmatrix} \dot{\mathbf{u}}_x \\ \dot{\mathbf{u}}_y \\ \dot{\mathbf{u}}_z \\ \dot{\boldsymbol{\theta}} \end{bmatrix} + \boldsymbol{\mathcal{K}} \begin{bmatrix} \mathbf{u}_x \\ \mathbf{u}_y \\ \mathbf{u}_z \\ \boldsymbol{\theta} \end{bmatrix} = \begin{bmatrix} \mathbf{Mf}_x \\ \mathbf{Mf}_y \\ \mathbf{Mf}_z \\ \mathbf{Mq} \end{bmatrix} \tag{10}$$

where u_x, u_y and u_z are the displacements in the x, y and z directions, respectively, $\boldsymbol{\mathcal{M}}$, $\boldsymbol{\mathcal{C}}$ and $\boldsymbol{\mathcal{K}}$, are the mass, velocity[2] and stiffness matrices. For more details on the matrices, please refer to [4].

[1]The *TED* under script refers to the thermoelastic damping. The quality factor can be defined as any damping.

[2]The term damping matrix should be avoided because the damping in the thermoelastic model is not completely contained in this matrix.

2.4 Harmonic solution

To get the solution of the harmonic problem, a Fourier transform must be applied to Equation 10:

$$\left(-\boldsymbol{\mathcal{M}}\omega^2 + \boldsymbol{\mathcal{C}}\omega\mathrm{i} + (\boldsymbol{\mathcal{K}} - \boldsymbol{\mathcal{K}}_\Theta)\right) \begin{bmatrix} \mathbf{U}_x \\ \mathbf{U}_y \\ \mathbf{U}_z \\ \boldsymbol{\Theta} \end{bmatrix} = \begin{bmatrix} \mathbf{MF}_x \\ \mathbf{MF}_y \\ \mathbf{MF}_z \\ \mathbf{MQ} \end{bmatrix} + \begin{bmatrix} \sum_i^{N_b} \mathbf{m}_i \mathbf{P}_x \\ \sum_i^{N_b} \mathbf{m}_i \mathbf{P}_y \\ \sum_i^{N_b} \mathbf{m}_i \mathbf{P}_z \\ \sum_i^{N_b} \mathbf{m}_i \mathbf{Q}_b \end{bmatrix}, \tag{11}$$

where ω is the angular frequency of the excitation and $\mathbf{U}$, $\boldsymbol{\Theta}$, $\mathbf{F}$, $\mathbf{Q}$, $\mathbf{P}$ and $\mathbf{Q}_b$ are the complex amplitudes of the displacements, temperature variation, body forces, body heat fluxes, boundary loads and boundary heat fluxes, respectively. The matrices $\boldsymbol{m}$ are the boundary integration matrices. The matrix $\boldsymbol{\mathcal{K}}_\Theta$ contains the Robin BC elements of the thermoelastic BCs, where$\boldsymbol{m}_{ni_x}$ are the boundary integration matrices weighted by the normal vector, [4]

$$\boldsymbol{\mathcal{K}}_\Theta = \begin{bmatrix} 0 & 0 & 0 & \sum_i^{N_b} \gamma \mathbf{m}_{ni_x} \\ 0 & 0 & 0 & \sum_i^{N_b} \gamma \mathbf{m}_{ni_y} \\ 0 & 0 & 0 & \sum_i^{N_b} \gamma \mathbf{m}_{ni_z} \\ 0 & 0 & 0 & 0 \end{bmatrix}. \tag{12}$$

Finally, to apply Dirichlet BCs, the system matrix must be decoupled accordingly.
To obtain the complex amplitudes (and the corresponding amplitudes and phases), Equation 11 is solved using the linear equation solver.

2.5 Energy computation in the finite element model

For a harmonic analysis, as stated by Equation 6, only the boundary energy fluxes and the work lost to irreversible Entropy need to be determined. To determine these quantities used the finite element model, Equation 4 must be discretized and integrated for a complete cycle ($0 \leq t < \frac{2\pi}{\omega}$). The discretized Gouy-Stodola theorem for a cycle is given by:

$$W_{S_{\text{cycle}}} = \frac{\pi}{T_0 \omega} \left(\Re(\boldsymbol{\Theta})^T \mathbf{K}_\theta \Re(\boldsymbol{\Theta}) + \Im(\boldsymbol{\Theta})^T \mathbf{K}_\theta \Im(\boldsymbol{\Theta}) \right), \tag{13}$$

where $\mathbf{K}_\theta$ is the stiffness matrix for the thermal part of the model, [4].
The equivalent hysteretic damping coefficient is determined by:

$$\eta(\omega) = \frac{W_{S_{\text{cycle}}}}{\pi \begin{bmatrix} \Re(\mathbf{U}) \\ 0 \end{bmatrix}^T \boldsymbol{\mathcal{K}} \begin{bmatrix} \Re(\mathbf{U}) \\ 0 \end{bmatrix}} \tag{14}$$

2.6 Geometries and materials

This work used four geometries: a circular-section beam, a square-section beam, a square plate, and a symmetrical ASTM A6 wide flange I-beam (W150x100x24). The length of

all beams in this study is 3.2m, guaranteeing a length/height ratio of 20 (meaning the maximum thickness of the beams is 0.16m). The square plate has dimensions of 3.2m by 3.2m by 0.16m.
All geometries are made of Copper, with the material properties shown in Table 1.

Property	**Unit**	**Copper**
Young modulus	GPa	120
Poisson coefficient	-	0.355
Density	kg/m^3	8960
Thermal expansion coefficient	K^{-1}	16.7×10^{-6}
Conductivity	$W/(m \cdot K)$	401
Specific heat capacity	$J/(kg \cdot K)$	385

Table 1: Properties of the materials used in this study. All properties are taken at a base temperature, T_0, of 293.15K.

3 RESULTS AND DISCUSSION

3.1 Validation Study

The software and models used in this study were validated against other models and works. Full details on the validation studies can be consulted in [16] and [4].
A mesh converge study was done for every geometry using the maximum displacement as the convergence criterion. The primary variable for the convergence was the number of length-wise elements (N_L). The number of elements in the other direction was set according to the length-wise element. For the I-beam, the equations that define the mesh are in [4]. The mesh convergence studies for bending can be seen in Figure 3.

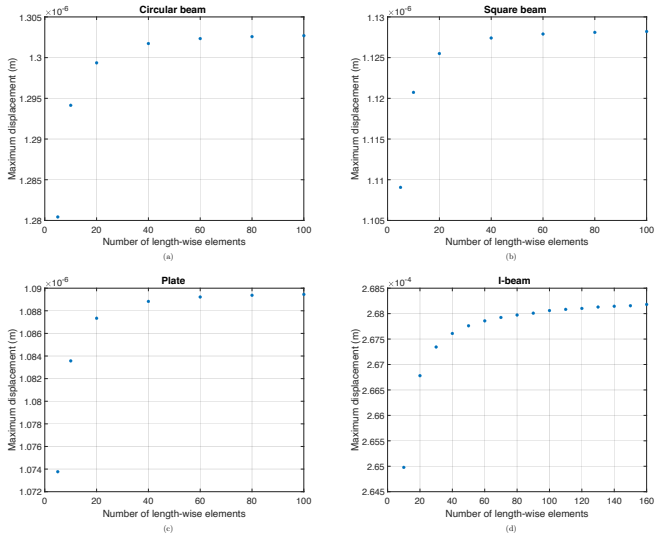

Figure 3: Mesh convergence studies for bending for: (a) circular beam, (b) square beam, (c) plate, (d) I-beam.

For torsion, it was verified that the convergence followed a similar pattern as bending. Also, for the circular beam, in torsion, quadratic elements give the exact solution; as such, fewer elements are needed. The final meshes can be seen in Figure 4.

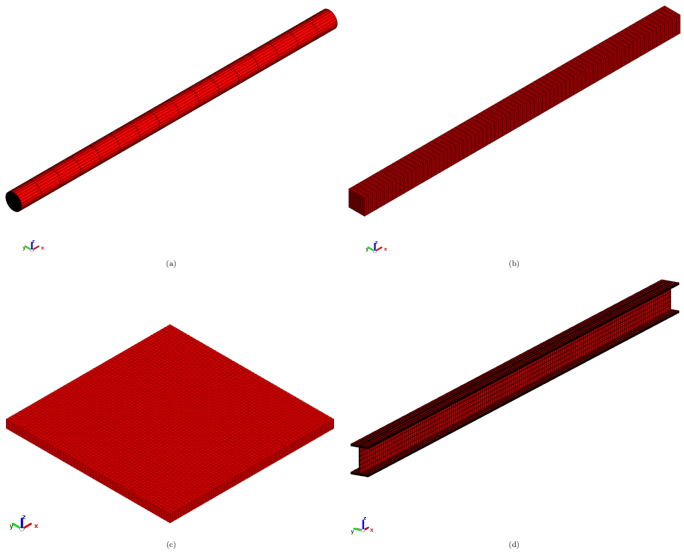

Figure 4: Meshes for: (a) circular beam, (b) square beam, (c) plate, (d) I-beam.

3.2 Case studies

In this study, the deformation and temperature variation of the four geometries were simulated for a clamped-free configuration (along the length in the x-axis), and an external load was applied at $x = L$. For bending cases, the load is constant along the section with an amplitude of 1Pa. For torsion cases, the external load varies across the surface to generate a distributed moment, given by:

$$f(y, z) = 10^7 \begin{bmatrix} -z \\ y \end{bmatrix} \text{(Pa)} \tag{15}$$

The loading for the circular and square beams can be seen in Figure 5. On the thermal

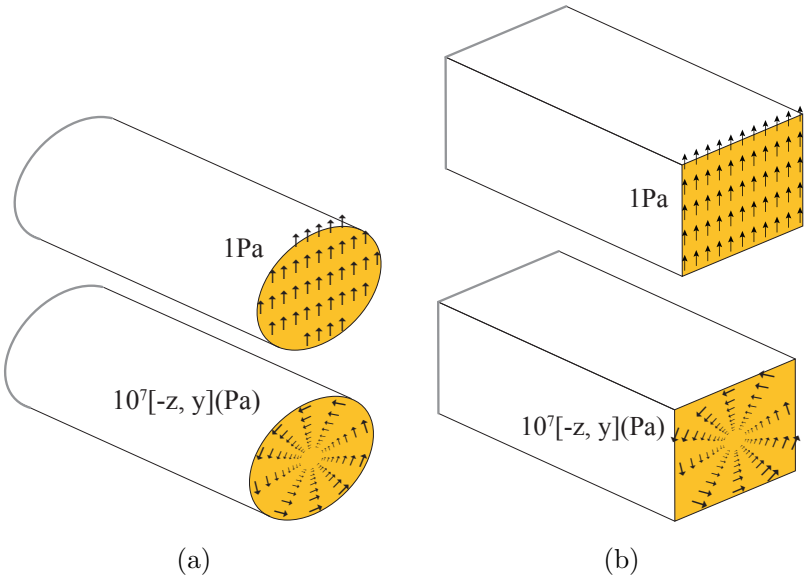

Figure 5: Loading can boundary conditions for: (a) circular beam, (b) square beam.

side, all boundaries were considered Adiabatic.

The objective of also including bending simulation in this study is to provide a reference for the magnitude of the damping generated by torsion.

All simulations were frequency sweeps from 0 to 200rad/s with an increasing sample rate. The maxima of the damping factor should be in this frequency range because the frequency interval of the maxima is defined by the smallest dimension of the enclosing parallelepiped, [6].

3.3 Results

3.3.1 Circular beam

Starting with the circular beam, results show that, as expected, the torsion does not generate thermoelastic damping, Figure 7.

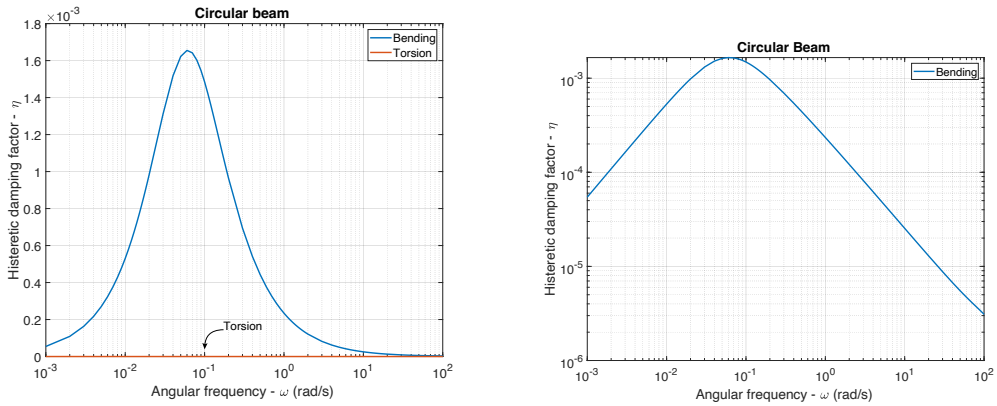

(a) (b)

Figure 6: Histeretic damping factor for the circular beam: (a) log-lin plot, (b) log-log plot (without torsion).

Because torsion in the circular beam does not generate volume changes, there are no temperature variations and, consequently, no thermoelastic damping. Equation 1 states that, in the absence of external heat flows, only material traction/compression generates temperature variation and, from Equation 4, Entropy loss. Torsion of circular members only generates shear deformations.

3.3.2 Square beam

Moving to the square cross-section beam, the results are now different, Figure 7a.
As seen in Figure 7a, the torsion generates damping. Since torsion of non-circular elements creates warping of the cross-section, some areas are under axial deformation and, as such, generate temperature variations, Figure 7b. However, in this case, when comparing with the damping generated by bending, torsional damping is much smaller, in conformity to what was reported by [24].

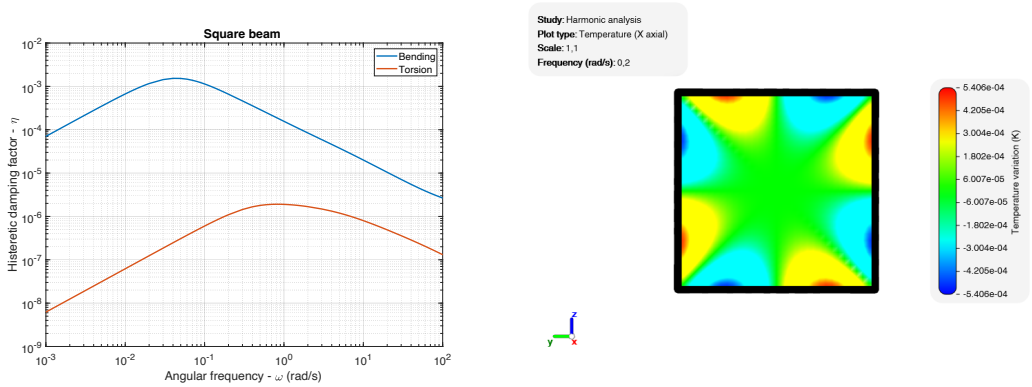

(a) (b)

Figure 7: (a) Hysteretic damping factor for the square beam under bending and torsion, (b) Temperature variation at the cross-section for torsion.

3.3.3 Plate

When studying the effect of torsion in a plate, the results are more pronounced, Figure 8.

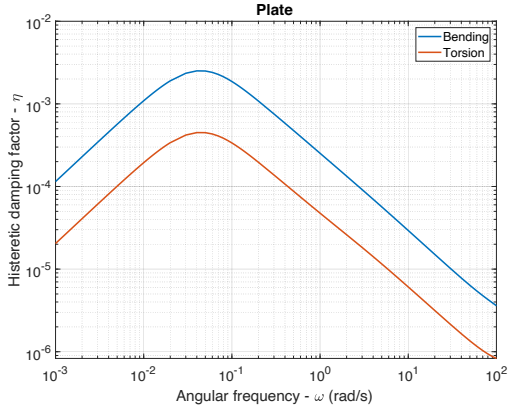

Figure 8: Histeretic damping factor for the plate under bending and torsion.

For plates under torsion, the thermoelastic damping, because it is only one order of magnitude smaller than the one generated by bending, cannot be dismissed as in the previous cases. Due to the very different aspect ratio of the cross-section of the plate, the warping generated by torsion is much higher than in the square beam, and, consequently, the temperature variations are much higher across the cross-section, Figure 9.

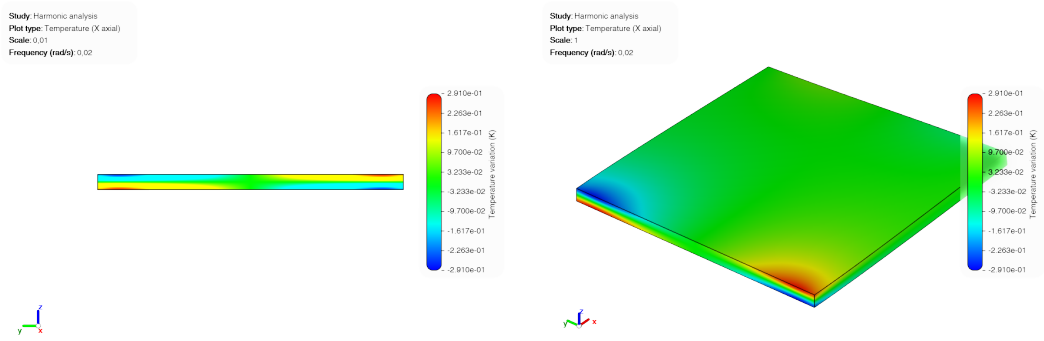

(a) (b)

Figure 9: Temperature variation for a plate under torsion: (a) at the cross-section, (b) across the plate.

3.3.4 I-beam

While I-beams are not common in the micro-scale, however, due to their cross-section, they make interesting cases to study, Figure 10.

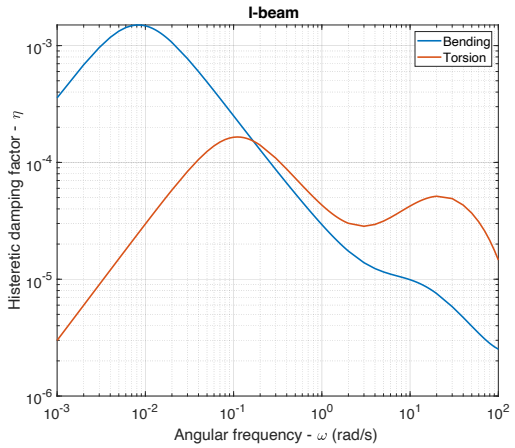

Figure 10: Histeretic damping factor for the I-beam under bending and torsion.

From Figure 10, it can be seen that the effect of damping in torsion is even more evident in this I-beam than it was in the plate. In this case, the torsion-damping factor is higher in higher frequencies than the one generated by bending. It can be seen in the bending damping (studied in more detail in, [4] and [6]) damping in torsion also has two maxima, showing an overall "mode" of damping in lower frequencies and a more local "mode" of damping, as it can be seen in Figure 11.

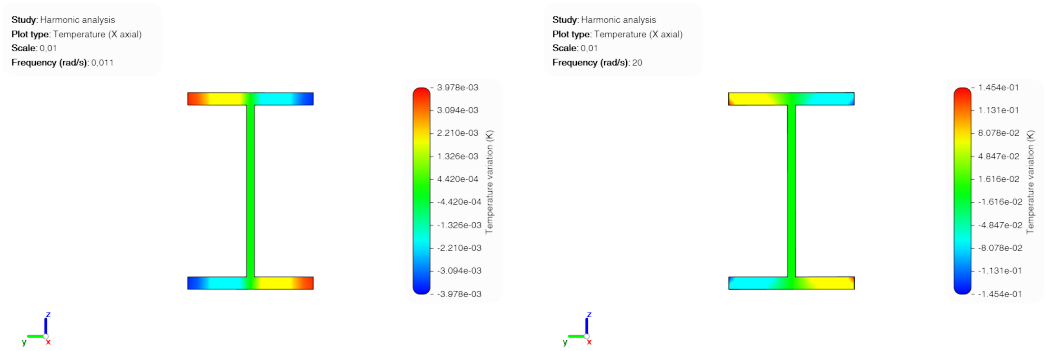

(a) (b)

Figure 11: Temperature variation at the cross-section for an I-beam under torsion: (a) for a frequency of 0.11rad/s, (b) for a frequency of 20rad/s.

3.3.5 Overall analysis

When comparing all damping factors for all geometries, Figure 12, it can be seen that in bending, the behavior of the damping factor with frequency is essentially the same (except the dual mode of the I-beam), both in magnitude and location of the maximum in frequency. This is justified by all geometries having a more or less similar behavior under bending and the proportions being also identical to each other, which is one of the most important defining factors in thermoelastic damping (more than the actual dimensions that affect only the frequency of the maxima) [4, 6].

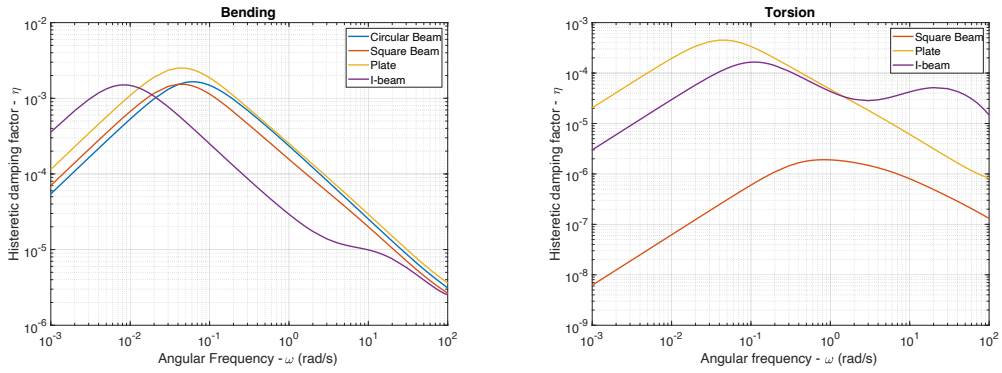

(a) (b)

Figure 12: Damping factors: (a) for bending, (b) for torsion.

When analyzing the behavior of damping when under torsion, there are notable differ-

ences, especially in magnitude, where the more complex cross-sections with higher aspect ratios have generally higher damping magnitudes, which means that higher warping is the defining factor in thermoelastic damping in torsion.

4 Conclusions

This study primarily aimed to investigate the damping behavior of the thermoelastic effect under torsional loads. The results obtained from simulations using harmonic Finite Element Analysis reveal the following:

- While the behavior of damping under being largely depends on the proportions of the geometries (length versus cross-section dimension), under torsion, convex, and more complex cross-sections have higher damping factors due to high warping.

- Torsional thermoelastic damping in circular and square beams can be safely ignored when also in the presence of bending deformation, but in plates and I-beams, it cannot.

- in higher frequency torsion deformations in I-beam, the torsional damping can be higher than the one created by bending.

This study prompts several questions for future research. Foremost is the imperative to experimentally validate the obtained results under controlled conditions. The model developed for this study can assist in designing the experiment and selecting suitable sensors and actuators. Another question to be explored in future work is the increase in resonant frequencies due to the absence of "thermal inertia" in the heat equation. The speed of the hypothetical thermal wave (or "second sound", as termed by some authors) should be studied for the materials used in this investigation to refine and update the thermoelastic model.

REFERENCES

[1] M. A. Biot. Thermoelasticity and irreversible thermodynamics. *Journal of Applied Physics*, 27(3):240–253, 1956.

[2] J.E. Bishop and V.K. Kinra. Thermoelastic damping of a laminated beam in flexure and extension. *Journal of Reinforced Plastics and Composites*, 12(2):210–226, 1993.

[3] B. A. Boley and A. D. Barber. Dynamic response of beams and plates to rapid heating. *J. Appl. Mech.*, 24(3):413–416, 1957.

[4] André Carvalho. Study of damping of bare and encased steel i-beams using the thermoelastic model. *Buildings*, 13(12), 2023.

[5] André Carvalho. Study of the influence of convection boundary condition on the damping factor in a thermoelastic beam using solid elements. In *Proceedings of 6th International Conference on Numerical and Symbolic Computation*, pages 151–168, 2023.

[6] André Carvalho. Harmonic behavior of functionally graded i-shaped beams using the thermoelastic model. In *ECCOMAS 2024*, 2024.

[7] A Fichera, A Pagano, and R Volpe. Microscale damper prototype: A preliminary study on suppressing air flow oscillations within microchannels. *Journal of Physics: Conference Series*, 2685(1):012022, jan 2024.

[8] Sayantan Guha and Abhishek Kumar Singh. Frequency shifts and thermoelastic damping in different types of nano-/micro-scale beams with sandiness and voids under three thermoelasticity theories. *Journal of Sound and Vibration*, 510:116301, 2021.

[9] F.L. Guo, G.Q. Wang, and G.A. Rogerson. Analysis of thermoelastic damping in micro- and nanomechanical resonators based on dual-phase-lagging generalized thermoelasticity theory. *International Journal of Engineering Science*, 60:59–65, 2012.

[10] S. S. Iyer, R. Vedad-Ghavami, H. Lee, M. Liger, H. P. Kavehpour, and R. N. Candler. Nonlinear damping for vibration isolation of microsystems using shear thickening fluid. *Applied Physics Letters*, 102(25):251902, 06 2013.

[11] Ehsan Kazemnia Kakhki, Seyed Mahmoud Hosseini, and Masoud Tahani. An analytical solution for thermoelastic damping in a micro-beam based on generalized theory of thermoelasticity and modified couple stress theory. *Applied Mathematical Modelling*, 40(4):3164–3174, 2016.

[12] Catherine A. Kerrigan, Ken K. Ho, K. P. Mohanchandra, and Gregory P. Carman. Microscale damping using thin film active materials. In Yuji Matsuzaki, Mehdi Ahmadian, and Donald J. Leo, editors, *Active and Passive Smart Structures and Integrated Systems 2007*, volume 6525, page 65250V. International Society for Optics and Photonics, SPIE, 2007.

[13] V. K. Kinra and K. B. Milligan. A Second-Law Analysis of Thermoelastic Damping. *Journal of Applied Mechanics*, 61(1):71–76, 03 1994.

[14] Ron Lifshitz and M. L. Roukes. Thermoelastic damping in micro- and nanomechanical systems. *Phys. Rev. B*, 61:5600–5609, Feb 2000.

[15] Xiao Liu, H. Haucke, J.F. Vignola, H.J. Simpson, J.W. Baldwin, B.H. Houston, and D.M. Photiadis. Understanding the internal friction of a silicon micro-mechanical

oscillator. *Materials Science and Engineering: A*, 521-522:389–392, 2009. 15th International Conference on Internal Friction and Mechanical Spectroscopy.

[16] M.A.R. Loja, André Carvalho, and Ines C.J. Barbosa. A study on the static behavior of functionally graded i-shaped beams. *AIMS Materials Science*, 11(1):28–57, 2024.

[17] Dileesh V. Parayil, Salil S. Kulkarni, and Dnyanesh N. Pawaskar. Analytical and numerical solutions for thick beams with thermoelastic damping. *International Journal of Mechanical Sciences*, 94-95:10–19, 2015.

[18] Yong-Lin Pi and Mark Andrew Bradford. Thermoelastic lateral-torsional buckling of fixed slender beams under linear temperature gradient. *International Journal of Mechanical Sciences*, 50(7):1183–1193, 2008.

[19] Enrico Serra and Michele Bonaldi. A finite element formulation for thermoelastic damping analysis. *International Journal for Numerical Methods in Engineering*, 78(6):671–691, 2009.

[20] J.N. Sharma and R. Sharma. Damping in micro-scale generalized thermoelastic circular plate resonators. *Ultrasonics*, 51(3):352–358, 2011.

[21] Alexandros G Solomou, Theodoros T Machairas, and Dimitris A Saravanos. A coupled thermomechanical beam finite element for the simulation of shape memory alloy actuators. *Journal of Intelligent Material Systems and Structures*, 25(7):890–907, 2014.

[22] Yuxin Sun, Daining Fang, and Ai Kah Soh. Thermoelastic damping in micro-beam resonators. *International Journal of Solids and Structures*, 43(10):3213–3229, 2006.

[23] Yuxin Sun and Masumi Saka. Thermoelastic damping in micro-scale circular plate resonators. *Journal of Sound and Vibration*, 329(3):328–337, 2010.

[24] Yongpeng Tai, Pu Li, and Yuming Fang. Thermoelastic damping in torsion microresonators with coupling effect between torsion and bending. *Journal of Sound and Vibration*, 333(5):1509–1525, 2014.

[25] Clarence Zener. Internal friction in solids. i. theory of internal friction in reeds. *Phys. Rev.*, 52:230–235, Aug 1937.

SYMCOMP 2025
Lisbon, 10-11 April 2025

HOW TEACHING METHODS CAN INFLUENCE THE CARBON FOOTPRINT

Rui B. Ruben[1,2]*, Luís Coelho[1,3], Judite Vieira[1,4], Marcelo Gaspar[1,2], Paulo Carvalho[1,5], Hachimi Abba[6], Jorma Sateri[7], Christian Gotz[8]

1: School of Technology and Management Polytechnic University of Leiria, Leiria, Portugal
e-mail: {rui.ruben;luis.coelho;judite.vieira;marcelo.gaspar;paulo.carvalho}@ipleiria.pt,
web: https://www.ipleiria.pt/estg/

2: CDRSP, Polytechnic University of Leiria, Leiria, Portugal
web: https://cdrsp.ipleiria.pt/

3: CFisUC, Centre for Physics of the University of Coimbra, Department of Physics, University of Coimbra, Coimbra, Portugal

4: ALiCE—Associate Laboratory in Chemical Engineering, Faculty of Engineering, University of Porto, Porto, Portugal

5: ADAI – Association for Development of Industrial Aerodynamics University of Coimbra, Coimbra, Portugal

6: Université Hauts de France, Valenciennes, France
e-mail: hachimi.abba@uphf.fr

7: Metropolia University of Applied Sciences, Helsinki, Finland
e-mail: jorma.sateri@metropolia.fi

8: DHBW Stuttgart, Germany
e-mail: christian.goetz@dhbw-stuttgart.de

Keywords: EFEU project, Teaching methods, Mobility, Carbon Footprint, Higher Education Institutions

Abstract *Students and staff transportation has a big impact in education carbon footprint. In order to study this issue, Higher Education Institutions from Germany, Finland, France and Portugal gathered students and teachers from engineering degrees to discuss and implement sustainability-driven initiatives among their peers.*

A survey was conducted to students and staff from all four Higher Education Institutions in the project. From the survey, 80% of students and 70% of staff have a public transportation stop no more than 10 minutes away from home. However, more than 40%

of students and 65% of staff uses fuel car daily. The average number of km are similar. Students do 25.11 km and staff 24.95 km, per trip.

These and other conclusions extracted from the survey where the base for a Leading Practice Publication. This publication tries to motivate students and staff to use public transportation or smooth mobility. At the same time, the publication highlights the importance of hybrid classes, presential and online, to reduce mobility. Teaching methods can reduce the carbon footprint of our students and increase quality of life.

This project main goal is to contribute to Emission Free European Universities (EFEU). Mobility is only one part of all EFEU project.

SYMCOMP 2025
Lisbon, 10-11 April 2025

OPTIMIZING HYPERSONIC INTAKES THROUGH 1D-BASED DESIGN EXPLORATION AND MULTI-OBJECTIVE SURROGATE MODELING

Ibrahim Gül, Professor Bayram Celik

1: Aeronautical and Astronautical Engineering Department
Istanbul Technical University
Maslak, 34469, Istanbul
e-mail: gul23@itu.edu.tr

2: Astronautical Engineering Department
Istanbul Technical University
Maslak, 34469, Istanbul
e-mail: celikbay@itu.edu.tr

Keywords: Hypersonic intake, evolutionary algorithms, surrogate-assisted prediction

Abstract *Hypersonic propulsion systems require efficient inlets to deliver the optimum performance under various operating conditions. In order to create an alternative, a surrogate-based multi-objective optimization framework for scramjet intake design is propounded in this study, and the evolutionary algorithm is deployed to minimize compression efficiency losses, aerodynamic drag and shock oscillation amplitudes, an objective that has not been fully addressed in the literature. In addition, a surrogate-based optimization framework of high performance scramjet intakes is integrated through a reduced-order analysis methodology to predict the effects of design parameters on overall aerodynamic performance. The scramjet intake design space is also ensured by a methodical approach of the intake subsystem through variation of essential parameters such as flight Mach number, ramp dimensions, internal contraction ratio and cowl lip radius. This methodology provides a framework for the optimization of the intake configuration for improved performance across a wide range of operating conditions. The optimization framework uses high-fidelity CFD simulations to model how the intake geometry parameters affect the flow characteristics such as total pressure recovery, shock system stability, and flow uniformity at the combustor entry. Surrogate modelling techniques are utilized to diminish the computational burden of optimization to acquire rapid convergence to globally optimal designs. In addition to the aforementioned numerical efforts, power spectral density distributions and shock hysteresis characteristics are compared for the optimized and baseline intake configurations. The study indicates that it is possible to use surrogate-assisted optimization to amplify intake performance while keeping computational cost low, which is decisive for the development of intrinsically robust and adaptable inlet designs for next-generation hypersonic propulsion systems.*

SYMCOMP 2025
Lisbon, 10-11 April 2025

MATHEMATICAL MODELING OF METABOLIC REPROGRAMMING AND NEW THERAPEUTIC STRATEGIES IN NON-SMALL CELL LUNG CANCER: A FLUX BALANCE AND VARIABILITY ANALYSIS APPROACH

João S. Lopes[2*], Cindy Mendes[45], Luís G. Gonçalves[3]; José A. Rodrigues[1], Jacinta Serpa[45]
1: CIMA and Mathematics Department of
Instituto Superior de Engenharia de Lisboa,
Portugal
e-mail: jose.rodrigues@isel.pt

2: Master in Biomedical Engineering,
Instituto Superior de Engenharia de Lisboa,
Portugal.
e-mail: a48534@alunos.isel.pt

3: Instituto de Tecnologia Química e Tecnológica (ITQB)
António Xavier da Universidade Nova de Lisboa,
Av. da República, 2780-157 Oeiras, Portugal.
e-mail: lgafeira@itqb.unl.pt

4: NOVA Medical School—Faculdade de Ciências Médicas,
Universidade NOVA de Lisboa,
Campo dos Mártires da Pátria, 130, 1169-056 Lisboa,
Portugal

5: Instituto Português de Oncologia de Lisboa Francisco Gentil (IPOLFG),
Rua Prof Lima Basto 1099-023 Lisboa,
Portugal
e-mail: {cindy.mendes,jacinta.serpa}@nms.unl.pt

Keywords: Metabolic reprogramming, Flux Balance Analysis (FBA), Flux Variability Analysis (FVA), Cancer metabolism, Non-small cell lung cancer (NSCLC), selenium-chrysin (SeChry)

Abstract. *Cancer cells, including non-small cell lung cancer (NSCLC) lines like H292, A549, and PC-9, exhibit metabolic reprogramming ensuring cancer cells' survival and tumor growth. This study investigates the metabolic responses of these cell lines to tselenium-chrysin (SeChry), a compound with anti-cancer effect, using computational tools such as COBRApy and Escher. Intracellular and extracellular metabolites' concentrations were integrated into Flux Balance Analysis (FBA) to assess metabolic shifts under control and SeChry conditions.*
Results revealed that the exposure to SeChry disrupts key metabolic pathways, including glycolysis, the pentose phosphate pathway, and the tricarboxylic acid (TCA) cycle,

DOI:10.5281/zenodo.15167960

significantly reducing metabolic flexibility and proliferation. The findings underscore the critical role of pyruvate kinase (PYK) in cancer cell metabolism and highlight potential metabolic vulnerabilities in NSCLC cells.

Furthermore, network robustness was evaluated using algebraic connectivity (λ_2), a key metric for assessing structural stability in metabolic networks. Our analysis demonstrates that the targeted removal of critical reactions leads to a substantial reduction in λ_2, decreasing from 0.3588 to 0.0812, reflecting an overall network fragility of 77.37%. This suggests that NSCLC metabolic networks depend on specific key reactions for maintaining functional integrity, revealing potential metabolic weak points that could be exploited for therapeutic targeting.

This research demonstrates the utility of computational modelling in elucidating cancer metabolism and paves the way for targeted metabolic therapies.

1 INTRODUCTION

Cancer cells are renowned for their ability to reprogram metabolism, facilitating rapid growth and proliferation by altering key metabolic pathways such as glycolysis and oxidative phosphorylation [1, 2]. NSCLC presents metabolic heterogeneity, and the genetic background deeply interferes with the metabolic profile of NSCLC cells ensuring the impact of growth factors on the adaptation to nutrients availability. An example is the role of EGF stimuli in the control of glucose and lactate metabolism even in EGFR-mutated NSCLC, representing both a challenge and an opportunity for therapeutic interventions [3]. Today it is known that cancer cells are characterized by elevated glycolytic activity, which does not necessarily mean the cessation of oxidative phosphorylation. Instead, in cancer, oxidative phosphorylation is primarily sustained by compounds derived from sources other than glucose [4]. However, the specific metabolic adaptations of these NSCLC cell lines, particularly in response to therapeutic treatments, remain insufficiently explored.

Metabolic flux analysis (MFA), a computational approach that predicts the rates of intracellular metabolic reactions, provides a robust framework for understanding these metabolic shifts. By integrating genome-scale metabolic models (GEMs) with experimental data, MFA enables the quantitative assessment of metabolic pathways, offering insights into cellular behaviour under varying environmental and genetic conditions. Techniques such as Flux Balance Analysis (FBA) and Flux Variability Analysis (FVA) allow for detailed exploration of the metabolic network, optimizing specific objective functions such as biomass production or ATP synthesis.

The application of FBA and FVA to cancer research has proven instrumental in elucidating metabolic vulnerabilities. For example, FBA optimizes metabolic reactions under the assumption of a steady-state system, while FVA evaluates the range of alternative flux distributions that sustain cellular objectives, revealing metabolic flexibility and robustness (Schellenberger et al., 2011). When applied to NSCLC cell lines, these techniques can provide valuable insights into how cancer cells adapt their metabolism to therapeutic stress, specifically in critical pathways like glycolysis and oxidative phosphorylation.

In this study, we utilize computational tools such as COBRApy, a Python-based framework for constraint-based modelling, and Escher, an interactive visualization platform for metabolic networks. These tools facilitate not only the simulation of metabolic fluxes but also the intuitive visualization of how treatments impact specific metabolic pathways . By focusing on the metabolic responses of H292, A549, and PC-9 cells exposed to selenium-chrysin (SeChry) a compound with anti-cancer effect[5,6] including against NSCLC [7,8], we aim to reveal critical regulatory mechanisms, such as the role of pyruvate kinase (PYK) in glucose dependent pathways, and elucidate the underlying metabolic reprogramming that supports cancer cell survival and proliferation, and might be disrupted by SeChry .

This research contributes to the growing understanding of NSCLC cell metabolism, paving the way for targeted metabolic therapies and advancing our knowledge of the metabolic vulnerabilities in cancer.

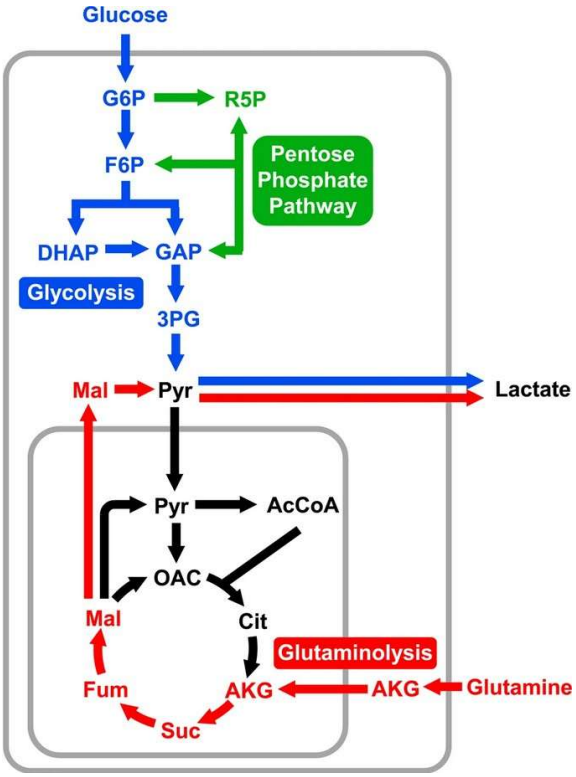

Figure 1: Metabolic network having pyruvate kinase (PYK) as a central player, gathering glucose-dependent pathways— glycolysis, pentose phosphate pathway (PPP) and the tricarboxylic acids (TCA) cycle—, and considering the anaplerotic role of glutamine in the supplementation of the TCA cycle and consequently the oxidative phosphorylation (OXPHOS).

As shown in Figure 1, the analysis of metabolic pathways dependent on glucose and on the TCA cycle anaplerotic supply by glutamine, reveals key insights into cellular adaptation and interconnective steps, which can be targeted in cancer cells.

2 Methods

2.1 Metabolic Model and Data Integration

To investigate the metabolic alterations in NSCLC cells (H292, PC-9, and A549) ^{1}H- nuclear magnetic resonance (^{1}H-NMR) spectroscopy metabolomic data was used. NSCLC were maintained in control conditions and exposed to SeChry, as published [7,8]. Data was analysed using a genome-scale metabolic model (GEM) tailored to represent cancer metabolism. GEMs provide a comprehensive framework for analyzing cellular metabolism

by incorporating reactions, metabolites, and stoichiometric coefficients that reflect the biochemical and (patho)physiological properties of specific cell types. The model was implemented using the COBRApy library, an established Python-based platform for constraint-based modeling.

The metabolic model was constrained to reflect the nutrient availability and environmental conditions resembling the modulation of the tumor microenvironment. These constraints included upper and lower flux bounds for exchange reactions and internal metabolic pathways, ensuring that the simulation remained pathophysiologically relevant. Additionally, experimental data on extracellular and intracellular metabolite concentrations, obtained by ^{1}H-NMR spectroscopy [7], were integrated to represent both control (untreated) and SeChry (treated) conditions. Data integration ensured a more accurate simulation of metabolic states, capturing the heterogeneity of tumor cell metabolism.

2.2 Flux Balance Analysis (FBA)

Flux Balance Analysis (FBA) is a constraint-based computational method used to predict steady-state flux distributions in metabolic networks. In this study, FBA was applied to both control and therapeutic conditions to estimate optimal reaction fluxes and identify key pathways affected by treatment. The FBA problem was formulated as a linear programming (LP) problem:

$$maximize Z = \mathbf{c}^T\mathbf{v}, \quad (1)$$

subject to the steady-state constraint:

$$S\mathbf{v} = 0, \quad (2)$$

and the flux bounds:

$$\mathbf{l} \le \mathbf{v} \le \mathbf{u}, \quad (3)$$

where Z represents the objective function, typically biomass production in control cells, S is the stoichiometric matrix, v is the flux vector, and l and u are the lower and upper bounds on fluxes, respectively. Using the COBRApy function "cobra.flux analysis.pfba()", we employed parsimonious FBA (pFBA) to minimize the total flux while maintaining optimal growth.

2.3 Flux Variability Analysis (FVA)

Flux Variability Analysis (FVA) extends FBA by determining the range of possible fluxes for each reaction while maintaining the optimal growth rate [9, 10]. This method provides insights into the flexibility and essentiality of metabolic reactions. For each reaction, the minimum and maximum flux values were calculated under the constraint of maintaining at least 90% of the optimal growth rate. The COBRApy function "*cobra.flux analysis.variability.flux variability analysis()"* was used to perform FVA, highlighting pathways with significant flux variability between control and therapeutic conditions.

2.4 Data-Driven Constraints and Experimental Validation

To ensure that the model represents a metabolic network with pathophysiological relevance, we explored the ^{1}H-NMR spectroscopy metabolic profilling regarding NSCLC cells exometabolome[7]. Concentrations of key metabolites, including glucose, lactate, pyruvate, glutamine, and glutamate, were measured under control and SeChry conditions. These data were used to set specific constraints on exchange reactions, reflecting nutrient uptake and secretion rates observed in cancer cells. Experimental proliferation curves in control conditions were used to validate the simulated biomass flux, ensuring model accuracy.

2.5 Visualization of Metabolic Flux Distributions

To interpret the simulation results, Escher Builder was employed to visualize metabolic flux distributions across the network. The "*RECON1.Glycolysis TCA PPP*" map was used to compare flux changes between control and SeChry conditions. This tool allowed for intuitive identification of differentially active pathways, particularly in glycolysis, the PPP, and the TCA cycle .

2.6 Key Metabolic Ratios and Pathway Analysis

Metabolic alterations in cancer cells were further assessed by calculating key metabolite ratios, such as pyruvate/oxaloacetate and glutamine/glutamate. These ratios provided insights into the metabolic state of the cells, revealing shifts in TCA cycle activity dependent on glucose or on glutamine A custom Python function, calculate combined ratios, automated this analysis to ensure reproducibility.

Pathway-specific analysis was conducted to identify reactions with significant flux changes, focusing on glycolysis, OXPHOS, and amino acid metabolism. These pathways were prioritized due to their established roles in supporting tumor growth and resistance to SeChry.

2.7 Optimization Techniques and Solver Implementation

Two linear programming techniques, the Simplex Method and the Interior-Point Method, were employed to solve optimization problems. The Simplex Method iteratively updated solutions by pivoting on variables, while the Interior-Point Method used barrier functions to explore feasible regions of the flux space. Both methods were implemented in COBRApy and validated for accuracy in predicting metabolic responses.

2.8 Statistical Analysis and Significance Testing

All flux distributions and metabolic ratios were statistically analysed to identify significant changes between control and SeChry conditions. Student's t-tests were performed with a significance threshold of $p < 0.05$. Additionally, pathway enrichment analysis was

conducted to determine the overrepresentation of altered pathways, providing a systems level view of metabolic reprogramming.

2.9 Background on Computational Tools

COBRApy: COBRApy is a Python-based platform for constraint-based modelling and analysis of metabolic networks. It supports a wide range of techniques, including FBA, FVA, and pFBA, making it a versatile tool for studying cancer metabolism [11].

Escher: Escher is a visualization tool for metabolic maps, enabling the intuitive interpretation of flux distributions and pathway activities. By integrating with COBRApy, Escher provides a user-friendly interface for exploring metabolic changes under stressful conditions [8].

2.10 Data Collection

Experimental and computational data used in this study were acquired through a combination of in vitro biological assays and constraint-based metabolic modeling. Data collection focused primarily on cell proliferation, cell death, and metabolites' concentration in three human NSCLC cell lines: A549, H292, and PC-9 [3].

2.11 Experimental Data Collection

Biological data - Control and Sechry treated cells were obtained through standardized cell culture protocols and experimental assays. Cell concentration data were collected using proliferation curves, established by counting viable cells at multiple time points (0, 6, 10, 24, 32, and 48 h) under control conditions. Cell death rates were assessed in control and SeChry conditions using flow cytometry analysis to determine the percentage of cells stained with annexin V-FITC and propidium iodide (PI). All experiments were performed in biological triplicates to ensure statistical robustness.

In parallel, extracellular and intracellular metabolite concentrations were quantified using ^{1}H-NMR spectroscopy. Samples were processed through methanol/chloroform/water extraction protocols, and metabolite identification and quantification were conducted using spectral matching with HMDB and Chenomx databases, as described [7].

2.12 Computational Data Collection

Experimental data were integrated into a genome-scale metabolic model (GEM) for NSCLC cells using the COBRApy framework. Constraints for exchange reactions were defined based on the experimentally obtained concentrations of key metabolites (e.g., glucose, lactate, glutamine, glutamate, pyruvate), ensuring the pathophysiological relevance of the simulations.

Cell proliferation rates derived from control conditions were used to validate the flux distributions obtained through Flux Balance Analysis (FBA) and Flux Variability Analysis (FVA). Computational simulations were performed using parsimonious FBA (pFBA) to

minimize total flux while maintaining optimal biomass production. FVA was applied to evaluate the flexibility of metabolic pathways and to identify reactions with altered flux ranges under SeChry conditions.

2.13 Data Integration

The integration of biological and computational data enabled cross-validation between observed phenotypes (e.g., proliferation, cell death) and predicted metabolic behavior. The agreement between experimental proliferation curves and in silico growth rate predictions confirmed the accuracy of the model. Furthermore, the correlation between metabolic flux alterations and cell death percentages under treatment conditions provided mechanistic insights into therapy-induced metabolic reprogramming.

2.14 Robustness: Graph Construction

The metabolic network was derived from an Escher model, loaded from a JSON file containing metabolic reactions. Metabolites were defined as graph nodes, and an edge was established between two metabolites if they participated in the same reaction.

2.15 Stoichiometric and Adjacency Matrix Definition

A stoichiometric matrix S was constructed to capture the quantitative relationships between metabolites and reactions. Based on S, we derived the adjacency matrix A, where $A_{ij} = 1$ if metabolites i and j were involved in the same reaction.

2.16 Algebraic Connectivity Computation

The Laplacian matrix L was defined as:

$$L = D - A$$

where D is the diagonal degree matrix. The eigenvalues of L were computed to determine algebraic connectivity (λ_2), the second-smallest eigenvalue of L, which reflects the network's robustness.

2.17 Identification and Removal of Critical Connections

To determine the most influential edges in maintaining network connectivity, we systematically tested the removal of each connection and recalculated λ_2. Only removals that did not isolate nodes were considered, ensuring that the network remained functionally connected. The edges with the highest impact on reducing λ_2 were selected for elimination.

2.18 Global Impact Assessment

The global impact of edge removals was quantified as:

$$GlobalImpact = \frac{\lambda_2^{original} - \lambda_2^{removed}}{\lambda_2^{original}}$$

This metric allowed us to estimate the relative importance of removed connections and their effect on network stability.

3 Results

3.1 Cancer Model - Control Group

Optimized Objective Function

The optimization of the cancer model for the three NSCLC cell lines, PC-9, H292, and A549, was conducted with the objective reaction set to PYK. The optimized objective function values were as follows:

- PC-9: 0.0924
- H292: 0.0904
- A549: 0.0897

These values suggest that all three cancer cell lines operate under a similar metabolic state that favors proliferation and growth, considering the PK-dependent reaction.

3.2 Comparison of Cell Proliferation Rates between Experimental Data and Model Predictions

The comparison between the experimental data for cell proliferation rates predicted by the metabolic model shows a consistent trend of rapid cell growth across the three cell lines in control conditions: PC-9, H292, and A549.

For the experimental data, the total cell number increases substantially during the first 24 h. For A549, the total cell number increased from 105,000 to around 570,000-710,500 cells, reflecting significant proliferation. H292 cell number increased from 140,000 to 510,000-925,000 cells, while PC-9 cell number increased from 135,000 to 230,000-470,000 cells, in the same time frame. When compared to the metabolic model predictions, the growth rates calculated for A549, H292, and PC-9 were 0.089, 0.090, and 0.092 h^1, respectively. Both the experimental data and the flux-based models indicate that the cells are in a highly proliferative state during this period, consistent with the accelerated metabolic flux through glycolysis.

While the experimental data show specific cell counts at different time points, the metabolic model provides a broader, continuous view of growth trends based on flux optimizations. The results indicate that the model captures the rapid proliferation behavior of cancer cells, though the direct relationship between model-based growth rate

predictions and experimental measurements highlights the dynamic nature of cellular growth in real-time experimental settings.

Flux Distribution

Key flux values for the three cancer cell types showed interesting similarities and differences:

- **PC-9:**

  FALDH (Acetaldehyde dehydrogenase): 0.5432
  EX ac e (Extracellular Acetate): 1.8214 (acetate secretion)
  EX glc D _e (Extracellular Glucose): -1.5141 (glucose uptake)

NADH16: 5.7890 (redox balance)

- **H292:**

  FALDH: 0.5483
  EX ac e: 1.8424 (acetate secretion)
  EX glc D _e: -1.4921 (glucose uptake)

NADH16: 5.7647

- **A549:**

  FALDH: 0.5247
  EX ac e: 1.8126 (acetate secretion)
  EX glc D _e: -1.4713 (glucose uptake)
  NADH16: 5.6981

These results suggest that all three cell lines rely heavily on glucose and acetate, glycolysis and putatively fatty acids oxidation (FAO), a major pathway producing of acetate[12]. The flux through glycolytic pathways is comparable across the cell types, though slight variations in values suggest subtle differences in metabolic flexibility.

Flux Variability Analysis (FVA)

The Flux Variability Analysis (FVA) provided the following flux ranges for key reactions: •

PC-9:

FALDH: Flux range from -7.1845 to 0.5432

FBA: Flux range from 0.9715 (minimum 0) •

H292:

FALDH: Flux range from -7.2268 to 0.5483
FBA: Flux range from 0.9636 (minimum 0)

- **A549:**

FALDH: Flux range from -7.1001 to 0.5247

FBA: Flux range from 0.9905 (minimum 0)

The variability in the flux through reactions like FALDH suggests metabolic plasticity, which may contribute to the survival and adaptability of cancer cells under different nutrient conditions.

3.3 Cell model do address the effect of SeChry

Optimized Objective Function
For the SeChry-effect cell models, the optimization was similarly conducted with PYK as the objective reaction. The optimized objective function values were:

- PC-9 (SeChry): 0.0154
- H292 (SeChry): 0.0132
- A549 (SeChry): 0.0147

These values indicate a constrained metabolic state in cells exposed to SeChry, focusing on minimizing flux through PYK.

Flux Distribution
Key flux values for the SeChry models were as follows: •

PC-9 (SeChry):

FALDH: 0.4981
EX ac e: 2.0385 (acetate secretion)
EX glc D _e: -0.6937 (glucose uptake)
NADH16: 4.6123

- **H292 (SeChry):**

FALDH: 0.4947
EX ac e: 2.026 (acetate secretion)
EX glc D _e: -0.6794 (glucose uptake)
NADH16: 4.3971

- **A549 (SeChry):**

FALDH: 0.5156
EX ac e: 2.0205 (acetate secretion)
EX glc D _e: -0.6801 (glucose uptake)
NADH16: 4.5342

Upon SeChry exposure, all three cell lines showed similar flux profiles, with acetate uptake and secretion being prominent, but with a decrease in glucose uptake compared to cells cultured in control conditions. The NADH values indicate a shift towards maintaining metabolic balance under therapy.

Flux Variability Analysis (FVA)
FVA results for the SeChry models showed the following flux ranges: •

PC-9 (SeChry):

FALDH: Flux range from -16.9473 to 0.4981

FBA: Flux range from 0.6794 (minimum 0) •

H292 (SeChry):

FALDH: Flux range from -16.9473 to 0.4947

FBA: Flux range from 0.6794 (minimum 0) •

A549 (SeChry):

FALDH: Flux range from -16.8537 to 0.5156 FBA:
Flux range from 0.6936 (minimum 0)

The flux variability analysis for the SeChry treated cells also indicates metabolic flexibility, with variability in key pathways like FAO that suggest potential metabolic adaptation under stressful conditions.

Proliferation Rate Calculation
The calculated growth rates for the SeChry models were constrained:

- PC-9 (SeChry): Minimal, near-zero biomass flux
- H292 (SeChry): Near-zero biomass flux
- A549 (SeChry): Near-zero biomass flux

These results indicate that the SeChry models are in a constrained metabolic state, focusing on reducing proliferative capacity. These results are purely simulations, needing confirmation with real data.

3.4 Comparing the NSCLC control and SeChry models

The comparison of the three NSCLC cell lines (PC-9, H292, and A549) reveals striking differences in metabolic activity. This change is particularly evident in the estimated near-zero proliferation rates and reduced glucose uptake in the SeChry treated cells, which reflects an attempt to limit cellular energy production and growth under stress.

The variability in fluxes across both conditions further highlights the metabolic adaptability of these cells. For example, while the flux ranges for FALDH are broader in the control models, indicating potential for metabolic flexibility under nutrient fluctuations, the SeChry models show a more constrained set of flux ranges.

The results from the extracellular and intracellular metabolites' concentrations also emphasize the differences in the metabolic states. The higher concentrations of pyruvate, glutamine, and glutamate in the cancer cells are indicative of active metabolic processes aimed at sustaining rapid growth. In contrast, SeChry treated cells exhibit a shift in metabolite ratios, which may be associated with attempts to counteract the anti-cancer effect of SeChry.

3.5 Comparison of Cell Death levels and Metabolic Fluxes

In this subsection, we compared the experimental data on cell death (%) with the metabolic flux values and proliferation rates for the A549, H292, and PC-9 cell lines. The data on cell death was obtained from 4 biological replicates, for both the control and SeChry conditions. We examined how the observed metabolic fluxes relate to the changes in cell death across the different experimental conditions.

3.5.1 PC-9 Cells

Cell Death: PC-9 cells showed the most dramatic response to SeChry treatment. The cell death percentages increased from 10.70% to 17,77% in the control condition, and 56.90% to 90.21% under SeChry treatment. This significant increase in cell death indicates that SeChry has a potent effect in inducing cell death in PC-9 cells.
Metabolic Fluxes: PC-9 cells had the highest proliferation rate of 0.092 h^{-1} in the control model, with acetate uptake (*EXac_e* = 1.8214) and glucose uptake (*EX glc D e* = 1.5141) consistent with high glycolytic activity. In SeChry condition, however, acetate uptake increased (*EX ace* = 2.0385) while glucose uptake decreased significantly (*EX glc D e* = -0.6937). The dramatic increase in cell death under SeChry treatment in conjunction with these metabolic shifts suggests that SeChry induces a strong metabolic reprogramming in PC-9 cells.

3.5.2 H292 Cells

Cell Death: In H292 cells, the control conditions yielded 5.99% to 14,75% cell death, which increased significantly under SeChry exposure, reaching 19.33% to 44.46%. This increase highlights the effect of SeChry in inducing cell death in these cells.

Metabolic Fluxes: The H292 cells showed a similar proliferation rate to A549 cells, at 0.090 h^{-1}. The fluxes through key reactions such as acetate uptake (*EX ac e* = 1.8424) and glucose uptake (*EX glc D _e* = -1.4921) were also comparable. Upon SeChry treatment, the

acetate uptake increased (*EX _ac e* = 2.026) with a notable reduction in glucose uptake (*EX glc D e* = -0.6794). This metabolic shift aligns with the increase in cell death.

3.5.3 A549 Cells

Cell Death: The A549 cells exhibited a moderate increase in cell death when treated with SeChry, ranging from 8,07% to 12,97% under control conditions, and 24.05% to 40.85% under SeChry treatment. This represents a moderate increase in cell death in response to the treatment.

Metabolic Fluxes: The metabolic flux analysis showed that A549 cells had a proliferation rate of 0.089 h^{-1} in the control model, with key fluxes including acetate uptake (*EX ac e* = 1.8126) and glucose uptake (*EX _glc D e* = -1.4713). Under SeChry exposure, the metabolic fluxes were reduced, with a shift towards acetate utilization (*EX ac e* = 2.0205) and reduced glucose uptake (*EX glc D e* = -0.6801). The reduced metabolic fluxes, similar to H292, correlate with the increased cell death.

Calculation of Metabolic Ratios

The metabolic ratios for PC-9, H292, and A549 cell lines were analyzed under control and SeChry conditions. These ratios highlight the shifts in metabolite utilization and metabolic fluxes between untreated cancer cells and cells under therapy.

PC-9 Cells

Control:

Pyruvate/Oxaloacetate: $\frac{[Pyruvate]_{extracellular}}{[Oxaloacetate]_{intracellular}} = 1.5058$

Pyruvate/Glutamine: $\frac{[Pyruvate]_{extracellular}}{[Glutamine]_{intracellular}} = 43.9009$

Glutamine/Glutamate: $\frac{[Glutamine]_{extracellular}}{[Glutamate]_{intracellular}} = 1.3292$

PCA/Glutamate: $\frac{[PCA]_{extracellular}}{[Glutamate]_{intracellular}} = 13.8412$

Glutamine/PCA: $\frac{[Glutamine]_{extracellular}}{[PCA]_{extracellular}} = 3.4005$

SeChry:

Pyruvate/Oxaloacetate: $\frac{[Pyruvate]_{extracellular}}{[Oxaloacetate]_{intracellular}} = 0.2441$

Pyruvate/Glutamine: $\frac{[Pyruvate]_{extracellular}}{[Glutamine]_{intracellular}} = 1.7962$

Glutamine/Glutamate: $\frac{[Glutamine]_{extracellular}}{[Glutamate]_{intracellular}} = 3.4943$

PCA/Glutamate: $\frac{[PCA]_{extracellular}}{[Glutamate]_{intracellular}} = 7.2828$

Glutamine/PCA: $\frac{[Glutamine]_{extracellular}}{[PCA]_{extracellular}} = 15.0208$

H292 Cells

Control:

Pyruvate/Oxaloacetate: $\frac{[Pyruvate]_{extracellular}}{[Oxaloacetate]_{intracellular}} = 0.0417$

Pyruvate/Glutamine: $\frac{[Pyruvate]_{extracellular}}{[Glutamine]_{intracellular}} = 0.1562$

Glutamine/Glutamate: $\frac{[Glutamine]_{extracellular}}{[Glutamate]_{intracellular}} = 0.9471$

PCA/Glutamate: $\frac{[PCA]_{extracellular}}{[Glutamate]_{intracellular}} = 0.0079$

Glutamine/PCA: $\frac{[Glutamine]_{extracellular}}{[PCA]_{extracellular}} = 153.4286$

SeChry:

Pyruvate/Oxaloacetate: $\frac{[Pyruvate]_{extracellular}}{[Oxaloacetate]_{intracellular}} = 0.6561$

Pyruvate/Glutamine: $\frac{[Pyruvate]_{extracellular}}{[Glutamine]_{intracellular}} = 3.9596$

Glutamine/Glutamate: $\frac{[Glutamine]_{extracellular}}{[Glutamate]_{intracellular}} = 0.4403$

PCA/Glutamate: $\frac{[PCA]_{extracellular}}{[Glutamate]_{intracellular}} = 3.2689$

Glutamine/PCA: $\frac{[Glutamine]_{extracellular}}{[PCA]_{extracellular}} = 2.5048$

A549 Cells

Control:

Pyruvate/Oxaloacetate: $\frac{[Pyruvate]_{extracellular}}{[Oxaloacetate]_{intracellular}} = 2.0838$

Pyruvate/Glutamine: $\frac{[Pyruvate]_{extracellular}}{[Glutamine]_{intracellular}} = 41.6760$

Glutamine/Glutamate: $\frac{[Glutamine]_{extracellular}}{[Glutamate]_{intracellular}} = 0.5537$

PCA/Glutamate: $\frac{[PCA]_{extracellular}}{[Glutamate]_{intracellular}} = 0.3401$

Glutamine/PCA: $\frac{[Glutamine]_{extracellular}}{[PCA]_{extracellular}} = 5.0746$

SeChry:

Pyruvate/Oxaloacetate: $\frac{[Pyruvate]_{extracellular}}{[Oxaloacetate]_{intracellular}} = 0.6104$

Pyruvate/Glutamine: $\frac{[Pyruvate]_{extracellular}}{[Glutamine]_{intracellular}} = 10.0893$

Glutamine/Glutamate: $\frac{[Glutamine]_{extracellular}}{[Glutamate]_{intracellular}} = 0.1952$

PCA/Glutamate: $\frac{[PCA]_{extracellular}}{[Glutamate]_{intracellular}} = 0.4260$

Glutamine/PCA: $\frac{[Glutamine]_{extracellular}}{[PCA]_{extracellular}} = 1.3273$

Analysis and Discussion

The metabolic ratios calculated for PC-9, H292, and A549 cell lines under Control and SeChryconditions reveal significant metabolic rewiring caused by SeChry. Notably, SeChry substantially reduced cell proliferation, thereby inducing cancer cell death and decreasing overall metabolic activity.

Key Observations

1. **Pyruvate/Oxaloacetate:**

In all three cell lines, the Pyruvate/Oxaloacetate ratio increased significantly under SeChry exposure compared to control conditions. For instance, in H292 cells, it rose from 0.0417 to 0.6561. This suggests that SeChry promotes decreased reliance on pyruvate metabolism, potentially due to increased flux of non-glucose derived compounds through the TCA cycle. Acetate from FAO and α-ketoglutarate deriving from glutamine-derived glutamate are potential suppliers of the TCA cycle. The shift to FAO aligns with the results obtained in FALDH fluxes, as FALDH oxidizes medium- or long-chain aliphatic aldehyde, shifting them to fatty acids to be degraded in FAO[13,14].

2. **Pyruvate/Glutamine:**

The Pyruvate/Glutamine ratio increased substantially under SeChry conditions in H292 and A549 cells, while PC-9 cells exhibited a sharp decrease (from 43.9009 to 1.7962). The increase in H292 and A549 cells could reflect increased utilization of glutamine in energy and biosynthetic pathways. The decrease in PC-9 cells indicates a cell-line-specific metabolic adaptation, as described previously, lactate is an important metabolic source for PC-9 [15]. Lactate is converted to pyruvate to be used by cells in the TCA cycle, as we observed an accumulation of pyruvate, it suggests that, upon SeChry, lactate-derived pyruvate is no longer a preferential metabolic source [7].

3. **Glutamine/Glutamate:**

The Glutamine/Glutamate ratio decreased significantly in H292 and A549 cells under therapy, consistent with increased glutaminase (GLS) activity and/or an increase in glutamine consumption. Conversely, in PC-9 cells, this ratio increased under therapy (from 1.3292 to 3.4943), suggesting compensatory mechanisms that may buffer the effects of metabolic stress and increased glutamate consumption.

4. **Pyroglutamate/Glutamate and Glutamine/Pyroglutamate:**

Therapy induced notable changes in pyroglutamate-related ratios across cell lines. In H292 cells, Pyroglutamate /Glutamate increased substantially (from 0.0079 to 3.2689), while Glutamine/ Pyroglutamate decreased markedly (from 153.4286 to 2.5048). These shifts suggest an accumulation of pyroglutamate, as it can be converted from both

glutamine and glutamate without a necessaery enzymatic intervention [16]. Pyroglutamate is a byproduct of impaired glutathione metabolism and increased oxidative stress[17]. The depletion of glutathione is described as an effect of SeChry on cancer cells [18]. In A549 and PC-9 cells, changes were more moderate but still indicated the same trends than H292.

Biological Implications

Therapeutic Impact on Metabolism and Cell proliferation:
The consistent reduction in celproliferation under SeChry exposure directly correlated with decreased metabolic activity, as evidenced by shifts in metabolite ratios. The increased reliance on glutamine metabolism, coupled with decreased pyruvate utilization, underscores the profound effect of SeChry in targeting key metabolic pathways critical for cancer cell proliferation and metabolism.

Cell-Type-Specific Adaptations:
The variability in metabolic responses among PC-9, H292, and A549 cells highlights the heterogeneity of SeChry effects. While SeChry overall disrupted metabolic fluxes, cell-specific adaptations—such as decreased Glutamine/Glutamate in PC-9 cells—may indicate mechanisms of resistance or survival that warrant further investigation.

Potential for Targeted Therapy:
The observed metabolic adjustements, particularly in pyruvate and glutamine pathways, suggest potential targets for novel therapies. Targeting enzymes such as glutaminase (GLS) or pyruvate dehydrogenase kinase (PDK) could further enhance the efficacy of therapeutic interventions by exacerbating metabolic stress [2].

Escher Simulations of Control and SeChry Conditions

The metabolic flux distributions for A549, PC-9, and H292 cells under control and SeChry conditions were analyzed using Escher simulations. Across all cell lines, significant metabolic rewiring was observed, particularly in glycolysis, the TCA cycle, and the PPP. Below, we present the results for each cell line.

PC-9 Cells

For PC-9 control cells (Figure 2), glycolytic and PPP activity dominate metabolic fluxes, while the TCA cycle is moderately active. SeChry exposure (Figure 3) results in reduced glycolysis and PPP activity and further suppression of the TCA cycle using glucose-derived

compounds. The reduction in metabolic fluxes aligns with decreased cell proliferation and increased cell death upon SeChry.

H292 Cells

The H292 control cells (Figure 4) show similar patterns of metabolic flux, with active glycolysis and PPP and moderate TCA cycle flux. Under the SeChry condition (Figure 5), glycolysis and PPP are significantly inhibited, and TCA cycle flux is further reduced using glucose-derived compounds, reflecting metabolic downregulation consistent with suppressed cell proliferation and increased cell death.

A549 Cells

In the A549 control cells (Figure 6), glycolysis and the PPP show strong flux activity (blue), while the TCA cycle exhibits moderate activity. Under the SeChry condition (Figure 7), glycolysis and the PPP are significantly suppressed (red), and TCA cycle flux is reduced using glucose-derived compounds, reflecting the impact of SeChry on cellular metabolism, concomitant with decreased cell proliferation and increased cell death.

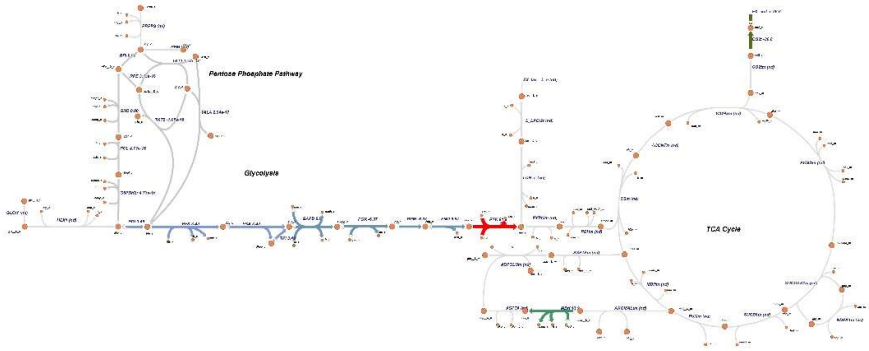

Figure 2: Escher simulation of PC-9 control cells. Blue regions indicate high flux, red indicates low or inhibited flux.

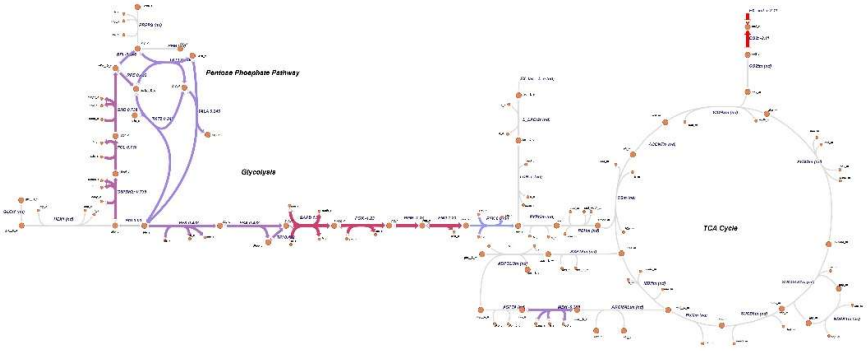

Figure 3: Escher simulation of PC-9 SeChry condition. Blue regions indicate high flux, red indicates low or inhibited flux.

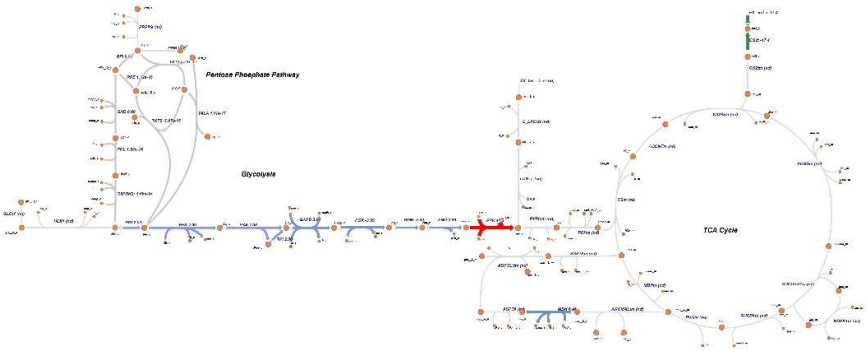

Figure 4: Escher simulation of H292 control cells. Blue regions indicate high flux, red indicates low or inhibited flux.

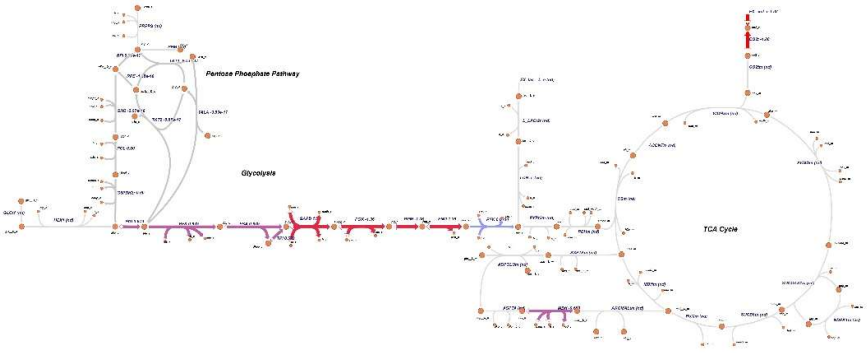

Figure 5: Escher simulation of H292 SeChry condition. Blue regions indicate high flux, red indicates low or inhibited flux.

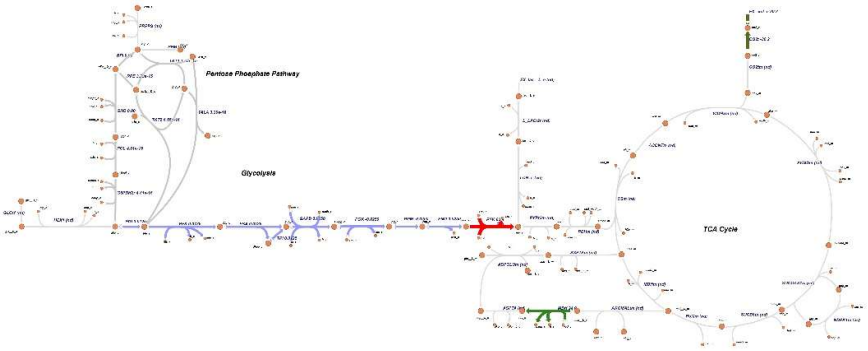

Figure 6: Escher simulation of A549 Control cells. Blue regions indicate high flux, red indicates low or inhibited flux.

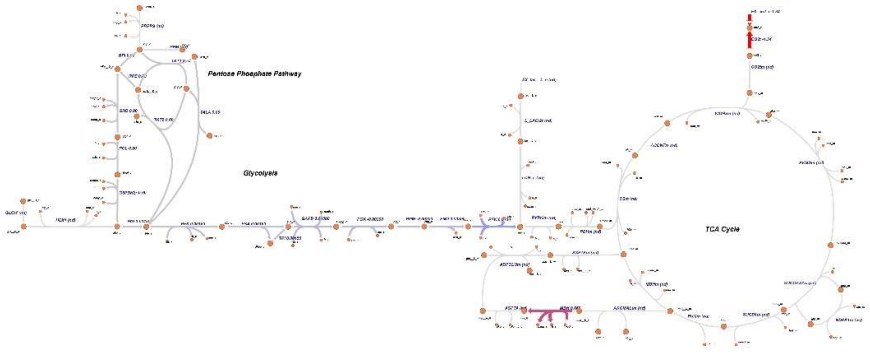

Figure 7: Escher simulation of A549 SeChry condition. Blue regions indicate high flux, red indicates low or inhibited flux.

General Observations Across All Cell Lines

Across all cell types, the following trends were observed:

- **Glycolysis:** SeChry intervention consistently reduced glycolytic flux, indicating a suppression of glucose metabolism, critical in control cells.
- **TCA Cycle:** The SeChry condition caused a significant decrease in TCA cycle flux using glucose-derived compounds, highlighting the activation of alternative TCA cycle suppliers.

  Pentose Phosphate Pathway (PPP): The PPP is a glucose-dependent pathway, benefiting from the deviation of glucose.6-phosphate from glycolysis, and it is essential for biosynthesis and redox balance. As expected with the reduction of glycolysis upon SeChry, the PPP was markedly suppressed pointing to disrupted nucleotide synthesis and oxidative stress management.
- **Overall Metabolism:** SeChry intervention universally reduced metabolic fluxes across pathways, underscoring the profound metabolic stress imposed on control

cells, thereby limiting their proliferation and survival. Interestingly, it seems that SeChry shifts glucose reliance into fatty acids and glutamine reliance.

4 Metabolic Network Robustness

The initial algebraic connectivity of the H292 Control Cell network (λ_2 = 0.3588) was progressively reduced through the sequential removal of critical reactions, leading to the following impacts:

- Removed: Phosphogluconate dehydrogenase (1956140) — New λ_2: 0.2888 (Impact: 19.50%)
- Removed: Pyruvate mitochondrial transport via proton symport (1955637) — New λ_2: 0.2318 (Impact: 19.73%)
- Removed: ASPGLUm (1955663) — New λ_2: 0.1036 (Impact: 55.32%)
- Removed: Malate dehydrogenase, mitochondrial (1955669) — New λ_2: 0.0968 (Impact: 6.54%)
- Removed: Fumarase, mitochondrial (1955639) — New λ_2: 0.0812 (Impact: 16.11%)

The total impact on network robustness was 77.37%, demonstrating that these reactions play a crucial role in preserving the structural integrity of the metabolic network.

Figure 8 visualizes the stepwise decrease in λ_2 as key reactions are removed, reinforcing the concept that metabolic networks exhibit hierarchical vulnerability.

Additional analysis indicated that the metabolic network retained connectivity despite significant perturbations, suggesting potential compensatory mechanisms through alternative pathways. However, the substantial reduction in λ_2 highlights an increased susceptibility to functional breakdown under targeted metabolic interventions.

These findings offer valuable insights into the structural dependencies of NSCLC metabolic networks and underscore the potential of disrupting cancer metabolism through targeted interventions on critical metabolic connections.

5 Discussion

The results of this study provide significant insights into the metabolic behavior of the three cancer cell lines (PC-9, H292, and A549) and their response to novel therapeutic conditions using SeChry as a drug. By analyzing optimized objective functions, flux distributions, flux variability, and metabolic ratios, we can better understand the metabolic strategies employed by these cells in proliferative and constrained states.

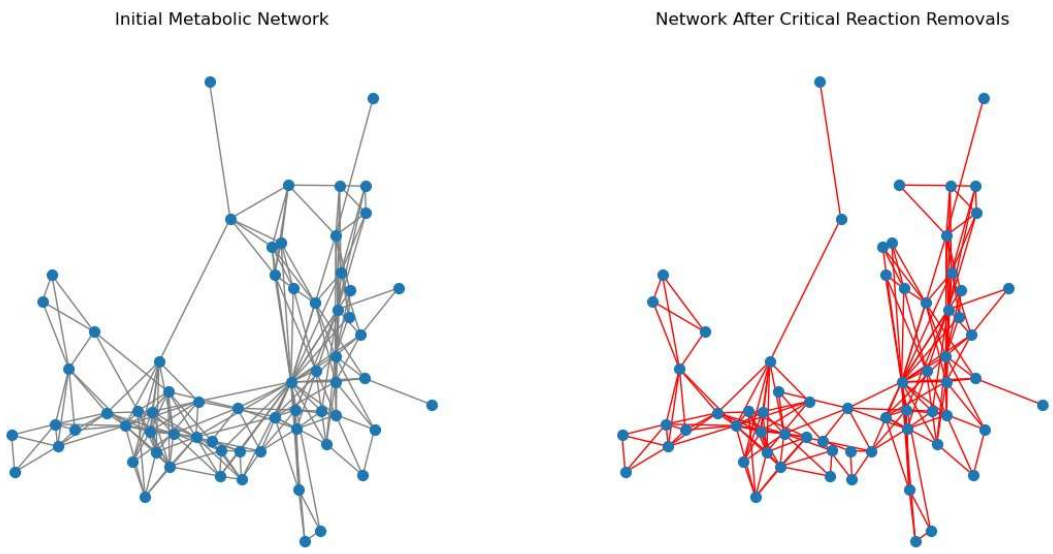

Figure 8: Metabolic Network before and after critical reaction removals.

5.1 Control Models

The analysis of cancer models revealed a high metabolic activity consistent with a glucose reliance, characterized by elevated glycolysis and lactate production [9]. The optimized objective function values for PC-9, H292, and A549 cell lines were close in magnitude, suggesting similar metabolic states that prioritize proliferation. Among these, PC-9 displayed a slightly higher optimized value, which may indicate a higher adaptability to glucose and lactate-dependent metabolic phenotype compared to H292 and A549, as it was described [15].

The flux distributions across key pathways reinforced the reliance of these cell lines on glucose and acetate as major metabolic substrates. Notably, glucose uptake rates were substantial, aligning with the enhanced glycolytic activity commonly observed in cancer cells. The secretion of acetate and other metabolic byproducts further shows the metabolic activity and highlights FAO as a key metabolic pathway [12].

FVA indicated significant metabolic flexibility in cancer cells, particularly in reactions such as FALDH, which aligns with FAO upregulation [13,14]. The broad flux ranges observed in these reactions suggest the ability of cancer cells to adjust their metabolic fluxes in response to varying environmental conditions, supporting their survival and growth.

5.2 Sechry Treated Cells – SeChry anti-cancer Models

Under therapeutic conditions, the metabolic landscape of the cells shifted dramatically. The optimized objective function values decreased substantially across all three cell lines,

indicating a constrained metabolic state. This reduction reflects the impact of SeChry in suppressing the metabolic activity that supports cancer proliferation and survival.

The flux distributions in SeChry models revealed a marked decrease in glucose uptake and lactate production compared to their control counterparts. This metabolic shift, coupled with a reduced flux through key glycolytic pathways, highlights the effectiveness of metabolism-based therapeutic strategies. Furthermore, the near-zero growth rates observed in SeChry models underscore the success of these interventions in limiting cellular proliferation.

Interestingly, the FVA results for SeChry models showed narrower flux ranges compared to control models. This reduced variability suggests that SeChry imposes stricter constraints on metabolic flexibility, potentially reducing or making more surgical the cells' ability to adapt to changing environments.

5.3 Comparison of Control and SeChry exposed Cancer Cells

The metabolic comparison between control and SeChry conditions underscores the profound impact of therapy on cellular metabolism. While cancer cells exhibit high metabolic activity and flexibility in control conditions, SeChry enforces a constrained metabolic regime, reducing proliferation and energy generation. This stark contrast is evident in the metabolic ratios, which highlight the shifts in substrate utilization and flux distributions.

The comparison of cell death and metabolic fluxes across the three cell lines indicates that SeChry treatment induces cell death in a dose-dependent manner, consistent with reduced metabolic activity. The cancer models for PC-9,H292, and A549, show high proliferation rates and substantial glycolytic fluxes, reflecting the the metabolic phenotype characteristic of rapidly proliferating cancer cells. However, under SeChry treatment, the metabolic fluxes decreased, with a notable reduction in glucose uptake and an increase in acetate utilization. This shift in metabolism, coupled with the increase in cell death, suggests that SeChry induces a metabolic stress response, likely limiting energy and biomass production and impairing the cells' ability to proliferate and survive.

The significant increase in cell death observed, particularly in PC-9 cells, may be indicative of a threshold effect where the therapeutic treatment overwhelms the cells' metabolic capacity, leading to cell death. These findings highlight the importance of metabolic flexibility in cancer cells, where SeChry-induced shifts in metabolism may be a key factor inanti-cancer efficacy.

For example, the Pyruvate/Oxaloacetate and Pyruvate/Glutamine ratios were significantly altered under SeChry conditions, reflecting a disruption in the balance of glucose-dependent pathways. Additionally, the increased extracellular glucose levels and acetate

secretion in SeChry models further demonstrate the shift away from a highly glucose-dependent phenotype and towards alternative metabolic sources such as glutamine and fatty acids.

5.4 Implications and Future Directions

The findings of this study have several implications for cancer metabolism research and novel therapeutic development. The observed metabolic flexibility in cancer cells suggests potential targets for therapy aimed at disrupting key pathways that enable adaptation. Conversely, the constrained metabolic state induced by SeChry highlights it as a potential anti-cancer drug and reinforces the importance of preventing metabolic reprogramming and resistance.

Future studies could expand on this work by incorporating time-course analyses to capture dynamic changes in metabolism during the transition from control to therapeutic states. Additionally, integrating multi-omics data, such as proteomics and transcriptomics, could provide a more comprehensive understanding of the molecular mechanisms underlying the observed metabolic shifts.

6 Conclusion

This study highlights the distinct metabolic behaviors of PC-9, H292, and A549 cancer cell lines and their dynamic responses under SeChry exposure. Metabolic constraints underly the reduction of cell proliferation rate and disrupt key pathways crucial for energy generation and biomass production.

The comparative analysis between control and SeChry exposure underscores the potential of targeting metabolic plasticity to enhance therapeutic efficacy. By imposing strict constraints on metabolic flexibility, therapeutic strategies can limit the adaptability of cancer cells, reducing the likelihood of resistance development.

Future work should focus on the temporal dynamics of these metabolic transitions and explore multi-omics approaches to unravel the complex interplay between metabolism and gene regulation in cancer progression and therapy. These insights could pave the way for novel metabolic interventions and optimized treatment regimens.

REFERENCES

[1] J.A. Papin, J.L. Reed, and B.O. Palsson. Metabolic pathway analysis using metabolic flux analysis and genome-scale models. *Nature Reviews Genetics*, 5(1):75–85, 2004.

[2] N.E. Lewis, H. Nagarajan, and B.O. Palsson. Omic data integration enables a better understanding of cellular metabolism. *Nature Reviews Molecular Cell Biology*, 13(10):735–749, 2012.

[3] C.A.L. Mendes. *MCT1: A peon in metabolic adaptation and a crucial target in lung cancer*. Doctoral dissertation, NOVA Medical School, Universidade NOVA de Lisboa, Lisboa, Portugal, 2023.

[4] Tufail, M., Jiang, CH. & Li, N. Altered metabolism in cancer: insights into energy pathways and therapeutic targets. *Mol Cancer* **23**, 203 (2024). https://doi.org/10.1186/s12943-024-02119-3

[5] Santos, I., Ramos, C., Mendes, C., Sequeira, C. O., Tomé, C. S., Fernandes, D. G. H., Mota, P., Pires, R. F., Urso, D., Hipólito, A., Antunes, A. M. M., Vicente, J. B., Pereira, S. A., Bonifácio, V. D. B., Nunes, S. C., & Serpa, J. (2019). Targeting Glutathione and Cystathionine β-Synthase in Ovarian Cancer Treatment by Selenium-Chrysin Polyurea Dendrimer Nanoformulation. *Nutrients*, *11*(10), 2523. https://doi.org/10.3390/nu11102523

[6] Martins, I. L., Charneira, C., Gandin, V., Ferreira da Silva, J. L., Justino, G. C., Telo, J. P., Vieira, A. J., Marzano, C., & Antunes, A. M. (2015). Selenium-containing chrysin and quercetin derivatives: attractive scaffolds for cancer therapy. *Journal of medicinal chemistry*, *58*(10), 4250–4265. https://doi.org/10.1021/acs.jmedchem.5b00230

[7] Mendes, C., Lemos, I., Hipólito, A., Abreu, B., Freitas-Dias, C., Martins, F., Pires, R. F., Barros, H., Bonifácio, V. D. B., Gonçalves, L. G., & Serpa, J. (2024). Metabolic profiling and combined therapeutic strategies unveil the cytotoxic potential of selenium-chrysin (SeChry) in NSCLC cells. *Bioscience reports*, *44*(7), BSR20240752. https://doi.org/10.1042/BSR20240752

[8] Hipólito, A., Mendes, C., Martins, F., Lemos, I., Francisco, I., Cunha, F., Almodôvar, T., Albuquerque, C., Gonçalves, L. G., Bonifácio, V. D. B., Vicente, J. B., & Serpa, J. (2023). H_2S-Synthesizing Enzymes Are Putative Determinants in Lung Cancer Management toward Personalized Medicine. *Antioxidants (Basel, Switzerland)*, *13*(1), 51. https://doi.org/10.3390/antiox13010051

[9] J.D. Orth, I. Thiele, and B.Ø. Palsson. What is flux balance analysis? *Nature Biotechnology*, 28:245–248, 2010.

[10] J. et al. Schellenberger. Quantitative prediction of cellular metabolism with constraintbased models: the cobra toolbox v2.0. *Nature Protocols*, 6:1290–1307, 2011.

[11] A. Ebrahim, J.A. Lerman, B.O. Palsson, and D.R. Hyduke. Cobrapy: Constraints based reconstruction and analysis for python. *BMC Systems Biology*, 7(1):74, 2013.

[12] Wang, J., Wen, Y., Zhao, W., Zhang, Y., Lin, F., Ouyang, C., Wang, H., Yao, L., Ma, H., Zhuo, Y., Huang, H., Shi, X., Feng, L., Lin, D., Jiang, B., & Li, Q. (2023). Hepatic conversion of acetyl-CoA to acetate plays crucial roles in energy stress. *eLife*, *12*, RP87419. https://doi.org/10.7554/eLife.87419

[13] Ashibe, B., & Motojima, K. (2009). Fatty aldehyde dehydrogenase is up-regulated by polyunsaturated fatty acid via peroxisome proliferator-activated receptor alpha and suppresses polyunsaturated fatty acid-induced endoplasmic reticulum stress. *The FEBS journal*, *276*(23), 6956–6970. https://doi.org/10.1111/j.1742-4658.2009.07404.x

[14] Berdyshev E. V. (2011). Mass spectrometry of fatty aldehydes. *Biochimica et biophysica acta*, *1811*(11), 680–693. https://doi.org/10.1016/j.bbalip.2011.08.018

[15] Mendes, C., Lemos, I., Francisco, I., Almodôvar, T., Cunha, F., Albuquerque, C., Gonçalves, L. G., & Serpa, J. (2023). NSCLC presents metabolic heterogeneity, and there is still some leeway for EGF stimuli in EGFR-mutated NSCLC. *Lung cancer (Amsterdam, Netherlands)*, *182*, 107283. https://doi.org/10.1016/j.lungcan.2023.107283

[16] Journal of Neuroscience Methods Volume 171, Issue 2Analysis of glutamine, glutamate, pyroglutamate, and GABA in cerebrospinal fluid using ion pairing HPLC with positive electrospray LC/MS/MS , 30 June 2008, Pages 190-196

[17] Venkataraman S S, Regone R, Ammar H M, et al. (July 24, 2019) Pyroglutamic Acidemia: An Underrecognized and Underdiagnosed Cause of High Anion Gap Metabolic Acidosis - A Case Report and Review of Literature. Cureus 11(7): e5229. doi:10.7759/cureus.5229

[18] Santos, I., Ramos, C., Mendes, C., Sequeira, C. O., Tomé, C. S., Fernandes, D. G. H., Mota, P., Pires, R. F., Urso, D., Hipólito, A., Antunes, A. M. M., Vicente, J. B., Pereira, S. A., Bonifácio, V. D. B., Nunes, S. C., & Serpa, J. (2019). Targeting Glutathione and Cystathionine β-Synthase in Ovarian Cancer Treatment by Selenium-Chrysin Polyurea Dendrimer Nanoformulation. *Nutrients*, *11*(10), 2523. https://doi.org/10.3390/nu11102523

SYMCOMP 2025
Lisbon, 10-11 April 2025

TIME-FRACTIONAL ADVECTION-DIFFUSION MODEL FOR TRANSIENT CURRENTS IN DISORDERED MATERIALS

L. F. Morgado[1], M. L. Morgado[2], L. L. Ferrás[3] and A. Falorca [4]

1: Department of Physics, University of Trás-os-Montes e Alto Douro and Instituto de Telecomunicações, Lisboa, Portugal
e-mail: lmorgado@utad.pt

2: Department of Mathematics, University of Trás-os-Montes e Alto Douro and Center for Computational and Stochastic Mathematics, Instituto Superior Técnico, Universidade de Lisboa, Portugal
e-mail: luisam@utad.pt

3: Faculty of Engineering, University of Porto, Portugal
e-mail: lferras@fe.up.pt

4: Leiden Observatory, Leiden University, The Netherlands
e-mail: falorca@strw.leidenuniv.nl

Keywords: Finite differences, advection-diffusion, fractional derivatives, concentration dependent mobility

Abstract. *This work reports on the development of a numerical scheme used to simulate the transient electrical current running through a thin layer of disordered semiconductor (e.g., organic) between parallel electrodes under a perpendicularly applied electric field. Extending previous research, it focuses on numerically approximating the solution of anomalous diffusion problems, expressed with time fractional derivatives, that arise from the multiple trapping model, considered tol effectively describe the complex charge transport mechanisms in these materials, accounting for the trapping and release of charge carriers. This study addresses the case of concentration-dependent charge carrier mobility, which introduces a nonlinearity into the advetion-diffusion (or drift-diffusion) equations. This nonlinearity, arising from the variable diffusion coefficient, requires specialized numerical techniques to accurately simulate the current flow. The model implements and investigates suitable numerical methods for these nonlinear, fractional-order equations, contributing for a more detailed understanding of charge transport in disordered semiconductors.*

Acknowledgments: This work is financially supported by national funds throughthe FCT/MCTES (PIDDAC), under the project 2022.06672.PTDC - iMAD - Improving the Modelling of Anomalous Diffusion and Viscoelasticity: solutions to industrial problems, with DOI 10.54499/2022.06672.PTDC.

SYMCOMP 2025
Lisbon, 10-11 April 2025

IMPROVING PD-L1 EXPRESSION PREDICTION IN NON-SMALL CELL LUNG CANCER USING RADIOMIC ANALYSIS AND ENSEMBLE MACHINE LEARNING MODELS ON WHOLE-BODY VS. LUNG PET/CT DATA

Steven Muyiwa Olawale[1,2], Azeem Saleem[2,3], Eline Roejkjaer[3], Ged Avery[2,3], Eva Sousa[1,3*]

1: Centre of Excellence for Data Science, Artificial Intelligence and Modelling, University of Hull, Hull, United Kingdom

e-mail: {s.olawale-2022, e.sousa}@hull.ac.uk
web: https://www.hull.ac.uk/work-with-us/research/institutes/data-science-artificial-intelligence-and-modelling

2: Castle Hill Hospital, Hull University Teaching Hospitals NHS Trust
e-mail: {steven.olawale, ged.avery1}@nhs.net

3: Hull York Medical School, University of Hull, Hull, United Kingdom
e-mail: {eva.sousa}@hyms.ac.uk
web: Centre for Biomedicine | Hull York Medical School

Keywords: Radiomics, NSCLC, Machine Learning, PD-L1, PET/CT, Metabolic Imaging

Abstract *Lung cancer remains the leading cause of cancer-related mortality globally. Non-small cell lung cancer (NSCLC) account for 85% of lung cancer cases. Programmed Death-Ligand 1 (PD-L1) is a critical biomarker in NSCLC for guiding immunotherapy, yet conventional detection methods, such as immunohistochemistry, are invasive and insufficiently capture tumour heterogeneity. This study explores the potential of radiomics-based machine learning (ML) models to predict PD-L1 expression using whole-body and lung [^{18}F]-FDG PET/CT imaging data. Radiomic features were extracted from 134,590 whole-body and 43,142 lung slices obtained from 308 NSCLC patients. The study evaluated the performance of ensemble models including random forest, and XGBoost at feature- and patient-level analyses. Models trained on whole-body data consistently outperformed those using lung data, highlighting the importance of systemic metabolic information. At the feature level, the random forest model achieved 99.1% accuracy and an ROC-AUC of 0.998. Similarly, at the patient-level, the random forest model also achieved 98% accuracy and an ROC-AUC of 0.995. The findings demonstrate the superiority of whole-body radiomic analysis over localised imaging for predicting PD-L1 expression. This approach underscores its potential as a non-invasive diagnostic tool, providing an advanced framework for precision oncology in NSCLC management.*

DOI:10.5281/zenodo.15161193

1. INTRODUCTION

Lung cancer remains the leading cause of cancer-related mortality worldwide, with 1.8 million people dying of lung cancer every year [1], highlighting the urgent need for more effective diagnostic and therapeutic strategies. In the United Kingdom, lung cancer is the third most prevalent cancer [2]. About 85% of lung cancer is classified as non-small cell lung cancer (NSCLC). Over the past decade, the treatment landscape for NSCLC has evolved significantly and in addition to traditional modalities such as surgery, radiotherapy and chemotherapy, more targeted therapies and immunotherapies determined by tumour expression of molecular markers have been added to the treatment armamentarium [3]. Personalized biomarker-driven NSCLC therapy targeting epidermal growth factor receptor (EGFR), anaplastic lymphoma kinase (ALK), and immunotherapy targeting the programmed death-ligand 1 (PD-L1) is now available [4].

Immunotherapy, particularly through the use of immune checkpoint inhibitors (ICIs) targeting the PD-1/PD-L1 pathway, have emerged as a key treatment modality of NSCLC management. By blocking the interaction between PD-L1 on tumour cells and PD-1 on T-cells, these agents reactivate the immune response, leading to significant improvements in progression-free and overall survival compared to traditional chemotherapy [5][6][7][8][9][10]. However, the standard method for assessing PD-L1 expression—immunohistochemistry (IHC)—requires invasive biopsies that may not capture tumour heterogeneity and can lead to complications [11][12][13]. This limitation underscores the need for non-invasive, comprehensive assessment methods.

To address these limitations, there is a growing interest in leveraging the radiomic features of computerised tomography (CT) and positron emission tomography/CT (PET/CT) with [^{18}F]fluorodeoxyglucose ([^{18}F]FDG) beyond its traditional diagnostic and monitoring roles, particularly in quantitative biomarker evaluation for immunotherapy response prediction [14]. Alongside conventional radiotracer uptake evaluation performed using Standardized Uptake Value (SUV), a widely used PET imaging metric for assessing tumor metabolism, advanced computational approaches such as artificial intelligence and machine learning enhance the extraction and interpretation of high dimensional features from PET/CT scans. By analyzing the shape, intensity, and texture features of tumors, radiomics provides a noninvasive method to assess tumor biology and predict therapeutic outcomes [15][16][17].

Early radiomics models for PD-L1 prediction, despite demonstrating moderate performance (with accuracies around 68% and AUCs ranging from 0.706 to 0.84 [18][19]), face a critical research gap. These models are predominantly based on small datasets, leading to overfitting and compromised generalizability which is a serious concern for clinical applications. Moreover, their focus on localized tumour regions neglects systemic metabolic activity, an important facet of tumour biology that could significantly enhance predictive accuracy. This oversight reveals a clear problem in current methodologies: the inability to fully capture the complex, systemic nature of tumour behaviour. Addressing this gap by incorporating systemic metabolic information into radiomic analyses is essential for developing more robust and clinically applicable models for PD-L1 prediction.

To overcome these challenges, ensemble machine learning models, particularly random forest and Extreme Gradient Boosting (XGBoost), have demonstrated strong performance in medical imaging analysis and disease classification by reducing overfitting and improving model interpretability. random forest has demonstrated significant success in disease risk classification, including maternal health risk prediction, where an ensemble model combining random forest and artificial neural networks (ANN) achieved high accuracy, precision, recall, and F1-score in classifying pregnancy-related complications [20]. Similarly, a study analysing highly imbalanced disease datasets found that random forest, coupled with repeated random sub-sampling, outperformed other classifiers in predicting the risk of eight chronic diseases, achieving superior sensitivity and specificity compared to traditional methods [21]. In clinical disease prediction, random forest models have effectively classified conditions such as diabetes, cardiovascular disease, and cancer, with a reported accuracy exceeding 90% in multiple datasets [22]. Likewise, XGBoost has been widely applied in cancer diagnostics, where it achieved an accuracy of 94.74% and a recall of 95.24% in breast cancer classification, underscoring its efficacy in early disease detection [23]. Additionally, XGBoost has been successfully utilized for classifying 28 different cancer types based on circulating tumour DNA, demonstrating its ability to handle complex, high-dimensional genetic data [24].

In NSCLC research, ensemble models have shown promise in non-invasive tumour characterization. A study comparing random forest models trained on CT radiomics versus semantic features found that models incorporating semantic descriptors interpreted by radiologists achieved higher accuracy in classifying NSCLC subtypes than radiomics-based models alone [25]. Further advancements in tumour microenvironment analysis have leveraged an expert-in-the-loop random forest model to distinguish adenocarcinoma from squamous cell carcinoma in fibrotic and non-fibrotic lung regions, highlighting the model's ability to capture subtle variations in tissue morphology [26]. Moreover, the integration of random forest and XGBoost in lung cancer prediction has significantly enhanced classification performance, with hyperparameter tuning and ensemble voting mechanisms improving predictive accuracy beyond standalone models [27]. These studies collectively underscore the potential of ensemble methods in improving cancer classification and prognosis.

Building on these advances, this study employs random forest and XGBoost to predict PD-L1 expression in NSCLC patients using radiomic features extracted from [^{18}F]FDG PET/CT scans. By integrating both whole-body and lung imaging data at the feature and patient levels, our approach aims to capture broader systemic metabolic activity and overcome the constraints of localized analysis. Ultimately, this strategy is expected to enhance the accuracy, robustness, and clinical applicability of PD-L1 expression prediction, providing a non-invasive and scalable framework to guide immunotherapy decisions in NSCLC patients.

2. MATERIALS AND METHODS

2.1. Data Collection

The present research utilized imaging and tissue expression data collated for an institutionally-approved audit from 308 patients diagnosed with non-small cell lung cancer (NSCLC) who

underwent ^{18}F-fluorodeoxyglucose ([^{18}F]FDG) positron emission tomography/computed tomography (PET/CT) examinations at the Nuclear Medicine Department of Castle Hill Hospital between December 2019 and January 2023. Among these patients, 207 were classified as PD-L1-positive and 101 as PD-L1-negative based on immunohistochemistry (IHC) analyses. Imaging data were stored in Digital Imaging and Communications in Medicine (DICOM) format and retrieved using Mirada DBx software. The scans consisted of fused PET/CT images with attenuation correction applied to enhance image quality and ensure quantitative accuracy. Each patient's PET/CT scan produced more than 300 axial slices representing cross-sectional images of the body. For targeted analysis, slices numbered 120 to 260, representing the thoracic region encompassing the lungs, were selected based on consultations with a radiologist and validation using the Mirada DBx viewer. To protect patient privacy, all data were anonymized in accordance with ethical guidelines. The dataset exhibited class imbalance, with 67% of cases classified as PD-L1-positive and 33% as PD-L1-negative. To address this imbalance, the Synthetic Minority Oversampling Technique (SMOTE) was employed during pre-processing to ensure balanced model training.

2.2. Data Preprocessing

All DICOM images were imported into Python 3.8 for pre-processing and analysis. Each axial slice was resized to a standard resolution of 512×512 pixels using bilinear interpolation to normalize input dimensions and maintain consistency across all scans. Pixel intensity values were normalized to a range between 0 and 1 by dividing each pixel value by the maximum intensity in the respective slice. A Gaussian filter with a sigma value of 1 was applied using the scikit-image library to reduce noise and enhance image quality.

2.3. Lung Segmentation

Lung regions were isolated from the PET/CT scans by selecting slices numbered 120 to 260, representing the thoracic region. Otsu's thresholding method, implemented via OpenCV, was applied to each slice to generate binary masks delineating lung tissue from surrounding structures. These masks were validated by radiologists to ensure accurate segmentation.

2.4. Feature Extraction

Radiomic features were extracted using PyRadiomics, which computes a wide range of quantitative descriptors (e.g., first-order statistics, texture, and shape-based metrics). Each slice was processed individually to capture relevant heterogeneity linked to PD-L1 expression.

Two parallel datasets were created:

1. Whole-body Dataset: Radiomic features from the entire PET/CT scan.
2. Lung dataset: Radiomic features only from the lung regions (slices 120–260).

Feature-Level vs. Patient-Level Analysis

- Feature-Level: Each slice’s radiomic features were treated as independent samples.
- Patient-Level: Radiomic features were aggregated by taking the mean value across all slices from each patient, resulting in a single feature vector per patient.

2.5. Feature Engineering

To enhance the model performance, feature engineering and selection were conducted in several steps. Initially, all extracted features were consolidated into a DataFrame, where non-numeric values were excluded, and missing values were replaced with zeros to ensure data completeness. Following this, feature scaling was conducted using the StandardScaler to normalize the features, making them comparable across different scales.
For the whole-body dataset at the feature level, Elastic Net regression with five-fold cross-validation using scikit-learn's ElasticNetCV was applied to identify the most predictive features, balancing L1 and L2 penalties to reduce overfitting. Features with non-zero coefficients were retained for further model development.
In contrast, for the Lung dataset and patient-level analyses, random forest feature importance was employed due to the Elastic Net's limited effectiveness in these contexts. A random forest classifier was trained, and feature importance scores were computed based on the Gini impurity criterion. Features exceeding a predefined importance threshold (importance > 0.01) were selected for model training.

2.6. Model Development, Training, and Evaluation

To predict PD-L1 expression, ensemble machine learning methods specifically random forest (RF) and Extreme Gradient Boosting (XGBoost) were employed. These models were trained using radiomic features extracted from [^{18}F]FDG PET/CT scans to classify NSCLC patients as PD-L1-positive or PD-L1-negative. Feature-level and patient-level analyses were conducted using both whole-body and Lung datasets.

2.6.1. Random Forest Models

The random forest model was developed iteratively through three phases to enhance predictive performance. Initially, a baseline model (RF Model 1) was implemented using default hyperparameters in scikit-learn as seen in Table 1 to establish a benchmark for performance evaluation. This provided a reference point for subsequent improvements. In the second phase, regularization techniques were introduced to prevent overfitting. The maximum depth of trees was constrained, and the minimum number of samples required for splitting and leaf nodes was increased. Additionally, the number of features considered per split was adjusted to ensure a balanced trade-off between model complexity and generalization.
To further refine performance, the third phase involved hyperparameter optimization, where a RandomizedSearchCV approach was applied to systematically explore and fine-tune key parameters. This process optimized the number of estimators, maximum depth, and minimum samples per split, ensuring that the model was both robust and efficient. Through this iterative approach, the random forest model was progressively improved, achieving an optimal balance between accuracy and generalizability in predicting PD-L1 expression.

2.6.2. XGBoost Models

XGBoost models were optimized in two stages. First, a baseline model (XGB Model 1) was trained using default hyperparameters to establish a benchmark. Next, hyperparameter optimization (XGB Model 2) was performed using RandomizedSearchCV to refine learning rate, maximum depth, subsample ratios, and regularization terms, improving predictive accuracy while reducing overfitting.

Model	Strategy	Parameters Tuned	Details
Random forest (RF)	Cross-validation on Base Model	Stratified 5-fold Cross-Validation	cv=5, shuffle=True, random_state=42
	Regularization (RF Model 2)	max_depth, min_samples_split, min_samples_leaf, max_features	max_depth=10, min_samples_split=5, min_samples_leaf=4, max_features='sqrt'
	Hyperparameter Tuning (RF Model 3)	Random search: n_estimators, max_depth, min_samples_split, min_samples_leaf, max_features	n_estimators=100-500, max_depth=None-50, min_samples_split=2-10, max_features=['sqrt', 'log2', None]
XGBoost	Hyperparameter Tuning (XGB Model 2)	Random search: n_estimators, learning_rate, max_depth, subsample, colsample_bytree, gamma	n_estimators=100-500, learning_rate=0.01-0.2, max_depth=3-11, subsample=0.6-1.0, gamma=0-0.3

Table 1. Summary of the hyperparameters used with the different models tested.

2.6.3. Training and Validation

The dataset was partitioned into training (80%) and testing (20%) subsets using stratified sampling to preserve class distribution. Stratified five-fold cross-validation was applied during model training to ensure robustness. Model performance was evaluated using key classification metrics, including accuracy, area under the receiver operating characteristic curve (ROC-AUC), precision, recall, F1-score, and log loss. The results were analyzed at both feature- and patient-levels, comparing whole-body and Lung datasets to determine the most informative approach for PD-L1 prediction.

2.6.5. Software and Libraries

All analyses were performed in Python using libraries including scikit-learn for machine learning, XGBoost for gradient boosting, and PyRadiomics for feature extraction.

3. RESULTS

3.1. Lung Segmentation and Visualization

The visualization and analysis of whole-body [^{18}F]FDG PET/CT images using the Mirada DBx viewer identified slices numbered 120 to 260 as the most relevant for analysis. These slices cover the thoracic region, where NSCLC tumours are typically located. Within this slice range, the lung anatomy and tumour sites were clearly visible, as demonstrated in Figure 1.

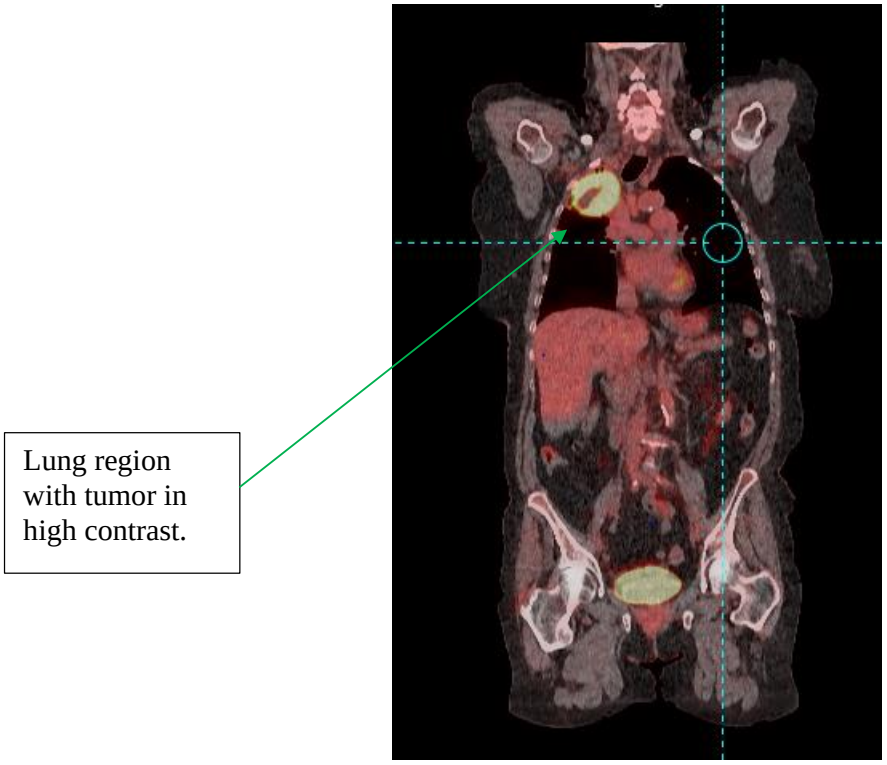

Figure 1. Fused coronal PET/CT image highlighting the tumour in the right upper lung region. The lung area is indicated by the arrow, showcasing the specific region where the tumour is located.

3.2. Feature Extraction, Selection and Preprocessing

Using PyRadiomics, 98 radiomic features were initially extracted from the PET scan data for both the whole-body and lung datasets. The whole-body dataset comprised 134,590 slices,

while the lung dataset contained 43,142 slices. For patient-level analysis, the features from all slices were aggregated using the mean, resulting in a dataset of 307 patients. These features spanned multiple categories, including statistical, texture-based, and shape-based descriptors. Feature selection methods were employed to reduce the dimensionality of the dataset. For the Whole-body dataset at feature-level, Elastic Net regression with five-fold cross-validation reduced the features to 27. In contrast, for the Lung dataset and patient-level analyses, random forest feature importance identified between 24 and 39 features, as summarized in Table 2.

Dataset	Level	Feature Selection Type	Features (Before)	Features (After)
Whole-body dataset	Feature Level	Elastic net	98	27
Whole-body dataset	Patient Level	Random forest	98	36
Lung dataset	Feature Level	Random forest	98	24
Lung dataset	Patient Level	Random forest	98	39

Table 2. Feature selection summary for whole-body and lung dataset

An initial class imbalance was observed, with PD-L1-positive cases constituting 67% of the dataset and PD-L1-negative cases 33%. SMOTE was applied to balance the dataset, resulting in an equal distribution of classes.

3.3. Model Performance (Feature-Level Analysis)

At the feature level, the random forest and XGBoost models were evaluated for both the whole-body and Lung datasets. The random forest model (RF Model 3) optimized through random search achieved the best performance on the whole-body dataset, as detailed in Table 3, with an accuracy of 99.1% and a ROC-AUC of 0.999. The cross-validation results for random forest Model 3, as shown in Table 4, reveal a consistent performance on the whole-body and Lung dataset, with mean accuracies of 0.993 and 0.758 across all five folds for the whole-body and Lung dataset respectively.

Dataset	Model	Configuration	Precision	Recall	F1-Score	Accuracy	ROC-AUC
Whole-body	Random forest	Baseline RF model (RF model 1)	0.99	0.99	0.99	0.991	0.997
		Regularization (RF model 2)	0.99	0.99	0.99	0.991	0.997
		Hyperparameter tuning with random search (RF Model 3)	**0.99**	**0.99**	**0.99**	**0.991**	**0.999**
	XGBoost	Baseline XGB model (XGB model 1)	0.99	0.99	0.99	0.991	0.997
		Hyperparameter tuning with random search (XGB model 2)	0.99	0.99	0.99	0.991	0.998
Lung	Random forest	Baseline RF model (RF model 1)	0.72	0.71	0.72	0.71	0.76
		Regularization (RF Model 2)	0.67	0.65	0.65	0.645	0.69
		Hyperparameter tuning with random search (RF Model 3)	0.73	0.73	0.73	0.77	0.72
	XGBoost	Baseline XGB model (XGB model 1)	0.69	0.69	0.69	0.69	0.71
		Hyperparameter tuning with random search (XGB model 2)	0.72	0.72	0.72	0.72	0.75

Table 3: Performance metrics for ensemble models (feature-level analysis). The best performing model is marked in bold.

	1st Fold	2nd Fold	3rd Fold	4th Fold	5th Fold	Mean Accuracy
Whole-body	0.994	0.993	0.993	0.993	0.993	0.993
Lung	0.760	0.763	0.745	0.756	0.765	0.758

Table 4: Cross-alidation accuracy scores for random forest in both whole-body and lung datasets (feature level analysis).

3.4. Model Performance (Patient-Level)

At the patient level, the random forest and XGBoost models were also evaluated and compared across both the whole-body and Lung datasets. The random forest model optimized through random search also exhibited the best performance, achieving the highest accuracy and ROC-AUC scores as presented in Table 5.
2qZ2qZ
Further Insight into the model's performance as depicted in Figure 2, shows high accuracy with the confusion matrix indicating correct classification of all 18 PD-L1 negative patients and 43 out of 44 PD-L1 positive patients, demonstrating near-perfect sensitivity and specificity. In **Figure 3**, the log loss analysis reveals consistently low values across most predictions, reflecting high confidence in the model's outputs. However, a distinct spike around sample index 20 suggests a single instance of high uncertainty, contrasting with the overall stability in predictive confidence throughout the dataset.

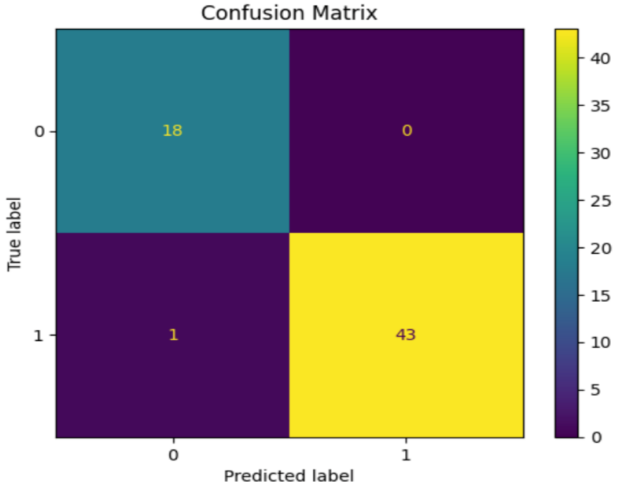

Figure 2: Confusion matrix for the random forest model optimized through random search (RF model 3) for the whole-body data at a patient level, which achieved the highest accuracy and ROC-AUC

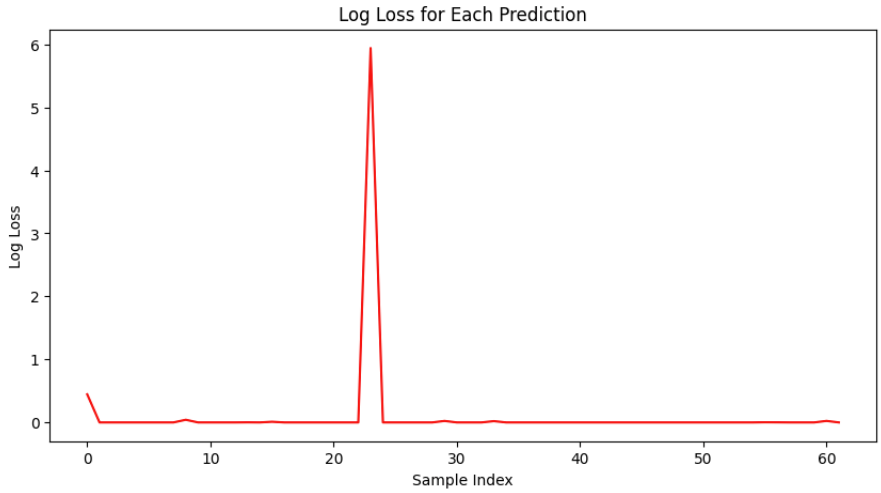

Figure 3: Log loss result for the random forest model optimised through random search (RF model 3), for the whole-body data at a patient level, which achieved the highest accuracy and ROC-AUC.

Dataset	Model	Configuration	Precision	Recall	F1-Score	Accuracy	ROC-AUC
Whole-body dataset	Random forest	Baseline RF model (RF model 1)	0.98	0.98	0.98	0.984	0.998
		Regularization (RF Model 2)	0.98	0.98	0.98	0.984	0.982
		Hyperparameter tuning with random search (RF model 3)	0.98	0.99	0.99	0.984	0.992
	XGBoost	Baseline XGB model (XGB model 1)	0.98	0.98	0.98	0.984	0.986
		Hyperparameter tuning with random search (XGB Model 2)	0.98	0.98	0.98	0.984	0.988
Lung Dataset	Random forest	Baseline RF model (RF model 1)	0.53	0.52	0.52	0.51	0.471
		Regularization (RF model 2)	0.58	0.55	0.56	0.553	0.50
		Hyperparameter tuning with random search (RF model 3)	0.58	0.56	0.57	0.565	0.511
	XGBoost	Baseline XGB model (XGB model 1)	0.61	0.61	0.61	0.613	0.558
		Hyperparameter tuning with random search (XGB model 2)	0.61	0.61	0.61	0.612	0.49

Table 5: Performance metrics for random forest (patient-level analysis)

4.0 DISCUSSION

The advent of PD-1/PD-L1 checkpoint inhibitors has transformed the treatment landscape for NSCLC, with numerous studies underscoring the importance of PD-L1 expression as a critical biomarker for predicting patient response to immunotherapy. Accurate assessment of PD-L1 levels is essential for guiding treatment decisions and optimizing outcomes in NSCLC patients [28][29][30].

In this study, radiomic features extracted from both whole-body and lung PET scan data were used to predict PD-L1 expression through feature-level and patient-level analyses. The results consistently demonstrated that whole-body data, which captures broader metabolic processes, outperformed lung data. This supports the growing evidence that incorporating whole-body imaging provides more comprehensive insights into disease processes and patient prognosis [31][32].

The evaluation of both datasets demonstrated that models trained on whole-body data consistently outperformed those trained on lung data across multiple metrics, including accuracy, precision, recall, F1-score, and ROC-AUC scores (Tables 3 and 5). At the feature level, random forest model, chosen for its robustness against overfitting and scalability to large datasets [32], achieved a remarkable 99.1% accuracy and an ROC-AUC of 0.998 on the whole-body dataset following random search optimization (RF Model 3). In contrast, the lung data produced significantly lower results, with a maximum accuracy of 77% and ROC-AUC of 0.75 (Table 3). These results suggest that radiomic features derived from the whole body, reflecting systemic metabolic activity, offer valuable predictive information that may be absent in localized imaging focused on the lungs.

Similarly, the XGBoost models showed superior performance with whole-body data compared to lung data, reinforcing the conclusion that features from tissues beyond the lung enhance predictive accuracy. The consistent superiority of whole-body analysis indicates that broader metabolic processes are crucial for understanding PD-L1 expression in NSCLC.

Further validation using confusion matrices and log loss metrics analysis confirmed the superiority of whole-body data. The random forest and XGboost models trained on whole-body data exhibited fewer misclassifications and lower log loss values, indicating greater model confidence and reliability compared to lung-segmented models.

To ensure the model's robustness and mitigate potential overfitting, cross-validation (K-fold) was employed on the best-performing model (RF Model 3). Cross-validation, widely used to assess model performance on different subsets of data [33], confirmed the generalizability of the model. An average accuracy of 99.3% across all folds (Table 4) further validated the model's stability and reliability, indicating that it is well-suited for predicting PD-L1 expression in NSCLC.

The patient-level analysis, designed to enhance model robustness and accuracy, involved aggregating features across multiple slices using mean aggregation. This method has been shown to improve prediction performance by offering more reliable outcomes and better generalization of models [34]. In this study, patient-level analysis of the whole-body dataset

resulted in high accuracies and ROC-AUC scores, with the random forest model achieving 98% accuracy and an ROC-AUC score of 0.992, this study achieved higher ROC-AUC compared to studies [18][19] which had lower ROC-AUC scores of 68 and 84% respectfully. By contrast, patient-level models trained on lung data yielded significantly lower accuracy (61.3%) and ROC-AUC (0.558**)**, reinforcing the value of whole-body radiomics in PD-L1 prediction.
Notably, a similar study focusing on lung data achieved a ROC-AUC of 0.82 [35], further demonstrating the limitations of localized imaging approaches. In contrast, the superior performance of whole-body data in this study underscores the value of incorporating systemic metabolic information for enhanced predictive accuracy.
Overall, these findings confirm that incorporating whole-body metabolic data in radiomic analyses offers significant predictive advantages over localized imaging approaches. Previous studies reported lower accuracies when focusing only on tumour regions [18] [19], whereas this study demonstrates that whole-body analysis achieves superior predictive accuracy (99% vs. 68% and 84%, respectively). This highlights the importance of considering systemic metabolic information, rather than relying solely on localized regions, for predicting PD-L1 expression and optimizing treatment strategies in NSCLC patients.
Future studies should further investigate the potential clinical applications of whole-body radiomic analysis for broader biomarkers and treatment responses in NSCLC. The consistent results obtained in this study suggest that whole-body PET/CT data could improve patient care by providing more holistic insights into disease processes, leading to more precise treatment decisions. However, larger datasets and external validation cohorts are needed to confirm the long-term reliability and generalizability of these findings across different populations.

5.0 CONCLUSION

This study provides compelling evidence that whole-body [^{18}F]FDG PET/CT imaging data, when analysed using machine learning models, offer a more accurate and comprehensive approach for predicting PD-L1 expression in NSCLC patients compared to lung data. The superior performance of models trained on whole-body data underscores the importance of systemic metabolic information in understanding PD-L1 expression.
By surpassing the predictive accuracy of previous studies that focused solely on localized tumor regions, this research highlights the potential clinical value of adopting a holistic imaging strategy. The incorporation of whole-body radiomic analysis could enhance patient stratification for immunotherapy, leading to improved personalized treatment strategies.
However, before this approach can be integrated into routine clinical practice, further validation in larger and more diverse patient cohorts is necessary. Future studies should also explore the integration of whole-body imaging with other data types, such as genomic and clinical information, to further enhance the predictive power of these models. Such multi-modal approaches hold promise for advancing personalized oncology care and optimizing treatment outcomes for NSCLC patients.

REFERENCES

[1] Sung, H., Ferlay, J., Siegel, R.L., et al. "Global cancer statistics 2020: GLOBOCAN estimates of incidence and mortality worldwide for 36 cancers in 185 countries", *CA: A*

Cancer Journal for Clinicians, vol. 71, no. 3, pp. 209–249, 2021. https://doi.org/10.3322/caac.21660.

[2] NHS Digital. "Cancer incidence by gender and age," *Cancer Registration Statistics, England, 2021 - Summary Counts Only*, NHS Digital, 2024. Available: https://digital.nhs.uk/data-and-information/publications/statistical/cancer-registration-statistics/england-2021---summary-counts-only/cancer-incidence-by-gender-and-age.
[32] NHS Digital. "Cancer incidence by gender and age," *Cancer Registration Statistics, England, 2021 - Summary Counts Only*, NHS Digital, 2024. Available: https://digital.nhs.uk/data-and-information/publications/statistical/cancer-registration-statistics/england-2021---summary-counts-only/cancer-incidence-by-gender-and-age.Liu, S.Y.M., Zheng, M.M., Pan, Y., et al. "Emerging evidence and treatment paradigm of non-small cell lung cancer", *Journal of Hematology & Oncology*, vol. 16, article 40, 2023. https://doi.org/10.1186/s13045-023-01436-2.

[3] Aisner, D.L., Riely, G.J. "Non-small cell lung cancer: recommendations for biomarker testing and treatment", *Journal of the National Comprehensive Cancer Network*, vol. 19, no. 5, pp. 610–613, 2021. https://doi.org/10.6004/jnccn.2021.5020.

[4] Lin, X., Kang, K., Chen, P., et al. "Regulatory mechanisms of PD-1/PD-L1 in cancers", *Molecular Cancer*, vol. 23, article 108, 2024. https://doi.org/10.1186/s12943-024-02023-w.

[5] Deslypere, G., Gullentops, D., Wauters, E., et al. "Immunotherapy in non-metastatic non-small cell lung cancer: can the benefits of stage IV therapy be translated into earlier stages?", *Therapeutic Advances in Medical Oncology*, vol. 10, 2018. https://doi.org/10.1177/1758835918772810.

[6] Kilaru, S., Panda, S.S., Moharana, L., et al. "PD-L1 expression and its significance in advanced NSCLC: real-world experience from a tertiary care center", *Journal of the Egyptian National Cancer Institute*, vol. 36, no. 3, 2024. https://doi.org/10.1186/s43046-024-00207-5.

[7] Rittmeyer, A., Barlesi, F., Waterkamp, D., et al. "Atezolizumab versus docetaxel in patients with previously treated non-small-cell lung cancer (OAK): a phase 3, open-label, multicentre randomised controlled trial", *The Lancet*, vol. 389, no. 10066, pp. 255–265, 2017. https://doi.org/10.1016/S0140-6736(16)32517-X.

[8] Wang, J., Wang, J., Huang, X., et al. "CT radiomics-based model for predicting TMB and immunotherapy response in non-small cell lung cancer", *BMC Medical Imaging*, vol. 24, article 45, 2024. https://doi.org/10.1186/s12880-024-01221-8.

[9] Reck, M., Rodríguez-Abreu, D., Robinson, A.G., et al. "Pembrolizumab versus chemotherapy for PD-L1–positive non–small-cell lung cancer", *New England Journal of Medicine*, vol. 375, no. 19, pp. 1823–1833, 2016. https://doi.org/10.1056/NEJMoa1606774.

[10] Dhar, M., Wong, J., Che, J., et al. "Evaluation of PD-L1 expression on vortex-isolated circulating tumor cells in metastatic lung cancer", *Scientific Reports*, vol. 8, article 2592, 2018. https://doi.org/10.1038/s41598-018-19245-w.

[11] Wu, X., Huang, Y., Zhao, Q., et al. "PD-L1 expression correlation with metabolic parameters of FDG PET/CT and clinicopathological characteristics in non-small cell lung cancer", *EJNMMI Research*, vol. 10, article 51, 2020.

https://doi.org/10.1186/s13550-020-00639-9.
[12] Tejerina, E., García Tobar, L., Echeveste, J.I., et al. "PD-L1 in cytological samples: a review and a practical approach", *Frontiers in Medicine*, vol. 8, 2021. https://doi.org/10.3389/fmed.2021.668612.
[13] Eze, C., Schmidt-Hegemann, N.S., Sawicki, L.M., et al. "PET/CT imaging for evaluation of multimodal treatment efficacy and toxicity in advanced NSCLC—current state and future directions", *European Journal of Nuclear Medicine and Molecular Imaging*, vol. 48, pp. 3975–3989, 2021. https://doi.org/10.1007/s00259-021-05211-8.
[14] Pinta, C. de la, Barrios-Campo, N., Sevillano, D. "Radiomics in lung cancer for oncologists", *Journal of Clinical and Translational Research*, vol. 6, no. 4, pp. 127–134, 2020.
[15] van Timmeren, J., Cester, D., Tanadini-Lang, S., et al. "Radiomics in medical imaging—'how-to' guide and critical reflection", *Insights into Imaging*, vol. 11, article 91, 2020. https://doi.org/10.1186/s13244-020-00887-2.
[16] Duron, L. and Fournier, L.S., "Radiomics: principles and applications in oncology," in *Multimodality Imaging and Intervention in Oncology*, Springer, Cham, 2023. Available at: https://doi.org/10.1007/978-3-031-28524-0_23.
[17] Zhao, X., Zhao, Y., Zhang, J., et al. "Predicting PD-L1 expression status in patients with non-small cell lung cancer using [^{18}F]FDG PET/CT radiomics", *EJNMMI Research*, vol. 13, article 4, 2023. https://doi.org/10.1186/s13550-023-00956-9.
[18] Meißner, A.K., Gutsche, R., Galldiks, N., et al. "Radiomics for the non-invasive prediction of PD-L1 expression in patients with brain metastases secondary to non-small cell lung cancer", *Journal of Neuro-Oncology*, vol. 163, pp. 597–605, 2023. https://doi.org/10.1007/s11060-023-04367-7.
[19] Togunwa, S. A., Babatunde, O. H., and Adebiyi, M. O. "Deep hybrid model for maternal health risk classification in pregnancy: synergy of ANN and random forest," *Frontiers in Artificial Intelligence*, vol. 6, 2023. https://doi.org/10.3389/frai.2023.1213436.
[20] Khalilia, M., Chakraborty, S., and Popescu, M. "Predicting disease risks from highly imbalanced data using random forest," *BMC Medical Informatics and Decision Making*, vol. 11, no. 1, p. 51, 2011. https://doi.org/10.1186/1472-6947-11-51.
[21] Chen, J., Chun, D., Patel, M., Chiang, E., and James, J. "AI-based smart prediction of clinical disease using random forest classifier," *The Journal of Supercomputing*, vol. 77, pp. 7919–7956, 2021. https://doi.org/10.1007/s11227-020-03481-x.
[22] Abou Jaoude et al., *Breast cancer classification using XGBoost algorithm*, World Journal of Advanced Research and Reviews, vol. 24, no. 6, pp. 245–252, 2024. https://wjarr.com/sites/default/files/WJARR-2024-0625.pdf.
[23] Li, Y., and Zhang, H. "Application of XGBoost algorithm in classification of 28 types of cancer," *AIP Conference Proceedings*, vol. 2970, no. 1, p. 040010, 2023. https://doi.org/10.1063/5.0110530.
[24] Arita et al., *Non-invasive classification of NSCLC: A comparison of RF models using CT radiomics and semantic features*, British Journal of Radiology, vol. 92, no. 1099, 2019. https://doi.org/10.1259/bjr.20190159.
[25] Li, Y., Li, X., and Yang, C. "Combined expert-in-the-loop—random forest multiclass segmentation U-net model for evaluating the tumor microenvironment in non-small cell

lung cancer," *Journal of Translational Medicine*, vol. 22, no. 1, p. 100, 2024. https://doi.org/10.1186/s12967-024-05394-2.

[26] Kumar, S., and Singh, M. "Enhanced lung cancer prediction using integrative random forest and XGBoost models," *International Journal of Novel Research and Development*, vol. 9, no. 10, pp. 245–252, 2024. https://www.ijnrd.org/papers/IJNRD2410245.pdf.

[27] Sacher, A.G. and Gandhi, L., "Biomarkers for the clinical use of PD-1/PD-L1 inhibitors in non-small-cell lung cancer: a review," *JAMA Oncology*, Vol. 2(9), pp. 1217–1222, 2016. Available at: https://doi.org/10.1001/jamaoncol.2016.0639.

[28] Passiglia, F., Bronte, G., Bazan, V., et al., "PD-L1 expression as predictive biomarker in patients with NSCLC: a pooled analysis," *Oncotarget*, Vol. 7(13), pp. 19738–19747, 2016. Available at: https://doi.org/10.18632/oncotarget.7582.

[29] Chaunzwa, T.L., Qian, J.M., Li, Q., et al., "Body composition in advanced non-small cell lung cancer treated with immunotherapy," *JAMA Oncology*, Vol. 10(6), pp. 773–783, 2024. Available at: https://doi.org/10.1001/jamaoncol.2024.1120.

[30] Leung, K.H., Rowe, S.P., Sadaghiani, M.S., et al., "Deep semisupervised transfer learning for fully automated whole-body tumor quantification and prognosis of cancer on PET/CT," *Journal of Nuclear Medicine*, 2024. Available at: https://doi.org/10.2967/jnumed.123.267048.

[31] Nie, C., Shi, J. and Huang, Y., "VARF: verifying and analyzing robustness of random forests," in *Formal Methods and Software Engineering. ICFEM 2020*, Lecture Notes in Computer Science, Vol. 12531, Springer, Cham, 2020. Available at: https://doi.org/10.1007/978-3-030-63406-3_10.

[32] Pedraza, A., Deniz, O. and Bueno, G., "On the relationship between generalization and robustness to adversarial examples," *Symmetry*, Vol. 13(5), p.817, 2021. Available at: https://doi.org/10.3390/sym13050817.

[33] Fernandez, C., Chen, C.S., Gaillard, P., et al., "Aggregation methods and comparative study in time-to-event analysis models," *International Journal of Data Science and Analytics*, 2024. Available at: https://doi.org/10.1007/s41060-024-00642-6.

[34] Mu, W., Jiang, L., Shi, Y., et al. "Non-invasive measurement of PD-L1 status and prediction of immunotherapy response using deep learning of PET/CT images", *Journal for ImmunoTherapy of Cancer*, vol. 9, e002118, 2021. https://doi.org/10.1136/jitc-2020-002118

SYMCOMP 2025
Lisbon, 10-11 April 2025

IMPROVING PD-L1 EXPRESSION PREDICTION IN NON-SMALL CELL LUNG CANCER USING RADIOMIC ANALYSIS AND DEEP LEARNING MODELS ON WHOLE-BODY VS LUNG ^{18}F-FDG PET/CT DATA

Steven Muyiwa Olawale[1,3], Azeem Saleem[2,3], Eline Roejkjaer[3], Ged Avery[2,3], Eva Sousa[1,3*]

1: Centre of Excellence for Data Science, Artificial Intelligence and Modelling, University of Hull, Hull, United Kingdom

e-mail: {s.olawale-2022, e.sousa}@hull.ac.uk
web: https://www.hull.ac.uk/work-with-us/research/institutes/data-science-artificial-intelligence-and-modelling

2: Castle Hill Hospital, Hull University Teaching Hospitals NHS Trust
e-mail: ged.avery1@nhs.net

3: Hull York Medical School, University of Hull, Hull, United Kingdom
e-mail: azeem.saleem@hyms.ac.uk; hyer11@hyms.ac.uk

Keywords: Radiomics, NSCLC, Deep Learning, PD-L1, PET/CT, Metabolic Imaging

Abstract *Lung cancer remains the leading cause of cancer-related deaths world-wide. Non-small cell lung cancer (NSCLC) account for 85% of lung cancer cases. Accurate assessment of Programmed Death-Ligand 1 (PD-L1) expression is essential for guiding immunotherapy decisions; however, conventional detection methods such as immunohistochemistry (IHC) are invasive and may not fully account for tumour heterogeneity. This study investigates the potential of deep learning-based models to predict PD-L1 expression using radiomic features extracted from full-body and lung-segmented ^{18}F-FDG PET/CT scans. Radiomic features were extracted from 134,590 full-body and 43,142 lung slices obtained from 308 NSCLC patients. Fully Connected Neural Networks (FCNNs) were trained and optimized with different network depths, activation functions, dropout rates, and optimizers. Models trained on whole-body data consistently outperformed those using lung data, emphasizing the importance of systemic metabolic information. At the feature level, the best FCNN model achieved 99% accuracy and an ROC-AUC of 0.997, while at the patient level, it achieved 98% accuracy and an ROC-AUC of 0.995. The findings highlight the superiority of deep learning-based full-body radiomic analysis over localized imaging in predicting PD-L1 expression. This approach demonstrates the potential of FCNNs as a non-invasive diagnostic tool, providing an advanced framework for precision oncology and NSCLC immunotherapy decision-making.*

DOI:10.5281/zenodo.15161219

1. INTRODUCTION

Lung cancer remains the leading cause of cancer-related mortality worldwide, with 1.8 million people dying of lung cancer every year [1], highlighting the urgent need for more effective diagnostic and therapeutic strategies. In the United Kingdom, lung cancer is the third most prevalent cancer [2]. About 85% of lung cancer is classified as non-small cell lung cancer (NSCLC). Over the past decade, the treatment landscape for NSCLC has evolved significantly and in addition to traditional modalities such as surgery, radiotherapy and chemotherapy, more targeted therapies and immunotherapies determined by tumour expression of molecular markers have been added to the treatment armamentarium [3]. Personalized biomarker-driven NSCLC therapy targeting epidermal growth factor receptor (EGFR), anaplastic lymphoma kinase (ALK), and immunotherapy targeting the programmed death-ligand 1 (PD-L1) is now available [4].

The PD-1/PD-L1 checkpoint pathway has emerged as one of the key targets in NSCLC management, with immune checkpoint inhibitors (ICIs) such as durvalumab, pembrolizumab, nivolumab, and atezolizumab significantly improving progression-free survival (PFS) and overall survival (OS) in PD-L1-positive patients [5][6][7][8][9][10]. Despite their success, accurate PD-L1 assessment remains challenging. Immunohistochemistry (IHC) is the current gold standard for PD-L1 quantification but suffers from several key limitations—it is invasive, prone to sampling errors, and fails to capture tumour heterogeneity, limiting its reliability as a predictive biomarker [11][12][13]. These challenges underscore the need for a non-invasive and comprehensive method for PD-L1 evaluation in NSCLC patients.

Given the limitations of IHC-based PD-L1 detection, there has been a growing interest in exploring radiomic features obtained from computed tomography (CT) and positron emission tomography/CT (PET/CT) with ^{18}F-fluorodeoxyglucose (^{18}F-FDG) imaging as a non-invasive alternative, extending its applications beyond traditional diagnostics [14]. Alongside conventional radiotracer uptake evaluation performed using Standardized Uptake Value (SUV) (a widely used PET imaging metric for assessing tumour metabolism), advanced computational approaches such as artificial intelligence and deep learning models enhance the extraction and interpretation of high dimensional features from PET-CT scans. By analysing the shape, intensity, and texture features of tumours, radiomics provides a non-invasive method to assess tumour biology and predict therapeutic outcomes [15][16][17].

Early radiomics models for PD-L1 prediction, despite demonstrating moderate performance (with accuracies around 68% and Area Under the Curves (AUCs) ranging from 0.706 to 0.84 [18][19]), face critical limitations. These models are predominantly based on small datasets, leading to overfitting and compromised generalizability which is a serious concern for clinical applications. Moreover, their focus on localized tumour regions neglects systemic metabolic activity, an important facet of tumour biology that could significantly enhance predictive accuracy. This oversight highlights a clear gap: the inability to fully capture the complex, systemic nature of tumour behaviour. Addressing this by integrating systemic metabolic information into deep-learning based radiomic analyses is essential for developing robust, clinically applicable PD-L1 prediction models.

Several studies have applied deep learning to PD-L1 assessment, demonstrating its potential to enhance accuracy and reproducibility. Deep learning-based IHC analysis has shown 96% accuracy in automated PD-L1 scoring from whole-slide histopathology images, matching

expert pathologist performance while reducing interobserver variability [20]. Additionally, weakly supervised deep learning models trained on PD-L1 IHC slides achieved AUCs of 0.88 in NSCLC cohorts, surpassing conventional manual scoring in predicting immunotherapy response [21]. Beyond histopathology, radiology-based deep learning models have been developed for non-invasive PD-L1 prediction, offering an alternative to biopsy-based assessments. A recent study trained a 3D residual CNN on FDG-PET/CT images from 697 NSCLC patients, achieving AUCs of ≥0.82 across internal and external cohorts, and showing prognostic value comparable to IHC-determined PD-L1 expression [22]. Similarly, a DenseNet-based CNN model analysing CT images combined with handcrafted radiomic features and clinical data achieved AUCs exceeding 0.90, reinforcing the importance of multimodal learning for PD-L1 prediction [23]. These studies indicate that deep learning can extract complex imaging patterns linked to PD-L1 expression, outperforming conventional radiomics approaches.

Furthermore, Fully Connected Neural Networks (FCNNs) have gained traction in oncology imaging due to their ability to capture high-dimensional patterns and learn hierarchical feature representations. A study on breast cancer Ki-67 classification integrated ultrasound radiomics with an FCNN, achieving high diagnostic accuracy and demonstrating clinical utility in biomarker-based cancer assessment [24]. A bibliometric analysis of Artificial Intelligence (AI) in breast cancer imaging further identified FCNNs as a key deep learning method for enhancing clinical decision-making [25]. Given these successes, applying FCNNs to whole-body PET/CT radiomics in NSCLC may enhance PD-L1 prediction by incorporating systemic metabolic activity into the analysis.

This study builds upon prior deep learning advancements by implementing an FCNN-based radiomics model to predict PD-L1 expression using whole-body and lung-segmented ^{18}F-FDG PET/CT scans. By analysing radiomic features at both the feature and patient levels, this approach seeks to capture systemic metabolic activity to overcome the limitations of localized tumour analysis, leverage deep learning's automated feature extraction to enhance PD-L1 prediction, and compare whole-body versus lung-segmented imaging to determine the most effective input for FCNN models. This study contributes to the growing field of AI-driven oncology diagnostics by demonstrating how deep learning can augment traditional radiomics to refine PD-L1 assessment, paving the way for non-invasive, data-driven approaches in immunotherapy decision-making.

2. MATERIALS AND METHODS

2.1. Data Collection

The present research utilized imaging and tissue expression data collated for an institutionally-approved audit from 308 patients diagnosed with NSCLC who underwent ^{18}F-FDG PET/CT examinations at the Nuclear Medicine Department of Castle Hill Hospital between December 2019 and January 2023. Among these patients, 207 were classified as PD-L1-positive, while 101 were PD-L1-negative, based on IHC analyses. All imaging data were stored in Digital Imaging and Communications in Medicine (DICOM) format and retrieved using Mirada DBx software. The scans consisted of fused PET/CT images with attenuation correction applied to

account for tissue photon attenuation and ensure quantitative accuracy. Each PET/CT scan contained over 300 axial slices, capturing cross-sectional representations of the body. For targeted analysis, slices numbered 120 to 260, corresponding to the thoracic region encompassing the lungs, were selected. These selections were validated through consultations with a radiologist and verified using the Mirada DBx viewer. To ensure compliance with ethical guidelines, all patient data was fully anonymized before analysis. The dataset exhibited an inherent class imbalance, with 67% of cases classified as PD-L1-positive and 33% as PD-L1-negative. To mitigate the impact of this imbalance and improve model generalizability, the Synthetic Minority Oversampling Technique (SMOTE) was applied during pre-processing, ensuring that the dataset remained balanced for training and evaluation.

2.2. Data Preprocessing

DICOM images were processed using Python 3.8. Each axial slice was resized to 512 × 512 pixels through bilinear interpolation to standardize image dimensions. Pixel intensity values were scaled between 0 and 1 by normalizing with the maximum intensity value of each slice. A Gaussian filter with a sigma value of 1 was applied using the scikit-image library to smooth the images.

2.3. Lung Segmentation

Lung regions were segmented from the PET/CT scans by selecting axial slices spanning the thoracic region (slices 120-260). Otsu's thresholding method, implemented via OpenCV, was applied to each slice to generate binary masks delineating lung tissue from surrounding structures. The segmentation results were reviewed and validated by a radiologist to ensure accuracy.

2.4. Feature Extraction

Radiomic features were extracted using PyRadiomics, capturing various quantitative descriptors, including first-order statistics, texture, and shape-based metrics. Each slice was processed separately to reflect heterogeneity associated with PD-L1 expression.

Two datasets were generated:

1. Whole-body dataset: Radiomic features from the entire PET/CT scan.
2. Lung dataset: Features extracted solely from segmented lung regions (slices 120–260).

For analysis, two approaches were applied:

- Feature-level: Each slice’s radiomic features were treated as independent data points.
- Patient-level: Features were aggregated by computing the mean across all slices per patient, creating a single feature vector per patient.

2.5. Feature Engineering

Feature engineering and selection were performed to optimize model performance. First, all extracted features were compiled into a DataFrame, with non-numeric values excluded and

missing data replaced with zeros. StandardScaler was then applied to normalize the feature set, ensuring uniformity across different scales. For the whole-body dataset at the feature level, Elastic Net regression with five-fold cross-validation was utilized to select the most relevant features. By incorporating both L1 and L2 regularization penalties, this approach helped mitigate overfitting, retaining only features with non-zero coefficients for model training. For the lung dataset and patient-level analysis, feature importance was assessed using a random forest classifier, as Elastic Net regression proved less effective in these contexts. Importance scores were calculated based on the Gini impurity criterion, and only features with a score above 0.01 were retained for further modelling.

2.6. Deep Learning Model Development, Training, and Evaluation

A FCNN was implemented to predict PD-L1 expression using radiomic features. The network architecture can be seen in Figure 1, and consisted of an input layer with neurons corresponding to the selected features, followed by two to three hidden layers with ReLU activation and dropout layers to reduce overfitting. The output layer contained a single neuron with sigmoid activation for binary classification. Model optimization was conducted in two iterations: the first (FCNN Model 2) involved increasing the number of hidden layers, reducing neurons per layer, and adjusting dropout rates, the optimizer, and batch size. The second iteration (FCNN Model 3) further refined dropout rates, neuron distribution, and learning rate adjustments. Hyperparameters were fine-tuned using RandomizedSearchCV, and the optimal configuration of the best-performing model is detailed in Table 1. The dataset was divided into training (80%) and testing (20%) subsets using stratified sampling to maintain class balance. Model performance was assessed using accuracy, ROC-AUC, and F1-score, while training and validation loss curves were examined to track convergence and detect potential overfitting.

Model	**Strategy**	**Parameters Tuned**	**Details**
FCNN	1st Hyperparameter Tuning (FCNN Model 2)	Hidden Layers, Dropout Rates, Optimizer, Epochs, Batch Size	Hidden_Layers=[64, 32, 16], Dropout_Rates=[0.2, 0.2, 0.1], Optimizer=sgd, Epochs=100, Batch_Size=16
	2nd Hyperparameter Tuning (FCNN Model 3)	Hidden Layers, Dropout Rates, Optimizer, Epochs, Batch Size	Hidden_Layers=[256, 128], Dropout_Rates=[0.2, 0.3], Optimizer=rmsprop, Epochs=50, Batch_Size=8

Table 1. Summary of the hyperparameters used with the different models tested.

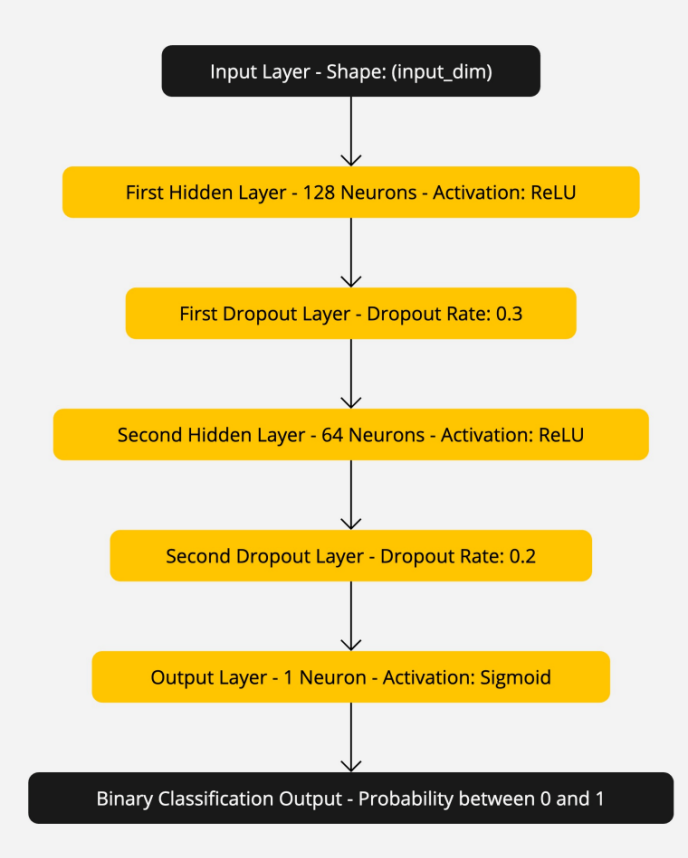

Figure 1: Fully Connected Neural Network (FCNN) Base Architecture (FCNN Model 1) for Binary Classification of PD-L1 Expression in NSCLC Patients.

2.6.5. Software and Libraries

All analyses were performed in Python using libraries including Tensorflow for FCNN training, Scikit-learn for data processing and model evaluation, PyRadiomics for feature extraction and Matplotlib for visualization.

3. RESULTS

3.1. Lung Segmentation and Visualization

The visualization and analysis of whole-body ^{18}F-FDG PET/CT images using the Mirada DBx viewer identified slices numbered 120 to 260 as the most relevant for lung related analysis. These slices cover the thoracic region, where NSCLC tumours are typically located. Within this slice range, the lung anatomy and tumour sites were clearly visible, as demonstrated in Figure 2.

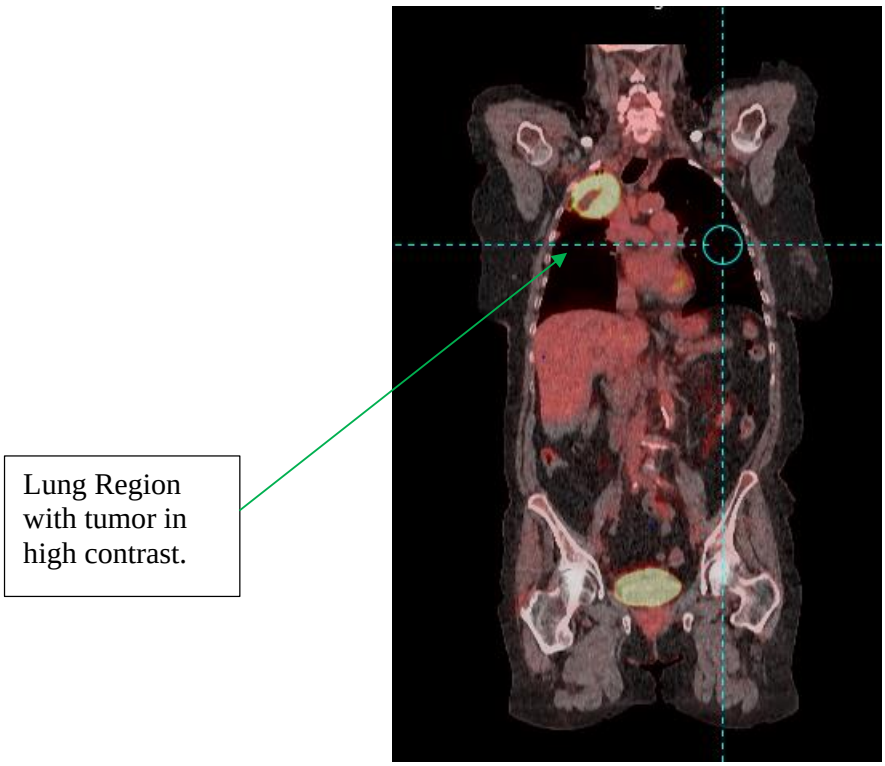

Figure 2. Fused coronal view of a FDG-PET/CT image highlighting the tumour seen as an area of high uptake in the right upper lung region. The lung area is indicated by the arrow, showcasing the specific region where the tumour is located.

3.2. Feature Extraction, Selection and Preprocessing

A total of 98 radiomic features were extracted from PET scan data for both the whole-body and lung datasets. The whole-body dataset comprised 134,590 slices, while the lung dataset contained 43,142 slices. Aggregating features at the patient level resulted in a dataset of 307 patients. Feature selection reduced the number of features across datasets. In the whole-body dataset at the feature level, Elastic Net regression with five-fold cross-validation selected 27 features. For the lung dataset at feature-level and patient-level analyses (whole-body and lung), random forest feature importance identified 24 to 39 key features (Table 2).

Dataset	Level	Feature Selection Type	Features (Before Selection)	Features (After Selection)
Whole-body dataset	Feature Level	Elastic net	98	27
Whole-body dataset	Patient Level	Random forest	98	36
Lung dataset	Feature	Random forest	98	24

	Level			
Lung dataset	Patient Level	Random forest	98	39

Table 2. Feature selection summary for whole-body and lung dataset

An initial class imbalance was observed, with PD-L1-positive cases constituting 67% of the dataset and PD-L1-negative cases 33%. SMOTE application resulted in **a** balanced 50:50 distribution of PD-L1-positive and PD-L1-negative cases**.**

3.3. Model Performance (Feature-Level Analysis)

The best-performing model at feature-level, FCNN Model 2, optimized through the first hyperparameter tuning, achieved the highest accuracy and ROC-AUC scores (Table 3). The confusion matrix (Figure 3) further illustrates the model's predictive capability, with 8,926 true negatives, 17,725 true positives, 12 false positives and 255 false negatives. The model exhibited low misclassification rates with minimal false positives and false negatives, indicating strong discrimination ability in PD-L1 classification. Additionally, the stable training and validation convergence observed (Figure 4) suggests good generalization performance across the dataset .

Dataset	Model Configuration	Precision	Recall	F1-Score	Accuracy	ROC-AUC
Whole-body dataset	Base Model (FCNN Model 1)	0.98	0.99	0.99	0.99	0.996
	1st Hyperparameter Tuning (FCNN Model 2)	**0.99**	**0.99**	**0.99**	**0.99**	**0.997**
	2nd Hyperparameter Tuning (FCNN Model 2)	0.98	0.99	0.99	0.99	0.994
Lung data	Base Model (FCNN Model 1)	0.69	0.57	0.55	0.71	0.695
	1st Hyperparameter Tuning (FCNN Model 2)	0.68	0.69	0.61	0.69	0.600
	2nd Hyperparameter Tuning (FCNN Model 2)	0.69	0.70	0.62	0.70	0.660

Table 3: Performance metrics for deep learning models (feature-level analysis). The best performing model (FCNN 2) is marked in bold.

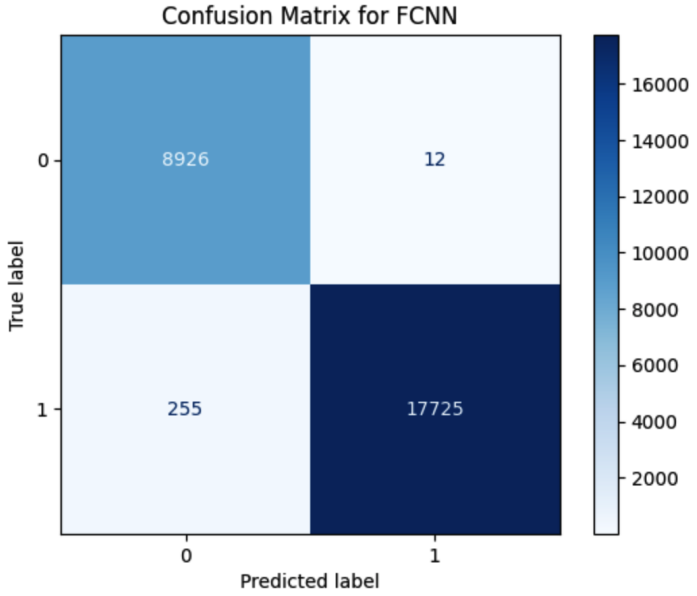

Figure 3: Confusion matrix for the best performing FCNN Model (FCNN model 2) on whole-body dataset at a feature level, the model achieved the highest accuracy and ROC-AUC.

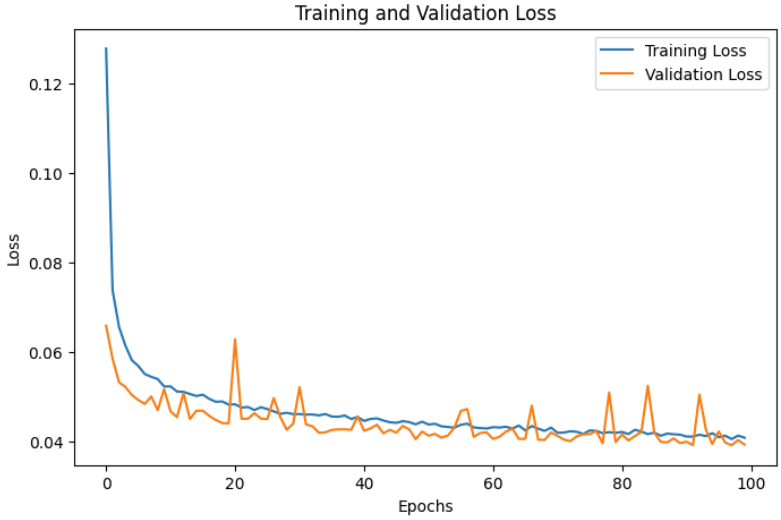

Figure 4: Training and validation loss curve for the FCNN Model 2 After first hyperparameter tuning at feature level.

3.4. Model Performance (Patient-Level)

The best-performing model at patient level was the FCNN Model 2 (first hyperparameter tuning), achieving high classification accuracy (98%), with an ROC-AUC of 0.990 for the whole-body dataset (Table 4). The confusion matrix (Figure 5) confirms strong classification performance, with a high true positive rate and minimal misclassifications. In contrast, models trained on lung data demonstrated significantly lower performance. The best lung dataset model (FCNN Model 2) achieved an accuracy of 71% and an ROC-AUC of 0.52, highlighting the inferior predictive power of localized imaging (Table 4).Additionally, training and validation loss curves (Figure 6) indicate that the FCNN model converged effectively, with minimal overfitting, suggesting good generalization ability.

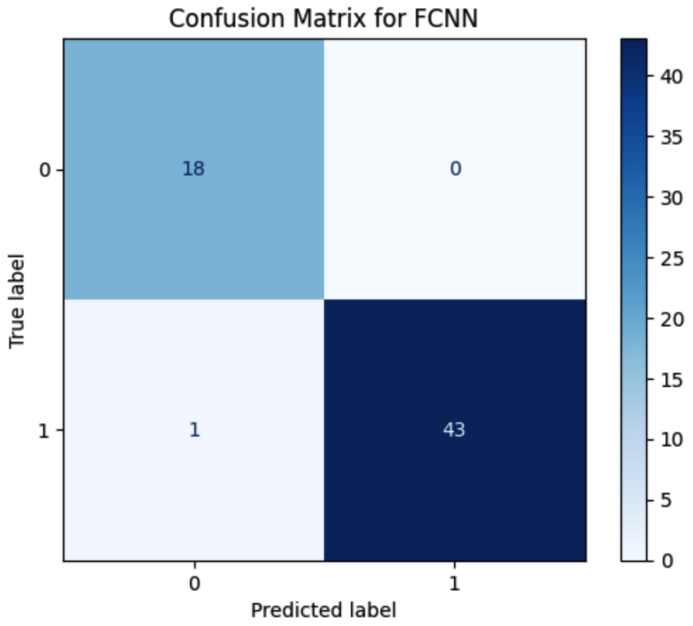

Figure 5: Confusion matrix for the best performing FCNN model (FCNN model 2) on whole-body dataset at a patient level, the model achieved the highest accuracy and ROC-AUC.

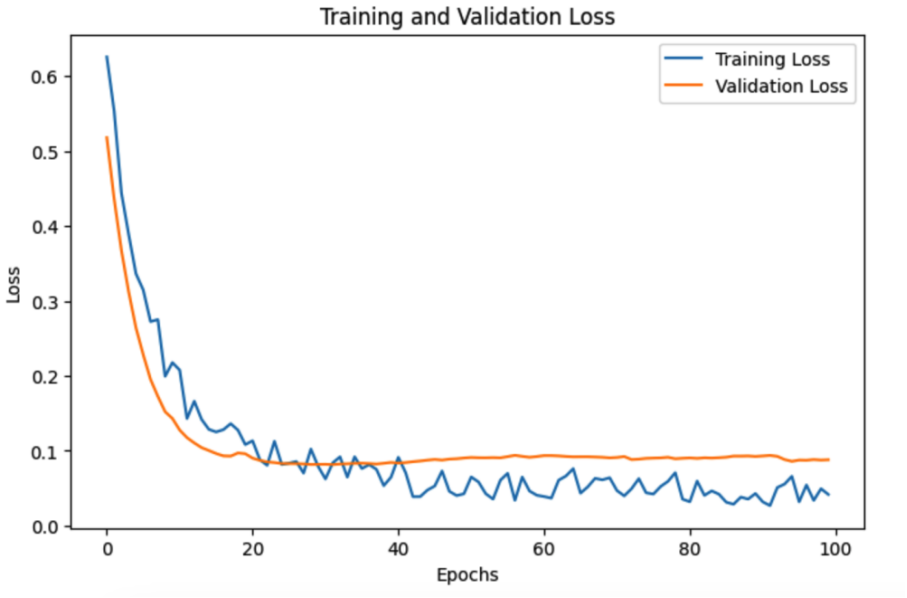

Figure 6: Training and validation loss curve for the FCNN model 2 after first hyperparameter tuning at patient level.

Dataset	Model configuration	Precision	Recall	F1-Score	Accuracy	ROC-AUC
Whole-body dataset	Base Model (FCNN Model 1)	0.98	0.98	0.98	0.98	0.995
	1st Hyperparameter Tuning (FCNN Model 2)	**0.98**	**0.98**	**0.98**	**0.98**	**0.990**
	2nd Hyperparameter Tuning (FCNN Model 3)	0.98	0.98	0.98	0.98	0.990
Lung Data	Base Model (FCNN Model 1)	0.63	0.68	0.64	0.68	0.42
	1st Hyperparameter Tuning (FCNN Model 2)	0.50	0.71	0.59	0.71	0.52
	2nd Hyperparameter Tuning (FCNN Model 2)	0.59	0.65	0.61	0.65	0.64

Table 4: Performance metrics for deep learning models (patient-level analysis). The best performing model (FCNN 2) is marked in bold

4.0 DISCUSSION

The emergence of PD-1/PD-L1 checkpoint inhibitors has revolutionized the treatment landscape for NSCLC, reinforcing the critical role of PD-L1 expression as a biomarker for predicting immunotherapy response. Accurate PD-L1 assessment is essential for guiding treatment decisions and optimizing patient outcomes [26][27]. However, conventional immunohistochemistry (IHC)-based PD-L1 evaluation remains invasive, prone to sampling bias, and limited in its ability to capture tumour heterogeneity. This study addresses these limitations by using radiomic features extracted from whole-body and lung PET/CT data to predict PD-L1 expression using both deep-learning based feature-level and patient-level analyses.

The results consistently demonstrated that models trained on whole-body PET/CT data outperformed those trained on lung-only data across multiple evaluation metrics, including accuracy, precision, recall, F1-score, and ROC-AUC (Tables 3 and 4). This finding aligns with previous research suggesting that systemic metabolic activity provides crucial prognostic information beyond localized tumour imaging [28][29]. Specifically, the FCNN model, chosen for its universal function approximation capability and ability to model complex nonlinear relationships, achieved superior predictive performance on radiomic datasets. By automatically capturing intricate feature interactions without the need for manual selection, the FCNN effectively leveraged the full predictive power of radiomic data [30][31][32]. Additionally, advancements in interpretability techniques such as saliency maps and layer-wise relevance propagation further enhance the explainability of FCNN-based predictions, making them a valuable tool for clinical decision support [33].

At the feature level, our FCNN model—after its first hyperparameter tuning (FCNN Model 2)—demonstrated exceptional performance on whole-body PET/CT data, achieving 99.1% accuracy and an ROC-AUC of 0.998. In contrast, when the same approach was applied to lung-segmented data, the performance dropped markedly, with accuracy declining to 71% and the ROC-AUC to 0.70 (Table 3). This disparity underscores the predictive value of systemic metabolic activity in PD-L1 assessment and suggests that limiting analysis to localized tumor regions may omit critical biomarker-related variations.

At the patient level, aggregation techniques such as mean feature aggregation improved model robustness and generalization. The tuned FCNN model trained on whole-body data achieved an impressive 98% accuracy and an ROC-AUC of 0.995, clearly outperforming previous studies that reported lower ROC-AUC values of 0.88 and 0.82 [21][22]. Conversely, models based solely on lung data demonstrated significantly poorer performance, with accuracy falling to 65% and the ROC-AUC decreasing to 0.64 (Table 4). These differences further emphasize the importance of incorporating systemic metabolic information for accurate PD-L1 prediction. A recent study focusing solely on lung-segmented PET/CT data reported an ROC-AUC of 0.82 for PD-L1 classification [35], which contrasts sharply with the 0.99 ROC-AUC achieved by our whole-body imaging approach. This clear disparity in predictive power demonstrates the enhanced benefits of integrating systemic metabolic information. Furthermore, while previous

deep learning studies based exclusively on tumor regions have reported ROC-AUC values ranging from 0.82 to 0.95 [36][37], our findings suggest that PD-L1 expression is influenced by broader metabolic activity beyond the tumor site. Together, these comparisons reinforce the need for a holistic radiomic assessment in NSCLC rather than relying solely on localized tumor imaging.

While this study demonstrates the predictive superiority of whole-body radiomics in PD-L1 assessment, several limitations must be acknowledged. First, the dataset used in this study was derived from a single institution, which may limit the generalizability of findings across diverse populations. Future research should validate these results using multi-centre datasets with a larger sample size. Additionally, although the FCNN model achieved high predictive performance, external validation on independent cohorts is necessary to confirm its clinical applicability. Lastly, while this study focused on PD-L1 prediction, future work should explore the potential of whole-body radiomics for assessing additional biomarkers and treatment response across a broader range of cancers.

Overall, these findings confirm that incorporating whole-body metabolic data into radiomic analyses significantly enhances PD-L1 prediction accuracy, surpassing traditional localized imaging approaches. By leveraging deep learning for automated feature extraction and systemic metabolic integration, this study contributes to the advancement of AI-driven oncology diagnostics. If validated in larger, multi-institutional cohorts, this approach could transform biomarker-based decision-making in NSCLC, leading to more precise and personalized immunotherapy strategies.

5.0 CONCLUSION

This study demonstrates that whole-body [18F]FDG PET/CT imaging, when analysed using deep learning models, significantly outperforms lung-only imaging in predicting PD-L1 expression in NSCLC patients. The superior performance of whole-body imaging models highlights the critical role of systemic metabolic activity in PD-L1 expression and immunotherapy response.

By outperforming prior studies that relied solely on localized tumor regions, this research reinforces the clinical value of a holistic imaging approach, which could improve patient stratification for immunotherapy. Incorporating whole-body radiomic analysis into routine clinical workflows may enhance personalized treatment strategies, leading to better therapeutic outcomes for NSCLC patients.

However, before this approach can be widely adopted in clinical practice, further validation with larger and more diverse patient cohorts is essential. Future research should integrate whole-body imaging with genomic and clinical data to enhance model accuracy and refine personalized treatment strategies. Such multi-modal strategies have the potential to revolutionize personalized oncology, improving treatment outcomes and guiding more effective immunotherapy decisions in NSCLC.

REFERENCES

[1] Sung, H., Ferlay, J., Siegel, R.L., et al. "Global cancer statistics 2020: GLOBOCAN estimates of incidence and mortality worldwide for 36 cancers in 185 countries", *CA: A*

Cancer Journal for Clinicians, vol. 71, no. 3, pp. 209–249, 2021. https://doi.org/10.3322/caac.21660.

[2] NHS Digital. "Cancer incidence by gender and age," *Cancer Registration Statistics, England, 2021 - Summary Counts Only*, NHS Digital, 2024. Available: https://digital.nhs.uk/data-and-information/publications/statistical/cancer-registration-statistics/england-2021---summary-counts-only/cancer-incidence-by-gender-and-age.
[32] NHS Digital. "Cancer incidence by gender and age," *Cancer Registration Statistics, England, 2021 - Summary Counts Only*, NHS Digital, 2024. Available: https://digital.nhs.uk/data-and-information/publications/statistical/cancer-registration-statistics/england-2021---summary-counts-only/cancer-incidence-by-gender-and-age.Liu, S.Y.M., Zheng, M.M., Pan, Y., et al. "Emerging evidence and treatment paradigm of non-small cell lung cancer", *Journal of Hematology & Oncology*, vol. 16, article 40, 2023. https://doi.org/10.1186/s13045-023-01436-2.

[3] Aisner, D.L., Riely, G.J. "Non-small cell lung cancer: recommendations for biomarker testing and treatment", *Journal of the National Comprehensive Cancer Network*, vol. 19, no. 5, pp. 610–613, 2021. https://doi.org/10.6004/jnccn.2021.5020.

[4] Lin, X., Kang, K., Chen, P., et al. "Regulatory mechanisms of PD-1/PD-L1 in cancers", *Molecular Cancer*, vol. 23, article 108, 2024. https://doi.org/10.1186/s12943-024-02023-w.

[5] Deslypere, G., Gullentops, D., Wauters, E., et al. "Immunotherapy in non-metastatic non-small cell lung cancer: can the benefits of stage IV therapy be translated into earlier stages?", *Therapeutic Advances in Medical Oncology*, vol. 10, 2018. https://doi.org/10.1177/1758835918772810.

[6] Kilaru, S., Panda, S.S., Moharana, L., et al. "PD-L1 expression and its significance in advanced NSCLC: real-world experience from a tertiary care center", *Journal of the Egyptian National Cancer Institute*, vol. 36, no. 3, 2024. https://doi.org/10.1186/s43046-024-00207-5.

[7] Rittmeyer, A., Barlesi, F., Waterkamp, D., et al. "Atezolizumab versus docetaxel in patients with previously treated non-small-cell lung cancer (OAK): a phase 3, open-label, multicentre randomised controlled trial", *The Lancet*, vol. 389, no. 10066, pp. 255–265, 2017. https://doi.org/10.1016/S0140-6736(16)32517-X.

[8] Wang, J., Wang, J., Huang, X., et al. "CT radiomics-based model for predicting TMB and immunotherapy response in non-small cell lung cancer", *BMC Medical Imaging*, vol. 24, article 45, 2024. https://doi.org/10.1186/s12880-024-01221-8.

[9] Reck, M., Rodríguez-Abreu, D., Robinson, A.G., et al. "Pembrolizumab versus chemotherapy for PD-L1–positive non–small-cell lung cancer", *New England Journal of Medicine*, vol. 375, no. 19, pp. 1823–1833, 2016. https://doi.org/10.1056/NEJMoa1606774.

[10] Dhar, M., Wong, J., Che, J., et al. "Evaluation of PD-L1 expression on vortex-isolated circulating tumor cells in metastatic lung cancer", *Scientific Reports*, vol. 8, article 2592, 2018. https://doi.org/10.1038/s41598-018-19245-w.

[11] Wu, X., Huang, Y., Zhao, Q., et al. "PD-L1 expression correlation with metabolic parameters of FDG PET/CT and clinicopathological characteristics in non-small cell lung cancer", *EJNMMI Research*, vol. 10, article 51, 2020.

https://doi.org/10.1186/s13550-020-00639-9.
[12] Tejerina, E., García Tobar, L., Echeveste, J.I., et al. "PD-L1 in cytological samples: a review and a practical approach", *Frontiers in Medicine*, vol. 8, 2021. https://doi.org/10.3389/fmed.2021.668612.
[13] Eze, C., Schmidt-Hegemann, N.S., Sawicki, L.M., et al. "PET/CT imaging for evaluation of multimodal treatment efficacy and toxicity in advanced NSCLC—current state and future directions", *European Journal of Nuclear Medicine and Molecular Imaging*, vol. 48, pp. 3975–3989, 2021. https://doi.org/10.1007/s00259-021-05211-8.
[14] Pinta, C. de la, Barrios-Campo, N., Sevillano, D. "Radiomics in lung cancer for oncologists", *Journal of Clinical and Translational Research*, vol. 6, no. 4, pp. 127–134, 2020.
[15] van Timmeren, J., Cester, D., Tanadini-Lang, S., et al. "Radiomics in medical imaging—'how-to' guide and critical reflection", *Insights into Imaging*, vol. 11, article 91, 2020. https://doi.org/10.1186/s13244-020-00887-2.
[16] Duron, L. and Fournier, L.S., "Radiomics: principles and applications in oncology," in *Multimodality Imaging and Intervention in Oncology*, Springer, Cham, 2023. Available at: https://doi.org/10.1007/978-3-031-28524-0_23.
[17] Zhao, X., Zhao, Y., Zhang, J., et al. "Predicting PD-L1 expression status in patients with non-small cell lung cancer using [^{18}F]FDG PET/CT radiomics", *EJNMMI Research*, vol. 13, article 4, 2023. https://doi.org/10.1186/s13550-023-00956-9.
[18] Meißner, A.K., Gutsche, R., Galldiks, N., et al. "Radiomics for the non-invasive prediction of PD-L1 expression in patients with brain metastases secondary to non-small cell lung cancer", *Journal of Neuro-Oncology*, vol. 163, pp. 597–605, 2023. https://doi.org/10.1007/s11060-023-04367-7.
[19] Togunwa, S. A., Babatunde, O. H., and Adebiyi, M. O. "Deep hybrid model for maternal health risk classification in pregnancy: synergy of ANN and random forest," *Frontiers in Artificial Intelligence*, vol. 6, 2023. https://doi.org/10.3389/frai.2023.1213436.
[20] Cheng, J., Tang, X., Zhao, Y., et al. "Automated PD-L1 scoring in histopathology images using deep learning: A high-accuracy AI system for NSCLC assessment," *Frontiers in Immunology*, vol. 13, article 874561, 2022. https://doi.org/10.3389/fimmu.2022.893198
[21] Ligero, M., Sancho, J., Tobalina, I., et al. "Weakly supervised deep learning for PD-L1 classification in non-small cell lung cancer: Insights into response prediction," *Cancer Research Communications*, vol. 4, no. 2, pp. 103–115, 2024. https://doi.org/10.1158/2767-9764.CRC-23-0287
[22] Mu, W., Jiang, L., Zhang, J., et al. "Deep learning PET/CT imaging biomarkers for predicting PD-L1 expression and survival in NSCLC," *Journal for ImmunoTherapy of Cancer*, vol. 9, no. 4, article e002118, 2021. https://doi.org/10.1136/jitc-2020-002118.
[23] Wang, C., Ma, J., Shao, J., Zhang, S., Liu, Z., Yu, Y., & Li, W. "Predicting EGFR and PD-L1 Status in NSCLC Patients Using Multitask AI System Based on CT Images," *Frontiers in Immunology*, vol. 13, article 813072, 2022. https://doi.org/10.3389/fimmu.2022.813072.
[24] Li, Y., Long, W., Zhou, H., Tan, T., & Xie, H. "Revolutionizing breast cancer Ki-67 diagnosis: ultrasound radiomics and fully connected neural networks (FCNN)

combination method," *Breast Cancer Research and Treatment*, vol. 207, pp. 453–468, 2024. https://doi.org/10.1007/s10549-024-07375-x.

[25] Wu, X., Xia, Y., Lou, X., Huang, K., Wu, L., & Gao, C. "Decoding breast cancer imaging trends: the role of AI and radiomics through bibliometric insights," *Breast Cancer Research*, vol. 27, article 29, 2025. https://doi.org/10.1186/s13058-025-01983-1.

[26] Sacher, A.G. and Gandhi, L., "Biomarkers for the clinical use of PD-1/PD-L1 inhibitors in non-small-cell lung cancer: a review," *JAMA Oncology*, Vol. 2(9), pp. 1217–1222, 2016. Available at: https://doi.org/10.1001/jamaoncol.2016.0639.

[27] Passiglia, F., Bronte, G., Bazan, V., et al., "PD-L1 expression as predictive biomarker in patients with NSCLC: a pooled analysis," *Oncotarget*, Vol. 7(13), pp. 19738–19747, 2016. Available at: https://doi.org/10.18632/oncotarget.7582.

[28] Chaunzwa, T.L., Qian, J.M., Li, Q., et al., "Body composition in advanced non-small cell lung cancer treated with immunotherapy," *JAMA Oncology*, Vol. 10(6), pp. 773–783, 2024. Available at: https://doi.org/10.1001/jamaoncol.2024.1120.

[29] Leung, K.H., Rowe, S.P., Sadaghiani, M.S., et al., "Deep semisupervised transfer learning for fully automated whole-body tumor quantification and prognosis of cancer on PET/CT," *Journal of Nuclear Medicine*, 2024. Available at: https://doi.org/10.2967/jnumed.123.267048.

[30] Hornik, K., Stinchcombe, M., & White, H. "Multilayer Feedforward Networks Are Universal Approximators," *Neural Networks*, vol. 2, no. 5, pp. 359–366, 1989. https://doi.org/10.1016/0893-6080(89)90020-8.

[31] LeCun, Y., Bengio, Y., & Hinton, G. "Deep Learning," *Nature*, vol. 521, pp. 436–444, 2015. https://doi.org/10.1038/nature14539

[32] Bengio, Y., Courville, A., & Vincent, P. "Representation Learning: A Review and New Perspectives," *IEEE Transactions on Pattern Analysis and Machine Intelligence*, vol. 35, no. 8, pp. 1798–1828, Aug. 2013. https://doi.org/10.1109/TPAMI.2013.50.

[33] Dong, H., Liu, B., Ye, D., & Liu, G. "Interpretability as Approximation: Understanding Black-Box Models by Decision Boundary," *Electronics*, vol. 13, no. 22, p. 4339, 2024. https://doi.org/10.3390/electronics13224339

[34] Fernandez, C., Chen, C.S., Gaillard, P., et al., "Aggregation methods and comparative study in time-to-event analysis models," *International Journal of Data Science and Analytics*, 2024. Available at: https://doi.org/10.1007/s41060-024-00642-6.

[35] Mu, W., Jiang, L., Shi, Y., et al. "Non-invasive measurement of PD-L1 status and prediction of immunotherapy response using deep learning of PET/CT images", *Journal for ImmunoTherapy of Cancer*, vol. 9, e002118, 2021. https://doi.org/10.1136/jitc-2020-002118

[36] Xu, T., Liu, X., Chen, Y., *et al.* "CT-based deep learning radiomics biomarker for programmed cell death ligand 1 expression in non-small cell lung cancer," *BMC Medical Imaging*, vol. 24, p. 196, 2024. https://doi.org/10.1186/s12880-024-01380-8.

[37] Wang, C., Ma, J., Shao, J., Zhang, S., Li, J., Yan, J., Zhao, Z., Bai, C., Yu, Y., & Li, W. "Non-Invasive Measurement Using Deep Learning Algorithm Based on Multi-Source Features Fusion to Predict PD-L1 Expression and Survival in NSCLC," *Frontiers in Immunology*, vol. 13, 2022. https://doi.org/10.3389/fimmu.2022.828560

SYMCOMP 2025
Lisbon, 10-11 April 2025

A FINITE ELEMENT MODEL TO STUDY POSTERIOR MALLEOLUS SURGERY APPROACH

Guilherme V. Lopes[1], Rui B. Ruben[2,3]*, Inês C.J. Barbosa[1,3,4], Joana Contente[5], and Sofia C. Dantas[6]

1: ISEL - Instituto Superior de Engenharia de Lisboa
Instituto Politécnico de Lisboa
Rua Conselheiro Emídio Navarro, 1
1959-007 Lisboa

2: CDRsp – Centre for Rapid and Sustainable Product Development
ESTG – Polytechnic Institute of Leiria
Rua de Portugal - Zona Industrial
2430-028 Marinha Grande
e-mail: rui.ruben@ipleiria.pt web: http://cdrsp.ipleiria.pt

3: IDMEC, ISEL, IPL, Lisboa, Portugal

4: CIMOSM – Centro de Investigação em Modelação e Otimização de Sistemas Multifuncionais
ISEL – Instituto Superior de Engenharia de Lisboa
Rua Conselheiro Emídio Navarro, 1
1959-007 Lisboa
e-mail: ines.barbosa@isel.pt web: http://www.cimosm.isel.pt

5: Departamento de Ortopedia e Traumatologia II
Centro Hospitalar de Leiria, Portugal
e-mail: joanacontentealmeida@gmail.com

6: Departamento de Ortopedia e Traumatologia
Hospital do Litoral Alentejano, Santiago do Cacém, Portugal
e-mail: sofiacdantas@outlook.com

Keywords: FEM, biomechanics, posterior malleolus

Abstract *The Posterior Malleolus, a key structure in the ankle joint, plays an essential role in maintaining joint stability and load distribution. Fractures of the Posterior Malleolus are often complex and typically result from rotational injuries, such as those sustained during high-impact activities or accidents. Due to the variability in fracture patterns and associated soft tissue damage, determining the optimal treatment approach is not consensual within the medical community. While some cases can be managed conservatively, others require surgical intervention to restore joint congruency and*

prevent long-term complications such as post-traumatic arthritis.

Given the challenges in establishing a standardized treatment protocol, this study aims to create a Finite Element model of the Posterior Malleolus that allows for the simulation of various surgical techniques and fixation methods. By evaluating different treatment approaches, their biomechanical and clinical outcomes may be better understanded and different strategies that optimize fracture healing, enhance joint function, and minimize complications may be identified.

SYMCOMP 2025
Lisbon, 10-11 April 2025

SOME COMPUTATIONAL TOOLS FOR SOLVING A SELECTION OF PROBLEMS IN CONTROL THEORY

Alexander Demin[1], Christina Katsamaki[2] and Fabrice Rouillier[2]

1: HSE University, Moscow, Russia
e-mail: asdemin_2@edu.hse.ru

2: Sorbonne Université, Paris Université, CNRS (IMJ-PRG), Inria Paris, Paris, France
e-mail: {christina.katsamaki, Fabrice.Rouillier}@inria.fr

Keywords: Polynomial Systems Solving, Software, Control Theory

Abstract. *We demonstrate how certified computational tools can be used to address various problems in control theory. In particular, we introduce* `PACE.jl`*, a Julia package that implements symbolic elimination techniques, including (among others) discriminant varieties and Rational Univariate Representation, while also supporting multi-precision interval computations. We showcase its applications to key control theory problems, including identification, stability analysis, and optimization, for both parameter-dependent and parameter-free systems.*

SYMCOMP 2025
Lisbon, 10-11 April 2025

SYMBOLIC COMPUTATION APPLIED TO FUNCTION FACTORIZATION CONCEPT: THE RATIONAL SCALAR CASE

Ana C. Conceição[1,2], Jéssica C. Pires[3] and Celestino Coelho[1]

1: Faculdade de Ciências e Tecnologia, Universidade do Algarve
Campus de Gambelas, 8005-139 Faro, Portugal
e-mail:aconcei@ualg.pt

2: Center for Research & Development in Mathematics and Applications
Campus Universitário de Santiago, 3810-193 Aveiro, Portugal

3: Faculdade de Economia, Universidade do Algarve
Campus de Gambelas, 8005-139 Faro, Portugal
e-mail: {aconcei,jccpires,ccoelho}@ualg.pt

Keywords: Symbolic computation, function factorization, operator theory algorithms, Cauchy singular integrals, Wolfram Mathematica

Abstract. *Operator theory has many applications in several main scientific research areas such as structural mechanics, aeronautics, quantum mechanics, probability theory, electrical engineering, among others. Factorization theory is closely related to the computation of singular integrals. Some progress has been achieved for some classes of functions whose properties allow the use of a particular strategy in the study of the factorization problem, but there is no general method for obtaining a factorization for a given function. In our work, we design and develop operator theory algorithms. By implementing these algorithms on a computer, using the numeric and symbolic computation capabilities of the Wolfram Mathematica computer algebra system, new tools are created, making the results of lengthy and complex calculations available in a simple way to researchers of different areas. The main goal of this talk is to present new rational factorization algorithms, which have applications in the study of the invertibility of singular integral operators and in the computation of the kernel of certain classes of operators. Several nontrivial examples computed with the algorithms are presented.*

Funding: This research was supported by Center for Research and Development in Mathematics and Applications (CIDMA) under the Portuguese Foundation for Science and Technology (FCT) Multi-Annual Financing Program for R&D Units.

DOI:10.5281/zenodo.15161235

1 INTRODUCTION

The factorization theory of matrix functions has a rich history dating back to Plemelj's work in 1908. It has been developed to solve problems arising from various fields in mathematics and physics. Currently, the theory has a wide range of applications, including the study of Riemann-Hilbert boundary value problems, Fredholm theory of singular integral operators, and non-linear and linear differential equations, diffraction of acoustic and electromagnetic waves, scattering theory, inverse scattering theory, and some branches of probability theory [1, 2, 3, 4, 5, 6, 7, 8]. For some classes of functions there has been some progress by the use of specific strategies to study the factorization problem, but there is no general and explicit method to find a factorization for a given function. Additionally, existing algorithms only demonstrate that some factorization is possible, but they are not suitable for computer implementation [9, 10]. Regarding partial indices, some advances have been made, but the methods are difficult to apply and not designed for computer implementation, even in the rational case [11, 12, 13]. Most of the explicit analytical factorization methods rely on finding the roots of scalar functions. Therefore, in many real-world applications, numerical analysis of such methods is unavoidable. However, the numerical approach to factorization theory is very challenging due to many instability issues, such as those affecting the factorization indices [5]. For this reason, the development of new analytical methods, even if only for some special classes of functions, remains crucial for the progress of this theory.

On the other hand, computer algebra systems (CAS) with extensive capabilities of numeric and symbolic computation have become accessible to the general public. These applications enable computers to perform all or a significant part of the symbolic and numeric calculations present in many mathematical algorithms. The authors use the computer algebra system Wolfram *Mathematica* to implement analytical operator theory algorithms. In [14], it is presented an algorithm that factorize special classes of rational and non-rational matrix functions. These classes are closely related to the solution of the non-linear Schrödinger equation, the generalized Riemann-Hilbert problem, and the study of singular operators that can be represented as a product of Hankel operators [4, 6, 8]. It is shown that for these special classes of matrix functions, a factorization can be obtained using the solutions of two non-homogeneous integral equations. The algorithm was implemented using the Wolfram *Mathematica*, and computes explicit factorizations for those classes of matrix functions using an inner-outer factorization of a component of a factorable matrix function. Regarding computer implementation, complete and explicit rational factorization algorithms (for both scalar and matrix cases) can be found in [15]. However, the algorithms assumes that the given rational function, defined on the unit circle, is factorable and that its zeros and poles are known to the user. Using algorithms described in the [16], which enable the identification of polynomial roots and their location relative to the unit circle, several improvements have been made to the design and implementation of complete factorization algorithms for scalar rational functions, defined

in the unit circle. This article presents an enhanced and highly efficient version of the scalar factorization algorithm described in [15], known as the $[\text{ARFact}]_{2.0}$ algorithm. This algorithm determines whether a rational function defined on the unit circle is factorable and, if so, identifies its factorization index, even for polynomials of the fifth degree or higher. Designed with the `Root` object concept of the Wolfram Mathematica computer algebra system (to represent solutions of one-variable algebraic equations), $[\text{ARFact}]_{2.0}$ also provides the explicit factors of a rational factorization. This improved version was made possible by the development of the [ASPPlusPMinus] algorithm [16], which calculates the projections associated with the Cauchy-type singular integral defined on the unit circle. The article also presents the new [AInnerOuterFact] algorithm, which determines whether a rational function is analytic inside the unit circle and, if so, provides an explicit inner-outer factorization. This can be used to enhance algorithms such as the one described in [14]. The outputs from these algorithms can be used to create or improve various other operator theory algorithms.
The paper is organized as follows: Section 2 covers fundamental concepts related to rational function factorization and the Cauchy-type singular integral operators used. It also provides a brief description of the operator theory algorithms [AZeros] and [APoles], which compute the zeros and poles of a rational function and determine their location relative to the unit circle [16] . Section 3 introduces the new $[\text{ARFact}]_{2.0}$ and [AInnerOuterFact] algorithms, which integrate the [AZeros] and [APoles] algorithms. The final section offers some concluding remarks.

2 FUNDAMENTAL NOTATIONS, CONCEPTS AND AUXILIARY ALGORITHMS

This section contains the fundamental notations and concepts related to the new operator theory algorithms presented in subsections 3.1 and 3.2. It also provides a brief description of the auxiliar operator theory algorithms [AZeros] and [APoles].

2.1 Singular integral Operator with Cauchy kernel

Let $\mathbb{T}$ represent the unit circle in the complex plane. Define $\mathbb{T}_+$ as the open unit disk and $\mathbb{T}_-$ as the exterior region of the unit circle (∞ included). Let $\mathcal{R}(\mathbb{T})$ denote the algebra of rational functions without poles on $\mathbb{T}$ and let $\mathcal{R}_\pm(\mathbb{T})$ be the subsets of $\mathcal{R}(\mathbb{T})$ whose elements have no poles in $\mathbb{T}_\pm$, respectively.
It is well known that the singular integral operator with Cauchy kernel, $S_\mathbb{T}$, defined almost everywhere on $\mathbb{T}$, by

$$S_\mathbb{T}\varphi(t) = \frac{1}{\pi i} \int_\mathbb{T} \frac{\varphi(\tau)}{\tau - t}\, d\tau,\ t \in \mathbb{T}, \tag{1}$$

where the integral is understood in the sense of its principal value, is a bounded linear operator in the Lebesgue space $L_2(\mathbb{T})$. In addition, $S_\mathbb{T}$ is an unitary and selfadjoint operator in $L_2(\mathbb{T})$. Thus, we can associate with $S_\mathbb{T}$ the two complementary Cauchy

projection operators

$$P_{\pm} = (I \pm S_{\mathbb{T}})/2, \tag{2}$$

where I represents the identity operator.
The projection operators (2) allow us to decompose the algebra $\mathcal{R}(\mathbb{T})$ in the topological direct sum

$$\mathcal{R}(\mathbb{T}) = \mathcal{R}_+(\mathbb{T}) \oplus \mathcal{R}_-^0(\mathbb{T}), \tag{3}$$

where $\mathcal{R}_+(\mathbb{T}) = P_+\mathcal{R}(\mathbb{T})$ and $\mathcal{R}_-^0(\mathbb{T}) = P_-\mathcal{R}(\mathbb{T})$. We also have $\mathcal{R}_-(\mathbb{T}) = \mathcal{R}_-^0(\mathbb{T}) \oplus \mathbb{C}$.

2.2 Rational function factorization

This subsection is dedicated to factorization concepts applied to rational functions r, from the traditional (for $r \in \mathcal{R}(\mathbb{T})$) and the inner-outer decomposition perspectives (for $r \in \mathcal{R}_+(\mathbb{T})$).
The success of obtaining a factorization of a rational function r, defined in the unit circle, depends on the possibility of finding zeros and poles by solving polynomial equations. Additionally, it is crucial to determine their locations relative to the curve where the function is defined. This task becomes particularly challenging when dealing with polynomials of the fifth degree or higher.

2.2.1 Scalar rational factorization

In this subsubsection it is considered the traditional rational factorization concept.

Definition 1 *Let $r \in \mathcal{R}(\mathbb{T})$. A decomposition*

$$r(t) = r_+(t)t^{\kappa}r_-(t), \tag{4}$$

where $r_+, 1/r_+ \in \mathcal{R}_+(\mathbb{T})$, $r_-, 1/r_- \in \mathcal{R}_-(\mathbb{T})$, and $\kappa \in \mathbb{Z}$, is called a scalar rational factorization *of the function r with respect to the curve $\mathbb{T}$. κ is called the* factorization index *of the rational function r.*

The integer κ is uniquely determined by the function r.
If $\kappa = 0$, then r is said to admit a *scalar rational canonical factorization*.
Any function $r \in \mathcal{R}(\mathbb{T})$, without zeros in $\mathbb{T}$, admits scalar rational factorizations with respect to the curve $\mathbb{T}$.

2.2.2 Inner-outer rational factorization

In this subsubsection it is considered another factorization concept, applied to rational functions without poles in the unit disk.

Definition 2 *Let $r \in \mathcal{R}_+(\mathbb{T})$. A decomposition*

$$r(t) = \theta(t)out(t), \tag{5}$$

where $\theta(t)$ is an inner function and $out(t)$ is an outer function, is called an inner-outer rational factorization *of the function r with respect to the curve $\mathbb{T}$.*

Obviously, in the rational case, θ is a Blaschke product and $out(t)$ does not have zeros in $\mathbb{T} \cup \mathbb{T}_+$.
Any function $r \in \mathcal{R}_+(\mathbb{T})$, without zeros in $\mathbb{T}$, admits an inner-outer rational factorization with respect to the curve $\mathbb{T}$.

2.3 [AZeros] and [APoles] algorithms

This subsection is dedicated to a brief description of the [AZeros] and [APoles] algorithms, designed and implemented by the authors [16]. Even in cases when polynomials of the fifth degree or higher are considered, the symbolic and numeric capabilities of Wolfram *Mathematica*[1] allow us to determine the zeros and the poles of a scalar rational function, and to identify their location relative to $\mathbb{T}$, $\mathbb{T}_+$, and $\mathbb{T}_-$.
Furthermore, the [AZeros] and [APoles] algorithms were created to be used as part of other more complex operator theory algorithms and to explore a list of values entered by the user. These algorithms can also be used independently through a *nb* format file where a rational function is input and the Mathematica's *Solve* command is used.

3 NEW OPERATOR THEORY ALGORITHMS

This section is dedicated to the description of new operator theory algorithms.
Subsection 3.1 is dedicated to the improved version of the scalar rational function factorization algorithm presented in [15], the $[\text{ARFact}]_{2.0}$ algorithm. The [AInnerOuterFact] algorithm described in Subsection 3.2, after validating the inserted rational function, gives an inner-outer factorization through an output of a Blaschke product and a rational function without zeros and poles in $\mathbb{T}_+$.

3.1 $[\text{ARFact}]_{2.0}$ Algorithm

This subsection is dedicated to the formal description of the $[\text{ARFact}]_{2.0}$ algorithm, which analyzes the factorability of a given rational function and calculates a scalar factorization[2]

[1] *Mathematica* uses the `Root` object concept to represent the solutions of a polynomial equation.

[2] $z_i^{\pm}$ $(i = 1, \cdots, m_{\pm})$ denote all the zeros of the function r in $\mathbb{T}_{\pm}$ (with regard to their multiplicities); $p_j^{\pm}$ $(j = 1, \cdots, n_{\pm})$ denote all the poles of the function r in $\mathbb{T}_{\pm}$ (with regard to their multiplicities).

(4) for the given factorable rational functions

$$r_+(t) = \lambda \frac{\prod_{i=1}^{m_-}(t - z_i^-)}{\prod_{j=1}^{n_-}(t - p_j^-)}, \qquad r_-(t) = \frac{\prod_{i=1}^{m_+}(1 - t^{-1}z_i^+)}{\prod_{j=1}^{n_+}(1 - t^{-1}p_j^+)}, \qquad \kappa = m_+ - n_+, \qquad \lambda \in \mathbb{C}. \quad (6)$$

The algorithm allows two input options for the rational function (Figure 1).

```
option =
  DialogInput[
   DialogNotebook[
    {Row[{DefaultButton["Insert r(t) directly.", DialogReturn[opt = 1]],
       CancelButton["Insert zeros, poles and λ.", DialogReturn[opt = 2]]}]}]];
```

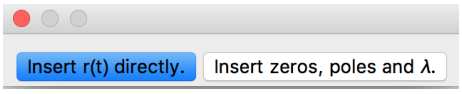

Figure 1: Part of the code structure of the $[\text{ARFact}]_{2.0}$ algorithm responsible for the input options for the rational function r.

If *Option 1* is chosen, a new box appears for entering the rational function. If *Option 2* is chosen, new boxes appear for indicating the constant λ and the existing number of zeros and poles (with reference to the multiplicity of each element).
With the integration of the [AZeros] and the [APoles] algorithms (Figure 2), it is possible to validate the input rational function r. Incorrect outputs that could occur with the algorithm presented in [15] (since, in that case, the responsibility for entering a valid factorable function falls on the user) are no longer possible to happen in this improved version.

```
<<"AZeros.m";

<<"APoles.m";


If[circlez ≠ 0, Print["r(t)=",r[t]," is not a factorable function."],
 If[circlep≠0, Print["r(t)=",r[t]," ∉ R(𝕀)"],
```

Figure 2: Part of the code structure of the $[\text{ARFact}]_{2.0}$ algorithm responsible for the integration of the [AZeros] and [APoles] algorithms, to validate the input rational function r.

The computation of the index of r and the factors r_+ and r_- of a factorization (4) is always possible using data obtained with algorithms applied to specific expressions.
Figure 3 contains the flowchart of the $[\text{ARFact}]_{2.0}$ algorithm.

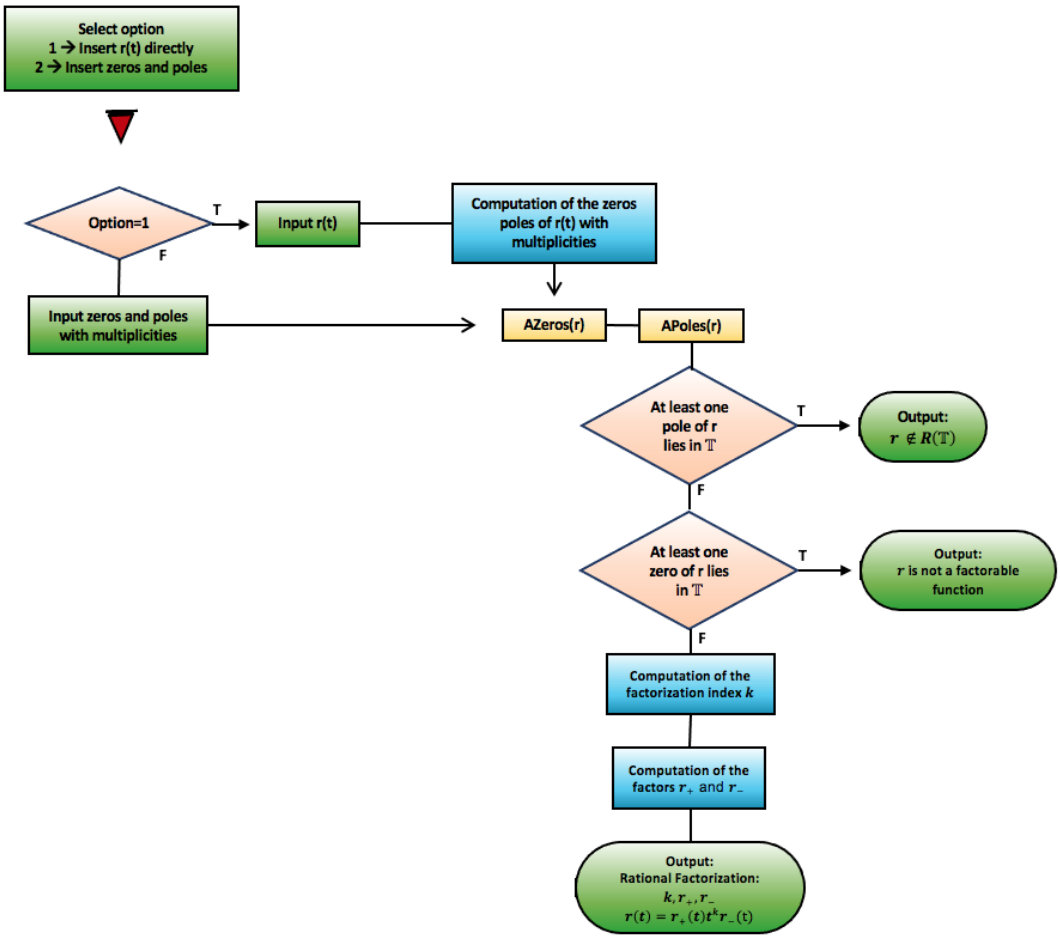

Figure 3: Flowchart of the $[\text{ARFact}]_{2.0}$ algorithm.

3.2 [AInnerOuterFact] Algorithm

This subsection is dedicated to the description of the [AInnerOuterFact] algorithm, which analyzes the factorability of a given rational function and computes an explicit inner-outer factorization (5) for the given factorable rational function $r \in \mathcal{R}_+(\mathbb{T})$, where[3]

$$\theta(t) = t^q \prod_{k=1}^{m} \frac{|z_k|}{z_k} \frac{z_k - t}{1 - \overline{z_k} t} \tag{7}$$

and

$$out(t) = \frac{r(t)}{\theta(t)}. \tag{8}$$

[3] z_k $(k = 1, \cdots, m)$ denote all the zeros of r in $\mathbb{T}_+$.

This algorithm also allows two input options for the rational function r (Figure 4).

```
DialogInput[{Row[{Button["Insert r(t) directly.",DialogReturn[opt=1]],
Button["Insert zeros, poles with multiplicities and λ.",DialogReturn[opt=2]]}]}];
```

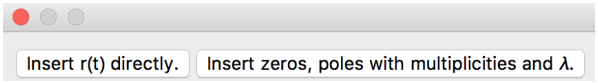

Figure 4: Part of the code structure of the [AInnerOuterFact] algorithm responsible for the input options for the rational function r.

The [AInnerOuterFact] algorithm uses [AZeros] and the [APoles] algorithms to validate the input rational function r (Figure 5).

```
<<"AZeros.m";

<<"APoles.m";

If[circlep!=0,Print["r(t)=",r[t]," ∉ R(T), so is not an inner-outer factorable function."],
If[diskp!= 0,Print["r(t)=",r[t]," ∉ \!\(\*SubscriptBox[\(R\), \(+\)]\)(T),
so is not an inner-outer factorable function."],
If[circlez!= 0,Print["1/r(t) ∉ R(T), so r is not an inner-outer factorable function."],
```

Figure 5: Part of the code structure of the [AInnerOuterFact] algorithm responsible for the integration of the [AZeros] and [APoles] algorithms, to validate the input rational function r.

The computation of the factors θ and *out*, for a factorization (5) result from the implementation of the formula (Figure 6).

```
m=Length[listzdisk];If[listzdisk=={},inner[t]=t^l,
inner[t_]=Product[t^l*Abs[listzdisk[[k]]]/listzdisk[[k]]*
(listzdisk[[k]]-t)/(1-Conjugate[listzdisk[[k]]]*t),{k,1,m}]];
out[t_]=Simplify[r[t]/inner[t]];
```

Figure 6: Part of the code structure of the [AInnerOuterFact] algorithm responsible for the computation of the factors θ and *out*.

Figure 7 contains the flowchart of the [AInnerOuterFact] algorithm.

4 FINAL REMARKS

The design and implementation of analytical operator theory algorithms can constitute a very interesting line of research.
The authors believe that the methods described in this article can be extended to other operator theory problems, at least in the rational case.

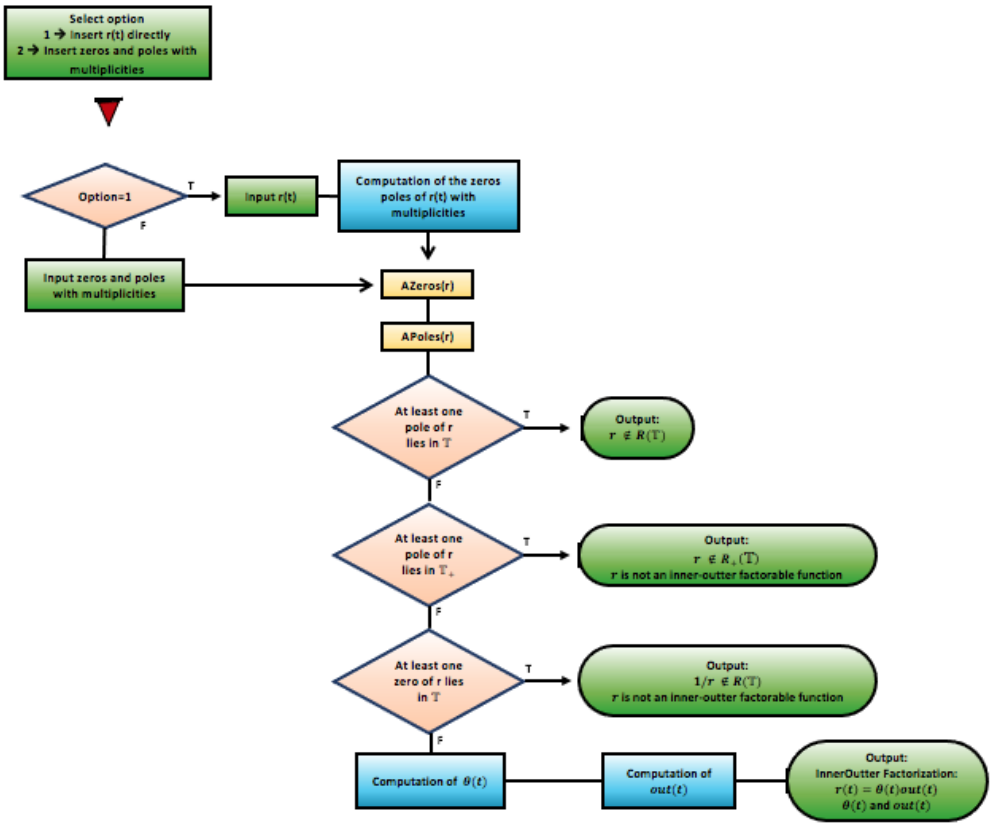

Figure 7: Flowchart of the [AInnerOuterFact] algorithm.

REFERENCES

[1] Ablowitz, M.J.; Clarkson, P.A. *Solitons, Nonlinear Evolution Equations and Inverse Scattering*; Cambridge University Press: Cambridge, UK, 1991

[2] Aktosun, T.; Klaus, M.; van der Mee, C. "Explicit Wiener–Hopf factorization for certain non-rational matrix functions", *Integral Equations and Operator Theory* , **15**, pp. 879-900, 1992

[3] Clancey, K.; Gohberg, I. Factorization of Matrix Functions and Singular Integral Operators; In *Operator Theory: Advances and Applications*; Birkhäuser Verlag: Basel, Switzerland, 1981

[4] Faddeev, L.D.; Takhatayan, L. *Hamiltonian Methods in the Theory of Solitons*; Springer: Berlin, Germany, 1987

[5] Gohberg, I., Kaashoek, M.A., Spitkovsky, I.M. "An Overview of Matrix Factorization Theory and Operator Applications", *Factorization and Integrable Systems, Operator Theory: Advances and Applications*, Birkhäuser Verlag, **141**, pp. 1-102, 2003

[6] Litvinchuk, G.S.; Spitkovskii, I.M. Factorization of Measurable Matrix Functions. In *Operator Theory: Advances and Applications*; Birkhäuser, Basel, *25*, 1987

[7] Prössdorf, S. *Some Classes of Singular Equations*; Elsevier: Amsterdam, North-Holland, 1978

[8] Litvinchuk, G.S. *Solvability Theory of Boundary Value Problems and Singular Integral Equations with Shift*; Kluwer Academic Publishers: Dordrecht, The Netherlands, 2000

[9] Ehrhardt, T., Speck, F.-O. "Transformation techniques towards the factorization of non-rational 2×2 matrix functions", *Linear Algebra and Its Applications*, **353(1-3)**, pp. 53-90, 2002

[10] Feldman, I., Gohberg, I., Krupnik, N. "An Explicit Factorization Algorithm", textit Integral Equations Operator Theory, **49(2)**, pp. 149-164, 2004

[11] Ball, J.A., Clancey, K.F. "An elementary description of partial indices of rational matrix functions", *Integral Equations Operator Theory*, *13(3)*, pp. 316-322, 1990

[12] Câmara, M.C., dos Santos, A.F. "Generalised Factorization for a Class of $n \times n$ Matrix Functions - Partial Indices and Explicit Formulas", *Integral Equations Operator Theory*, **20(2)**, pp. 198-230, 1994

[13] Voronin, A.F. "A method for determining the partial indices of symmetric matrix functions", *Siberian Mathematical Journal*, **52**, pp. 41-53, 2011

[14] Conceição, A.C.; Kravchenko, V.G.; Pereira, J.C. "Factorization Algorithm for Some Special Non-rational Matrix Functions", *Operator Theory: Advances and Applications*, Birkhäuser Verlag: Basel, Switzerland, **202**, pp. 87-109, 2010

[15] Conceição, A.C.; Kravchenko, V.G.; Pereira, J.C. "Rational functions factorization algorithm: A symbolic computation for the scalar and matrix cases ", *Proceedings of the 1st National Conference on Symbolic Computation in Education and Research*, Lisboa, Portugal, 2–3 April, 2012

[16] Conceição, A.C., Pires. J.C. "Symbolic Computation Applied to Cauchy Type Singular Integrals", *Mathematical and Computational Applications* , **27(1)-3**, 2022

SYMCOMP 2025
Lisbon, 10-11 April 2025

COMPUTATIONAL ANALYSIS OF LEVENBERG-MARQUARDT METHOD IN NONLINEAR LEAST SQUARES PROBLEMS

Vasco Ricardo[1], Celestino Coelho[1], Ana C. Conceição[1,2] and Jéssica C. Pires[3]

1: Faculdade de Ciências e Tecnologia, Universidade do Algarve
Campus de Gambelas, 8005 - 139 Faro, Portugal

2: Center for Research & Development in Mathematics and Applications
Campus Universitário de Santiago, 3810 - 193 Aveiro, Portugal

3: Faculdade de Economia, Universidade do Algarve
Campus de Gambelas, 8005 - 139 Faro, Portugal

e-mail: {a79789, ccoelho, aconcei, jccpires}@ualg.pt

Keywords: Nonlinear least squares, parameter estimation, Gauss-Newton method, Levenberg-Marquardt method

Abstract. *The Levenberg-Marquardt (LM) method is a widely used optimization algorithm for solving nonlinear least squares problems, particularly in parameter estimation and curve fitting. This work presents a comprehensive study of the method, analyzing its theoretical foundations, convergence properties, and computational performance. The LM method is an iterative algorithm that combines the advantages of gradient descent for global convergence and the Gauss-Newton method (GN) for fast local convergence. The algorithm introduces a damping parameter that dynamically adjusts between the two methods, enhancing stability and efficiency when solving ill-conditioned or highly nonlinear problems.*

This work explores the role of the damping parameter in the convergence process, the sensitivity to initial parameter guesses, and the numerical stability of the algorithm. The implementation of the LM method is carried out in Python, with comparative analysis against the `nls()` *function from R software, which uses GN method. Practical examples are used to illustrate the algorithm's performance. The results highlight the advantages of the LM method in terms of convergence speed and robustness, especially in cases where traditional methods like GN method struggle to converge. This analysis contributes to a better understanding of the LM method's application in nonlinear regression problems and its suitability for different problem scenarios.*

Funding: This research was supported by Center for Research and Development in Mathematics and Applications (CIDMA) under the Portuguese Foundation for Science and Technology (FCT) Multi-Annual Financing Program for R&D Units.

DOI:10.5281/zenodo.15161249

1 INTRODUCTION

Complex phenomena that occur in many scientific areas are often studied using mathematical models. These models can be divided into two groups, linear and nonlinear. Linear models are widely used, and their mathematical foundations are easier to understand. The exponential model is found among the nonlinear models, and it is one of the most applied models in scientific studies. The range of scientific applications of this model ranges from health sciences, when exploring the growth of COVID-19 cases, [Kasilingam et al., 2021], to biology, modeling the growth of bacteria count data, [Rumpf, 2021], and economics, to study firm capital structure,[Ramalho et al., 2018], ...

To estimate the unknown parameters of a mathematical model, such as the exponential model, it is common to fit the parameterized model to the collected data. This procedure consists in taking the sum of squared errors between the measured and fitted values as an objective function and applying numerical optimization algorithms ([Björck, 1996]; [Nocedal and Wright, 2006]) to obtain approximations for the unknown parameters of the model, such that the objective function is minimized and the estimates of the parameters are as close as possible to the true values.

The LM method is a widely used optimization algorithm for solving nonlinear least-squares problems. It is particularly effective in scenarios where models need to be fitted to empirical data, such as parameter estimation in exponential models. The method is an adaptive approach that combines the advantages of both the GN method and gradient descent, making it well-suited for problems where the Jacobian matrix is ill-conditioned or nearly singular, leading to numerical instability. Regularization techniques, such as the LM method, help mitigate these issues by introducing adaptive damping parameters to balance between rapid convergence and numerical robustness.

In this work, we explore the application of these two methods, GN and LM, using implemented code in Python and the `nls()` function available in R statistical software. One of the main purposes of this work is to understand how these methods behave in terms of convergence when using initial approximations far from the real estimates of the parameters of the model.

This paper is structured as follows: Section 2 covers the theoretical analysis related to nonlinear least-squares regression problems and the derivation of numerical algorithms to solve this kind of problems; Some of the numerical results obtained are presented in Section 3; Section 4 is used to draw some final remarks.

2 THEORETICAL ANALYSIS

2.1 Nonlinear least-squares problem

The main goal in a least-squares problem is to minimize the Euclidean norm of the residual. The residual function r depends on the n parameters to estimate and has m components, generally m is much larger than n.

If the model to fit is linear on the dependent variable, we will get a linear least-squares

problem whose solution can be easily obtained using the normal equations or the QR decomposition.
The nonlinear least-squares problem arises most commonly from data-fitting applications, when we attempt to fit the data (x_i, y_i), $i = 1, \ldots, m$, with a mathematical model $\phi(\beta; x)$ that is nonlinear in β. In such cases, each component of the residual function is given by

$$r_i(\beta) = \phi(\beta; x_i) - y_i, \ i = 1, \ldots, m, \tag{1}$$

and the nonlinear least-squares problem consists of choosing β so that the fit is as close as possible in the sense that the sum of the squares of the residuals is minimized, which is equivalent to minimize the objective function:

$$f(\beta; x, y) \equiv f(\beta) = \frac{1}{2}\|r(\beta)\|^2 = \frac{1}{2} r(\beta)^T r(\beta). \tag{2}$$

The sum-of-squares measure for data fitting is justified by statistical considerations and the problem can be stated as follows:

$$\min_{\beta \in \mathbb{R}^n} f(\beta) = \min_{\beta \in \mathbb{R}^n} \frac{1}{2} \sum_{i=1}^{m} \left(\phi(\beta, x_i) - y_i\right)^2. \tag{3}$$

Taking the first derivative of the objective function presented in (2) we get:

$$\nabla f = \sum_{i=1}^{m} r_i \cdot \nabla r_i = J^T r \tag{4}$$

where $J \in \mathbb{R}^{m \times n}$ is the Jacobian matrix with $J_{ij} = J(\beta)_{ij} = \dfrac{\partial r_i}{\partial \beta_j}(\beta)$.
Analogously, the second derivative is given by:

$$\begin{aligned} \nabla^2 f &= \sum_{i=1}^{m} \left(\nabla r_i \cdot \nabla r_i^T + r_i \cdot \nabla^2 r_i\right) \\ &= \sum_{i=1}^{m} \left(\nabla r_i \cdot \nabla r_i^T\right) + \sum_{i=1}^{m} \left(r_i \cdot \nabla^2 r_i\right) \\ &= J^T J + S, \end{aligned} \tag{5}$$

where S denotes the second order terms in $\nabla^2 f$. Therefore, taking the second order approximation from Taylor series expansion around β_c we get:

$$\begin{aligned} f(\beta_c + h) &\approx f(\beta_c) + \nabla f(\beta_c)^T h + \frac{1}{2} h^T \nabla^2 f(\beta_c) h \\ &\approx \frac{1}{2} r(\beta_c)^T r(\beta_c) + r(\beta_c)^T J(\beta_c) h + \frac{1}{2} h^T \left(J(\beta_c)^T J(\beta_c) + S(\beta_c)\right) h \end{aligned} \tag{6}$$

where $h = \beta - \beta_c$. Applying the idea that underlies Newton's method derivation we get the iterative scheme:

$$\beta^{(k+1)} = \beta^{(k)} - \left(J_k^T J_k + S_k\right)^{-1} J_k^T r^{(k)}. \tag{7}$$

where $J_k = J\left(\beta^{(k)}\right)$, $S_k = S\left(\beta^{(k)}\right)$ and $r^{(k)} = r\left(\beta^{(k)}\right)$. The derivations of GN ([Björck, 1996]; [Nocedal and Wright, 2006]) and LM ([Levenberg, 1944]; [Marquardt, 1963]; [Björck, 1996]; [Nocedal and Wright, 2006]) algorithms are based in equation (7).

2.2 Exponential fitting model

A common application of nonlinear least squares is the fitting of an exponential model of the form:

$$y_i = \beta_0 e^{\beta_1 x_i} + \epsilon_i, \tag{8}$$

where β_0 and β_1 are the parameters to be estimated and ϵ_i are the errors which are assumed to be i.i.d. normal with constant variance. Given a set of data points (x_i, y_i), $i = 1, 2, \ldots, m$, with $m > 2$, due to the nature of the problem, the residuals can be defined by:

$$r_i = \beta_0 e^{\beta_1 x_i} - y_i, \ i = 1, 2, \ldots, m. \tag{9}$$

From (9) we can obtain the Jacobian matrix of the residual function, J, whose entries are defined by the first-order derivatives of the residuals with respect to the parameters:

$$J(\beta) \equiv J = \begin{bmatrix} \dfrac{\partial r_1}{\partial \beta_0} & \dfrac{\partial r_1}{\partial \beta_1} \\ \dfrac{\partial r_2}{\partial \beta_0} & \dfrac{\partial r_2}{\partial \beta_1} \\ \vdots & \vdots \\ \dfrac{\partial r_m}{\partial \beta_0} & \dfrac{\partial r_m}{\partial \beta_1} \end{bmatrix} = \begin{bmatrix} e^{\beta_1 x_1} & \beta_0 x_1 e^{\beta_1 x_1} \\ e^{\beta_1 x_2} & \beta_0 x_2 e^{\beta_1 x_2} \\ \vdots & \vdots \\ e^{\beta_1 x_m} & \beta_0 x_m e^{\beta_1 x_m} \end{bmatrix}. \tag{10}$$

Attending that the objective function $f(\beta)$ is a continuous function that depends on parameters β_0 and β_1, the estimates for theses parameters should satisfy the following conditions when the objective function reaches its minimum:

$$\begin{aligned} \nabla f(\beta) = 0 \Leftrightarrow & \begin{cases} \dfrac{\partial f}{\partial \beta_0} = 0, \\ \dfrac{\partial f}{\partial \beta_1} = 0 \end{cases} \\ \Leftrightarrow & \begin{cases} \displaystyle\sum_{i=1}^{m} \left(\beta_0 e^{\beta_1 x_i} - y_i\right) e^{\beta_1 x_i} = 0, \\ \displaystyle\sum_{i=1}^{m} \beta_0 x_i \left(\beta_0 e^{\beta_1 x_i} - y_i\right) e^{\beta_1 x_i} = 0. \end{cases} \end{aligned} \tag{11}$$

Since we cannot solve the system (11) to obtain analytical expressions for β_0 and β_1, we have to apply numerical optimization algorithms to find a numerical approximation to the solution of this problem. When the convergence conditions are verified, these algorithms generate a sequence that converges to the solution of (11). Among the most common optimization algorithms applied to solve this problem we find the steepest descent method, GN method and LM method.

In the steepest descent method, the objective function is iteratively minimized by updating the estimates of the parameters in the direction opposite to the gradient of the objective function, that is,

$$\beta^{(k+1)} = \beta^{(k)} - \lambda_k \nabla f^{(k)},\ i = 0, 1, \ldots, \tag{12}$$

where $\lambda_k > 0$ is the step factor and $\nabla f^{(k)}$ is the gradient of the objective function f evaluated at $\beta^{(k)}$.

The GN method consists of a modification of Newton's method for minimizing the sum of squared residuals. One of the main advantages of using the GN method is that the second derivatives of the objective function, which can be challenging to compute, are not required, since the Hessian matrix of the objective function in (5) is approximated by $J^T J$. Applying this strategy, the iteration is given by:

$$\beta^{(k+1)} = \beta^{(k)} + p_k \tag{13}$$

where p_k is the solution of the system of linear equations

$$J_k^T J_k p_k = -J_k^T r^{(k)}, \tag{14}$$

where J_k and $r^{(k)}$ are the Jacobian matrix of the residual function and the residual function evaluated in $\beta^{(k)}$, respectively, and $\beta^{(k)} = \left(\beta_0^{(k)}, \beta_1^{(k)}\right)$ is the numerical approximation for the estimates.

The LM method combines the steepest descent method with the GN method and is widely applied in many nonlinear minimization problems. This algorithm behaves like a steepest descent method and increases the step factor when the estimates fall far from their true values. When the objective function is reduced, the step factor is decreased and the method behaves like the GN method. Therefore, the LM method modifies the GN update rule by introducing a damping parameter λ_k:

$$(J_k^T J_k + \lambda_k I) p_k = -J_k^T r^{(k)}, \tag{15}$$

where p_k is the update step and I is the identity matrix. The damping parameter λ_k controls the transition between GN (for small λ_k) and gradient descent (for large λ_k). It is dynamically adjusted to ensure adequate descent and improve convergence stability.

3 NUMERICAL RESULTS

In this section we will see how to apply the methods, GN and LM, to solve nonlinear regression problems, more precisely, exponential regression problems. When a multiplicative change characterizes the relationship between the explanatory and response variables, it means that we will have exponential growth or exponential decay, and the best model to fit the data is the exponential model.
One of the goals of the least squares problems is to find the best model function ϕ for the observations (x_i, y_i), $i = 1, 2, \ldots, m$. Therefore, residuals will represent the difference between the values observed for the dependent variable and the correspondent predicted values, $\widehat{y}_i = \phi\left(\widehat{\beta}, x_i\right)$,

$$r_i = y_i - \widehat{y}_i,\ i = 1, 2, \ldots, m, \tag{16}$$

where $\widehat{\beta} = \left(\widehat{\beta}_0, \widehat{\beta}_1, \ldots, \widehat{\beta}_n\right)$, $n < m$, are the estimates of the parameters. Estimates for the parameters of the mathematical model are achieved by minimizing the sum of squares residuals (SSR), defined in (3), which is a special case of an unconstrained optimization problem that requires the use of specific algorithms, such as GN or LM. Since both algorithms are iterative, we need to define a stopping criterion to end the iterative process. Usually two stopping conditions are combined, one for the maximum number of iterations to be performed and another related to the convergence of the sequence generated by the method being used. A widely used stopping criterion for iterative optimization methods is based on the gradient norm of the objective function, $\|\nabla f(\beta)\| \equiv \|\nabla f\|$. Attending to the result presented in (4), the iteration process ends when the Euclidean norm of the gradient of the objective function falls below a predefined tolerance δ, ensuring that the solution is sufficiently accurate,

$$\|J^T r\| < \delta. \tag{17}$$

This criterion ensures that the optimization process stops when the residuals cannot be significantly reduced, indicating convergence to a local minimum.
The example that folows uses data observed for milk demand (price and sales) and it will be solved using the code implemented for GN and LM methods, as well as with the `nls()` function available in R software [R Core Team, 2025].

3.1 Milk demand

In this example, we use a dataset that describes the milk demand[1]. This dataset was obtained in a "stated preference" study, which is intended to measure someone's willingness to pay for a good or service. This study is based on the idea of giving the participants a hypothetical grocery budget, such as a menu of goods with their respective prices, and then asking them to allocate their budget as they wish. By manipulating menu prices, it

[1]Data set from https://bookdown.org/jgscott/DSGI/

is possible to analyze people's sensitivity to buying goods at various prices. The data collected consists of 116 observations describing the relationship between the price of milk on the menu (price) and the number of participants willing to buy milk at that price (sales). A graphical representation of this data is in figure 1. According to the graph,

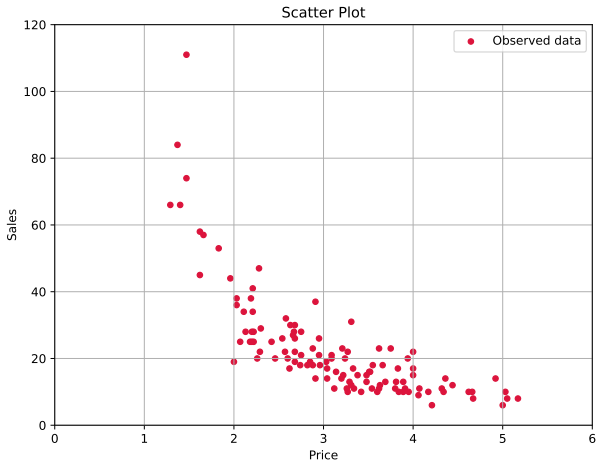

Figure 1: Milk demand observations.

is evident that people are less willing to buy milk when prices are higher. The idea is to fit a model to this data, and in this case, the chosen is the exponential regression model.

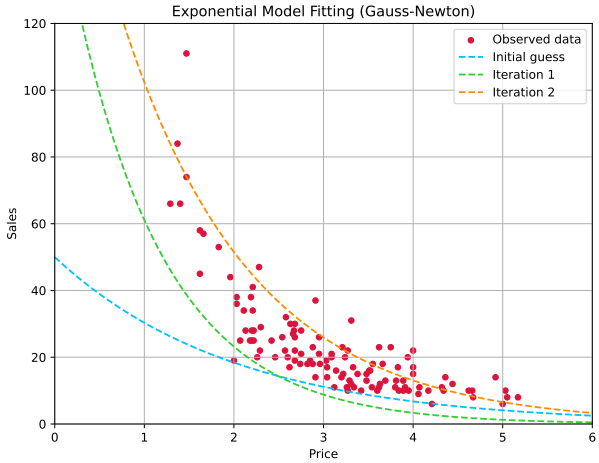

Figure 2: First iterations obtained with Gauss-Newton.

k	$\beta_0^{(k)}$	$\beta_1^{(k)}$	$f\left(\beta^{(k)};x,y\right)$	$\frac{\|\beta^{(k+1)}-\beta^{(k)}\|}{\|\beta^{(k+1)}\|}$	$\|\nabla f\left(\beta^{(k)};x,y\right)\|$
0	50.0	-0.5	16369.504	0.689	44300.0
1	161.00382	-0.96925715	12678.118	0.209	43700.0
2	203.44808	-0.68683065	6405.2700	0.0537	61600.0
3	193.07701	-0.75318498	3709.1803	0.0397	5220.0
4	201.06064	-0.78238895	3669.1529	0.0131	144.0
5	203.7311 0	-0.78844924	3668.3376	0.00235	25.5
6	204.21179	-0.7895287	3668.3119	0.000406	6.62
7	204.29464	-0.78971976	3668.3111	7.13e-05	1.24
8	204.30921	-0.78975354	3668.3111	1.26e-05	0.221
9	204.31179	-0.78975951	3668.3111	2.23e-06	0.0391
10	204.31224	-0.78976057	3668.3111	—	0.00692

Table 1: Results obtained with implemented code for GN method applied to milk demand data set.

Figure 2 shows the data collected, the initial guess used to apply the GN method, and the results returned for the first and second iterations. This gives us a graphical insight into the idea of how convergence is processed when using this method.
The `nls()` function with the initial guess

$$\beta^{(0)} = \left(\beta_0^{(0)}, \beta_1^{(0)}\right) = (50, -0.5) \tag{18}$$

and setting the tolerance to 0.5×10^{-1} for the Euclidean norm of the gradient of f, the results obtained are presented in table 1.
Next, we use the `nls()` function available in R software to estimate the parameters of the exponential model. The output is presented below, and it corroborates the results achieved with our code.

```
Nonlinear regression model
  model: sales ~ beta0 * exp(beta1 * price)
   data: parent.frame()
   beta0    beta1
204.3118  -0.7898
 residual sum-of-squares: 7337

Number of iterations to convergence: 9
Achieved convergence tolerance: 2.364e-06
```

From this output (or from table 1) we obtain the following mathematical expression of the estimated exponential model:

$$\widehat{y}_{Sales_i} = 204.312e^{-0.7898Price_i},\ i = 1, \ldots, 116. \tag{19}$$

Next, we apply LM method to solve the same problem using `gsl_nls()` function available in `gslnls` package in R software.

```
iter   1: ssr = 28871.4, par = (50.0126, -0.152326)
iter   2: ssr = 18370.6, par = (50.0304, -0.254971)
iter   3: ssr = 18232.8, par = (50.0782, -0.271097)
iter   4: ssr = 18197.9, par = (50.2052, -0.271162)
iter   5: ssr = 18095.6, par = (50.5840, -0.273709)
iter   6: ssr = 17801.4, par = (51.6954, -0.280943)
iter   7: ssr = 17020.2, par = (54.8253, -0.300889)
iter   8: ssr = 15311.5, par = (62.7797, -0.348652)
iter   9: ssr = 12704.8, par = (79.3688, -0.435222)
iter  10: ssr = 10306.8, par = (102.892, -0.52939)
iter  11: ssr = 8612.71, par = (131.630, -0.620521)
iter  12: ssr = 7690.65, par = (163.170, -0.703107)
iter  13: ssr = 7386.73, par = (187.751, -0.756493)
iter  14: ssr = 7339.82, par = (199.827, -0.780482)
iter  15: ssr = 7336.75, par = (203.403, -0.787752)
iter  16: ssr = 7336.63, par = (204.146, -0.789379)
iter  17: ssr = 7336.62, par = (204.282, -0.789692)
iter  18: ssr = 7336.62, par = (204.307, -0.789748)
iter  19: ssr = 7336.62, par = (204.311, -0.789759)
iter  20: ssr = 7336.62, par = (204.312, -0.78976)
iter  21: ssr = 7336.62, par = (204.312, -0.789761)
iter  22: ssr = 7336.62, par = (204.312, -0.789761)
iter  23: ssr = 7336.62, par = (204.312, -0.789761)
iter  24: ssr = 7336.62, par = (204.312, -0.789761)
******************
summary from method 'multifit/levenberg-marquardt'
number of iterations: 24
initial ssr: 32739
final ssr: 7336.62
ssr/dof: 64.3563
ssr achieved tolerance: -9.09495e-13
function evaluations: 78
jacobian evaluations: 0
fvv evaluations: 0
```

```
status: success
******************
Nonlinear regression model
  model: y ~ beta0 * (exp(beta1 * x))
   data: milk
   beta0    beta1
204.3123  -0.7898
 residual sum-of-squares: 7337

Algorithm: multifit/levenberg-marquardt, (scaling: levenberg, solver: qr)

Number of iterations to convergence: 24
Achieved convergence tolerance: -9.095e-13
```

The results obtained show that in an initially stage the algorithm converges slowly, this is because the damping factor tends to be large to ensure convergence, i.e. the algorithm behaves like the steepest descent method. This happens because we are starting with an initial approximation that lies far from the solution of the system (11). As approximations become closer to the limit, the damping factor tends to be smaller, close to zero, and the algorithm starts to behave like GN method, converging faster to the limit.
Figure 3 shows the data points, the initial guess, and the first two iterations obtained with this method.

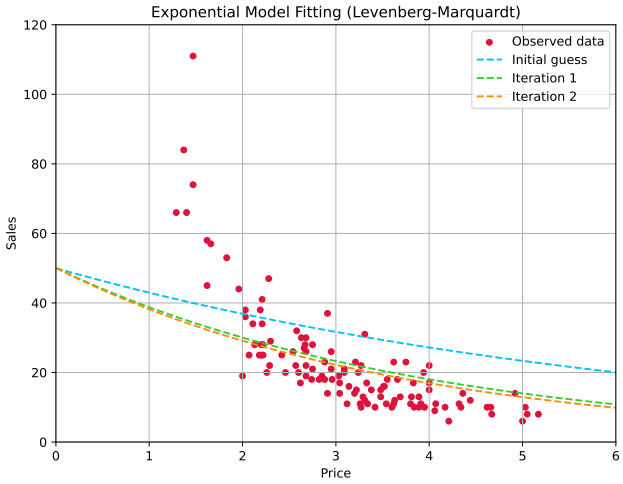

Figure 3: First iterations obtained with Levenberg-Marquardt.

4 FINAL REMARKS

In Numerical Analysis, some algorithms were developed to find a solution to linear least squares problems. However, although linear regression models generally present good results in most practical applications, there are situations where considering a nonlinear model is more appropriate. This preliminary study relies on the knowledge acquired in Numerical Analysis, where finding a computational solution in some complex situations is possible. In this context, Numerical Optimization provides a set of algorithms that can be applied to solve nonlinear regression problems, such as the GN and LM methods, which were implemented and used in the statistical software through `nls()` and `gsl_nls()` functions. Both tools were applied to obtain estimates of parameters in exponential regression problems.

The global convergence of the LM method is ensured under mild conditions and exhibits local superlinear convergence when residuals are small. Compared to other methods such as the GN method, this method provides a more stable and computationally efficient framework for solving linear least-squares problems, particularly in the cases of overdetermined systems or high-dimensional parameter spaces.

REFERENCES

[Björck, 1996] Björck, Åke. (1996). *Numerical methods for least squares problems*. Society for Industrial and Applied Mathematics.

[Kasilingam et al., 2021] Kasilingam, D., Sathiya Prabhakaran, S. P., Rajendran, D. K., Rajagopal, V., Santhosh Kumar, T., and Soundararaj, A. (2021). Exploring the growth of covid-19 cases using exponential modelling across 42 countries and predicting signs of early containment using machine learning. *Transbound Emerg Dis.*, 68:1001–1018.

[Levenberg, 1944] Levenberg, K. (1944). A method for the solution of certain non-linear problems in least squares. *Q. Appl. Math.*, 2:164–168.

[Marquardt, 1963] Marquardt, D. (1963). An algorithm for least-squares estimation of nonlinear parameters. *J. Soc. Ind. Appl. Math.*, 11:431–441.

[Nocedal and Wright, 2006] Nocedal, J. and Wright, S. (2006). *Numerical optimization*. Springer, 2. ed. edition.

[R Core Team, 2025] R Core Team (2025). *R: A Language and Environment for Statistical Computing*. R Foundation for Statistical Computing, Vienna, Austria.

[Ramalho et al., 2018] Ramalho, E., Ramalho, J., and Coelho, L. (2018). Exponential regression of fractional-response fixed-effects models with an application to firm capital structure. *Journal of Econometric Methods*, 7(1).

[Rumpf, 2021] Rumpf, A. (2021). Fitting exponential and logistic growth models to bacterial cell count data. *QB@CC FMN Bridging Mathematics and Biology*.

SYMCOMP 2025
Lisbon, 10-11 April 2025

COMPUTACIONAL MODELLING OF INCIDENT SOLAR RADIATION AND APPLICATION FOR THERMAL LOADS CALCULATION IN BUILDINGS

Abel Agostinho[1*], Fernando Carreira[2] and Cláudia Casaca[3]

1: ISEL – Instituto Superior de Engenharia de Lisboa, IPL
R. Conselheiro Emídio Navarro, 1, 1959-007 Lisboa, Portugal
e-mail: A47386@alunos.isel.pt web: www.isel.pt

2: IDMEC, UniRE, ISEL– Instituto Superior de Engenharia de Lisboa, IPL
R. Conselheiro Emídio Navarro, 1, 1959-007 Lisboa, Portugal
e-mail: fernando.carreira@isel.pt web: www.isel.pt

3: IDMEC, CIMOSM, ISEL– Instituto Superior de Engenharia de Lisboa, IPL
R. Conselheiro Emídio Navarro, 1, 1959-007 Lisboa, Portugal
e-mail: claudia.casaca@isel.pt web: www.cimosm.isel.pt

Keywords: Solar radiation, Computational modelling, Building Thermal Loads, Python

Abstract *Solar radiation is a significant factor in the heat gains of buildings, directly affecting indoor comfort and increasing the demand for air conditioning systems, and consequently, energy consumption. The present work aims at computationally modelling incident solar radiation, allowing its integration into the calculation of thermal loads in buildings. The adopted methodology considers three main components: the sun position, the radiation intensity and the characteristics of the surfaces exposed to this radiation. The sun position is determined based on latitude, longitude, date, and local time. Radiation intensity is estimated according to the sun position on a given day and time of analysis. The radiation model was developed and implemented in Python and validated by comparing its results with those of a commercial reference program. The results showed differences of less than 0.1% in the maximum annual analysis and a maximum deviation of 4.9% during hours of increased irradiance variation. The annual analysis, considering a building located in Lisbon, revealed that the maximum irradiance on North-facing surface occurred in June (219 W/m²), while the maximum for the East and West surfaces was verified in April (812 W/m²). The maximum irradiance on the South-facing surface was observed in January (913 W/m²). The hourly analysis on the day of maximum thermal load showed that the highest irradiance was verified on the East-facing surface (747.8 W/m² at 8 a.m.), followed by West-facing surface (744.7 W/m² at 4 p.m.) and the South-facing surface (734.5 W/m² at 12 p.m.), with the lowest irradiance observed on the North-facing surface (117.9 W/m²). The model was evaluated for various locations, demonstrating that latitude variation influence both the maximum irradiance and the duration of solar exposure, with these factors depending on the specific period of the year. The variation in longitude resulted in a time shift in the irradiance profile throughout the day.*

DOI:10.5281/zenodo.15161263

1. INTRODUCTION

Thermal loads in buildings refer to the heat exchange between the indoor and outdoor environments, leading to variations in indoor temperature and humidity. These variations can significantly impact indoor environmental conditions, potentially requiring the implementation of air conditioning systems to ensure thermal comfort. The thermal loads of a building originate from both external and internal sources. External thermal loads are influenced by climatic conditions and the thermal properties of the building envelope, including walls, roofs, windows, among others. Internal thermal loads, on the other hand, are the result from activities within the building and are primarily associated with occupancy, equipment and artificial lighting. The heat transfer by conduction and convection is highly dependent on climatic conditions, particularly external temperature. When an indoor space is directly exposed to the exterior, radiative heat transfer must also be considered, taking into account incident solar radiation on external elements such as external walls, roof and windows.

Solar radiation is defined as the energy emitted by the sun in the form of electromagnetic waves. This radiation constitutes a mode of heat transfer that occurs whenever a body has a temperature above absolute zero (0 K). Unlike other heat transfer mechanisms, such as conduction or convection, energy transfer via electromagnetic waves does not require the presence of a material medium.

In the study shown by An et al., (2020) [1], methods used in building energy modelling programs for direct incident solar radiation calculations are first analysed and an improved method is proposed. The algorithm assumes that the solar irradiance changes linearly within a 1-h period and can be estimated based on the solar irradiance at the half clock and slope. The collected direct normal solar irradiance data from various stations in China were used to evaluate the performance of proposed method and compare the results with those from three conventional methods used in building energy modelling programs. The results of the estimated direct incident solar radiation show that the proposed method achieves the best accuracy, followed by the methods used in DOE 2, EnergyPlus, and DeST. The proposed method obtains more accurate results when using the middle point of every timestep and by applying a shorter timestep, which can be adopted in current building energy modelling programs to improve the accuracy of a simulated building performance and photovoltaic energy production.

A new methodology of calculation of the direct, diffuse and reflected incident solar radiation, was developed in all type of surfaces [2]. This methodology is applicable in problems related to solar access (space heating in buildings, shadowing of open spaces), solar gains (space cooling in buildings), and daylighting. The proposed methodology is based on a method of characterization that can take into account the surfaces that can block or reflect the solar radiation toward the building. The proposed methodology contemplates the complete process, beginning with how to characterize surfaces and volumes, and finishing with the calculation of all the components of the incident solar radiation on an external surface. The quantitative characterization of the phenomenon has been carried out on a real case, and a new concept has

been defined: the modified albedo. With the help of this parameter, it has been possible to compare the solution given by a simplified model, and the one obtained from the proposed methodology.

The main contribution of the research presented by Marino et al., (2018) [3] is the development of a new methodology to obtain the external surface temperature of walls, considering diurnal variations of the external environment temperature. The theoretical calculation of the surface temperature requires knowing the evolution of the air external temperature, the total incident solar radiation on the wall and the external surface thermal resistance of the air boundary layer. The effect of solar radiation on the heat transfer through the building envelope can be considered, while the parameters related to the sol-air temperature calculation can be experimentally validated at the construction's specific location. The results were compared to measurements performed applying Infrared thermography. The results improve the understanding of the dynamic response of the different layers that compose the wall and the contribution of these layers to the global thermal behaviour of the wall.

An approach for predicting global radiation on any window plane has been presented [4]. Optical and thermal properties of window glazing system have been analysed to evaluate the glazing performance in increasing the inside temperature due to the incidence of global radiation. The thermal model considers laminar heat transfer for natural and forced convection process according to the ambient conditions. A mathematical model simulating the glazing temperature due to global radiation and hence the solar heat gain of building interior through window has been developed. The simulated glazing temperatures with the corresponding window plane global radiation were validated by experimental values. The estimated error between simulated and experimental values of window plane radiation and the corresponding glazing temperature are obtained below 5%. Thus, the radiation and thermal simulation models may be used for predicting the thermal performance of building due to solar radiation.

Demain et al., (2023) [5] presented a study that evaluates the performance of various models transposing solar radiation from horizontal to inclined surface. This study is relevant since global and diffuse solar radiation intensities are, in general, measured on horizontal surfaces, whereas stationary solar conversion systems (both flat plate solar collector and solar photovoltaic) are mounted on inclined surface to maximize the amount of solar radiation incident on the collector surface. Solar radiation data measured in Uccle, Belgium were used for validation purposes. Individual model performance is assessed between the calculated and measured solar global radiation on a south-oriented tilted surface using statistical methods. Since statistical validation procedures revealed that none of the considered model performs well under all types of sky conditions, a new model, resulting from the coupling of three models acting under different sky conditions, was developed for Belgium. The ability of the coupled model to handle hourly and daily data is discussed, concluding that bests results are obtained for hourly data.

An update status of research and applications of various methods was shown for determining solar panel tilt angle using various optimization techniques [6]. Determining the optimum tilt

angle allows for maximum incident solar radiation, resulting in optimum sizing of solar systems. This paper describes solar radiation modelling on sloped surfaces, defining solar time, solar geometry and radiation distribution. Solar radiation on sloped surfaces can defined considering Isotropic model or Anisotropic model. The optimum tilt angles are determined by changing tilt angle from 0º to 90º in different steps and using optimization techniques such as Genetic Algorithm, Simulated Annealing and Artificial Neural Network. For better accuracy of optimum tilt angle calculations different anisotropic models and optimization techniques can be tested at different sites. The study shows that for maximum energy gain, the optimum tilt angle for solar systems must be determined accurately for each location.

This article aims to implement a computational model for incident solar radiation, enabling its integration into thermal loads calculation for buildings. The adopted methodology is based on three main components: the solar position, the intensity of incident radiation and the characteristics of the surfaces exposed to this radiation.

2. THERMAL LOADS CALCULATION

Thermal loads can be calculated by computational models that include the building characteristics and the various heat transfer modes. ASHRAE [7] presents the computational methods such as the Transfer Function, the Cooling Load Temperature Difference method and Total Equivalent Temperature Difference/Time Averaging method. More recent editions of the ASHRAE Handbook [8] present the Heat Balance Method and the Radiant Time Series Method as refined approaches for calculating thermal loads, with a particular focus on accurately incorporating solar radiation effects.

The present study evaluates a computational application for thermal load calculation, as detailed in Agostinho, et al. (2024) [9]. This application implements the Transfer Function Method to estimate the thermal loads of a building while utilising external temperature and solar radiation data sourced from other programs. According to the Transfer Function Method, heat gain through external walls and roofs is determined by equation 1 [7]. This heat gain is dependent on the surface area of the analysed wall or roof, the indoor air temperature and the conduction transfer function coefficients. The conduction transfer function allows the modelling of conduction heat transfer through the wall. Additionally, the heat gain in external walls and roofs also is affected by the sol-air temperature, which accounts for the influence of solar radiation and outdoor conditions.

$$q_{e,\theta} = A \cdot \left[\sum_{n=0} b_n \left(t_{sol,\theta-n} \right) - \sum_{n=1} d_n \left(\frac{q_{e,\theta-n}}{A} \right) - t_{in} \sum_{n=0} c_n \right] \quad (1)$$

where:

$q_{e,\theta}$ – heat gain through wall or roof, at calculation hour θ [W];
A – surface area [m²];
$t_{sol,\theta-n}$ – sol-air temperature at hour θ-n [ºC];
t_{in} – indoor air temperature [ºC];
b_n, c_n e d_n – conduction transfer function coefficients [-].

The sol-air temperature is the outdoor air temperature that, in the absence of all radiation sources, results in the same heat flux into a surface as would the combined effect of incident solar radiation and convective heat exchange with the outdoor air. Thus, it is the equivalent of temperature considering the outdoor air temperature and the influence of solar radiation.

Heat gain through windows is obtained from the combination of two forms of heat transfer: conduction and radiation. The conductive heat gain of windows depends on the overall heat transfer coefficient (U-value), the surface area and outdoor and indoor air temperature, as shown in equation 2 [7].

$$q_{w,c} = U \cdot A \cdot (t_{out} - t_{in}) \quad (2)$$

where:

$q_{w,c}$ – conduction heat gain through window [W];
U – overall heat transfer coefficient [W/(m²·K)]
A – surface area [m²];
t_{out} – outdoor air temperature [ºC];
t_{in} – indoor air temperature [ºC].

The radiation heat gain through windows is determined as shown in equation 3 [7]:

$$q_{w,r} = A \cdot SHGF \cdot SC \quad (3)$$

where:

$q_{w,r}$ – radiation heat gain through window [W];
A – surface area [m²];
SHGF – solar heat gain factor [W/m²];
SC – shading coefficient [-].

The shading coefficient (SC) is a characteristic of a window that quantifies the amount of incoming solar energy in relation to a reference window. This coefficient can either be provided by the manufacturer or calculated based on the composition of the glazing system, considering the number of glass layers and their characteristics. The solar heat gain factor (SHGF) represents the fraction of incident solar irradiance that crosses the glazing and contributes to the heat gain inside the space. This includes both the directly transmitted component of irradiance and the portion that is absorbed by the glazing and subsequently re-emitted as heat.

In summary, solar radiation influences the thermal loads of buildings through external envelope elements, such as external walls roofs and windows. The impact of solar radiation is accounted for using sol-air temperature for external walls and roofs, and the solar heat gain factor for windows. Both parameters depend on the intensity of incident solar irradiance on the respective surface.

3. METHODOLOGY

3.1. CALCULATION OF SOLAR RADIATION

The solar radiation follows a sequence of three main variables: 1) solar time; 2) solar position and 3) solar irradiance. Solar time is estimated from the apparent angular motion of the sun, considering that noon is the moment when the sun passes in the local meridian. The solar time is calculated from the local time by equation 4 [10].

$$h_{solar} = h_{local} + \left(ET + 4 \cdot (l_{st} - l_{local})\right) \cdot \frac{1}{60} \quad (4)$$

where:

h_{solar} – solar time [h];
h_{local} – local time [h];
ET – equation of time [min];
l_{st} – local standard time meridian [º];
l_{local} – local longitude [º].

The equation of time (ET) establishes the relationship between the mean solar time and apparent solar time, accounting for seasonal variations. This value fluctuates throughout the year and can be obtained from tables, such as those provided by ASHRAE [7], or calculated using specific equations, as presented in Goswami (2015) [10]. The local longitude corresponds to the geographical longitude of the building under analysis. On the other hand, the local standard time meridian represents the central longitude of a given time zone, determined by multiplying the time difference from Greenwich Mean Time (GMT) by 15 degrees per hour.

Once the solar time is determined, the sun position can be characterised by two fundamental angular parameters, as illustrated in Figure 1: solar altitude and solar azimuth.

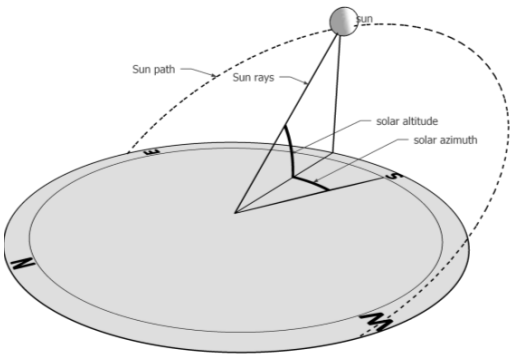

Figure 1. Position of the sun, its path and defining angles

Solar altitude is the angle between the sun's rays and the horizontal plane, which can be obtained using equation 5 [7].

$$\sin Alt_{sl} = \cos Lat \cdot \cos \delta_{solar} \cdot \cos h_{ang} + \sin Lat \cdot \sin \delta_{solar} \quad (5)$$

where:

Alt_{sl} – solar altitude [º];
Lat – latitude [º];
δ_{solar} – solar declination [º];
hang – solar hour angle [º].

The angle of solar hour describes the sun position relative to the local meridian, defined as the angular displacement between the sun current position and its position at solar noon. This angle is determined by the difference in hours between the given solar time and noon, multiplied by the Earth's angular velocity of 15º per hour. Since the Earth completes a full rotation of 360º in approximately 24 hours, its angular velocity is 15º/h.

The solar declination is the angle formed between the Earth's equatorial plane and the imaginary line that connects the centre of the Earth to the centre of the sun. This angular variation results from the inclination of the Earth's rotational axis relative to its orbital plane around the sun. Throughout the year, the declination varies between +23.45º and -23.45º. In the northern hemisphere, the maximum solar declination occurs at the summer solstice (+23.45°) and the minimum occurs at the winter solstice (−23.45°). The declination is null at both equinoxes.

The solar azimuth angle is the angle between the horizontal projection of the sun's rays and the true south direction, as illustrated in Figure 1. This angle is considered positive when westward and negative when eastward. The solar azimuth angle is calculated using the equations 6 and 7 [11].

$$\cos Az_{sl} = \frac{\sin Alt_{sl} \cdot \sin Lat - \sin \delta_{solar}}{\cos Alt_{sl} \cdot \cos Lat} \quad (6)$$

$$Az_{sl} = \begin{cases} 1 \cdot \arccos(cos\, Az_{sl}), & h_{ang} \geq 0 \\ -1 \cdot \arccos(cos\, Az_{sl}), & h_{ang} < 0 \end{cases} \quad (7)$$

where:

Az_{sl} – solar azimuth [º];
h_{ang} – solar hour angle [º];
Alt_{sl} – solar altitude [º];
Lat – latitude [º];
δ_{solar} – solar declination [º].

The following step is the calculation of the sun position in relation to the surface in analysis. This is achieved from the altitude angle and azimuth angle, that characterize the direction of sun's rays, as well as the orientation and inclination of the surface, that characterize the surface direction, resulting in the incident angle, as show in Figure 2. The calculation of the solar rays' incident angle on the surface in analysis is shown in equation 8 [7].

$$\cos \theta = \cos Alt_{sl} \cdot \cos\left(Az_{sl} - Az_{sp}\right) \cdot \sin Incl_{sp} + \sin Alt_{sl} \cdot \cos Incl_{sp} \quad (8)$$

where:

θ – incident angle [º];
Alt_{sl} – solar altitude [º];
Az_{sl} – solar azimuth [º];
Az_{sp} – surface azimuth [º];
$Incl_{sp}$ – surface tilt [º].

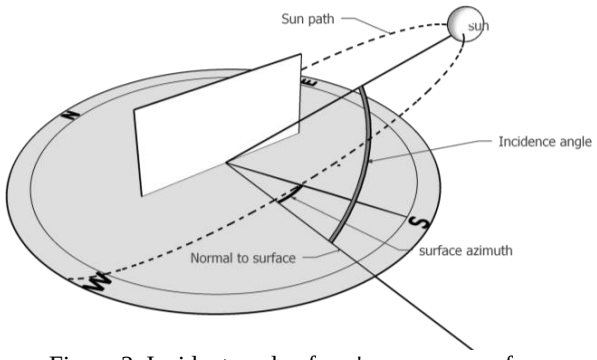

Figure 2. Incident angle of sun's rays on a surface

The solar irradiance is the solar radiant flux received by a surface per unit area. The total irradiance can be decomposed into three components: direct, diffuse and reflected. Direct irradiance refers to solar radiation that crosses the atmosphere and reaches the surface without suffering any dispersion in its trajectory, presenting rays parallel to the sun direction. On the other hand, diffuse irradiance results from the scattering of solar radiation caused by gases, particles and molecules present in the atmosphere. This scattering causes the rays to fall on the surface randomly, in various directions. Reflected irradiance corresponds to solar radiation that hits surrounding surfaces and is subsequently reflected towards the surface under analysis. The total solar irradiance is obtained by summing these three components, as expressed in equation 9.

$$I_T = I_D + I_{ds} + I_{dg} \tag{9}$$

where:

I_T – total irradiance [W/m²];
I_D – direct irradiance [W/m²];
I_{ds} – diffuse irradiance [W/m²];
I_{dg} – reflected irradiance [W/m²].

Direct normal irradiance, I_{DN}, is the incident solar radiation per unit area on a surface oriented perpendicularly to the direction of the sun's rays. According to the ASHRAE Handbook [7], I_{DN} is determined using equation 10:

$$I_{DN} = A_{sl} \cdot e^{\frac{-B}{\sin Alt_{sl}}} \tag{10}$$

where:

I_{DN} – direct normal irradiance [W/m²]
A_{sl} – apparent solar irradiation [W/m²]
B – atmospheric extinction coefficient [-]
Alt_{sl} – angle of solar altitude [º]

The direct irradiance incident on a surface that is not perpendicular to the sun's rays is determined using equation 11 [7]. For this calculation, the irradiance will be considered negligible if the angle of incidence, defined as the angle between the surface normal and the direction of the sun's rays, exceeds 90º or is less than -90º. This condition ensures that irradiance is only calculated for valid incident angles, i.e. for situations where the surface is effectively exposed to direct solar radiation.

$$I_D = \begin{cases} I_{DN} \cdot \cos\theta, & cos\,\theta > 0 \\ 0, & cos\,\theta \leq 0 \end{cases} \quad (11)$$

where:

I_D – direct irradiance [W/m²];
I_{DN} – direct normal irradiance [W/m²];
θ – incident angle [º].

The diffuse irradiance, I_{ds}, is determined by applying equation 12 [7], which models the distribution of diffuse solar radiation as a function of various atmospheric and geographic parameters.

$$I_{ds} = \begin{cases} C \cdot Y \cdot I_{DN}, & Incl_{sp} = 90º \\ C \cdot I_{DN} \cdot \dfrac{1 + \cos Incl_{sp}}{2}, & Incl_{sp} \neq 90º \end{cases} \quad (12)$$

where:

I_{ds} – diffuse irradiance [W/m²];
C – sky diffuse factor [-];
Y – ratio of vertical/horizontal sky diffuse;
I_{DN} – direct normal irradiance [W/m²];
$Incl_{sp}$ – surface tilt [º];

The sky diffuse factor, C, is a tabulated value and can be found in ASHRAE Handbook (1997) [7]. The calculation of vertical/horizontal sky diffusion ratio is detailed in the ASHRAE Handbook [7]. The irradiance reflected by the ground and surrounding surfaces, I_{dg}, is calculated using equation 13 [7].

$$I_{dg} = I_{DN} \cdot (C + \sin Alt_{sl}) \cdot \rho_g \left(\frac{1 - \cos Incl_{sp}}{2}\right) \quad (13)$$

where:

I_{dg} – reflected irradiance [W/m²];
I_{DN} – direct normal irradiance [W/m²];

C – sky diffuse factor [-];
Alt_{sl} – solar altitude [º];
ρ_g – ground reflectance [-];
$Incl_{sp}$ – surface tilt [º].

As previously presented, the sol-air temperature is used to estimate the heat gains on external wall and roof, and it considers the effects of outdoor air temperature and incident solar radiation, being calculated using equation 14 [7],

$$t_{sol} = t_{ext} + \frac{\alpha I_T}{h_0} - \varepsilon \frac{\Delta R}{h_0} \quad (14)$$

where:

t_{sol} – sol-air temperature [ºC];
t_{out} – outdoor temperature [ºC];
α – absorptivity of surface for solar radiation [-];
I_T – solar total irradiance [W/m²];
h_0 – coefficient of heat transfer by convection at outer surface [W/m²K];
ε – hemispherical emittance of surface [-];
ΔR – difference between long-wave radiation incident on surface from sky and surroundings and radiation emitted by blackbody at outdoor air temperature [W/m²].

According to ASHRAE Handbook [7], the absorptivity value α is defined to 0.45 for light surfaces and 0.90 for dark surfaces or when no other information is available. For the convection coefficient at the outer surface, h_0, is considered a value of 17 W/(m²K), while it is assumed that hemispheric emittance, ε, is 1. The difference between the reflected radiation that falls on the surface and the radiation emitted by the black body, ΔR, is 63 W/m² on the horizontal surfaces and null (0 W/m²) for the vertical surfaces.

The solar heat gain factor, SHGF, is defined as the fraction of the total irradiance, I_T, that is transmitted directly into the interior of space, I_{trans}, or absorbed by the glass, I_{abs}. After the irradiance is absorbed by the glass, only a fraction, N_i, is transmitted into the space. This factor is used in the calculation of the heat gain from radiation transmitted through the windows and is determined using equation 15 [7].

$$SHGF = I_{trans} + N_i \cdot I_{abs} \quad (15)$$

where:

SHGF – solar heat gain factor [W/m²];
I_{trans} – transmitted irradiance [W/m²];
N_i – inward heat transfer fraction [-];
I_{abs} – absorbed irradiance [W/m²]

The fraction of the heat absorbed towards the space interior, N_i, is directly influenced by the type of glass used. According to ASHRAE Handbook [7], when no data is available, it can be

applied the reference glass value of 0.267 [7]. The irradiance transmitted and absorbed by the glass is determined using equations 16 and 17 [7], respectively. The thermal transmission coefficients, t_j, and thermal absorption coefficients, a_j, are parameters defined according to the type of glass, that can be found in the ASHRAE Handbook [7].

$$I_{trans} = I_D \sum_{j=0}^{5} (t_j \cdot \cos^j \theta) + 2 \cdot I_d \sum_{j=0}^{5} \left(\frac{t_j}{j+2}\right) \quad (16)$$

$$I_{abs} = I_D \sum_{j=0}^{5} (a_j \cdot \cos^j \theta) + 2 \cdot I_d \cdot \sum_{j=0}^{5} \left(\frac{a_j}{j+2}\right) \quad (17)$$

where:

I_{trans} – transmitted irradiance [W/m²];
I_{abs} – absorbed irradiance [W/m²];
I_D – direct irradiance [W/m²];
I_d – sum of diffuse and reflected irradiance [W/m²];
t_j – glass transmission coefficients[-];
a_j – glass absorption coefficients[-];
θ – incident angle [º]

3.2. COMPUTATIONAL MODELLING

The solar radiation model was implemented in a computational program developed in Python, allowing for the integration of the proposed equation across various scenarios. Python is an interpreted, object-oriented and high-level programming language with dynamic semantics. Its simplicity, ease to learn syntax emphasizes readability and, consequently, reduces program maintenance costs. Furthermore, Python supports modules and packages, which encourages program modularity and code reuse [12].

The data used for modelling solar radiation follows the previously presented methodology. The solar radiation calculation algorithm requires input data regarding three key aspects: Date & time; Location and Surfaces, as shown in Figure 3. From the date and time, parameters such as the hour, day since the start of the year and month can be obtained. The month is used to retrieve values for apparent solar irradiation, A_{sl}, atmospheric extinction coefficient, B, sky diffuse factor, C, and solar declination, δ_{solar}, by searching the tables available in ASHRAE Handbook [7]. The location data includes latitude, longitude and time zone, while surface data determine orientation and tilt.

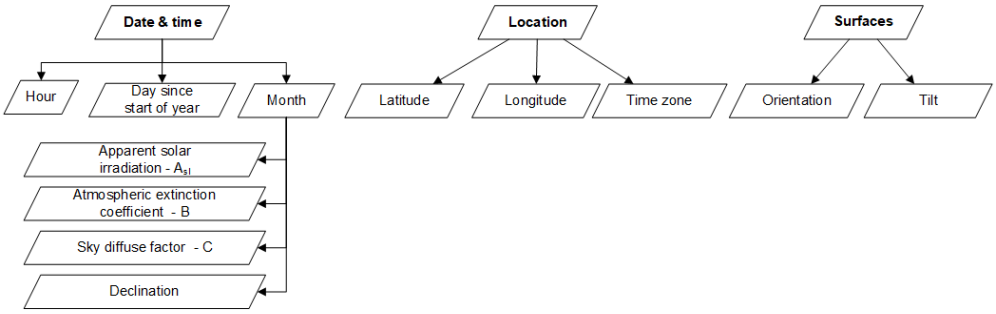

Figure 3. Necessary data for solar radiation calculation

The developed computational model can be used by an user or an application, being necessary to provide the follow input arguments: date and time as datetime object; the latitude, longitude, time zone and surface tilt as a numerical data type (latitude, longitude and surface tilt must be in degrees); the surfaces orientation defined as strings indicating the cardinal directions (ex.: N, S, E, NE, etc…). Then, it is converted to corresponding orientation angle in degrees with a function as shown in Figure 4. This function employs a match-case structure to compare the input direction against predefined cardinal points, reading the argument of the function, and assign the corresponding angle (*orient_deg* variable), where south is 0º, east is -90º and west is 90º. If the input does not match any predefined direction, the function defaults to an angle equivalent to the south orientation (line 58-59), as this represents the worst-case scenario for locations in northern hemisphere.

```
24  def convert_orient_str_deg(orient_str: str):
25      match orient_str:
26          case "N":
27              orient_deg = -180
28          case "NNE": ···
30          case "NE": ···
32          case "ENE": ···
34          case "E":
35              orient_deg = -90
36          case "ESE": ···
38          case "SE":
39              orient_deg = -45
40          case "SSE": ···
42          case "S":
43              orient_deg = 0
44          case "SSO": ···
46          case "SO": ···
48          case "OSO": ···
50          case "O":
51              orient_deg = 90
52          case "ONO": ···
54          case "NO": ···
56          case "NNO": ···
58          case _:
59              orient_deg = 0
60      return orient_deg
```

Figure 4. Function to convert orientation as a string to degrees in Python

The developed computational model implements the equations detailed in section 3, through dedicated programming functions. For instance, Figure 5 presents the function that computes the solar altitude based on equation 5. This function receives latitude, solar declination and the solar hour angle as input parameters and returns the value of solar altitude in radians. Non-calculated values angles, such as latitude or declination, are converted to radians. The solar hour angle is determined using a specific function, that returns an angle in radians, avoiding the need to convert it into radians later. The native Math library is required to compute trigonometric functions. After computing the sine of solar altitude, the angle of solar altitude is obtained using the inverse sine (*asin* – line 14) function, ensuring that the output remains in radians. A similar methodology was applied to implement all equations within the module.

```python
def calc_solar_altitude(latitude, declinacao_solar, solar_hour_angle):
 # Calculates the solar altitude [sl_alt], in radians, based on latitude, solar declination and solar hour angle,
 # Latitude - In degrees
 # Solar_declination - In degrees
 # Solar hour angle - In radians (calculated from the "calc_solar_hour_angle" function)

 latitude_rad = math.radians(latitude)
 declinacao_solar_rad = math.radians(declinacao_solar)

 sen_sl_alt = (math.cos(latitude_rad) * math.cos(declinacao_solar_rad) * math.cos(solar_hour_angle)
               + math.sin(latitude_rad) * math.sin(declinacao_solar_rad))
 sl_alt = math.asin(sen_sl_alt)

 return sl_alt
```

Figure 5. Function to calculate solar altitude in Python

After developing the functions necessary to compute all equations, it is created a function that implement the main algorithm and all functions that compute the individual functions. For example, Figure 6 illustrates the function that encases all functions needed to compute the solar heat gain factor, that will be used to estimate the heat gains on windows. The application of modular programming makes to code more structured, readable, reusable and easier to maintain and allows that different programs or users can use only specific functions in specific applications.

```python
def calc_solar_heat_gain_factor_all(data_hora, longitude, TZN, latitude, orient_str, sf_incl, rho_g=0.2):
    (...)

    solar_time = calc_solar_time(hour, longitude, TZN, ET)

    ang_hora_solar = calc_ang_hora_solar(solar_time)
    sl_alt = calc_solar_altitude(latitude, declinacao_solar, ang_hora_solar)
    sl_az = calc_solar_azimuth(latitude, declinacao_solar, sl_alt, ang_hora_solar)
    sl_sf_incid_ang = calc_solar_surface_incident_angle(sl_alt, sl_az, sf_orient, sf_incl)

    I_DN = calc_EDN(A, B, sl_alt)
    I_D = calc_ED(I_DN, sl_sf_incid_ang)
    I_ds = calc_E_ds(C, sl_sf_incid_ang, I_DN, sf_incl)
    I_dg = calc_E_dg(C, I_DN, sl_alt, rho_g, sf_incl)

    SHGF = solar_heat_gain(sl_sf_incid_ang, I_D, I_ds + I_dg)

    return SHGF
```

Figure 6. Set of functions to calculate solar heat gain factor

In opposite to the solar heat gain factor, the sol-air temperature is computed from the data of the total solar irradiance and the outdoor air temperature. This would require introducing weather data into the solar radiation module, which falls beyond the scope of this module and this paper. Instead, a function is developed to estimate the total solar irradiance by implementing the corresponding equations in the code, as presented in Figure 6. The Figure 7 illustrates the algorithm used to estimate both the total solar irradiance and the solar heat gain factor, indicating also the required data for each equation/function.

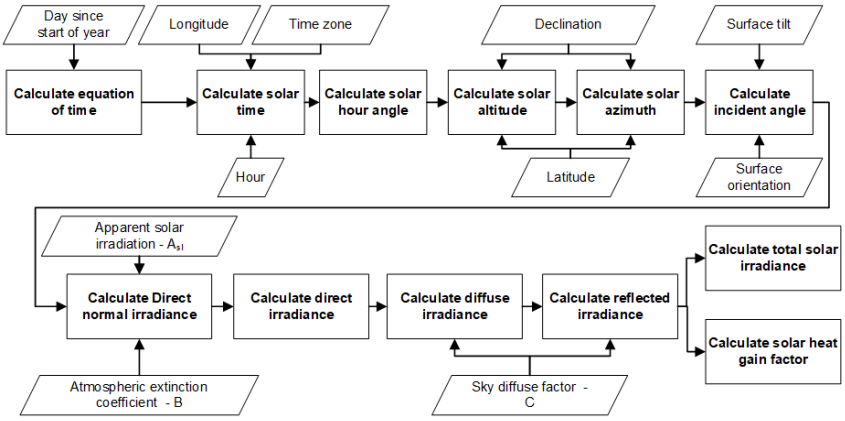

Figure 7. Sequence of total solar irradiance and solar heat gain factor calculation

This module can be imported by users to estimate solar radiation via the command line. However, it is intended to include this module in applications, such as those for calculating the thermal load in buildings, as shown in Agostinho et al., (2024) [9].

4. VALIDATION

The computational module developed to estimate solar radiation incident on a surface was validated carrying out simulation tests considering the solar radiation on four surfaces, each one oriented towards the main cardinal directions. In these tests, the model computed solar radiation over an entire year, estimating the maximum values achieved in each month, for each surface. Furthermore, the developed model calculated the hourly radiation for the design day, defined as the day when thermal loads for a given space are at their peak. The results were compared with those obtained using the commercial program, Hourly Analysis Program (HAP) [13] version 4.8. Additionally, after validation, the solar radiation model was further tested and evaluated for multiple locations.

The HAP is a program developed by Carrier and it is widely used for the design Heating, Ventilation and Air Conditioning (HVAC) systems. This program allows the determination of thermal loads in a building and estimate the energy consumed. Additionally, it calculates the solar radiation incident on the building surfaces and incorporates this information into thermal load calculations, providing reports with detailed data. This allows the solar radiation results estimated by this commercial program to be used to validate the developed computational model.

The validation tests were performed considering a building located in Lisbon, with latitude 38,8 ºN, longitude 9.1 ºW and in the time zone of Greenwich Mean Time (GMT+0).

After defining the building location and considering that the vertical surfaces were oriented towards the north, east, south and west directions, respectively, the total solar irradiance was calculated using both the developed module and the HAP, for the design day of the month, throughout the year. Figure 8 shows the maximum solar irradiance in each month calculated by the developed model, in Python, and by HAP.

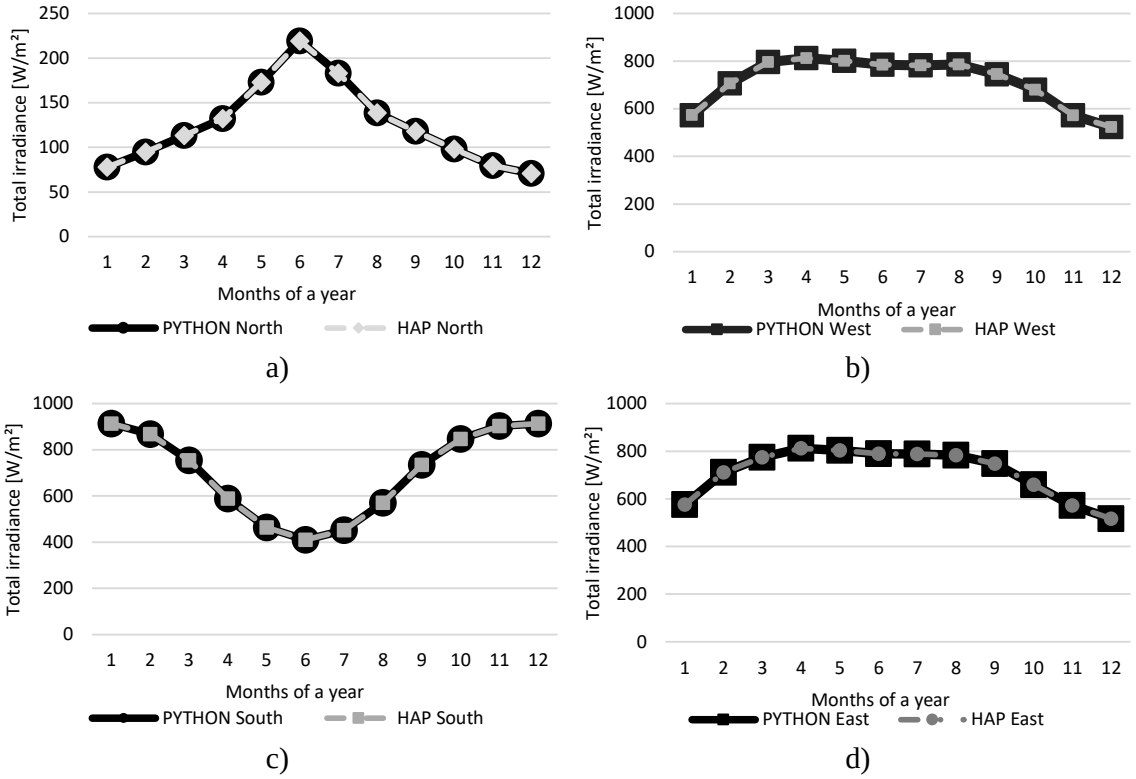

Figure 8. Monthly maximum total solar irradiance for 12 months to a) North, b) West, c) South and d) East

Analysing the Figure 8, it is observed that the surface towards to the north orientation reaches the maximum irradiance of 219 W/m² in June; For surfaces facing east and west, the peak irradiance of 812 W/m² occurs in April; and in the south-facing surface, the maximum irradiance of 913 W/m² occurs in January. The deviation between the Python module and HAP is less than 0.1%. It should be noted that the annual irradiance profile for the south-facing orientation exhibits an opposite trend compared to other orientations, with a maximum in January and a minimum in June. This behaviour is mainly attributed to the solar altitude angle, which is lower in January and higher in June, due to the variation in the solar declination angle, as computed by the equation 5. Consequently, this results in a smaller incidence angle of solar radiation in January and a greater angle in June, in accordance with equation 8.

When comparing the maximum solar irradiance for all month, it is also essential to evaluate the irradiance absorbed by surfaces at each hour of a given day, particularly on the day when maximum irradiance occurs. Analysing the Figure 8, it is possible to observe that the maximum irradiance occurs in different months depending on the orientation.

To utilise this module for the computation of thermal loads in buildings, the python module is applied to the day on which the maximum thermal load for a given space is observed. For this

purpose, a test was conducted using a model with four walls, each with a window, oriented towards north, west, south and east. The characteristics of the walls and windows are detailed in Table 1. These parameters were introduced in HAP to estimate the thermal loads in the building along the year. The results indicate that the maximum thermal load in the space occurs in September at 3 p.m. This analysis enables the characterisation of combined effect of solar irradiance from all orientations on thermal loads of building, although there is some effect due to variation of outdoor temperature.

Type	Orientation	Area [m²]	U	α (wall) /SC (window)
Wall	North, West, South, East	50	0.24	0.45
Window	North, West, South, East	10	1.6	0.61

Table 1. Characteristics of wall and windows for thermal loads analysis

The analysis of the total irradiance evolution on the day of the highest thermal load, which occurred in September, was estimated using Python program and with the HAP. The results are presented in Figure 9.

Considering the surfaces orientation and the geographic location in the northern hemisphere, the irradiance observed from sunrise until 12.p.m on west-facing surface and from 12 p.m. until sunset in east orientation is the same as that observed in north orientation, in those hours. This indicates that, during these hours, irradiance is predominantly diffuse. Outside these periods, the irradiance is primarily direct. The irradiance recorded on the south-facing surface from sunrise to sunset results from a combination of direct and diffuse components.

Analysing the obtained data, it is observed that in the north orientation, the maximum irradiance was recorded at 12 p.m., reaching 117.9 W/m² with a maximum deviation of 0.2%, occurring at 7 a.m., corresponding to the first hour of solar radiation incidence. On the west-facing surface, the maximum irradiance was obtained at 4 p.m., with a value of 744.7 W/m², while the highest deviation of 4.9% occurred at 12 p.m., corresponding to the first hour that direct irradiance was obtained. The maximum irradiance in the south-facing orientation was also observed at 12 p.m., with a value of 734.5 W/m², and the maximum deviation of 0.1% occurred at 5 p.m., corresponding to the last hour of solar radiation. Finally, the maximum irradiance in the east-facing surface was reached at 8 a.m., with a value of 747.8 W/m², and the highest deviation of 0.3% occurred at 12 p.m., which corresponds to the last hour that direct irradiance was obtained.

Overall, it is observed that, in all orientations, the highest deviations occurred during periods of greater variation in solar radiation. Nevertheless, these deviations remain relatively low, indicating a strong agreement in the irradiance calculations throughout the day.

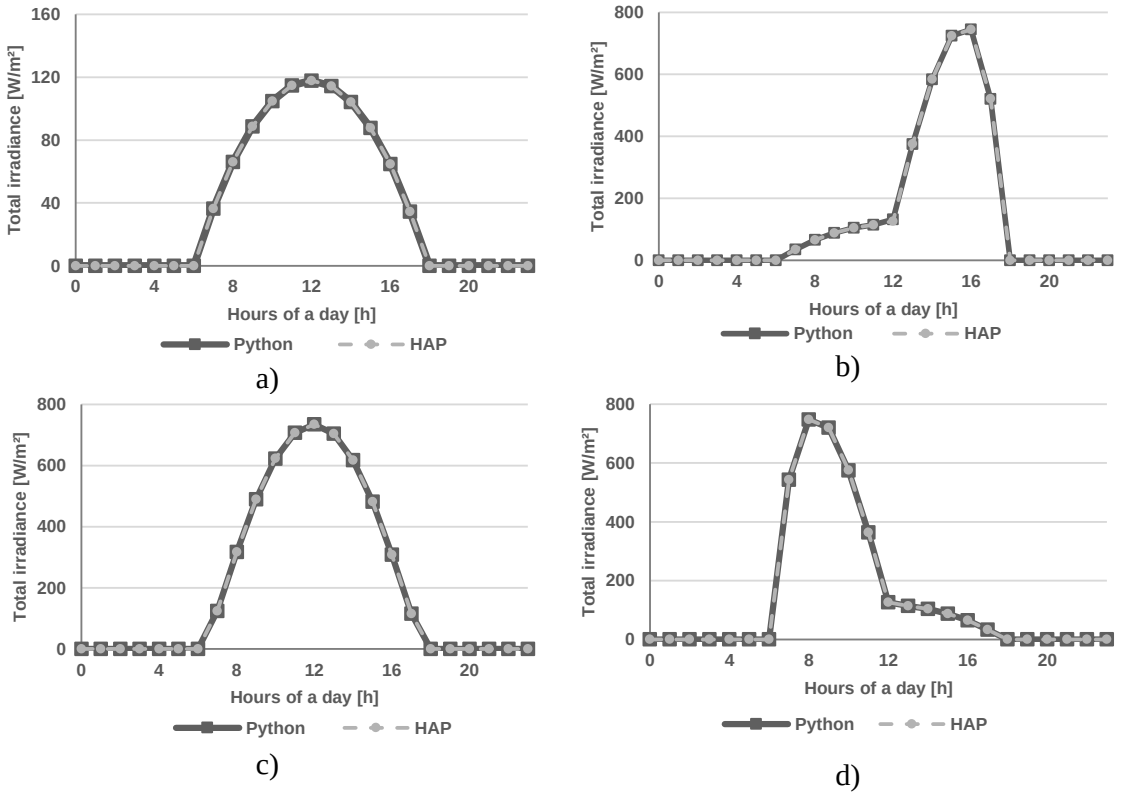

Figure 9. Hourly total solar irradiance for maximum thermal load day to a) North, b) West, c) South and d) East

In order to validate the radiation model at different locations, the same tests were carried out in four different cities: Lisbon, Portugal; Paris, France; Stockholm, Sweden and Houston, Texas, U.S. As illustrated in Figure 3, solar radiation is influenced by the latitude, longitude and time zone of a given location. Table 2 presents the latitude, longitude and corresponding time zone of each city, adopting the convention that westward longitudes are positive, while eastward longitudes are negative.

City, Country	Latitude	Longitude	Time zone
Lisbon, Portugal	38.8 ºN	9.1 ºW	GMT 0
Paris, France	48.5 ºN	2.1 ºE	GMT -1
Stockholm, Sweden	59.4 ºN	18.0 ºE	GMT -1
Houston, Texas, U.S.	30.0 ºN	95.4 ºW	GMT 6

Table 2. Geographical data and time zone data of Lisbon, Paris, Stockholm and Houston.

Figure 10a shows the hourly solar irradiance as a function of solar time for the day with the highest thermal load, considering a south-facing orientation. Figure 10b shows the same relationship for a day in December. In the developed model, the use of solar time eliminates the influence of equation 4, which accounts for the calculation of solar time, thereby ensuring

that solar irradiance is independent of local longitude and time zone. Consequently, variations in location affect only the latitude.

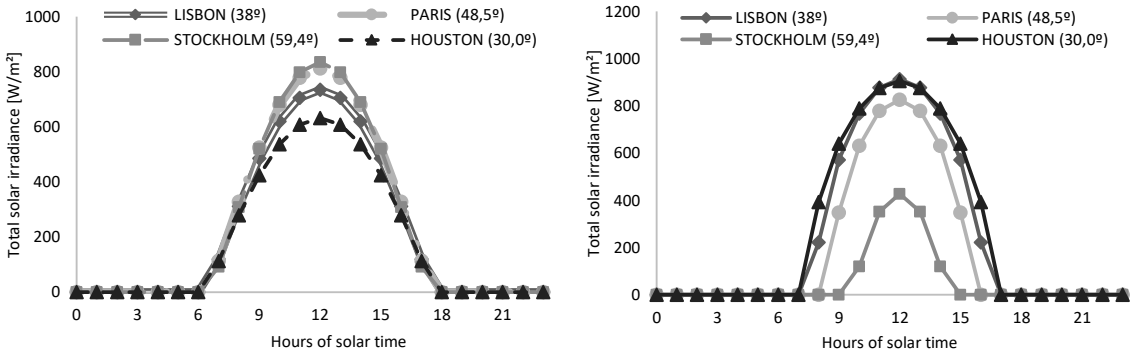

Figure 10. Total solar irradiance for south orientation for various locations in a) September and b) December as a function of solar time

The first notable aspect in Figure 10a is that the duration of solar exposure is identical for all locations. This occurs because in September is the equinox, during which day and night have equal duration regardless of geographical position. The irradiance in September (Figure 10a) is higher at locations with greater latitude. This is due to the fact that higher latitude correspond to lower solar altitude (equation 5), which results in a lower incidence angle (equation 8). As demonstrated in equation 11, a lower incidence angle leads to higher direct irradiance.

Analysing Figure 10b, the duration of solar exposure is greater for locations at lower latitudes. In this case, the graph represents the winter solstice. The irradiance in December (Figure 10b) is higher for locations with lower latitude. This occurs because, in equation 5, the solar declination is negative, whereas it was zero in September. Consequently, in December, the reduction in solar altitude is less noticeable for location with lower latitude. In other words, locations at higher latitudes experience a lower altitude angle. From equation 10, it follows that direct normal irradiance decreases as the solar altitude angle decreases.

After analysing solar radiation as a function of solar time, which depends solely on latitude, it is also necessary to evaluate solar radiation based on local time. This means that equation 4 is considered. This equation introduces the effect of local longitude and time zone of each location. Figure 11 shows the hourly irradiance as function of local time for September (Figure 11a) and December (Figure 11b). The noticeable difference compared to Figure 10 is a time shift in the irradiance profile throughout the day. This results from the l_{st}-l_{local} term in equation 4, indicating that irradiance is influenced by displacement between the local longitude and the standard meridian longitude, rather than by longitude alone. However, the maximum irradiance remains approximately the same.

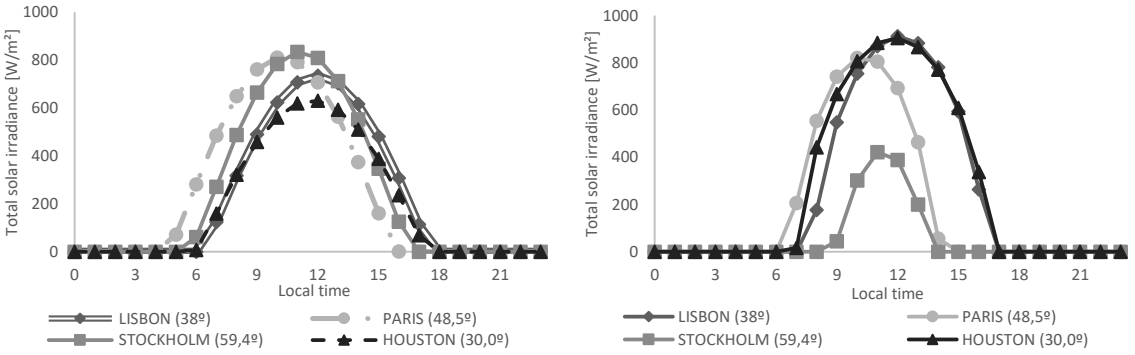

Figure 11. Total solar irradiance for south orientation for various locations in a) September and b) December as a function of local time

5. CONCLUSIONS

The presented study aimed to develop a computational model for incident solar radiation and evaluate its application in the calculation of thermal loads in buildings. This was achieved through the implementation of equations that compute solar time, solar position angles and estimate the solar radiation on an oriented surface, hourly, throughout the year. For radiation on opaque elements such as walls and roofs, the effect of solar radiation is considered through sol-air temperature. In the case of radiation on windows, the impact of solar radiation was considered through solar heat gain factor.

These calculations were developed as a module in Python, where each equation was implemented as an individual function. The model relies on input data such as the building's geographical location, date and time, and the characteristics of the surfaces such as orientation and tilt. This module can operate as a standalone tool for direct solar radiation calculations. On the other hand, this is intended to be used on thermal load calculation program such as presented in Agostinho et at., (2024) [9].

The validation process involved comparing the results obtained with those generated by a commercial reference program, HAP. For the maximum monthly irradiance calculated over a year in Lisbon, the highest observed deviation was below 0,1%. The maximum irradiance occurred in January for south-facing surfaces, in April for east and west-facing surfaces, and in June for north-facing surfaces. The maximum thermal load of the space was considered to account for the contribution of irradiance from all orientations. The observed deviations remained below 5%, demonstrating the composition of direct and diffuse irradiance in the total incident solar irradiance.

Subsequently, the effect of location on solar irradiance was evaluated by considering both solar time and local time. When using solar time, irradiance was found to depend solely on the latitude, influencing both the peak irradiance and the duration of solar exposure depending on the specific time of year. In contrast, considering local time includes also the effect of longitude and time zone, introducing a time shift in the irradiance profile throughout the day

compared to the irradiance profile based on solar time.

In summary, the presented paper enables the modelling of solar radiation, with results demonstrating a strong correlation with those obtained from other software tools.

REFERENCES

[1] J. An, D. Yan, S. Guo, Y. Gao, J. Peng, and T. Hong, "An improved method for direct incident solar radiation calculation from hourly solar insolation data in building energy simulation," *Energy Build*, vol. 227, p. 110425, Nov. 2020, doi: 10.1016/J.ENBUILD.2020.110425.

[2] F. J. S. De La Flor, R. O. Cebolla, J. L. M. Félix, and S. Á. Domínguez, "Solar radiation calculation methodology for building exterior surfaces," *Solar Energy*, vol. 79, no. 5, pp. 513–522, Nov. 2005, doi: 10.1016/J.SOLENER.2004.12.007.

[3] B. M. Marino, N. Muñoz, and L. P. Thomas, "Calculation of the external surface temperature of a multi-layer wall considering solar radiation effects," *Energy Build*, vol. 174, pp. 452–463, Sep. 2018, doi: 10.1016/J.ENBUILD.2018.07.008.

[4] S. Pal, B. Roy, and S. Neogi, "Heat transfer modelling on windows and glazing under the exposure of solar radiation," *Energy Build*, vol. 41, no. 6, pp. 654–661, Jun. 2009, doi: 10.1016/J.ENBUILD.2009.01.003.

[5] C. Demain, M. Journée, and C. Bertrand, "Evaluation of different models to estimate the global solar radiation on inclined surfaces," *Renew Energy*, vol. 50, pp. 710–721, Feb. 2013, doi: 10.1016/J.RENENE.2012.07.031.

[6] A. K. Yadav and S. S. Chandel, "Tilt angle optimization to maximize incident solar radiation: A review," *Renewable and Sustainable Energy Reviews*, vol. 23, pp. 503–513, Jul. 2013, doi: 10.1016/J.RSER.2013.02.027.

[7] ASHRAE, *1997 ASHRAE Handbook: Fundamentals*. in ASHRAE Handbook Fundamentals. 1997.

[8] ASHRAE, *2021 ASHRAE handbook: Fundamentals*. 2021.

[9] A. Agostinho, F. Carreira, and C. Casaca, "Desenvolvimento de uma aplicação computacional para o cálculo de cargas térmicas em edifícios," in *International Congress on Engineering (ICEUBI 2024) Sustainability and Resilience: Innovation and Solutions, Covilhã, Universidade da Beira Interior, Portugal, 27-29 novembro*, 2024. doi: /10.25768/9239-05-0.

[10] D. Y. Goswami, *Principles of Solar Engineering*, Third edition. CRC Press, 2015. doi: 10.1201/b18119.

[11] J. A. Duffie and W. A. Beckman, *Solar engineering of thermal processes*, Fourth Edition. Wiley, 2013.

[12] "What is Python? Executive Summary | Python.org." Accessed: Mar. 21, 2025. [Online]. Available: https://www.python.org/doc/essays/blurb/

[13] Carrier, "HAP v4.8," 2013.

SYMCOMP 2025
Lisbon, 10-11 April 2025

ANALYTICAL AND NUMERICAL STUDY OF CARBON/EPOXY COMPOSITE PLATES SUBJECTED TO UNIAXIAL AND BIAXIAL LOADS

Simão Gamito[1*] and Afonso Leite[2]

1: CIMOSM, ISEL – Centro de Investigação em Modelação e Optimização de Sistemas Multifuncionais
Instituto Superior de Engenharia de Lisboa
Instituto Politécnico de Lisboa
Rua Conselheiro Emídio Navarro, 1 1959-007 Lisboa, Portugal
e-mail: s.gamito@sapo.pt

2: CIMOSM, ISEL – Centro de Investigação em Modelação e Optimização de Sistemas Multifuncionais
Instituto Superior de Engenharia de Lisboa
Instituto Politécnico de Lisboa
Rua Conselheiro Emídio Navarro, 1 1959-007 Lisboa, Portugal
e-mail: afonso.leite@isel.pt web: http://www.isel.pt

Keywords: symbolic computation, finite element method, biaxial loading, composite plates, carbon fibre, classical lamination theory

Abstract. *In this work analytical and numerical approaches are taken to study the mechanical behavior of carbon fiber-based composite plates with an epoxy matrix. Different stacking sequences are studied, including non-symmetric and non-balanced. Also uniaxial and biaxial loadings are employed and their effect investigated. Analytic calculation of stresses and strains is attained by using the Classical Lamination Theory, implemented in the symbolic computation software MAPLE. The first-ply failure is studied using the failure criteria of Maximum Stress, Tsai-Hill, Tsai-Wu and Hashin-Rotem. Numerical validation is made by using the Finite Element Method (FEM) by means of FEM commercial software, using (1) ANSYS Parametric Design Language (APDL) with User programmable Features for non builted-in criteria and (2) using ANSYS Workbench suite. Comparison of the three approaches is made and the expected tension-extension and tension-bending coupling effects are discussed.*

SYMCOMP 2025
Lisbon, 10-11 April 2025

SIMULATING STRESSES AND STRAINS IN SOLID MECHANICS DIRECTLY FROM IMAGES USING CONVOLUTIONAL NEURAL NETWORKS

Beatriz Vieira[1*], José A. Rodrigues[2], Saurabh Deshpande[3] and Stéphane Bordas[4]

1: Department of Mathematic
Lisbon School of Engineering
Polytechnic University of Lisbon
R. Conselheiro Emídio Navarro 1, 1959-007 Lisboa
e-mail: A44960@alunos.isel.pt,
2: Department of Mathematic
Lisbon School of Engineering
Polytechnic University of Lisbon
R. Conselheiro Emídio Navarro 1, 1959-007 Lisboa
e-mail: jose.rodrigues@isel.pt,
3: Department of Engineering
Indian Institute of Technology Madras
Indian Institute Of Technology, Chennai, Tamil Nadu 600036, India
e-mail: saurabhd@alumni.iitm.ac.in,
4: Department of Engineering
Faculty of Science, Technology and Medicine
University of Luxembourg
2 Av. de l'Universite L, 4365, Esch-Belval Esch-sur-Alzette, Luxembourg
e-mail: stephane.bordas@uni.lu

Keywords: Deformation Prediction, Convolutional Neural Networks, Image Analysis

Abstract. *In this paper, we introduce a new method for predicting how solid materials deform and the stresses they experience directly from images. Instead of using traditional numerical methods that solve complex equations, our approach uses convolutional neural networks (CNNs) to learn the mapping from applied forces to the resulting deformations. We built a dataset that includes both the visual information of the material and the corresponding force and deformation data. Our experiments show that the CNN model can recognize patterns in the images and accurately predict deformations based on the strength and location of the forces. This simple, data-driven method offers a more efficient way to simulate material behavior and could be used for real-time analysis in engineering applications.*

DOI:10.5281/zenodo.15164468

1 INTRODUCTION

The finite element method (FEM) has long been the standard for simulating stress and strain in complex materials and structures. However, its computational cost and simulation time can become very large, particularly for large-scale or real-time applications. In contrast, Convolutional Neural Networks (CNNs) have emerged as a promising alternative, capable of processing extensive datasets and autonomously learning the intricate patterns that govern material behavior.

In this paper, we use CNNs to predict stress and strain directly from image data. By converting images into formats suitable for deep learning, our approach eliminates the need for the computationally intensive procedures typically associated with traditional FEM, while enabling the direct calculation of deformations from images. This method not only accelerates analysis but also provides a more direct means of assessing deformations.

We describe the network architecture and training methodology tailored for this application, and offer a comparative analysis of CNN performance versus traditional FEM simulations. Our results demonstrate that the deformations predicted from images exhibit a high degree of accuracy, along with significant improvements in computational efficiency. These results enable faster, image-based assessments of material behavior, with potential uses in real-time monitoring and design optimization.

The remainder of this paper is organized as follows: Sections II and III review the related literature on the MAgNET deep learning framework and the process of creating a mesh from an image, respectively; Section IV presents experimental results and comparative analyses; and Section V concludes with discussions on future research directions.

2 MAgNET DEEP LEARNING FRAMEWORK

In this chapter, we introduce the MAgNET deep learning framework, a novel approach that extends conventional U-Net architectures to mesh-based simulations using graph neural networks. We detail the design of its core components: the multi-channel aggregation (MAg) layer, which adapts convolution operations to irregular graph structures, and the graph pooling and unpooling layers, which efficiently capture hierarchical features in non-grid data. This chapter builds on the foundational work by Deshpande et al. [1] presented in their paper *MAgNET: A Graph U-Net Architecture for Mesh-Based Simulations*.

The MAgNET graph neural network is a type of graph U-Net and serves as an extension to the popular convolution-based U-Net architectures.

The graph U-Net is composed of several key components: aggregation (similar to convolution), pooling, unpooling, and concatenation layers, all of which have been adapted to handle general, non-grid structures for both inputs and outputs. Its architecture is divided into two main stages: encoding and decoding. During the encoding stage, the network first applies one or more aggregation layers, which work as the equivalent of convolution layers in standard U-Net models. This is followed by a graph pooling layer, which contracts the graph and reduces its complexity by downsampling the problem. This process

of aggregation followed by pooling is repeated multiple times until the desired level of contraction is achieved. At the most condensed representation of the graph, additional aggregation layers refine the features before transitioning to the next stage. The decoding stage then reverses this process. At each step, a graph unpooling layer expands the graph structure, followed by one or more aggregation layers that refine the information. This continues until the graph reaches its original size. At the final step, the last aggregation layer applies a linear activation function to generate the final output.
This structure allows the graph U-Net to effectively capture hierarchical relationships within graph-structured data, mirroring the way traditional U-Net models process images but adapting the approach to more flexible, non-grid-based topologies.
Formally, the Graph U-Net network, $\mathcal{G}$, is constructed as follows. The input layer, d^0, consists of N nodes, where each node is represented by a vector of input values (features or channels) of fixed length c^0. From this input, successive layers d^l are added to form the U-Net architecture.
Each layer d^l is connected to the previous layer d^{l-1} through the transformation:

$$d^l = T^l(d^{l-1}; \theta^l) \tag{1}$$

where θ^l represents the trainable parameters (such as weights and biases, $\theta^l = k^l \cup b^l$), and $T^l(\cdot)$ is one of the three transformations: *MAg()*, *gPool()*, or *gUnpool()*, which will be defined in detail later. Additionally, the model includes remote concatenation links between corresponding layers in the encoding and decoding stages.
The output layer, d^L, follows the same mesh format as the input layer but may have a different number of channels, c^L. Finally, the Graph U-Net can be formally expressed as a parameterized transformation:

$$\mathcal{G}(d^0, \theta) = d^L = T^L(T^{L-1}(T^{L-2}(...); \theta^{L-1}); \theta^L), \tag{2}$$

where

$$\theta = \bigcup_{l=1}^{L} \theta^l \tag{3}$$

represents the concatenated vector of all network parameters.
The parameters of the Graph U-Net are optimized through supervised learning by training on a dataset with known input-output pairs. The training dataset is represented as:

$$D_{tr} = \{(f_1, u_1), ..., (f_{M_{tr}}, u_{M_{tr}})\}, \tag{4}$$

where the data follows a mesh structure. The learning process aims to minimize the mean squared error (MSE) between the predicted outputs and the true outputs. This is achieved by optimizing the following loss function:

$$L(D_{tr}, \theta) = \frac{1}{M_{tr}} \sum_{m=1}^{M_{tr}} \|\mathcal{G}(f_m, \theta) - u_m\|^2. \tag{5}$$

This function measures the difference between the predicted values, $\mathcal{G}(f_m, \theta)$, and the actual target values, u_m, across all training samples. The optimization process updates the model's parameters, θ, to minimize this error and improve the accuracy of predictions [1].
The optimal parameters, θ^*, are obtained by solving the following minimization problem:

$$\theta^* = \arg\min_{\theta} L(D_{tr}, \theta). \tag{6}$$

In this work, we focus on sparse graphs derived from data that is spatially organized as meshes. These meshes can be one-dimensional (1D), two-dimensional (2D), or extend to higher dimensions, with an arbitrary connection topology.
The graph structure is represented using a symmetric, square, Boolean adjacency matrix A, where the order of A corresponds to the number of nodes in the original mesh. To simplify notation, we assume that each node (vertex) is self-connected, meaning it has a loop, which ensures ones along the diagonal of A.
This self-loop assumption simplifies the formulation of various graph operations used in this study, including computing the k-th power of the adjacency matrix A and selecting pooling subgraphs.

2.1 Multi-channel Aggregation (MAg) layer

The proposed MAg layer is a multi-channel local aggregation layer designed for graph-structured data. It extends the standard convolutional layer in CNNs, which is typically constrained to grid-based data due to its shareable convolution window. Instead, the MAg layer employs fully trainable, local weighted aggregations based on a message-passing scheme, where each node's neighborhood is determined by the graph connectivity (adjacency matrix).
By incorporating multiple channels, the MAg layer enhances the network's ability to capture nonlinearities. In this setup, each node holds a vector of features, effectively creating multiple channels within the same graph structure. The transformation from input to output multi-channel graphs is achieved by performing multiple MAg aggregations across vector data, generating corresponding output components. While the input and output channels of the network usually have predefined meanings, the number of channels in hidden layers is flexible and can be chosen by the network designer.
Formally, the MAg layer is defined as a parameterized transformation between input and output nodes:

$$d_{i,\alpha}^{l+1} = \sigma\left(b_{i,\alpha}^{l+1} + \sum_{\beta=1}^{c_l} \sum_{j \in N_i} k_{i,j,\alpha,\beta}^{l+1} d_{j,\beta}^{l}\right), \tag{7}$$

where $N_i = \{j \mid A_{ij} = 1\}$ represents the neighborhood of node i, and α and β denote the output and input channels, respectively. The parameters $k_{i,j,\alpha,\beta}^{l+1}$ and $b_{i,\alpha}^{l+1}$ are trainable weights and biases. Unlike traditional convolutional layers, these kernel parameters are not shared, they can be trained independently for each aggregation window, providing greater flexibility in the learning process.

2.2 Graph pooling and unpooling layers

The approach used in this network divides the graph into disjoint cliques (i.e., fully connected subgraphs) and contracts each clique into a single vertex, with new edges representing previously connected cliques. The partitioning is performed statically during the graph U-Net construction and remains independent of the input data.
Given an input graph G, defined by a set of vertices S, and an adjacency matrix A, it is generated a partition of S into N non-overlapping cliques $G_1, G_2, \ldots, G_N$, such that:

$$S = \bigcup_{i=1}^{N} S_i, \quad \forall i,\ \forall j,k \in S_i, \quad A_{jk} = 1, \quad \text{and} \quad S_i \cap S_j = \emptyset \text{ for } i \neq j. \tag{8}$$

Each set S_i represents the nodes belonging to the respective subgraph G_i. The resulting pooled graph $\tilde{G}$ consists of vertices:

$$\tilde{S} = \{1, 2, \ldots, N\}, \tag{9}$$

with edges defined by the pooled adjacency matrix $\tilde{A}$. The pooling operation is then performed as:

$$d_{i,\beta}^{l+1} = \text{aggr}_{j \in S_i}\, d_{j,\beta}^{l}, \tag{10}$$

where the aggregation function (aggr) can be max, min, or average. Importantly, the number of channels remains unchanged, as pooling is applied independently to each input channel.
Graph pooling can be applied multiple times in the encoding stage of the U-Net. To enable future unpooling operations, after each pooling step, we store the original graph G, adjacency matrix A, and the pooling subgraphs G_i. Then, we update the graph as:

$$G \leftarrow \tilde{G}, \quad A \leftarrow \tilde{A}. \tag{11}$$

Graph unpooling is the inverse operation of pooling, restoring the original topology of the input graph from the corresponding pooling layer. This operation is defined using the previously stored subgraphs G_j with nodes S_j:

$$d_{i,\beta}^{l+1} = d_{j,\beta}^{l}, \quad \forall i \in S_j. \tag{12}$$

Here, the features of node j are replicated to the nodes in S_j, making it analogous to the upsampling operation in CNNs.
Concatenation, also known as skip connections, is a key feature of U-Net architectures. It allows layers in the decoder to access features from the encoder, mitigating vanishing gradient issues and preserving information lost during pooling.
In this framework, concatenation is applied at each unpooling stage by stacking the output of an unpooling layer l with the input of the corresponding pooling layer l':

$$d_{i,c_l+\alpha}^{l+1} = d_{i,\alpha}^{l'}. \tag{13}$$

Here, c_l represents the number of channels in the unpooling inputs, leading to an output with $c_l + c_{l'}$ channels.
During a forward pass of the MAg layer, aggregation occurs locally at each node, meaning information exchange is limited to directly connected nodes in the adjacency matrix A. Nodes that are not directly connected do not exchange information in a single MAg operation.
To facilitate long-distance information flow, it is used a method to increase the support of the MAg operation by considering higher powers of the adjacency matrix, such as A^2 or A^3, effectively expanding the receptive field.
The motivation behind using pooling and unpooling layers is to reduce the effective graph size while preserving important feature information. The pooled graph provides a coarsened representation of the original, where each pooled node aggregates information from multiple parent nodes. This hierarchical representation enables long-range information exchange with fewer MAg layers. Furthermore, nested pooling operations result in an exponential reduction of graph diameter, improving efficiency.

3 IMAGE MESH GENERATION

In this chapter, we present a comprehensive pipeline for image mesh generation, a process that converts pixel-based image representations into structured and unstructured mesh formats. We begin by detailing methods for generating both structured grids, using a uniform lattice based on the image domain, and unstructured grids, which involve adaptive sampling along boundaries and within interiors. We then explore techniques such as Delaunay triangulation to ensure well-formed triangular meshes and apply Laplacian smoothing to enhance mesh quality. This framework is adapted from the methodologies described in the literature [2].
An image can be represented as a 2D array of pixels, each corresponding to a point in a Cartesian coordinate system. For a grayscale image, a mesh can be generated based on the object of interest, allowing for structured representation of its shape.

3.1 Structured and Unstructured Grid Generation

To generate a structured grid, the image domain (W, H) is discretized into a uniform lattice of points spaced at intervals of $\Delta x = \Delta y = 10$, given by:

$$x_i = i \times \Delta x, \quad y_j = j \times \Delta y. \tag{14}$$

Filtered points are extracted using the binary mask, retaining only those satisfying:

$$I_{\text{binary}}(x_p, y_p) = 255. \tag{15}$$

For enhanced flexibility, an unstructured grid is introduced, where boundary points are sampled and distributed evenly along the segmented region. Given an ordered boundary set $B = \{b_1, b_2, \ldots, b_n\}$, new points along the boundary are placed at:

$$\mathbf{p}_i = b_i + t(b_{i+1} - b_i), \tag{16}$$

where $t = \frac{d - \text{current\_length}}{L_i}$ ensures even spacing d. Interior points are sampled via Poisson disk sampling, maintaining minimum distances $d_{\min}$ within the region and d_{boundary} from the boundary.

3.2 Delaunay Triangulation and Laplacian Smoothing

Delaunay triangulation ensures well-shaped triangles by enforcing the circumcircle property: for a given set of points P, no point lies inside any triangle's circumcircle. Given three points p_i, p_j, p_k, the condition is satisfied when:

$$|\mathbf{p}_i - \mathbf{p}_j| \cdot |\mathbf{p}_j - \mathbf{p}_k| \cdot |\mathbf{p}_k - \mathbf{p}_i|. \tag{17}$$

Once triangulated, the mesh quality is refined using Laplacian smoothing. Each interior point $\mathbf{p}_i$ is updated iteratively based on its neighbors $N(i)$:

$$\mathbf{p}_i^{\text{new}} = \frac{1}{|N(i)|} \sum_{j \in N(i)} \mathbf{p}_j. \tag{18}$$

This ensures a well-conditioned mesh while preserving the boundary structure.

4 MATHEMATICAL ANALYSIS OF THE LOSS FUNCTION

The loss function $L(D_{tr}, \theta)$ plays a pivotal role in the supervised learning framework of the Graph U-Net, guiding the model's optimization process. It quantifies the discrepancy between the predicted outputs, $\mathcal{G}(f_m, \theta)$, and the true target values, u_m, across the training dataset. By minimizing this loss, the model iteratively refines its parameters, ultimately converging toward an optimal set, θ^*, that enhances predictive accuracy and generalization.

As shown above, the loss function is defined as:

$$L(D_{tr}, \theta) = \frac{1}{M_{tr}} \sum_{m=1}^{M_{tr}} \|\mathcal{G}(f_m, \theta) - u_m\|^2, \tag{19}$$

where:

- D_{tr} is the training dataset, consisting of M_{tr} input-output pairs: $\{(f_1, u_1), \ldots, (f_{M_{\text{tr}}}, u_{M_{\text{tr}}})\}$,
- f_m is the m-th input feature (in this case, mesh-based data),
- u_m is the corresponding m-th target output,
- $\mathcal{G}(f_m, \theta)$ represents the output of the MAgNET (Graph U-Net) given input f_m and parameters θ,
- θ is the set of all trainable parameters in the network,
- $\|\cdot\|$ denotes the L_2 norm (Euclidean distance),
- The summation is over all M_{tr} training examples,
- The loss is the mean squared error between the network's predictions $G(f_m, \theta)$ and the true outputs u_m.

The goal of training is to find the optimal parameters θ^* that minimize this loss function:

$$\theta^* = \arg\min_{\theta} L(D_{\text{tr}}, \theta) \tag{20}$$

This formulation demonstrates that MAgNET employs a standard mean squared error loss function, commonly used in regression tasks such as predicting displacement fields in mesh-based simulations. The U-Net architecture is integrated through the function G, representing the forward pass through the entire MAgNET Graph U-Net. The loss function computes the mean squared error over all M_{tr} training samples, ensuring the model minimizes the average squared difference between predictions and true values for accurate generalization.
To gain deeper insights into the optimization process, we examine the loss function's behavior by analyzing its convexity and smoothness properties. Understanding these characteristics is crucial for assessing convergence, stability, and overall performance of the optimization algorithm.

4.1 Convexity and Smoothness Analysis

The loss function defined by (19) is inherently non-convex due to the nonlinearity introduced by the activation functions, pooling operations, and learnable parameters in the Graph U-Net. However, in local neighborhoods where gradients are well-behaved, the function may exhibit local convexity [6].
To formally analyze convexity, we examine the Hessian matrix for (19). The Hessian is given by:

$$H = \nabla_\theta^2 L(D_{tr}, \theta). \tag{21}$$

To determine local convexity, we examine the Hessian matrix $\nabla_\theta^2 L$. We will abbreviate $L(D_{tr}, \theta)$ as $L(\theta)$. If the Hessian is positive semi-definite ($\nabla_\theta^2 L \succeq 0$) in a neighborhood, the loss is locally convex there. However, due to the high dimensionality of θ, computing the full Hessian is computationally expensive. Instead, we approximate local convexity using second-order Taylor expansions:

$$L(\theta + \Delta\theta) \approx L(\theta) + \nabla_\theta L \cdot \Delta\theta + \frac{1}{2}\Delta\theta^T \nabla_\theta^2 L \Delta\theta. \tag{22}$$

Local convexity holds if the quadratic term $\frac{1}{2}\Delta\theta^T \nabla_\theta^2 L \Delta\theta \geq 0$ for all $\Delta\theta$. [7]
In neural networks, the Hessian can have both positive and negative eigenvalues, indicating the presence of saddle points and local minima, which confirms the general non-convex nature of the loss landscape. However, certain architectures and regularization techniques, such as weight decay, can promote local convexity in regions of interest.

Theorem 1. *Suppose that the function $\mathcal{G}(f_m, \theta)$ (19) is twice continuously differentiable with respect to θ. Then, the Hessian matrix $\nabla_\theta^2 L$ is locally positive semi-definite.*

Proof. The loss function (19) is a sum of squared differences, which can be rewritten as:

$$L(\theta) = \frac{1}{M_{tr}} \sum_{m=1}^{M_{tr}} \left(\mathcal{G}(f_m, \theta) - u_m\right)^T \left(\mathcal{G}(f_m, \theta) - u_m\right). \tag{23}$$

To compute the Hessian, we begin by calculating the gradient with respect to the variable θ:

$$\nabla_\theta L = \frac{2}{M_{tr}} \sum_{m=1}^{M_{tr}} J_m^T (\mathcal{G}(f_m, \theta) - u_m), \tag{24}$$

where $J_m = \dfrac{\partial \mathcal{G}}{\partial \theta}(f_m, \theta)$ is the Jacobian matrix.
Now, differentiating again,

$$\nabla_\theta^2 L = \frac{2}{M_{tr}} \sum_{m=1}^{M_{tr}} \left(J_m^T J_m + \sum_i (\mathcal{G}(f_m, \theta) - u_m)_i \frac{\partial^2 (\mathcal{G})_i}{\partial \theta^2}(f_m, \theta) \right). \tag{25}$$

The first term of (25), $J_m^T J_m$, is a Gram matrix [8], which is positive semi-definite because for any vector v, we have:

$$v^T J_m^T J_m v = \|J_m v\|^2 \geq 0. \tag{26}$$

The second term of (25) involves second derivatives but is a weighted sum of Hessians of $\mathcal{G}$. If $\mathcal{G}$ is linear or approximately linear in θ, this term vanishes, leaving only $J_m^T J_m$, which is positive semi-definite. Even when this term does not vanish, it does not necessarily introduce negative eigenvalues.
In regions where the second term is small (e.g., near minima where the Hessian is dominated by the first term and is therefore positive semi-definite.

$$(\mathcal{G}(f_m, \theta) - u_m)_i \approx 0 \tag{27}$$

Thus, $\nabla_\theta^2 L$ is locally positive semi-definite, proving the theorem. □

Theorem 2. *The loss function* (19) *is L_s-smooth if its gradient is Lipschitz continuous, i.e., there exists a constant $L_s > 0$ such that*

$$\|\nabla L(\theta_1) - \nabla L(\theta_2)\| \leq L_s \|\theta_1 - \theta_2\|, \quad \forall \theta_1, \theta_2. \tag{28}$$

The presence of activation functions such as ReLU introduces piecewise linearity, potentially causing non-smooth regions where the gradient is discontinuous. In contrast, sigmoid and tanh activations ensure smoothness but can lead to vanishing gradient issues, affecting optimization dynamics.

Proof. The smoothness of $L(\theta)$ depends on the properties of the function $\mathcal{G}(f_m, \theta)$. We analyze the gradient behavior to establish Lipschitz continuity.
As in (24), the gradient of $L(\theta)$ is given by:

$$\nabla_\theta L = \frac{2}{M_{tr}} \sum_{m=1}^{M_{tr}} J_m(f_m, \theta)^T (\mathcal{G}(f_m, \theta) - u_m), \tag{29}$$

where $J_m(f_m, \theta)$ is the Jacobian of $\mathcal{G}$ with respect to θ.
To establish the Lipschitz condition, we analyze the difference:

$$\|\nabla L(\theta_1) - \nabla L(\theta_2)\| = \left\| \frac{2}{M_{tr}} \sum_{m=1}^{M_{tr}} J_m(f_m, \tilde{\theta})^T \left(\mathcal{G}(f_m, \theta_1) - \mathcal{G}(f_m, \theta_2)\right) \right\|, \tag{30}$$

where $\tilde{\theta}$ is an intermediate point between θ_1 and θ_2.
Using the submultiplicative property of norms,

$$\|\nabla L(\theta_1) - \nabla L(\theta_2)\| \leq \frac{2}{M_{tr}} \sum_{m=1}^{M_{tr}} \|J_m(f_m, \tilde{\theta})^T\| \cdot \|\mathcal{G}(f_m, \theta_1) - \mathcal{G}(f_m, \theta_2)\|. \tag{31}$$

If $\mathcal{G}$ is Lipschitz with constant $L_{\mathcal{G}}$, i.e.,

$$\|\mathcal{G}(f_m, \theta_1) - \mathcal{G}(f_m, \theta_2)\| \leq L_{\mathcal{G}} \|\theta_1 - \theta_2\|, \tag{32}$$

and the Jacobian is bounded such that $\|J_m(f_m, \tilde{\theta})^T\| \leq J_{\max}$, then

$$\|\nabla L(\theta_1) - \nabla L(\theta_2)\| \leq \frac{2 J_{\max} L_{\mathcal{G}}}{M_{tr}} \sum_{m=1}^{M_{tr}} \|\theta_1 - \theta_2\|. \tag{33}$$

Thus, setting $L_s = 2 J_{\max} L_{\mathcal{G}}$, we obtain the desired Lipschitz condition.
The impact of activation functions on smoothness is significant:

- **ReLU:** Since it is piecewise linear, it can introduce non-smooth points where the gradient is discontinuous [9].
- **Sigmoid and Tanh:** These functions ensure smoothness but suffer from vanishing gradients, making optimization difficult [10].

Thus, the choice of activation functions plays a crucial role in maintaining smoothness while ensuring effective gradient-based optimization.

□

Overall, the interplay between convexity and smoothness in the loss function significantly influences optimization efficiency. These properties aids in selecting suitable training strategies, such as adaptive gradient methods, second-order optimization techniques, and appropriate regularization schemes to enhance convergence stability.

5 RESULTS

In this chapter, we present the experimental results that evaluate the performance of our proposed approach. For this purpose, we utilize two images with irregular forms. The process begins with image processing and mesh generation, followed by finite element method (FEM) simulations to create reference data, and concludes with the MAgNET simulation.
Our process starts by reading an input image, which is then converted to a binary image using Otsu's thresholding. Contours are detected from the binary image, and the contour representing the object of interest is selected. This contour defines the object's boundary, which is used for mesh generation. The mesh is generated using the method described in Chapter 3.
Figure 1a shows the generated mesh overlaid on the original image for Image 1, with the boundary points highlighted and the triangulation clearly visible. Similarly, Figure 1b illustrates the mesh for Image 2.
To create these meshes, we used the parameters presented in Table 1.

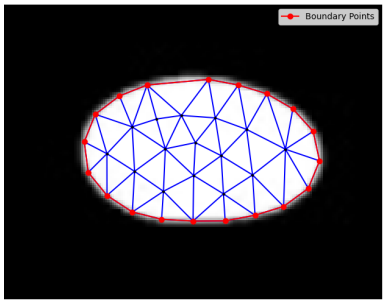

(a) Mesh overlay on the first image, showing the extracted boundary and Delaunay triangulation.

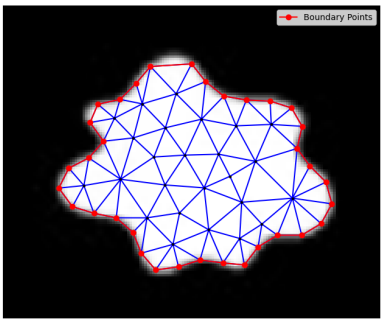

(b) Mesh overlay on the second image, displaying the refined mesh with Delaunay triangulation.

Figure 1: Meshes generated for two different images after applying Delaunay triangulation.

A FEniCS mesh is then constructed from the transformed points and the validated triangles. This mesh serves as the computational domain for our elasticity simulation. The mesh will be transferred to the neural network using the corresponding adjacency matrix. For the FEM simulation, we define a two-dimensional elasticity problem using a linear elastic material model. The material properties are characterized by Young's modulus and Poisson's ratio. Boundary conditions are applied on the left boundary to fix the displacement, and a subset of nodes is designated as fixed to simulate additional constraints. Random force values are applied to specific nodes (representing force application points) to generate a variety of simulation scenarios. For each simulation, the weak form of the elasticity problem is assembled and solved using a direct solver, yielding the displacement field across the mesh.

To create the dataset, multiple simulation samples are generated. For each sample, the resulting displacement field is extracted and stored, while the applied force vectors are recorded as features. The displacement results are concatenated into a single vector for each sample, and the entire dataset is split into training and testing subsets. These data arrays are then saved to CSV files for subsequent deep learning tasks.

Table 1 lists the key parameters used throughout the process for two images.

With the FEM-generated dataset and corresponding mesh connectivity now available, we proceed to implement the MAgNET deep learning framework.

The MAgNET simulation begins with data preprocessing, where the FEM-generated displacement and force data are formatted for input into the network. The model is then

Table 1: Key parameters used for Image-to-Mesh Conversion, FEM Simulation, and Dataset Creation for two images.

Parameter	**Image 1**	**Image 2**	**Description**
Number of Boundary Points	20	35	Points uniformly sampled along the contour.
Number of Interior Points	15	25	Interior points are uniformly sampled from within the contour.
Minimum Distance (Interior)	10	10	Minimum separation between interior points.
Minimum Distance to Boundary	15	10	Minimum separation of interior points from the boundary.
Young's Modulus, E	500	600	Elastic modulus used in the FEM simulation.
Poisson's Ratio, ν	0.3	0.3	Material Poisson's ratio used to derive the Lamé parameters.
Number of FEM Samples	5000	5000	Total number of simulation samples generated for the dataset.
Force Range	8 to 12	8 to 12	Range of force values applied at designated force nodes, in Newton.

trained on the training subset of the dataset, optimizing its parameters to minimize the error between the predicted displacements and the FEM reference values.
After training, we evaluate the performance of MAgNET on the testing subset. Figure 2 shows a comparison between the displacement fields predicted by MAgNET for Image 1 and those obtained from FEM simulations for a representative sample. Similarly, Figure 3 presents the corresponding comparison for Image 2.
The results demonstrate that MAgNET accurately reproduces the displacement patterns, offering a substantial improvement in computational efficiency over conventional FEM methods.
These findings suggest that MAgNET is a promising alternative for rapid, image-based assessment of material behavior, with significant potential for real-time monitoring and design optimization in engineering applications.

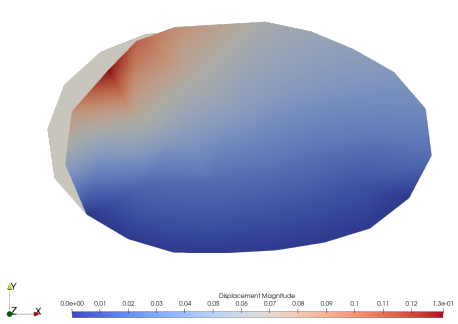

(a) FEM displacement field for Image 1.

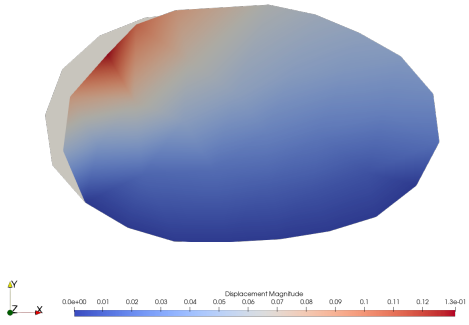

(b) MAgNET-predicted displacement field for Image 1.

Figure 2: Comparison of displacement fields for Image 1: FEM simulation versus MAgNET predictions.

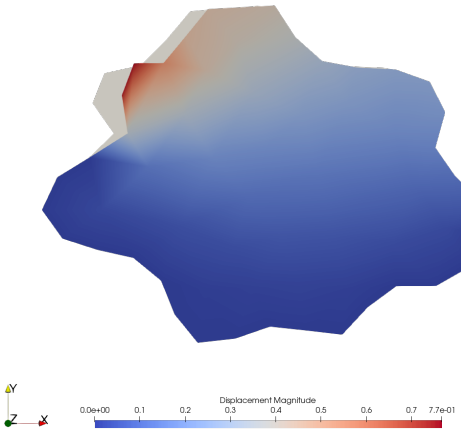

(a) FEM displacement field for Image 2.

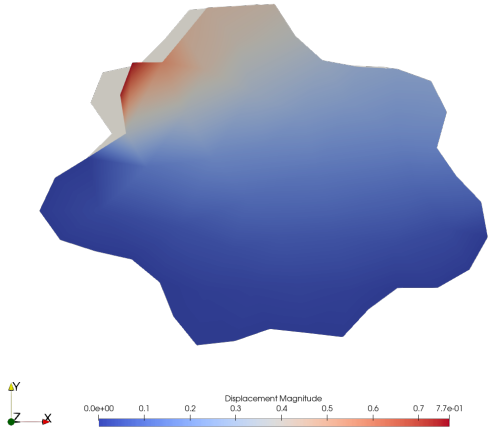

(b) MAgNET-predicted displacement field for Image 2.

Figure 3: Comparison of displacement fields for Image 2: FEM simulation versus MAgNET predictions.

6 CONCLUSIONS

In this work, we developed a comprehensive workflow that integrates image processing, mesh generation, FEM simulations, and a deep learning framework (MAgNET) to predict displacement fields directly from image data. Our experimental results demonstrate that the MAgNET framework is capable of closely reproducing the displacement fields obtained via traditional FEM simulations, while significantly reducing computational overhead.

This approach has the potential to enable rapid, image-based assessments of material behavior, which is particularly beneficial for real-time monitoring and design optimization in engineering applications.
Despite the promising results, certain limitations were identified, such as challenges in mesh quality for highly irregular shapes and the dependency on specific simulation parameters. Future research could address these limitations by refining the mesh generation process, exploring alternative deep learning architectures, and extending the methodology to a wider variety of materials and loading conditions.
Overall, this study contributes a novel method for coupling traditional simulation techniques with advanced neural network models, paving the way for more efficient and accessible simulation tools in engineering practice.

REFERENCES

[1] S. Deshpande, S. P. A. Bordas, and J. Lengiewicz, "MAgNET: A graph U-Net architecture for mesh-based simulations," *Engineering Applications of Artificial Intelligence*, vol. 133, p. 108055, Jul. 2024, doi: 10.1016/j.engappai.2024.108055.

[2] J. A. Rodrigues and B. Vieira, "A Mathematical Analysis of Image Mesh Generation Using Delaunay Triangulation and Image Processing Techniques," in *Proceedings of the 4th ROME International Conference on Challenges in Engineering, Medical, Economics and Education: Research & Solutions (CEMEERS-24b)*, Rome, Italy, Dec. 2024. [Online]. Available: https://hal.science/hal-04822865.

[3] Hong, H.,Jakuš, D. "Testing Positiveness of Polynomials", *Journal of Automated Reasoning* , Springer Netherlands Vol. **21(1)** , pp. 23-38, 1998

[4] Kunkle, D., "Roomy: a system for space limited computations", *PASCO '10 Proceedings of the 4th International Workshop on Parallel and Symbolic Computation* , Ed. Marc Moreno Maza and Jean-Louis Roch, Grenoble - France, pp. 22-25 , 2010.

[5] Reddy, J.N., *Mechanics of Laminated Composite Plates. Theory and Analysis*, CRC Press, New York, 1997.

[6] Hastie, T., Tibshirani, R., & Friedman, J., *The Elements of Statistical Learning*, Springer, 2009.

[7] Nocedal, J., & Wright, S. J., *Numerical Optimization*, Springer, 2006.

[8] Boyd, S., & Vandenberghe, L., *Convex Optimization*, Cambridge University Press, 2004.

[9] Glorot, X., Bordes, A., & Bengio, Y., *Deep Sparse Rectifier Neural Networks*, In Proceedings of the Fourteenth International Conference on Artificial Intelligence and Statistics, 2011.

[10] LeCun, Y., Bottou, L., Orr, G. B., & Müller, K. R., *Efficient Backprop*, In Neural Networks: Tricks of the Trade, 1998.

SYMCOMP 2025
Lisbon, 10-11 April 2025

A SPRING-CABLE MULTIBODY MODEL FOR ENERGY ABSORBING STRUCTURES IN RAILWAY VEHICLE CRASHWORTHINESS

João Milho[1,2], David Bronze[1]
1: CIMOSM, Instituto Superior de Engenharia de Lisboa, Instituto Politécnico de Lisboa, Lisboa, Portugal
e-mail: joao.milho@isel.pt, web: http://www.cimosm.isel.pt

2: IDMEC, Instituto Superior de Engenharia de Lisboa, Instituto Politécnico de Lisboa, Lisboa, Portugal

Keywords: Multibody Dynamics, Spring-Cable Model, Energy Absorption, Crashworthiness, Railway Vehicle

Abstract *Railway vehicle crashworthiness relies on crush zone structures to absorb impact energy during collisions. Due to the high costs of full-scale crash tests, numerical models, particularly multibody methods, have been widely used for their accuracy and efficiency. Traditional approaches use plastic-hinge models requiring specialized software, as general-purpose multibody tools lack nonlinear crushing models. This study proposes a spring-cable crushing multibody model for broader applicability in such software. The proposed crushing model was implemented using a linear spring model and a cable model which are updated with a spring stiffness corresponding to the current deformation state of the energy absorbing structure and a cable deformation length that prevents the spring elastic recovery. The model was validated using a real railway crash scenario, where a moving train collides with stationary cars. Simulation results accurately capture the nonlinear crushing dynamics, showing strong correlation with experimental data in terms of velocity and energy absorption. These findings demonstrate the model's suitability for railway crashworthiness design.*

HOW TO CITE THE FULL PAPERS – APA

List of articles with DOI and their citation

ID	DOI	Title	Citation
2	10.5281/zenodo.15150483	Synthetic Microscopic Platelets Images Generation using WGAN-GP	Abidoye, I., Ikeji, F., Coupland, C. A., Calaminus, S. D. J., & Sousa, E. (2025, April 4). Synthetic Microscopic Platelets Images Generation using WGAN-GP. SYMCOMP 2025 – 7th International Conference on Numerical and Symbolic Computation: Developments and Applications (SYMCOMP 2025), Lisboa, Portugal. https://doi.org/10.5281/zenodo.15150483
4	10.5281/zenodo.15160265	Incidence of Reputational Periodicity	Mitic, P. (2025, April 5). Incidence of Reputational Periodicity. 7th International Conference on Numerical and Symbolic Computation: Developments and Applications (SYMCOMP 2025), Lisboa, Portugal. https://doi.org/10.5281/zenodo.15160265
8	10.5281/zenodo.15160848	Computational Treatment of the Hierarchy of General and Evolution Algebras	Ruiz, A. V., Ruiz, R. V., & Valdés, J. N. (2025, April 5). Computational Treatment of the Hierarchy of General and Evolution Algebras. 7th International Conference on Numerical and Symbolic Computation: Developments and Applications (SYMCOMP 2025), Lisboa, Portugal. https://doi.org/10.5281/zenodo.15160848
12	10.5281/zenodo.15160962	A Pilot Study on Fine-tuning Named Entity Recognition for Clinical Tag Extraction Using Pretrained Language Models: The Tut-All Experience	Gbadamosi, A. V., Montero, A., Deutsch, M., Sander, N., Cashmore, C., & Sousa, E. (2025, April 5). A Pilot Study on Fine-tuning Named Entity Recognition for Clinical Tag Extraction Using Pretrained Language Models: The Tut-All Experience. 7th International Conference on Numerical and Symbolic Computation: Developments and Applications (SYMCOMP 2025), Lisboa, Portugal. https://doi.org/10.5281/zenodo.15160962
14	10.5281/zenodo.15161092	Automating the Derivation of Equations for 1D Mass Spring Damper Models in Matlab	Neves, M. M., & Policarpo, H. (2025, April 5). Automating the Derivation of Equations for 1D Mass-Spring-Damper Models in Matlab. 7th International Conference on Numerical and Symbolic Computation: Developments and Applications (SYMCOMP 2025), Lisboa, Portugal. https://doi.org/10.5281/zenodo.15161092

ID	DOI	Title	Citation
19	10.5281/zenodo.15161113	MS6 - Measuring Thoracic Muscle by Chest CT to Foresee Sarcopenia in Post-Covid 19 Patients	Ribeiro, M. M. C. P., & Sarmento, M. S. C. (2025, April 5). MS6 - Measuring Thoracic Muscle by Chest CT to Foresee Sarcopenia in Post-Covid 19 Patients. 7th International Conference on Numerical and Symbolic Computation: Developments and Applications (SYMCOMP 2025), Lisboa, Portugal. https://doi.org/10.5281/zenodo.15161113
23	10.5281/zenodo.15161128	Preliminary Simulation Results of a Molten Salt Thermal Storage Tank for Concentrated Solar Power	Mané, J., Malico, I., Domingues, N., Ait El Cadi, R., & Horta, P. (2025, April 5). Preliminary Simulation Results of a Molten Salt Thermal Storage Tank for Concentrated Solar Power. 7th International Conference on Numerical and Symbolic Computation: Developments and Applications (SYMCOMP 2025), Lisboa, Portugal. https://doi.org/10.5281/zenodo.15161128
30	10.5281/zenodo.15164512	Advanced Imaging of Parkinson's: Evaluating the Striatum and Substantia Nigra with Datscan Spect and T2W MRI	Mesquita, L., Ribeiro, M. M., & Vieira, L. (2025, April 6). Advanced Imaging of Parkinson's: Evaluating the Striatum and Substantia Nigra with Datscan Spect and T2W MRI. 7th International Conference on Numerical and Symbolic Computation: Developments and Applications (SYMCOMP 2025), Lisboa, Portugal. https://doi.org/10.5281/zenodo.15164512
34	10.5281/zenodo.15167567	Analysis of Thoracic Aortic Aneurysm CTA Scans Using Spatial Statistics	Oviedo Rodríguez, K., Carvalho, A., Valente, R., Xavier, J., & Tomás, A. (2025, April 7). Analysis of Thoracic Aortic Aneurysm CTA Scans Using Spatial Statistics. 7th International Conference on Numerical and Symbolic Computation: Developments and Applications (SYMCOMP 2025), Lisboa, Portugal. https://doi.org/10.5281/zenodo.15167567
50	10.5281/zenodo.15161179	Reliability Analysis and Failure Forecast of Critical Components Under Warranty	Sobral, J., & Subotin, F. (2025, April 5). Reliability Analysis and Failure Forecast of Critical Components Under Warranty. 7th International Conference on Numerical and Symbolic Computation: Developments and Applications (SYMCOMP 2025), Lisboa, Portugal. https://doi.org/10.5281/zenodo.15161179

ID	DOI	Title	Citation
51	10.5281/zenodo.15164446	Damping from Thermoelasticity in Structures Under Torsional Loading	Carvalho, A. R. D. (2025, April 6). Damping from Thermoelasticity in Structures Under Torsional Loading. 7th International Conference on Numerical and Symbolic Computation: Developments and Applications (SYMCOMP 2025), Lisboa, Portugal. https://doi.org/10.5281/zenodo.15164446
54	10.5281/zenodo.15167960	Mathematical Modeling of Metabolic Reprogramming and Therapeutic Strategies in Non-Small Cell Lung Cancer: A Flux Balance and Variability Analysis Approach	Lopes, J. S., Mendes, C., Gonçalves, L. G., Rodrigues, J. A., & Serpa, J. (2025, April 7). Mathematical Modeling of Metabolic Reprogramming and Therapeutic Strategies in Non-Small Cell Lung Cancer: A Flux Balance and Variability Analysis Approach. 7th International Conference on Numerical and Symbolic Computation: Developments and Applications (SYMCOMP 2025), Lisboa, Portugal. https://doi.org/10.5281/zenodo.15167960
56	10.5281/zenodo.15161193	Improving PD-L1 Expression Prediction in non-Small Cell Lung Cancer Using Radiomic Analysis and Ensemble Machine Learning Models on Whole-Body vs 18F-FDG Lung PET/CT Data	Olawale, S. M., Saleem, A., Roejkjaer, E., Avery, G., & Sousa, E. (2025, April 5). Improving PD-L1 Expression Prediction in non-Small Cell Lung Cancer Using Radiomic Analysis and Ensemble Machine Learning Models on Whole-Body vs 18F-FDG Lung PET/CT Data. 7th International Conference on Numerical and Symbolic Computation: Developments and Applications (SYMCOMP 2025), Lisboa, Portugal. https://doi.org/10.5281/zenodo.15161193
57	10.5281/zenodo.15161219	Improving PD-L1 Expression Prediction in non-Small Cell Lung Cancer Using Radiomic Analysis and Deep Learning Models on Whole-Body VS Lung 18F-FDG PET/CT Data	Olawale, S. M., Saleem, A., Roejkjaer, E., Avery, G., & Sousa, E. (2025, April 5). Improving PD-L1 Expression Prediction in non-Small Cell Lung Cancer Using Radiomic Analysis and Deep Learning Models on Whole-Body VS Lung 18F-FDG PET/CT Data. 7th International Conference on Numerical and Symbolic Computation: Developments and Applications (SYMCOMP 2025), Lisboa, Portugal. https://doi.org/10.5281/zenodo.15161219
61	10.5281/zenodo.15161235	Symbolic Computation Applied to Function Factorization Concept: The Rational Scalar Case	Conceição, A. C., Pires, J. C., & Coelho, C. (2025, April 6). Symbolic Computation Applied to Function Factorization Concept: The Rational Scalar Case. 7th International Conference on Numerical and Symbolic Computation: Developments and Applications (SYMCOMP 2025), Lisboa, Portugal. https://doi.org/10.5281/zenodo.15161235

ID	DOI	Title	Citation
62	10.5281/zenodo.15161249	Computational Analysis of Levenberg-Marquardt Method in Nonlinear Least Squares Problems	Ricardo, V., Coelho, C., Conceição, A. C., & Pires, J. C. (2025, April 6). Computational Analysis of Levenberg-Marquardt Method in Nonlinear Least Squares Problems. 7th International Conference on Numerical and Symbolic Computation: Developments and Applications (SYMCOMP 2025), Lisboa, Portugal. https://doi.org/10.5281/zenodo.15161249
63	10.5281/zenodo.15161263	Computational Modelling of Incident Solar Radiation and Application for Thermal Loads Calculation in Buildings	Agostinho, A., Carreira, F., & Casaca, C. (2025, April 6). Computational Modelling of Incident Solar Radiation and Application for Thermal Loads Calculation in Buildings. 7th International Conference on Numerical and Symbolic Computation: Developments and Applications (SYMCOMP 2025), Lisboa, Portugal. https://doi.org/10.5281/zenodo.15161263
65	10.5281/zenodo.15164468	Simulating Stresses and Strains in Solid Mechanics Directly from Images Using Convolutional Neural Networks	Vieira, B., Rodrigues, J., Deshpande, S., & Bordas, S. (2025, April 6). Simulating Stresses and Strains in Solid Mechanics Directly from Images Using Convolutional Neural Networks. 7th International Conference on Numerical and Symbolic Computation: Developments and Applications (SYMCOMP 2025), Lisboa, Portugal. https://doi.org/10.5281/zenodo.15164468

Author Index